Universidad del País Vasco
Euskal Herriko Unibertsitatea

DEPARTAMENTO DE INGENIERÍA QUÍMICA
INGENIARITZA KIMIKOA SAILA

Alumina and zeolite supported catalysts for CO_2 methanation: catalyst design, reaction mechanism and kinetics

Adrián Quindimil Rengel

Leioa, septiembre de 2021

para mi madre

por todo

En primer lugar, agradezco a mis directores, Dres. Juan Ramón González-Velasco y José Antonio González-Marcos, el apoyo, afecto y la confianza depositada en mi para realizar esta tesis doctoral. Gracias por acogerme en el grupo de investigación Tecnologías Químicas para la Sostenibilidad Ambiental (TQSA) desde inicios de mi carrera, lo cual contribuyó a despertar mi conciencia ambiental, y darme las pautas necesarias para llevar a cabo investigación con rigor y fundamento científico. También quisiera transmitir especial agradecimiento a el Dr. Beñat Pereda-Ayo, por motivarme y contagiarme su vocación no solo por la investigación sino también por la docencia.

A TODOS los miembros del grupo TQSA, por vuestra cordialidad y por haberme hecho sentir uno más desde el inicio. Me gustaría destacar la ayuda técnica y siempre inmediata recibida por los Dres. José I. Gutiérrez-Ortiz y Zouhair Boukha en la puesta a punto de equipos y diseño de protocolos experimentales. Por otra parte, agradezco el afecto, así como la ayuda en la redacción científica recibidos por el Dr. Unai De-La-Torre durante los primeros años de la tesis. Además, me siento muy afortunado por haber colaborado con el Dr. Ignacio Iglesias, quien logró contagiar su pasión por la ciencia e investigación aún en un breve periodo de tiempo. Por último, me gustaría transmitir mi agradecimiento y cariño a mis compañeros, Alberto J. Reynoso-Estévez, Juani Martín-Martín y Jon A. Onrubia-Calvo por los múltiples e inolvidables buenos momentos compartidos dentro y fuera de los laboratorios.

Thanks to professors Carlos Henriques and José M. Madeira Lopes for giving me the opportunity to join the CATHPRO group during my training stay in Instituto Superior Técnico (IST, in Lisbon) as well as for making me feel part of your group and sharing your knowledge. Likewise, many thanks to Carminha Bacariza for her professionalism and for getting fully involved in my research work at IST from the beginning of the stay and also to Ismail Mohamed for being the perfect lab partner, with whom I enjoyed very interesting conversations. Thank you both! The stay in Lisbon would not have been the same without your friendship.

A los técnicos del Servicio General de Análisis (SGIKER) de la UPV/EHU, Ana Martínez, Javier Sangüesa y María Belén Sánchez, por su excelente atención y trabajo.

A Aitor Arandia, por promover el compañerismo y por las buenas experiencias vividas. Por supuesto, no me olvido de mi cuadrilla de amigos (Ainhoa, Gontzal, Itxasne, Oier y Xabi), de Vicente e Irene, ni tampoco de Andrés, Cristina y la pequeña Carla, quienes siempre me han animado y ayudado a desconectar de formas variopintas.

Finalmente, el haber llegado hasta aquí se lo debo sin duda a mi familia. Mil gracias a mis padres y hermano por su incondicional cariño y apoyo durante el desarrollo del doctorado. Merece una mención especial mi madre, María Nieves Rengel Aguado, quien continuamente se involucró en las primeras etapas de mi formación, dándome la confianza que necesitaba para lograr el éxito académico. Gracias de corazón a mi pareja, Adriana Morales-Marín, por confiar ciegamente en mí y por levantarme una y otra vez en uno de los años más complicados de mi vida.

Este trabajo ha sido posible gracias al apoyo financiero de la Universidad del País Vasco a través de la beca de doctorado (PIF-15/351). Asimismo, el autor y sus directores agradecen al Ministerio de Economía y Competitividad (CTQ2015-67597-C2-1-R) y al Gobierno Vasco (IT657-13 y IT1297-19) por la financiación del proyecto.

INDEXES

CONTENTS, FIGURES AND TABLES

INDEX OF CONTENTS

INDEX OF FIGURES

INDEX OF TABLES

Chapter 1

INTRODUCTION

ABSTRACT

Progressive reduction of carbon dioxide emissions, considered the main route to decrease the impact of greenhouse effect on climate, is one of the mayor environmental challenge of today´s society. Since Paris agreement was adopted by most world´s countries in 2015, the number of projects to face that challenge have significantly increased. Although the replacement of fossil fuels with renewable energy sources is the best strategy to decarbonize the energy system and reduce CO_2 emissions, the renewable power installed today is still very far from meeting world´s energy demand. Consequently, the parallel development and implementation of alternative technologies is necessary to accelerate the transition into more resilient and cleaner energy system. The use of CO_2 to produce chemicals and fuels, will play an important role in meeting climate goals. The CO_2 methanation is attracting a lot of interest since it is thermodynamically the most favourable reaction. As the hydrogen employed in this reaction is produced via renewable electrolysis, not only CO_2 emissions are reduced but also renewable energy is stored in form of energy vector, such as methane. While it is known that Ni and Ru are the most active and selective metals to carry out CO_2 methanation, the catalytic performance of current supported catalysts still admits room for improvement at low temperature. The main objectives as well as the scope of this thesis are presented at the end of this chapter.

1. INTRODUCTION

Climate change is considered one of the greatest environmental threats of our time and its main cause is the increasing CO_2 emissions derived from the production of energy by fossil fuels combustion. During the last decades, not enough effort has been made to develop energy alternatives and renewable energy sources that reduce the amount of emitted CO_2. However, the consumption of fossil fuels is expected to fast increase in the coming years due to the inherent need for transportation, the growing global energy demand mainly caused by emerging economies and the exponential increase in population. In fact, if the current trend continues, it is estimated that CO_2 emissions could exceed 40 Gt/year by 2030 [1].

The replacement of fossil fuels by renewable energy sources, such as wind and solar PV, is currently a major challenge. Unfortunately, the electrical power obtained from wind turbines or solar panels is intermittent and, besides, is produced in places where it is not directly consumed. Therefore, there is a growing interest in the long-distance transport and storage of renewable energies [2]. As a solution, these green energies can be used to produce hydrogen by electrolysis of water, which subsequently can be combined with carbon dioxide, captured from the combustion of natural gas and other sources, and catalytically converted into synthetic natural gas (SNG) or methane (CH_4) according to the CO_2 methanation or Sabatier's reaction ($CO_2 + 4H_2 \rightleftarrows CH_4 + 2H_2O$).

This mitigation strategy aims to produce SNG from the use of CO_2 as carbon source, especially in heavy industries (e.g., power, steel and cement plants) where its decarbonisation is inviable. On that way, the amount of imported or purchased natural gas for the generation of electricity or heat is reduced (i.e., there is a saving in production costs), while potentially expensive CO_2 emissions (around 50 €/t) are diminished and the introduction of renewables into the energy system is facilitated. The SNG gas production from CO_2 and renewable H_2 is a viable catalytic process that was earliest verified by Hashimoto et al. [3] in a Japanese prototype plant. The different steps of the process are shown in Figure 1.1. The plant is provided by photovoltaic solar

panels, electrolytic cells for the production of H_2, two fixed bed reactors in which CO_2 methanation is carried out and a unit for the combustion of CH_4 and subsequent recovery of CO_2.

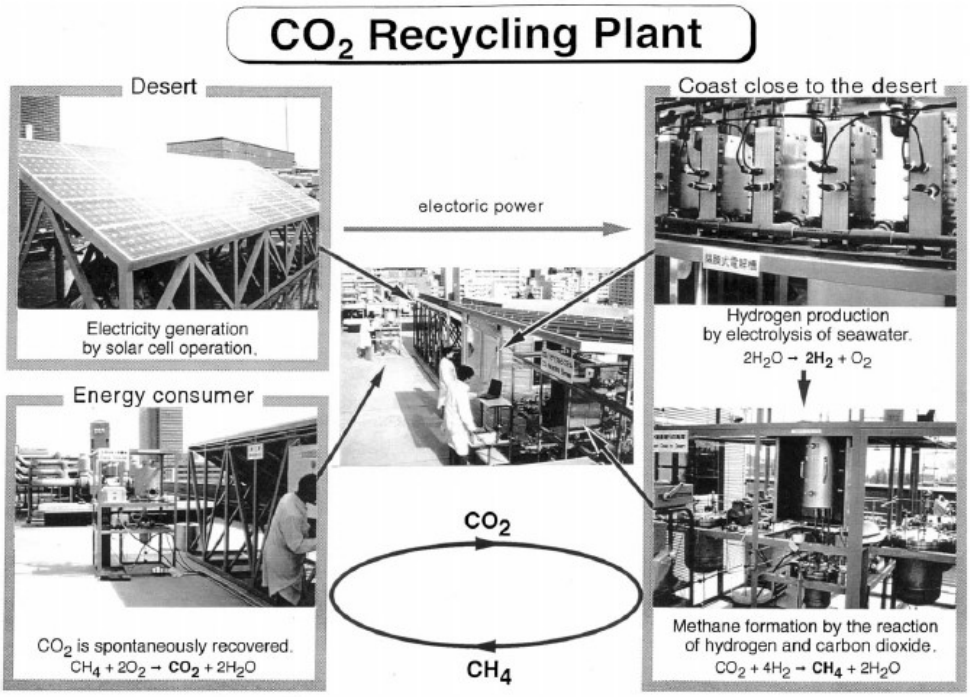

Figure 1.1. CO_2 recycling and SNG production prototype plant. Source: Ref. [3].

1.1. GREENHOUSE EFFECT, GLOBAL WARMING AND CLIMATE CHANGE

The privilege Earth´s position in the solar system and the presence of water are not the only conditions that make it a habitable planet. The other condition is that, unlike the moon, it has an atmospheric mechanism by which the heat is kept at night and reflected during the day, avoiding high temperature changes: the greenhouse effect. Responsible for this effect are the so-called greenhouse gases (GHG) which are retained by atmosphere and are of vital importance due to its ability to trap solar radiation. In fact, in the absence of greenhouse gases, the average global temperature would be -16 °C and our planet could not support life [4]. Noteworthy, only the 1% of

atmosphere´s volume is formed by greenhouse gases. The main GHG are water vapour (H_2O), carbon dioxide (CO_2), methane (CH_4), nitrous oxide (N_2O), chlorofluorocarbons (CFC) and ozone (O_3) [4-6].

Figure 1.2 depicts the energy budget (the balance between the incoming radiant energy from the sun and the outcoming energy from Earth back out to space) of the Earth-atmosphere system, where GHG play an important role.

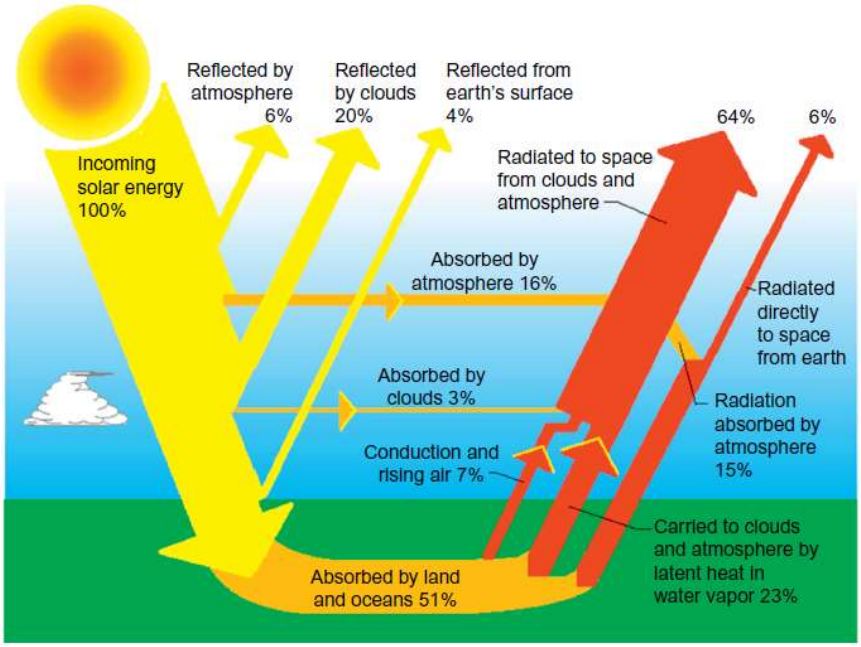

Figure 1.2. Earth´s energy budget. Source: Ref. [4].

It can be observed that around half of shortwave solar radiation (51% of the sun's incoming energy) hits the earth´s surface where it is adsorbed by lands and oceans, whereas the rest is directly absorbed by clouds and atmosphere (19%) or reflected back out to space (30%). Of total absorbed by the surface, 23% will be carried into the atmosphere by water vapour, 7% by conduction and rising air and the rest (21%) will be reflected as longwave infrared or thermal radiation, which can be trapped by greenhouse gases of the atmosphere [7].

As GHG absorb thermal infrared energy, their temperature rises and consequently, they randomly radiate an increasing amount of heat in all directions. The heat that is spread upwards will radiate freely to space at an altitude of around 5-6 km, whereas that spread downwards will come back into contact with and absorbed by the Earth´s surface giving rise to the above-mentioned natural greenhouse effect. Due to that mechanism and GHG, the surface temperature is higher than it would be if only heated by direct sunlight [4, 6].

Noteworthy, the energy budget of the system is constantly trying to maintain a thermostatic balance, being its average temperature the result of the heat leftover from the overall solar energy that is absorbed in one way or another. If the Earth´s energy budget is unbalanced through either natural phenomena or man´s activities, the Earth´s average temperature will eventually increase or decrease in order to restore the balance. Whatever affects the energy budget is called radiative forcing and can be classified into natural or anthropogenic type [4]. The former group includes changes in the Sun´s brightness, Milankovitch cycles (small variations in the shape of Earth´s orbit and its axis of rotation that occur over thousands of years) and large volcanic eruptions. The latter, instead, include aerosols emissions; deforestation, which changes how the surface reflects and absorbs sunlight; and the rising concentration of atmospheric carbon dioxide along with other greenhouse gases, which decrease heat radiated to space [8].

According to Intergovernmental Panel on Climate Change (IPCC) [1, 9], the Earth has experienced unprecedented global warming (the process by which average temperature increases globally) over the last century. The evolution of Global Mean Surface Temperature (GMST) with respect to the average temperature of the pre-industrial reference period (1850-1900) is shown in Figure 1.3. The GMST is calculated as the weighted average of near-Surface Air Temperature (SAT) changes over lands and Sea-Surface Temperature (SST) changes over the oceans. Note that GMST change (blue line) has exponentially increased since 1900, observing in 2018 around 1 °C global warming. In fact, the level of warming has increased at 0.3-0.7 °C per 30 years-period (1986-2015), being the rate of warming in 2017 0.15-0.35 °C higher than average

warming over that period [9]. Accordingly, the 1986-2005 period and 2006-2015 decade were 0.63 °C and 0.87 °C warmer than the preindustrial reference period, respectively.

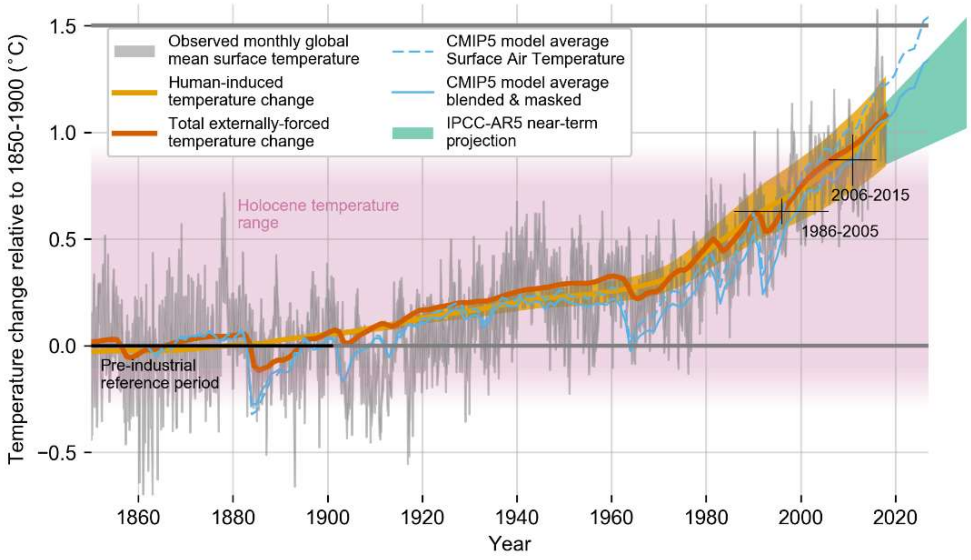

Figure 1.3. Evolution of global mean surface temperature (GMST) from 1850. Source: Ref. [9].

There is no doubt that anthropogenic forcings (yellow region), specifically CO_2 emissions, are the main cause of the observed fast global warming [5]. Nevertheless, global warming is not only reflected in the global temperature change of the atmosphere but also in changes of other climate system elements, such as the hydrosphere and cryosphere, which are grouped in the so-called climate change phenomenon. Among the climate change effects, the mentioned rise in global temperature, changes in precipitation patterns, increased frequency of droughts as well as heatwaves and sea-level growth due to the melting of poles are remarkable [10]. Consequently, many ecosystems are experiencing difficulties in the worst affected areas, having several species become extinct. In fact, it is estimated that a 1.5 °C global warming may put 20-30% of species at risk of extinction and warming higher than 2 °C will seriously struggle most ecosystems [1].

1.2. ANTHROPOGENIC CO_2 EMISSIONS

CO_2 is a colourless, odourless and inert gas. The acidic molecule has linear geometry with a double bond between the carbon and oxygen atoms (O = C = O). It is an essential source of carbon in the photosynthesis of plants and crops and constitutes 0.42% (417 ppm in May 2020) of the volume of the atmosphere. This section details the sources and evolution of CO_2 emissions.

1.2.1. Evolution and sources

The energy system of modern societies is roughly based on combustion of fossil fuels, among which the most relevant are coal, oil and natural gas. The complete oxidation of any of those hydrocarbons produces mainly H_2O and CO_2 (the lower the H/C ratio, the higher the amount of emitted CO_2), which until recently was considered a harmless gas. However, nowadays, it is widely and scientifically demonstrated that anthropogenic CO_2 emissions from fossil fuel combustion are the main cause of global warming and climate change [11-13]. The growth of atmospheric CO_2 concentration from 1960 as well as evolution of CO_2 emissions over the last 120 years are shown in Figure 1.4. It can be observed that atmospheric CO_2 concentration has steadily increased over the course of 60 years according to Mauna Loa observatory in Hawaii (see inset graph). The concentration of CO_2 is currently around 410 ppm, which represents a 47% increase since the beginning of industrial period (280 ppm) and an 11% increase since 2000 (370 ppm). It is known that this growth is mainly due to human activities, since CO_2 produced from fossil fuels combustion has different ratio of heavy-to-light carbon atoms ($^{13}C/^{12}C$), so it leaves a distinct “fingerprint” that instruments can measure [11].

As above-mentioned, the main cause of CO_2 concentration is fossil fuels burning. In fact, note that the CO_2 global emissions (blue line) from combustion processes have analogously increased over the last century. This rapid general rise is not only related to development of economies but also to exponential increase in world´s population, which is increasingly demanding more and more energy. However, emissions have also experienced particular decreases throughout 120-years period due to several historical

events such as Great depression (1929) and World War II (1939-1945), which also caused the decline of economies and energy demand.

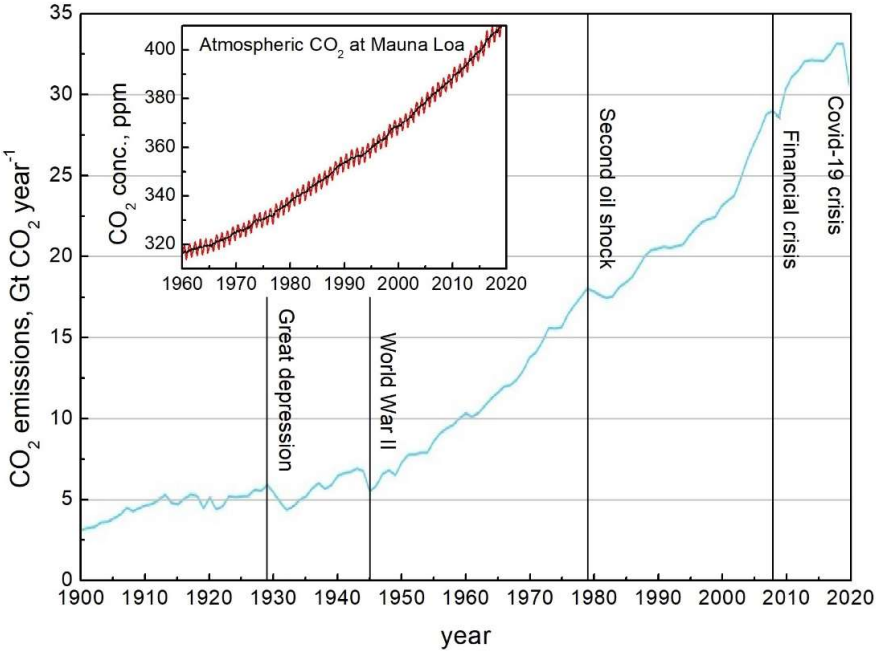

Figure 1.4. Global energy-related CO_2 emissions. Adapted from: Refs. [11, 12].

Similarly, the global CO_2 emissions, which achieved maximum value of 33.51 Gt in 2018, have rapidly decline in 2020 due to the Covid-19 crisis. According to the International Energy Agency (IEA) [12], the amount of CO_2 emitted during 2020 was 30.8 Gt, almost 8% lower than in 2019 and the lowest level recorded since 2010. Noteworthy, such reduction is the largest ever recorded, six times larger than the previous record reduction of 0.4 Gt in 2009 due to the financial crisis and twice as large as the combined total of all previous reductions since the end of World War II.

Regarding CO_2 emissions sources, it should be mentioned that they are not evenly distributed throughout the territories. In fact, only China, United States of America and India, which emitted 9.57, 4.92 and 2.31 Gt CO_2 in 2018, accumulated around 50% of global CO_2 emissions [13]. The fourth and fifth places were occupied by the Russian

Federation and Japan, which reported CO_2 emissions of 1.59 and 1.08 Gt CO_2 that same year. The amount of emitted CO_2 per country depends on many factors such as the degree of development or industrialization, the type of energy generated and the population of the territory. Likewise, the classification of CO_2 emissions per sector is not the same in all countries.

As an example, Figure 1.5 shows the distribution of total CO_2 emissions by sector of Spain in 2018. Unlike in many other countries, the sector with the highest number of CO_2 emissions is transport (37%) rather than power and heat generation sector (28%). This is because Spain is a developed country with a warm climate that does not demand much electricity and heat. On the contrary, the contribution of power and heat generation sector to CO_2 emissions in a cold territory such as Russian Federation is 50%. Besides, data indicate that in Spain Industry sector is not as important as, for example, in China, which contribution to CO_2 emissions in 2018 was around double (28.0 vs. 13.7%). Finally, note that the contribution of commercial and public services sector is similar to the residential one, which indicates that it is a very important activity in Spain´s economy.

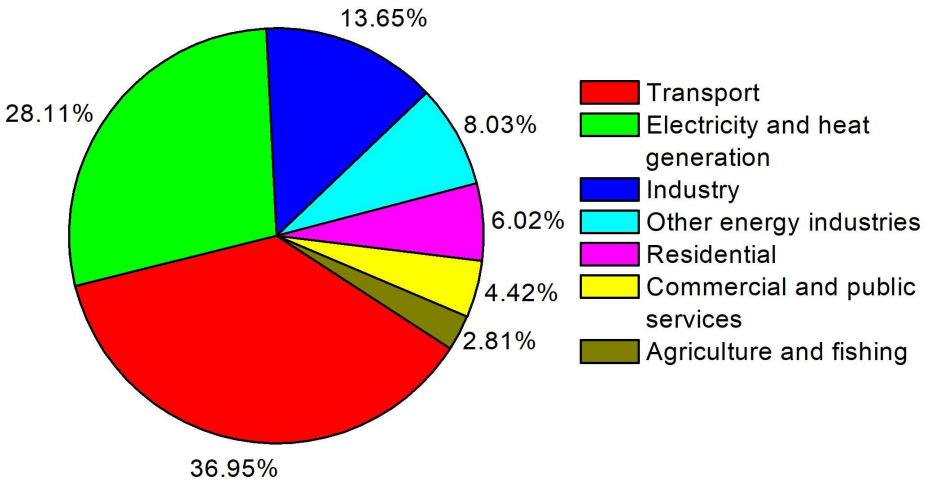

Figure 1.5. Spain's CO_2 emission by sector in 2018.

1.2.2. Climate action

Nowadays, the main international agreement to mitigate climate change is the United Nations Framework Convention on Climate Change (UNFCCC) [14], which ultimate objective is to stabilize greenhouse gas concentrations at a level that would prevent dangerous anthropogenic interference with the climate system. This convention was entered into force in 1994 and is currently ratified by 197 members, including industrialized countries as well as economies in transition. The member countries have met annually at the Conference of the Parties (COP) since 1994, where discussions on climate issues are held in order to find better environmental solutions. The most important COP sessions were those celebrated in Japan (COP3) and France (COP21), where Kyoto protocol and Paris agreement were adopted, respectively.

The Kyoto protocol was an international treaty divided into two periods that committed 37 industrialized countries and the European Union to carry out specific actions or policies that reduce CO_2 emissions in accordance with agreed individual targets [15]. The state parties fulfilled the commitment of reducing GHG emissions around 5% against 1990 levels during the first period (2008-2012) and in the second period (2013-2020), a more ambitious GHG emissions reduction of at least 18% below 1990 levels was committed. However, the participation of parties was lower in the latter period, staying out countries with high environmental impact such as Japan, Russia and United States.

On the other hand, the Paris Agreement is a legally binding international treaty on climate change that was adopted by 196 Parties in 2016 [16]. Unlike Kyoto protocol, the Paris agreement bring almost all nations into a common cause to undertake ambitious efforts to combat climate change and adapt to its effects. This agreement enters into force in 2021 and its main goal is to limit global warming to well below 2 °C, preferably to 1.5 °C, compared to preindustrial levels. To avoid exceeding the 1.5 °C threshold, the global CO_2 emissions in 2030 must reduce 45% with respect to 2010 and must be zero by mid-century, according to the last report of Intergovernmental Panel on Climate Change (IPCC) [9]. To ensure that the objectives are met, state parties must submit the actions they will take to reduce GHG emissions and to build resilience

against global warming within the Nationally Determined Contributions (NDCs). Besides, countries must report on actions taken and progress in climate change mitigation by the Enhanced Transparency Framework (ETF).

Finally, as many state parties, Spain is in the process of developing a new climate change and energy transition law [17] to meet its international commitments by 2030, which are GHG emissions reduction of 23% with respect to 1990 and to achieve a contribution of renewable energies in final energy consumption of at least 42% (against actual 20%). The law proposes remarkable issues in transport, electric and construction sectors, such as promoting the replacement of internal combustion engine vehicle by electric ones, increasing the share of renewable electricity generation and enhancing the energy efficiency of buildings sectors by rehabilitation and renovation plans, respectively. Besides, the law promotes integration of fuels produced by renewable energy. In this context, research on the catalytic synthesis of natural gas or methane from renewable H_2, which is the main goal of the present thesis, results potentially useful and interesting.

1.3. DECARBONIZATION OF THE ENERGY SYSTEM

Global anthropogenic CO_2 emissions were reduced about 8% (2.6 Gt of CO_2) in 2020, as a result of the Covid-19 crisis [12]. This fact, although results from lockdown measures and economy slowdown, may turn into the starting point from which CO_2 emissions progressively decline in the future if adequate actions are taken. According to IEA, governments which committed to Paris agreement have now the chance to accelerate the transition into a more resilient and cleaner energy system, while rebooting their economies and creating new jobs. Making the right investments, the economic growth can work together with a sustainable recovery plan, which might lead to air pollution emissions decrease of 5% by 2023 [18]. This plan, among other objectives, contemplates: (i) accelerating the installation of low carbon energy sources (such as renewable wind and solar PV) along with the expansion and modernisation of electricity grids; (ii) turn fuels production and utilization more sustainable; and (iii)

boost innovation in crucial technology areas including hydrogen, batteries, CO_2 utilisation and small modular nuclear reactors.

There is no doubt that the first strategy constitutes the most suitable alternative to decarbonize the energy system. Unfortunately, the complete replacement of fossil energy by immature renewable green energies takes a lot of time and financial effort, which allows for the parallel development and implantation of alternative strategies at medium term. Among others, Carbon Capture and Storage (CCS) along with Carbon Capture and Utilization (CCU) technologies seem to have an important and diverse role in meeting global energy and climate goals [19, 20]. Both processes first involve the capture of CO_2 from large point sources (e.g., power generation plants) that burn both fossil fuels and biomass or direct CO_2 trapping from atmosphere. Then, if not being used *in situ*, the captured CO_2 is compressed and transported by pipeline, ship, rail or truck to finally be used either in a range of applications following CCU route or injected into deep geological formations which trap CO_2 for permanent storage (CCS route). While combination of both routes (CCUS) contributes to climate change mitigation, the technologies for the CO_2 capture and geological storage are expensive and energetically intensive, so using CO_2 as a carbon source – instead of storing as a waste – is presented as a better alternative.

It must be highlighted that this strategy aims to reduce atmospheric CO_2 emissions by the use of “recycled carbon”, so that “fossil carbon” burning is avoided as much as possible. In other words, it is about complement the natural carbon cycle by developing man-made industrial processes in which “spent carbon” or CO_2 is converted into “working carbon”, as that present in valuable chemicals and fuels [21]. In this sense, it is expected that CCUS will play four strategic roles in the energy transition to net zero [20]:

1. Trickling emissions from existing infrastructure. CCUS can be retrofitted to existing power and industrial plants which could otherwise still emit 8 Gt CO_2 in 2050.
2. A cost-effective pathway for low-carbon hydrogen production from reforming and gasification processes, specifically in developing countries.

3. A solution for the most challenging emissions of heavy industry. This technology can tackle emissions in sectors where other options are limited, such as cement, steel and paper industries.
4. Removing carbon from the atmosphere by combining it with bioenergy or direct air capture to balance emissions that are technically difficult to abate.

As shown in Figure 1.6, CO_2 can be used as raw material in a range of production processes and services.

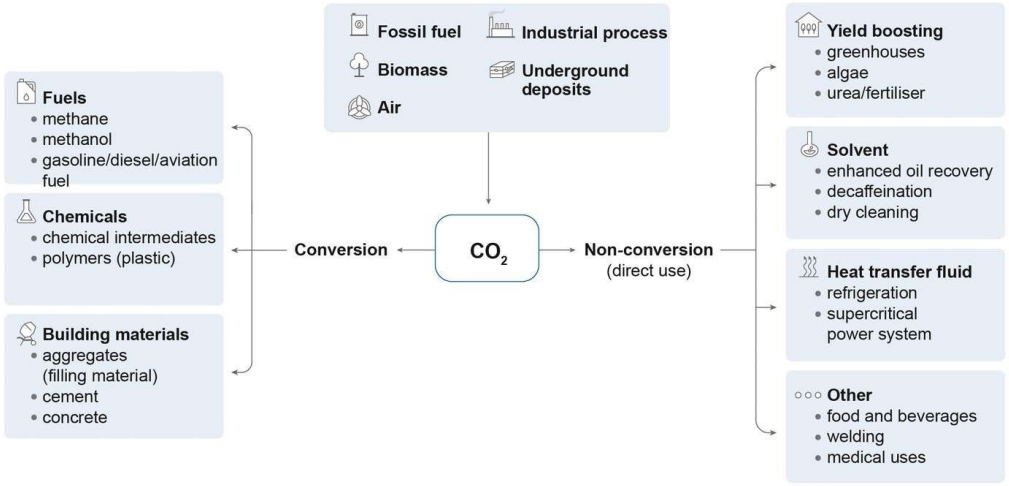

Figure 1.6. CO_2 utilisation pathways. Source: Ref. [22].

The potential application for CO_2 use includes direct use (non-conversion) and the transformation of CO_2 into useful products through chemical and biological processes (conversion). According to IEA [22], today around 230 Mt of CO_2 are used globally each year, primarily to produce fertilisers (around 125 Mt/year) and for enhanced oil recovery (around 70-80 Mt/year). Besides, CO_2 is commercially used in food and beverage production, in cooling systems as heat transfer fluid and for yield boosting in crop greenhouses. Regarding new CO_2 conversion pathways, those include fuels synthesis, chemicals production, and building materials manufacturing. While all routes will contribute to climate goals, the synthesis of green fuels is clearly the most important, since the amount of CO_2 emitted from fossil fuels combustion in power

generation and industrial plants is two orders of magnitude higher than the employed in direct use or chemicals production [23].

1.3.1. Fuels production from renewable H_2 and CO_2

Nowadays, hydrogen represents a versatile energy vector, with a great potential to help address various critical energy challenges [24, 25]. Hydrogen can be produced through conventional thermal processes, such as oil or natural gas reforming and coal gasification, or non-thermal production processes, among which water electrolysis is the more extended. As conventional routes emit a significant amount of CO_2, low carbon water electrolysis is the main rational way to produce H_2 for fuels production. Electrolysers enable the production of clean hydrogen from renewable electricity and water. In recent years, the number of projects and installed electrolyser capacity have expanded considerably: from less than 1 MW in 2010 to more than 25 MW in 2019 [24]. Alkaline electrolysers constitute the most mature electrolysis technology. However, many new projects are now opting for polymer electrolyte membrane (PEM) designs, since they can operate more flexibly and are therefore more compatible with variable renewable electricity generation.

Although H_2 is the fuel with the highest calorific value (33,900 kcal kg^{-1}) and no CO_2 is formed from its combustion, it presents some significant drawbacks [26]: (i) very expensive and emissions-intensive cryogenic storage owing to its low density; (ii) infeasibility of large-scale transport due to incompatibility with the current gas grid; and (iii) low implementation or availability of large-scale power generation systems (fuel cells). Accordingly, hydrogen is already used in some industries as raw material, but it has not yet realized its potential to support clean energy transitions. Still ambitious, targeted and near-term actions are needed to further overcome barriers and reduce costs [25]. Nevertheless, H_2 can be combined with CO_2 and catalytically converted into several energy vectors and fuels with major current applicability: from C1-type molecules (CO, CH_3OH) to higher molecular weight hydrocarbons, such as dimethyl ether, alkanes and olefins. Both homogeneous and heterogeneous catalysts can be used for that purpose. However, the latter are preferable in terms of stability, separation, handling and reuse as well as reactor design, which reflects in lower

costs [27]. The description of the main CO_2 hydrogenation routes into fuels is shown in Table 1.1.

Table 1.1. Summary of the main CO_2 hydrogenation routes into fuels.

Route and reaction	Description
CO_2 to CO (RWGS): $CO_2 + H_2 \rightleftarrows CO + H_2O$	The Reverse Water Gas Shift (RWGS) is one of the main routes of syngas (H_2 + CO) production, which constitutes the starting point towards higher hydrocarbons. The RWGS is an endothermic reaction that occurs at many high-temperature processes, wherever CO_2 and H_2 are present in the reaction mixture. Mostly it is catalysed by copper-based and iron-based catalysts [27, 28]. The former is normally promoted by a thermal stabilizer, namely Fe, to avoid Cu particle sintering, whereas the latter is usually promoted by Cr^{3+} that inhibit the recrystallization of the magnetite (Fe_3O_4). Recently, Ce-based catalysts (PTGM/CeO_2 and Ni/CeO_2) have demonstrated to be suitable for this process [29, 30].
CO_2 to CH_4 (CO_2 meth.): $CO_2 + 4H_2 \rightleftarrows CH_4 + 2H_2O$	Catalytic hydrogenation of CO_2, also known as CO_2 methanation, is currently becoming an important catalytic process with a range of applications including ammonia syngas stream purification and production of synthetic natural gas (SNG). CO_2 methanation is a thermodynamically favourable exothermal reaction, but with high kinetic limitations (eight-electron reduction process). It requires a catalyst active at mild temperature to achieve acceptable rates and selectivities. Generally, supported Ni and Ru formulations are employed for this process [31].
CO_2 to CH_3OH: $CO_2 + 3H_2 \rightleftarrows CH_3OH + H_2O$	The hydrogenation of CO_2 into methanol is another effective way for CO_2 valorization. In fact, methanol is nowadays either used as a solvent, alternative fuel or raw material in the chemical industry [32]. The exothermic reaction, with decreasing number of moles, is favoured by increasing pressure and temperature. Generally, the formulation used is the same as employed to conduct CO hydrogenation into methanol. Although catalysts with several active sites (e.g., Ag and Au) have been studied, Cu-based ones continue to be the most active. Those are often modified by the addition of different oxides (e.g., ZnO, ZrO_2, Al_2O_3, TiO_2 and Ga_2O_3) to improve their activity and stability [33, 34].

Table 1.1. Summary of the main CO_2 hydrogenation routes into fuels.

Route and reaction	Description
CO_2 to CH_3OCH_3 (2 steps): $CO_2 + 3H_2 \rightleftarrows CH_3OH + H_2O$ $2CH_3OH \rightleftarrows CH_3OCH_3 + H_2O$	The synthesis of dimethyl ether (DME) from CO_2 is the result of two reactions in series (two-step process): the above-described methanol synthesis followed by methanol dehydration into DME [32]. DME is a potential substitute for diesel due to its better combustion properties, such as high cetane number and low N content. It also can be produced in a single-step process using a multifunctional catalyst able to perform the two reactions simultaneously [35]. The bifunctional catalyst must content a methanol forming component (e.g, Cu-ZnO) and an acid component (e.g., H-ZSM5 zeolite) where methanol is subsequently dehydrated.
CO_2 to C_xH_y (FT): Direct route: $CO_2 \rightarrow CO \rightarrow C_nH_{2n+2}$ Indirect route: $CO_2 \rightarrow CH_3OH \rightarrow C_nH_{2n}$	The production of hydrocarbons from CO_2 is essentially a modification of Fischer-Tropsch (FT) synthesis, where CO_2 is used rather than CO and in which the catalyst composition is tailored to maximize the production of light alkanes and olefins [27]. It can be carried out by direct or indirect routes. In the direct route, CO_2 is hydrogenated into hydrocarbons by RWGS followed by FT, whereas in the indirect route CO_2 is first converted into methanol intermediate and then into light olefins or gasoline. However, the direct route is more common. The formulations employed on this kind of reactions usually present similar compositions to those used in FT synthesis, but with little modifications so that they can simultaneously hydrogenate both CO and CO_2. For instance, Fe-Al_2O_3-Cu-K catalyst has resulted to be a suitable catalyst for this application [36]. In this formulation, Al_2O_3 acts as excellent support for CO_2 hydrogenation into CO and K promoter suppress the formation of CH_4. On the other hand, Cu favours the reducibility of the catalyst and provides additional sites for H_2 dissociation.

Among the different conversion alternatives, CO_2 methanation is known to be one of the most thermodynamically favourable reactions. In fact, the standard Gibbs free energy of CO_2 methanation has proved to be the lowest (ΔG° = – 113 kJ/mol) according to a study on the thermodynamics of the main CO_2 hydrogenation routes. In comparison, the standard Gibbs energy of methanol and dimethyl ether synthesis were 3.5 and – 4.9 kJ mol^{-1}, respectively. This is one of the main characteristics that

motivated the choice of CO_2 methanation reaction, as CO_2 utilisation route, in the present doctoral thesis on catalysis.

1.4. CO_2 METHANATION

As above mentioned, the replacement of renewable energy is presented as the better strategy to overcome climate change. By 2050, this carbon-free sustainable energy is expected to play an important role in a mixed energy system. At present, however, renewable energy sources remain considerably less efficient and therefore less profitable than fossil energy sources. The lower efficiency of renewable energies is in part due to their intermittency: wind and solar energy are fluctuating and have to be balanced for electric grid stability purposes. This also implies that part of the renewable power may be lost during low energy demand periods. For that reason, there is a growing interest in the development of renewable energy storage form [2].

In this sense, the emerging Power-to-Gas (PtG) technology could contribute to solving the problem. The PtG process links the power grid with the gas grid by converting surplus power into a grid-compatible gas via a two steps process: H_2 production via electrolysis and CO_2 methanation [37, 38]. As depicted in Figure 1.7, carbon dioxide captured from flue gas can be combined with H_2 generated from surplus renewable energy (via electrolysis) and catalytically converted into methane or synthetic natural gas (SNG). Thus, CO_2 is used as raw material instead of being emitted as waste and renewable energy is stored in form of a low-carbon fuel such as methane. Besides, as H_2 is produced via water electrolysis in low electricity demand periods, renewable power is better exploited, which promotes its development and expansion. The produced CH_4 can be easily stored or widely distributed in the current gas grid and, afterwards, can be used again for power and heat generation in private homes, mobility sector or industry [38].

The viability of this process at industrial scale has already been demonstrated by the e-gas plant of Audi Motor Company located in Werlte (Germany). This plant, which is the biggest Power-to-Gas type worldwide, efficiently produces 1000 tons of SNG per year, combining renewable hydrogen and concentrated CO_2 from a nearby biogas plant

in cooled in fixed-bed reactors, where fundamental CO_2 methanation reaction takes place on a catalyst. In the following sections, an analysis of the thermodynamic aspects is carried out, as well as a brief review of formulations employed to catalyse it.

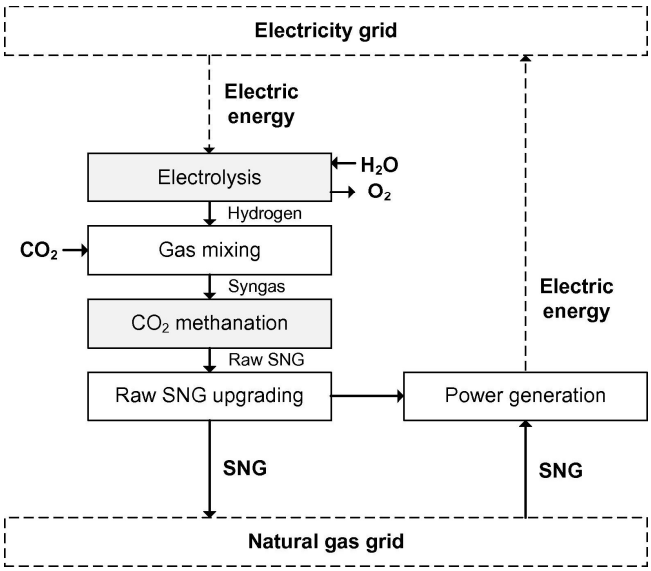

Figure 1.7. Exemplary Power-to-Gas plant. Source: Ref. [37].

1.4.1. Thermodynamics

The CO_2 methanation is also known as Sabatier reaction, since it was discovered by Paul Sabatier and Jean-Baptiste Senderens in 1902. As mentioned, it is a highly exothermic reaction ($\Delta H = -165$ kJ mol^{-1}) through which CO_2 is hydrogenated into CH_4:

$$CO_2 + 4H_2 \rightleftarrows CH_4 + 2H_2O \quad (1.1)$$

However, under Sabatier reaction conditions, other reactions can take place, which are summarized in Table 1.2. Among the side reactions, Reverse Water Gas Shift (RWGS) is the most probable. In fact, CO_2 methanation can be considered the sum of two reaction in series: first the RWGS (Equation 1.2) and then CO methanation reactions (Equation 1.3).

Table 1.2. Possible reactions involved in CO_2 methanation.

Reaction	Formula	ΔH (kJ mol^{-1})	Eq.
Reverse WGS	$CO_2 + H_2 \rightleftarrows CO + H_2O$	41.2	(1.2)
CO methanation	$CO + 3H_2 \rightleftarrows CH_4 + H_2O$	– 206.1	(1.3)
Dry reforming	$CO_2 + CH_4 \rightleftarrows 2CO + 2H_2$	247.3	(1.4)
Boudouard reaction	$2CO \rightleftarrows C + CO_2$	– 172.4	(1.5)
CO reduction	$CO + H_2 \rightleftarrows C + H_2O$	– 131.3	(1.6)
CO_2 reduction	$CO_2 + 2H_2 \rightleftarrows C + 2H_2O$	– 90.1	(1.7)

In recent literature, various studies on CO_2 methanation thermodynamics are available [39-42], in which the effect of some operational parameters (e.g., temperature, pressure and H_2/CO_2 feed ratio) on equilibrium CO_2 conversion and CH_4 selectivity is studied based on Gibbs free energy minimization. The influence of pressure on CO_2 within 200-800 °C temperature range is displayed in Figure 1.8. It can be observed that CO_2 conversion decreases with temperature, whereas it increases as pressure is elevated from 1 to 100 atm at T < 600°C. The former is related to the exothermic character of the reaction: the equilibrium constant becomes smaller as the temperature increases, which results in shifting the reaction to the left, reducing the amount of converted CO_2 [39]. The latter, instead, is due to CO_2 methanation is volume reducing reaction that is favoured by increasing pressure [40].

In addition, it can be deduced that conversion increases with pressure to linear saturation. Thus, in the 1-10 atm pressure range, the CO_2 conversion at 400 °C increases a remarkable 10% (from 85 to 95%), while in the 10-100 atm range only a 4% (from 85 to 99%). Regarding selectivity, similar trends are observed. The significant decrease of CH_4 selectivity is mainly attributed to CO formation via endothermic reverse water gas shift, which starts to dominate from 400 °C. In fact, in the worst case (P = 1), the methane equilibrium selectivity is reduced from 100 to around 55% with increasing temperature from 400 to 600 °C. However, the formation of carbon deposits seems negligible at H_2/CO_2 = 4 since it is avoided by the high H_2 partial pressure and water formation [41, 42].

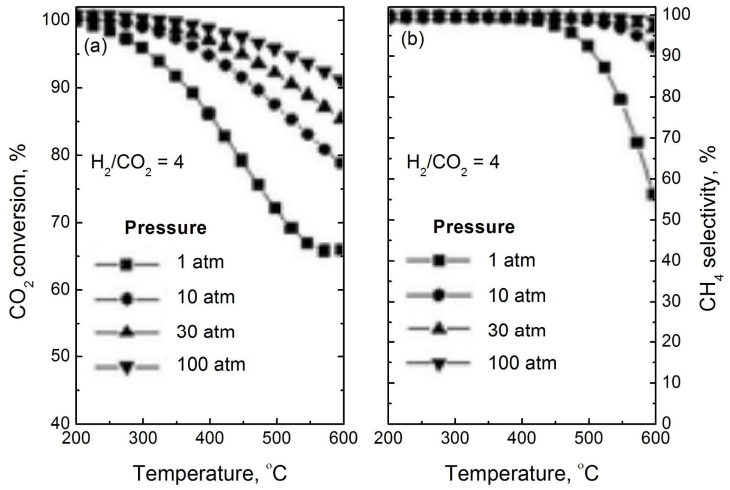

Figure 1.8. Influence of total pressure on equilibrium (a) CO_2 conversion and (b) CH_4 selectivity at H_2/CO_2 = 4. Adapted from: Ref. [39].

Analogously, Figure 1.9 shows the effect of the H_2/CO_2 ratio on activity and selectivity at 1 and 30 atm. In general, the catalytic performance is considerably affected by the feed ratio, observing an enhancement of CO_2 conversion and CH_4 selectivity when increasing H_2/CO_2 stoichiometric ratio. In fact, CO_2 conversion is increased from 85 to 99.5% by switching H_2/CO_2 ratio from 4 to 6 at 1 atm and 400 °C. On the other hand, it should be mentioned that, regardless of the pressure, only about 50-70% CO_2 equilibrium conversion and maximum CH_4 selectivity of 73-88% can be achieved at a H_2/CO_2 ratio of 2. In this line, the formation of undesirable coke could be up to 50% below 500 °C when working at sub-stoichiometric feed ratios according to Gao et al. [39].

Therefore, based on the thermodynamic data, the CO_2 methanation reaction must be conducted at temperatures between 250-400 °C and pressure not much greater than 10 atm to achieve industrial levels of CO_2 conversion (X_{CO_2} > 90%) and CH_4 selectivity (S_{CH_4} > 99%). Besides, H_2/CO_2 should not be lower than 4 even at high pressure (P = 30 atm) to avoid the formation of coke and consequent catalyst deactivation.

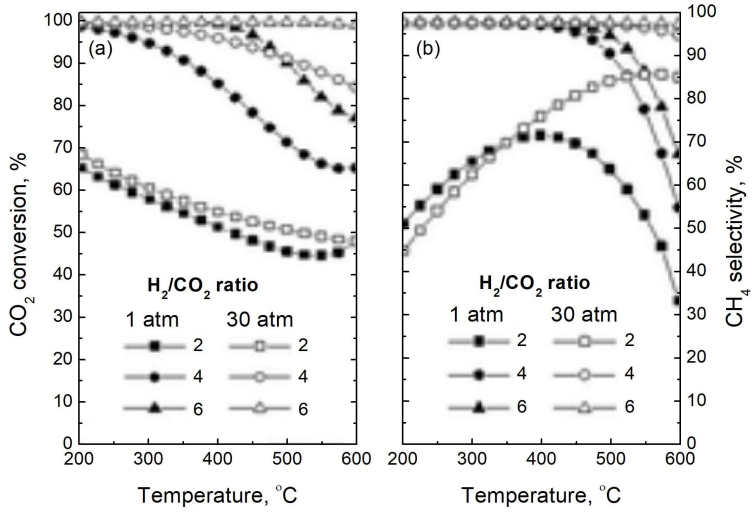

Figure 1.9. Effect of H_2/CO_2 feed ration on equilibrium (a) CO_2 conversion and (b) CH_4 selectivity at P = 1 or 30 atm. Adapted from: Ref. [39].

On the other hand, an operational gas hour space velocity (GHSV) as low as possible is recommended (the lower the GHSV, the higher the contact time and CO_2 conversion). As reported by Lazdans et al., it ranges from 4000-20,000 h^{-1} in industry. Finally, regarding the gas feed composition, the presence of O_2 that would react with H_2 reagent and other pollutants (e.g, NO_x, SO_x and CO) must be avoided to prevent the catalyst from fast deactivation.

1.4.2. Catalysts

As previously mentioned, the CO_2 methanation is a thermodynamically favourable reaction but with high kinetic limitations due to the eight-electron transfer requirement for the complete reduction of CO_2 into CH_4. Then, while achieving an almost 100% CO_2 conversion with high selectivity into CH_4 is thermodynamically available at low temperature, the presence of a very active catalyst is needed to overcome those kinetic barriers.

Accordingly, many catalysts have been developed since CO_2 methanation reaction was discovered by Sabatier more than 100 years ago. Generally, catalysts used in CO_2

methanation are heterogeneous type and consists of group VIII transition metals supported over mesoporous solid oxides. The metal acts as active phase, while the oxide as support. On the one hand, Ni and Ru have been the most used metals of such group [31]. This is because Ni and Ru, in their reduced state, are able to effectively dissociate the hydrogen that reacts with adsorbed CO_2. Ni-based catalysts have been extensively investigated because of their high activity and low price [43-47], whereas Ru-based catalysts due to their excellent activity and selectivity at low temperature [48-52]. It seems that Ni-based catalysts require high metal loadings and are easily deactivated by sintering or coke deposition, in a more extension than Ru based catalysts, which in turn are much more expensive.

On the other hand, mesoporous solids are usually used, such as Al_2O_3 [44], SiO_2 [53], TiO_2 [50], ZrO_2 [46], CeO_2 [47] and Ce-Zr mixed oxides [54]. The type of support is an important factor to be considered in the design of heterogeneous catalysts for CO_2 methanation, since it plays an important role in active phase dispersion, activity and stability. In fact, the interaction between the support and the metal (active phase) usually has a great effect on catalytic performance. The support influence the catalyst properties mainly in three aspects: (i) improving the dispersion of the active site, (ii) promoting the formation of the inactive spinel phases, and (iii) modifying the reducibility of the oxide precursors through manipulating the interaction between the active phase and support [43]. Therefore, a catalytic component is required to activate CO_2 for a further reduction,as the aluminium oxide (Al_2O_3), and also a metal component (here Ni or Ru) that is able to dissociate H_2. Providing that both functionalities are present, activity, selectivity and deactivation of the catalyst seem to be significantly dependent on the metal particle size and morphology [44, 48] as well as the type of support [55]. Nevertheless, in some cases, a third electronic or structural promoter component is used to improve metal dispersion as well as CO_2 adsorption (e.g., CeO_2 and La_2O_3) [56, 57] or to avoid fast deactivation by sintering and fouling (e.g., V_2O_3 and Zr_2O_3) [58, 59].

1.5. MOTIVATION, OBJECTIVES AND SCOPE OF THE THESIS

Nowadays, the effects of climate change are increasingly evident and, consequently, the society is waking up and becoming aware that it is necessary to take action. In this scenario, there is no doubt that scientists along with politicians must play an important role. Thus, since the 2015 Paris Agreement (COP 21) established the basis of a plan for the transition to a zero-carbon world, the scientific community has been developing new green technologies, processes and strategies. Among them, the Power-to-Gas (Gas = methane) process, in which catalytic CO_2 methanation is a fundamental step, is of great interest. Through this strategy "two birds are killed with one stone": CO_2 emissions are reduced and in turn, surplus renewable power is stored in form of CH_4 energy vector, which increases efficiency of renewable energies and boosts their expansion.

Given the climate action urgency, the CO_2 methanation is gaining popularity in XXI century even though it was discovered more than 100 years ago. The increased interest of CO_2 methanation can be verified by checking the number of publications in the last decade (Figure 1.10).

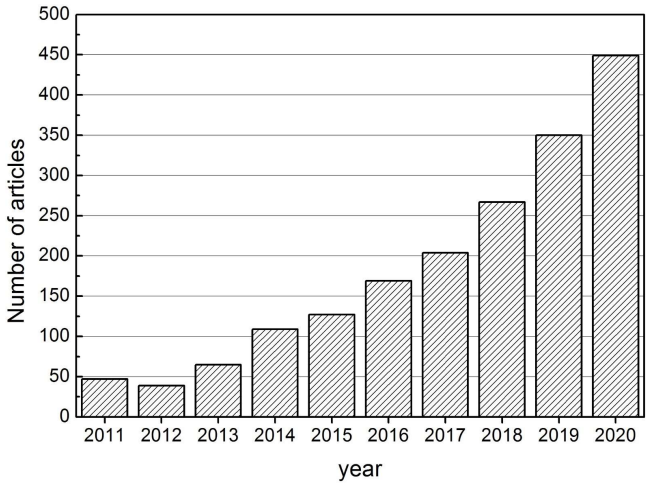

Figure 1.10. Evolution of the number of research works on CO_2 methanation in the last decade. Source: Web of Science ISI database.

Note that the number of articles dealing with CO_2 methanation has exponentially increased since 2011, which could have been the starting point of several power to gas projects around the world. Although much progress had been made till 2016, CO_2 methanation still was far from its maturity. Still research and progress were needed on the following fields: development of active, selective and stable catalysts; insights on reaction mechanism and intrinsic kinetics; mechanistic modelling and design of efficient reactors.

The aforementioned background motivated us to define the main objective of the research proposed for the present doctoral thesis: *Explore and stablish innovations in the design, reaction mechanism and kinetics of Me/support catalytic formulations to carry out the methanation of CO_2 with renewable H_2 at mild operation conditions (low temperature and pressure), which significantly reduce the energy requirements of the process.*

This main objective can be defined in a more concrete way as the achievement of a series of partial objectives, which can be divided into two blocks attending the nature and composition of the studied supported metal catalysts.

Concrete objectives of block 1:

- Examine and compare the effect of metal type and content on Ni and Ru formulations, paying special attention on particle size and morphology.
- Develop synthesis routes alternative to conventional ones (impregnation) in order to improve the catalytic properties of the starting formulations, identifying which factors are responsible for the improvements.
- Boost the catalytic performance of Ni/Al_2O_3 formulation by addition of small contents of Ru, determining its role as a promoter.
- Identify the type and evolution with temperature of reaction intermediate species involved on CO_2 methanation over the prepared monometallic and bimetallic catalysts with the aim of elucidating the reaction pathways.
- Study the intrinsic kinetics on Ni/Al_2O_3 formulation and define the mechanistic model or rate equation that best fits the kinetic results.

Concrete objectives of block 2:

- Prepare innovative zeolite Y and BETA supported Ni based catalysts and determine which zeolite structure is better based on catalytic performance.
- Enhance the CO_2 adsorption capacity of the elected zeolite support modulating its basicity by the addition of Na^+ and La_2O_3.
- Optimize the La_2O_3 loading and evaluate the stability of the optimal catalytic formulation.
- Systematically study the type and evolution of species involved in CO_2 adsorption on different protonic, Na^+-exchanged and La_2O_3-containing zeolites, elucidating the CO_2 adsorption mechanism.
- Define the role of La_2O_3 on CO_2 methanation reaction mechanism on Ni-La_2O_3/Na-BETA by means of adsorbed reaction intermediates.

The specific objectives are progressively fulfilled throughout the chapters of the present thesis. In chapter 1, the current actions to face the climate challenge are introduced and the development of Power-to-methane (i.e., CO_2 methanation) as one of the transition technologies to recycle or use CO_2 is justified. Additionally, the thermodynamics and main properties of catalysts already developed to carry out CO_2 methanation are briefly described.

In chapter 2, the methods employed to characterize the catalytic formulations are featured, including short explanations of theoretical basis and detailed descriptions of experimental protocols. Besides, the reaction set up is described and the parameters employed to measure the catalytic performance, such as CO_2 conversion or CH_4/CO selectivity, are defined.

Chapter 3 includes a direct comparison of the activity and stability of alumina supported Ni and Ru catalysts prepared by conventional impregnation method at same reaction conditions, establishing relationships between their physicochemical properties and catalytic performance. Additionally, the effect of Ni and Ru loadings on the CO_2 methanation performance is studied.

In Chapter 4, firstly, a new synthesis route of Ni/Al_2O_3 and Ru/Al_2O_3 catalysts alternative to incipient wetness impregnation is presented with the aim of improving the properties (metal dispersion, metal-support interaction) of starting catalysts. In second place, the potential promoting effect of co-impregnation of small amounts of Ru is examined within $Ni\text{-}Ru/Al_2O_3$ bimetallic systems by several characterization techniques along with catalytic tests. To conclude, further insights into CO_2 methanation mechanism over alumina supported mono- and bimetallic catalysts are deduced by operando FTIR measurements, identifying the type and evolution with temperature of reaction intermediate species involved in the reaction and determining the individual roles of Al_2O_3, Ni and Ru.

In chapter 5, the intrinsic kinetics on Ni/Al_2O_3 catalyst with low metal content are studied at wide range of experimental conditions from differential to thermodynamic equilibrium regimes. First, the kinetic data are fixed to various empirical and LHHW-type mechanistic models, which are developed according to the proposed reaction mechanisms. After that, the model discrimination or the election of the model with the minimum residuum is carried out by differential analysis method together with least squares optimization. Lastly, the kinetic and adsorption constants of the elected model are defined by the more complex integral method, including all kinetic data series in the mathematical fix.

In Chapter 6, the potential efficiency of zeolites as CO_2 methanation catalytic supports is explored. In this line, various Y and BETA zeolite supported Ni catalysts are prepared, characterized and tested for CO_2 methanation. The first part of the chapter seeks to establish relationships between catalytic performance and the physico-chemical properties of the catalysts, which depend on the type of zeolite framework, composition as well as metal support interaction. In the second part, the influence of La_2O_3 addition on the surface basicity and active phase dispersion is analysed. With these modifications, it is sought to obtain a formulation able to reach equilibrium conversion at mild temperature (T = 250 – 350 °C) and atmospheric pressure.

Chapter 7 comprises operando FTIR analysis of CO_2 adsorption and CO_2 hydrogenation mechanisms over zeolite BETA supported samples. First of all, the CO_2

adsorption over bare zeolite is studied and then, it is examined over the same zeolitic support to which different basic elements (i.e., Na^+, La_2O_3 and Ni) are systematically added, so that their role in adsorption mechanism is elucidated according to differences in the type and concentration of intermediate species. Additionally, the CO_2 methanation over supported Na-BETA catalysts with and without La_2O_3 is studied with the purpose of defining the reaction pathways and mechanistic role of La_2O_3.

In Chapter 8, the overall summary is presented as well as the main conclusions that can be drawn from the thesis.

Finally, in Chapters 9 and 10 nomenclature and scientific bibliography employed throughout the thesis are presented, respectively.

Chapter 2

EXPERIMENTAL

ABSTRACT

This chapter provides general information related to materials (supports and reagents), catalysts synthesis procedures as well as methods together with apparatus employed for the characterization and activity performance evaluation of catalytic formulations developed along this thesis. First, the materials and the procedures employed for the preparation of the catalysts are detailed. After that, information about characterization techniques and protocols is given, including TGA-MS, N_2-physisorption, H_2-chemisorption, XRD, XRF, XPS, CO_2-TPD, H_2-TPR, TEM, STEM-EDX, UV-Vis-NIR and operando FTIR. Finally, the reaction setup and protocols employed for evaluating catalysts in CO_2 methanation are described.

2. EXPERIMENTAL

This chapter encompasses the materials, catalysts, characterization techniques and reaction set-up employed during the development of the doctoral thesis. Firstly, the reagents used in the synthesis as well as gases employed in characterization and activity evaluation of catalysts are detailed. After that, the catalysts synthesis routes are described, and all prepared catalytic formulations are listed. In the third part, information related to the theoretical foundation of characterization techniques and description of the experimental protocols are included. Finally, the last section describes the reaction system formed by three parts (feed, reaction and analysis sections) as well as the reaction conditions and activity parameters employed to determine the catalytic performance of the formulations.

2.1. MATERIALS

Throughout this thesis, a wide number of supported catalysts with different composition have been prepared from the supports, metal precursors and reagents included in this section.

2.1.1. Supports

In all cases, commercial porous solids were employed as catalyst supports. Mesoporous gamma-alumina (γ-Al_2O_3) was used to synthesize catalysts of block 1, whereas various types of microporous zeolites to prepare catalysts of block 2. The specifications of all catalyst carriers are summarized in Table 2.1.

Table 2.1. Specifications of the commercial supports.

Support	Code	Manufacturer	Surface area ($m^2\ g^{-1}$)	Pore/Unit cell size (Å)
γ-Al_2O_3	SA6173	Saint Gobain NorPro	200	70
H-Y	CBV400	Zeolyst International	730	24.5
Na-Y	CBV100	Zeolyst International	900	24.65
NH_4-BETA	CP814E	Zeolyst International	680	n.a.

2.1.2. Reagents

On the other hand, all metal precursors employed consisted of nitrate salts. The precursor as well as the additional reagents employed in the catalysis synthesis are listed in Table 2.2.

Table 2.2. Specifications of the used reagents.

Name	Chemical formula	CAS number	Supplier	Purity or concentration
Nickel (II) nitrate hexahydrate	$Ni(NO_3)_2{\cdot}6H_2O$	13478-00-7	Sigma Aldrich	≥ 99.0%
Ruthenium (III) nitrosyl nitrate	$Ru(NO)(NO_3)_3$	34513-98-9	Sigma Aldrich	1.5% (w/v)
Nitric acid	HNO_3	7697-37-2	Merck	65% (v/v)
Glycerol	$C_3H_8O_3$	56-81-5	PanReac	≥ 99.5%
Sodium nitrate	$NaNO_3$	7631-99-4	Merck	≥ 99.5%
Lanthanum (III) nitrate hexahydrate	$LaNO_3{\cdot}6H_2O$	10277-43-7	Sigma Aldrich	≥ 99.0%
Ammonia solution	NH_4OH	1336-21-6	Sigma Aldrich	25% (v/v)

Finally, the gases employed in the different characterization techniques were Ar, He, H_2 and N_2 with 99.999% purity along with 5% CO_2/He, 5%H_2/Ar and 5%O_2/He calibrated gaseous mixtures supplied by Praxair. The gases used in catalytic and kinetic tests, instead, were Ar, He, H_2, N_2, CO_2 and CH_4 supplied by Air Liquide with a purity of at least 99.99%.

2.2. SYNTHESIS OF CATALYSTS

All supported catalysts studied along this doctoral thesis were prepared by mounting methods, such as impregnation, which comprise three general steps: (i) contacting the support with the impregnating solution for a certain period of time, (ii) drying the sample to remove the imbibed liquid and (iii) activating the catalyst by calcination, reduction or other appropriate thermochemical procedure. The catalysts were divided in two blocks attending the type of support: alumina or zeolite.

2.2.1. Preparation of alumina supported catalysts (Block I)

First of all, alumina supported catalysts with different Ni or Ru contents were synthesized by a simple, fast and well-known preparation method such as Incipient Wetness Impregnation (IWI). This method consists in contacting the support with the $Ni(NO_3)_2{\cdot}6H_2O$ or $Ru(NO)(NO_3)_3$ precursor solution (see specifications in Table 2.2) of appropriate concentration, corresponding in quantity to the total known pore volume (V_{pore}). On that way, the solution is driven into the pores by capillary forces rather than by diffusion (slower process) [60, 61]. In total, 5 Ni-based catalysts were prepared varying the Ni nominal content from 4 to 20 wt%. Firstly, a volume of $Ni(NO_3)_2{\cdot}6H_2O$ aqueous solution 1.2 times larger than catalysts pore volume (V_{pore}) was impregnated dropwise over Al_2O_3 (V_{pore} = 0.5 $cm^3\ g^{-1}$) by a volumetric pipette to assure the complete filling of mesopores. Secondly, the impregnated samples were dried during 6 h at 60 °C and further 6 h at 120 °C to remove the solvent so that high temperature gradients were avoided (progressive drying). Finally, the catalysts were calcined at 500 °C for 4 h with a heating rate of 5 °C min^{-1}.

Regarding Ru-based catalysts, 5 additional samples were synthesized by successive impregnations, varying Ru loading from 1 to 5 wt%. Due to Ru precursor solubility limitations, a maximum of 1% Ru was incorporated in each impregnation. As in the case of Ni based catalysts, $Ru(NO)(NO_3)_3$ solution volume 1.2 times greater than V_{pore} was impregnated, after adjusting the pH of the solution to 1 by nitric acid addition in order to avoid precursor precipitation. After each impregnation, samples were dried in the same way and calcined at 400 °C during 4 h with a heating rate of 1 °C min^{-1}. Note that all catalyst were calcined under air (uncontrolled atmosphere) in a muffle. The catalysts were labelled xNi/Al_2O_3 or yRu/Al_2O_3, where x and y represent the Ni and Ru weight percent, respectively.

In a next step, two additional alumina-supported monometallic Ni and Ru catalysts, as well as bimetallic $Ni\text{-}Ru/Al_2O_3$ samples were prepared by a slightly different synthesis route. In this case, the metal solution was introduced by Glycerol Assisted Impregnation (GAI) method and the precursor was calcined under a controlled atmosphere. The GAI method, which was developed by Gudyka et al. [62], also consists

in the typical dry impregnation but employs a glycerol/water solution as the solvent instead of bare H_2O. In principle, glycerol might react with the precursor forming an organic matrix, which envelops metal crystallites and prevents them from excessive growing during calcination [63]. Considering results reported in literature [62] as well as the alumina pore volume and solubility of the metal precursors, a 30%$C_3H_8O_3$/water solution was used.

Table 2.3. General information of the prepared alumina supported Ni and Ru catalysts.

Short name	Long name/ Composition	Preparation method*	Calcination atmosphere	$T_{calc.}$ (°C)	Location
4NiAl	4%Ni/Al_2O_3	IWI	Air	500	Chapter 3
8NiAl	8%Ni/Al_2O_3	IWI	Air	500	Chapter 3
10NiAl	10%Ni/Al_2O_3	IWI	Air	600	Chapter 5
12NiAl or $NiAl_{IWI}$	12%Ni/Al_2O_3	IWI	Air	500	Chapters 3 and 4
$NiAl_{GAI}$	12%Ni/Al_2O_3	GAI	20% H_2/N_2	550	Chapter 4
16NiAl	16%Ni/Al_2O_3	IWI	Air	500	Chapter 3
20NiAl	20%Ni/Al_2O_3	IWI	Air	500	Chapter 3
1RuAl	1%Ru/Al_2O_3	IWI	Air	400	Chapter 3
2RuAl	2%Ru/Al_2O_3	IWI	Air	400	Chapter 3
3RuAl or $RuAl_{IWI}$	3%Ru/Al_2O_3	IWI	Air	400	Chapters 3 and 4
$RuAl_{GAI}$	3%Ru/Al_2O_3	GAI	20% H_2/N_2	550	Chapter 4
4RuAl	4%Ru/Al_2O_3	IWI	Air	400	Chapter 3
5RuAl	5%Ru/Al_2O_3	IWI	Air	400	Chapter 3
Ni-0.5RuAl	12%Ni-0.5%Ru/Al_2O_3	GAI	20% H_2/N_2	550	Section 4.2
Ni-1.0RuAl	12%Ni-1.0%Ru/Al_2O_3	GAI	20% H_2/N_2	550	Sections 4.2 and 4.3
Ni-1.5RuAl	12%Ni-1.0%Ru/Al_2O_3	GAI	20% H_2/N_2	550	Section 4.2

First, the required amounts of $Ni(NO_3)_2{\cdot}6H_2O$ and $Ru(NO)(NO_3)_3$ precursors dissolved in aqueous glycerol solution were impregnated dropwise in order to attain two catalysts with 12 wt% Ni and 3 wt% Ru nominal metal contents. After impregnation, samples were dried overnight and calcined in a tubular oven under 50

mL·min^{-1} of 20%H_2/N_2 (controlled atmosphere) at 550 °C for 2 h (with 10 °C min^{-1} heating rate). These two catalysts were labelled according to their composition and impregnation method as follows: $NiAl_{GAl}$ and $RuAl_{GAl}$.

Finally, once results of monometallic catalysts were analyzed, three bimetallic catalysts were prepared by GAI method along with reductive calcination varying the Ru content from 0.5 to 1.5 wt%. In all cases, the nominal Ni content was set at 12 wt% and small amounts of Ru were incorporated by co-impregnation. After that, samples were also dried overnight at 120 °C and calcined under the same conditions described above. These samples were named Ni-xRuAl, where variable x represents the Ru content (0.5, 1.0 or 1.5 wt%). The nomenclature, nominal compositions, general synthesis route specifications and location of block I catalysts are listed in Table 2.3.

2.2.2. Preparation of zeolite supported catalysts (Block II)

The block II formulations consisted of zeolite supported Ni catalysts, some of them promoted by La. On the one hand, three types of zeolites were used as a support supplied by Zeolyst International: H-Y (Si/Al = 2.6), Na-Y (Si/Al = 2.6) and NH_4-BETA (Si/Al 12.5). From NH_4-BETA, zeolite H-BETA and Na-BETA were obtained by different ways. The protonic form of BETA zeolite was achieved by simple calcination or thermal decomposition (TD) at 550 °C for 4 h with a heating rate of 1 °C min^{-1}. However, the Na-BETA zeolite was prepared by the metal Ion Exchange (IE) procedure, which is another mounting synthesis method. The IE consists of exchanging either protons or ammonium groups on the carrier surface with cationic and anionic species in solution. The adjustment of the pH is a key factor to have an electronic interaction between the support and the metal precursor [61, 64]. In our case, the suitable amount of $NaNO_3$ (Merck, 99.5%) was dissolved in deionized water (0.5 M solution); then, NH_4-BETA was added to this solution (10 mL/g) and the suspension was continuously stirred for 24 h at 60 °C. During the preparation pH = 7 was kept by the addition of ammonia solution drops. After the ion exchange, the support was filtered, washed twice with deionized water and dried at 110 °C overnight. This procedure was repeated twice and finally the exchanged zeolite was calcined for 4 h at 550 °C with a heating rate of 1 °C min^{-1}.

The incipient wetness impregnation procedure was also used for preparing four Ni/zeolite catalysts. This method consisted in adding the $Ni(NO_3)_2$ solution (Sigma Aldrich, 99.99%) dropwise to zeolite support so that the solute was driven into pores by capillary forces. In all cases, the precursor was $Ni(NO_3)_2 \cdot 6H_2O$, the nominal content of nickel was 10% and, after impregnation, the catalysts were calcined at 550 °C for 6 h with a heating rate of 5 °C·min^{-1}. Lastly, other three zeolite supported catalysts were prepared with La_2O_3 promoter nominal contents of 5, 10 and 15%. In this case, the metals were introduced by successive impregnations (first La_2O_3 and then Ni). After each impregnation, samples were calcined at same conditions as unpromoted catalysts. Table 2.4. summarizes the nomenclature, nominal compositions, synthesis details and location of the seven prepared zeolite supported catalysts.

Table 2.4. General information of the prepared zeolite supported catalysts.

Name/composition	Preparation method	T_{calc} (°C)	Location
Ni/H-Y	IWI	550	Section 6.1
Ni/Na-Y	IWI	550	Section 6.1
Ni/H-BETA	TD and IWI	550	Section 6.1
Ni/Na-BETA	IE AND IWI	550	Chapters 6 and 7
Ni-5La_2O_3/Na-BETA	IE and IWI	550	Section 6.2
Ni-10La_2O_3/Na-BETA	IE and IWI	550	Section 6.2 and Chapter 7
Ni-15La_2O_3/Na-BETA	IE and IWI	550	Section 6.2

2.3. CHARACTERIZATION METHODS

The physicochemical properties of the catalysts were determined by several characterization techniques. The calcination temperature of the catalysts was defined by thermo-gravimetric analysis; their textural properties as well as metal dispersion by physical and chemical adsorption; the crystallinity, crystallite size, bulk and surface composition by X-ray based methods; the basicity and reducibility by temperature programmed techniques; the metal particle size and morphology by electron microscopy; and finally, the metal coordination and type of adsorbed species by UV-visible and FTIR spectroscopy.

2.3.1. Thermogravimetric analysis coupled to mass spectroscopy

Thermogravimetric analysis is very useful tool to detect small mass variations in a given solid sample (e.g., a catalyst precursor). This analysis is carried out in a thermobalance apparatus, which is able to monitor sample mass change under an atmosphere of controlled composition as the temperature linearly increases or at isothermal conditions. Generally, the mass variation that takes place in the solid is due to drying process, volatilization or thermal decomposition [65]. The depiction of mass loss or gain percentage as a function of time or temperature is called thermogram or TG curve, which shape is characteristic of the given sample. To better know the mass change events, the results can also be represented differentially (dTG curves) deriving the TG profiles.

Frequently, Mass Spectroscopy (MS) analytic technique is employed to know the gas products that are formed during decomposition processes by coupling a mass spectrometer to the thermobalance. This method is based on ionizing the unknown gas mixture so that the resulting ions that compose it can be separated according to their mass/charge (*m/z*) ratio. After little amount of gas mixture enter to the chamber at vacuum pressure, it is immediately ionized by electronic bombardment forming molecular ions in a first step. These molecular ions have unpaired electrons, what makes them unstable and prone to decompose into fragment ions. As the ions have positive charge, these can be transferred by an electrical field to a mass analyzer, where are separated according to their *m/z* ratio. The relative concentration of each ion can be represented as function of its mass value or time (mass spectra).

Experimental protocol

The thermogravimetric analysis was carried out in a *Setsys Evolution* thermobalance of *Setaram* brand equipped with cylindrical graphite furnace and temperature control (TIC). The atmospheric composition was established by means of mass flow controllers at thermobalance entrance. In all cases, a mass between 50 and 100 mg was placed in 30 µL Al_2O_3 crucible, which is hung on the microbalance so that it stays centered inside the oven by a platinum wire system. On the other hand, the

flue gas stream composition was monitored by a Cirrus mass spectrometer. This was operated in secondary electron multiplier mode to record the evolution of the m/z signals corresponding to H_2 (*m/z* =2), He (*m/z* =4), C (*m/z* =12), CH_4 (*m/z* =15), H_2O (*m/z* =18), N_2 or CO (*m/z* =28), NO (*m/z* = 30), CO_2 or N_2O (*m/z* = 44), Ar (*m/z* = 40) and NO_2 (*m/z* = 46).

The TG-MS analysis was performed either to determine the suitable calcination temperature of catalyst precursors or to analyze the possible formation of carbon deposits after stability tests (24h on stream or more) of the best catalysts. In both cases, the sample was dried at a temperature higher than 100 °C. The first type of experiments was carried out varying the temperature from 125 to 625 °C with 5 °C min^{-1} heating rate and under 50 mL min^{-1} of oxidative (5% O_2/He) or reductive (5% H_2/Ar) stream, depending on the preparation procedure. On the other hand, the coke presence analysis consisted of heating the aged catalyst from 150 to 850 °C and under 5%O_2/He flow in order to assure burning of all carbon compounds.

2.3.2. Physical and chemical adsorption of gases

The adsorption is a fundamental step in heterogeneous catalysis since it is the step prior to the reaction. It can be physical or chemical. The former is characterized by a low energetic interaction, poor specificity, and reversible nature, whereas the latter by an elevated metal-gas interaction, high selectivity, and almost complete irreversibility at low temperature [66, 67]. As discussed below, the essential properties of a supported catalyst can be measured from techniques based on physical and chemical adsorption.

2.3.2.1. N_2-physisorption

The physical adsorption of gases is the main method to determine textural properties of porous solids, including specific surface area (S_{BET}) and pore volume (V_{pore}). Typically, many surface atoms of a porous solid present unbalanced electric charge that generates attraction forces over gaseous molecules. As a result of such gas-solid interactions or so-called Van der Waals forces, the gas molecule is weakly

adsorbed (adsorbate formation) releasing little heat (ΔH = 4-40 kJ mol^{-1}) and giving rise to the phenomenon known as physisorption. Due to the poor specificity of the process, gas molecules first tend to lie side-by-side until completely cover the solid surface forming a monolayer. Thus, knowing the area occupied by each adsorbing gas molecule, the specific surface area of the solid can be calculated from the amount of molecules forming the layer. The most commonly used adsorbing gas is N_2 at – 196 °C (boiling point), being its molecular transversal area 0.162 nm^2 in such conditions.

The adsorption type as well as capacity of a porous solid is determined from the isotherm curves, which represent the volume of adsorbed gas as a function of its relative pressure at constant given temperature. Depending on the characteristic of the solid, Brunauer, Emmet and Teller [68] proposed five different isotherm curve models, to which Sing latter added a sixth and last one [69]. All types of adsorption isotherms are depicted in Figure 2.1.

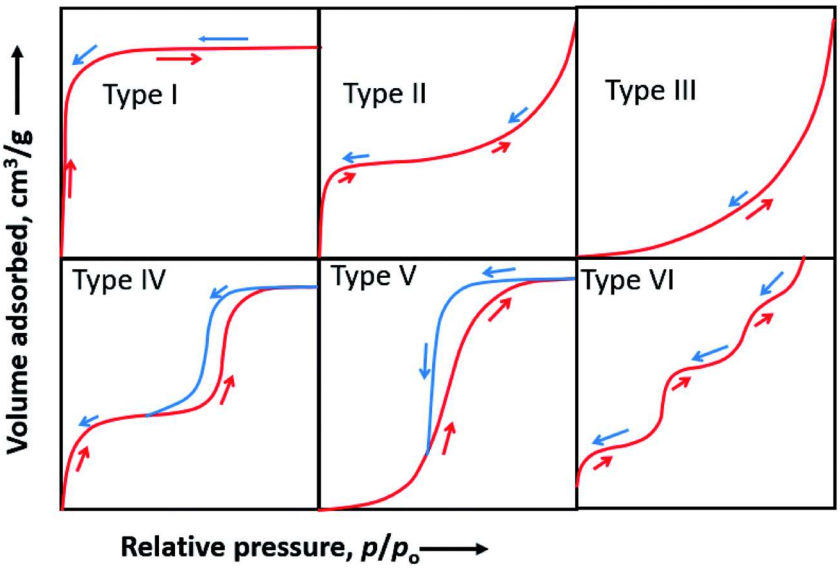

Figure 2.1. Most common types of adsorption isotherms according to IUPAC.

The type II isotherm is characteristic of macroporous solids with pore sizes (d_{pore}) superior to 50 nm or non-porous one, the type IV isotherm corresponds to mesoporous solids (d_{pore} = 2 – 50 nm) and, finally, the type I isotherm is attributed to microporous

solids (d_{pore} < 2 nm). Note that in some cases the capillary condensation of N_2 that takes place within the pores at high relative pressures hinders desorption of adsorbing gas specially from those with lower size and hence, the adsorption and desorption curves do not usually have the same shape giving rise to a hysteresis loop, as observed for type IV and V isotherms (Figure 2.1). The shape as well as the relative pressure at which the loop appears allow estimating the pore size distribution. According to IUPAC, there are four types of hysteresis loops depending on the pore morphology: cylindrical and uniform (H1), cylindrical with bottleneck (H2), grid shaped and uniform (H4) and grid shaped but not uniform (H3) [70].

Through the mathematical analysis of isotherm curves, the volume required to completely cover the surface of the solid can be calculated and, accordingly, its accessible surface area. The fit of Brunauer, Emmet and Teller equation, known as BET equation, is the most extended method to determine the specific surface area. After linearizing and simplifying BET equation is as follows:

$$\frac{P}{V_{ads}\left(P_0 - P\right)} = \frac{1}{V_m C} + \frac{C-1}{V_m}\frac{P}{P_0} \tag{2.1}$$

where V_{ads} ($cm^3\ g^{-1}$) is the volume of gas adsorbed in equilibrium at a given pressure or P (kPa); V_m ($cm^3\ g^{-1}$) is the required volume of N_2 to form a monolayer; P_0 (kPa) is the saturation pressure of the adsorbing gas at specific operating conditions; and C is a parameter associated with adsorption and desorption enthalpies [71].

The fit of isotherms' data to the model at relative pressures from 0.05 to 0.2, allows the determination of parameters V_m and C from both slope and intercept values. Once known V_m, the BET surface area (S_{BET}, $m^2\ g^{-1}$) can be calculated by this expression:

$$S_{BET} = 10^{-18}\frac{V_m \cdot N_A}{m \cdot V_{mol}} \times A_m \tag{2.2}$$

where N_A is the Avogadro number; V_{mol} is the adsorbate molar volume ($cm^3\ mol^{-1}$); A_m is the transversal area of N_2 (nm^2); and m is the mass of the solid to analyse (g).

Regarding the total pore volume (V_{pore}, $cm^3\ g^{-1}$), it is nothing but the adsorbed volume at a relative pressure of 0.98, which represents the gas volume required to fill all pores. On the other hand, the pore size distribution for mesoporous solids is usually determined by the method proposed by Barrett, Joyner and Halenda (known as BJH method). The model is based on Kelvin equation of capillary condensation and employs data from desorption isotherm as follows:

$$r_{pore} = 10^3 \frac{2\psi \cdot V_{ads} \cdot \cos\upsilon}{R \cdot T \cdot \ln\left(P/P_0\right)} + e \qquad (2.3)$$

being r_{pore} the pore radius (nm), ψ the surface tension of adsorbate (N m^{-1}), υ the contact angle between the condensated N_2 and solid walls (rad), T the temperature (K), R the ideal gas constant (J mol^{-1} K^{-1}) and e the thickness of adsorbed layer (nm).

Experimental protocol

Textural properties of samples (S_{BET}, V_{pore} and mesopore size distribution) were determined from N_2 adsorption-desorption isotherms measured at 77 K (- 196 °C) using a *Micromeritics TRISTAR II 3020* equipment. The analysis is more accurate when the mass of solid contains a surface area between 20 and 50 m^2 and hence, sample mass values providing areas within that range were attempted to employ. Prior to the analysis, samples were degassed overnight by a N_2 continuous flow at 350 °C to completely clean the sample surface.

Regarding the isotherms, the adsorption curve is automatically obtained by adding successive N_2 injections and recording equilibrium pressure values among them up to the dew point of N_2 (P = 101.3 kPa). The N_2 adsorption values among 0.06 and 0.2 are employed to calculate the BET surface area (Equation 2.2). After that, desorption curve is obtained evacuating known N_2 volumes and recording equilibrium pressure values until closing hysteresis loop. In this case, the data collected among 0.14-0.99 partial pressure range is used to determine both pore volume and mesopore size distribution by BJH method (Equation 2.3).

2.3.2.2. H_2-chemisorption

The metal dispersion is a fundamental parameter in characterization of supported catalysts, since it defines what fraction of total metallic atoms are in the surface or, in other words, the fraction of metallic atoms that can take part in the reaction as active sites. Typically, dispersion is indirectly determined by a volumetric method based on chemical adsorption of gases known as chemisorption, which, unlike physisorption, involves an exothermal reaction between the metal surface and the gas.

This method consists in measuring the amount of chemisorbed volume at increasing probe gas pressures and isothermal conditions. In practice, immediately after catalyst surface being exposed to gas molecules at vacuum pressure, those are selectively attached to metal particles through a short-range chemical bond. As the pressure increases, more molecules are chemisorbed until metal surface is completely covered by a monolayer, which will determine the dispersion. However, in volumetric analysis conditions, certain amount of gas is also physically adsorbed. Thus, after carrying out first isotherm involving both type of adsorptions, catalyst must be evacuated to remove the physisorbed part. After that, a second consecutive isotherm is performed to calculate the volume related to physisorption. Finally, the subtraction of both isotherms allows determining the amount of chemisorbed gas [66].

To determine the number of metallic surface atoms (N_S) per total metal atoms (N_T), previously is necessary to know the stoichiometric factor (*SF*) of gas adsorption over the metal., i.e., the ratio of the number of surface metal atoms per adsorbed gas molecules. Knowing this value as well as the chemisorption experiment results, the dispersion (D_{Me}, %) can be calculated as:

$$D_{Me} = \frac{N_S}{N_T} \times 100 = \frac{V_m / V_{mol} \cdot N_A \cdot SF}{F_{Me} / MW_{Me} \cdot N_A} \times 100 \qquad (2.4)$$

where *Me* is the metal type (Ni or Ru), V_m is the chemisorbed volume ($cm^3\ g^{-1}$), V_{mol} is the molar gas volume ($cm^3\ mol^{-1}$), N_A is the Avogadro number ($6.023\ 10^{23}$ atom·mol^{-1}),

F_{Me} is the metal fraction of the catalyst (g_{Me} $g_{cat.}^{-1}$) and MW_{Me} is the molecular weight of the metal (g_{Me} mol^{-1}).

Likewise, the metallic surface area (S_{Me}, m^2 $g_{cat.}^{-1}$) or the total active metal surface area available for interaction with the adsorbate can be determined as follows:

$$S_{Me} = \frac{N_A}{V_{mol}} \cdot V_m \cdot SF \cdot atA_{Me} \quad (2.5)$$

where atA_{Me} is the atomic area of Ni (6.49 10^{-20} m^2 $atom^{-1}$) or Ru (6.13 10^{-20} m^2 $atom^{-1}$).

Generally, hydrogen, carbon monoxide and oxygen are the adsorbing gas employed in chemisorption analysis. Among them, hydrogen is the most frequently used since, unlike CO and O_2, it is not physically and chemically adsorbed by most of the supports and its adsorption stoichiometry on Ni or Ru is clear (both Ni/H_2 and Ru/H_2 stoichiometric ratios are assumed to be 2), which results in reliable dispersion measurements. However, it is important to choose suitable analysis conditions to avoid some difficulties, such us the H_2 spill over to support surface or formation of subsurface hydrogen species, which can lead to wrong metal surface estimation [72, 73].

Experimental protocol

The chemical adsorption of H_2 was studied employing a Micromeritics ASAP 2020 apparatus together with a *Chemisorption Controller* device, which is responsible of providing required operation conditions to carry out sample pretreatment and subsequent chemisorption experiment. Prior to chemisorption tests, samples are conditioned following the next steps: (i) reduction of supported Ni or Ru catalyst by H_2 flow for 2h at 500 and 350 °C, respectively; (ii) degassing of catalyst at ultra-vacuum pressure for 90 min at a temperature 10°C higher to that of reduction; (iii) cooling down of catalyst to 35 °C (chemisorption temperature); and (iv) a second degasification for 1 h at low temperature (35 °C).

The test is based on collection of two isothermal curves varying the pressure from 50 and 450 mmHg with an evacuation in between. Subtracting the volume values of

the second isotherm (only associated with physisorption) to those of the first (result of a combined physical and chemical adsorption), the amount of chemisorbed H_2 (V_m) is evaluated. Note that V_m is the volume intercept derived from the best linear fit to the volume differences of recorded isotherms, from which metallic dispersion (D_{Me}, Equation 2.4) as well as metal surface area (S_{Me}, Equation 2.5) can be calculated.

2.3.3. X-ray based methods

Like visible light, X-rays are electromagnetic waves emitted by atoms as a consequence of perturbations formed within its electronic structure. The main difference among X-rays and ordinary light lies in his wavelength (λ), being shorter for the former. As them pass though the matter, X-rays suffer a series of interactions depicted in Figure 2.2.

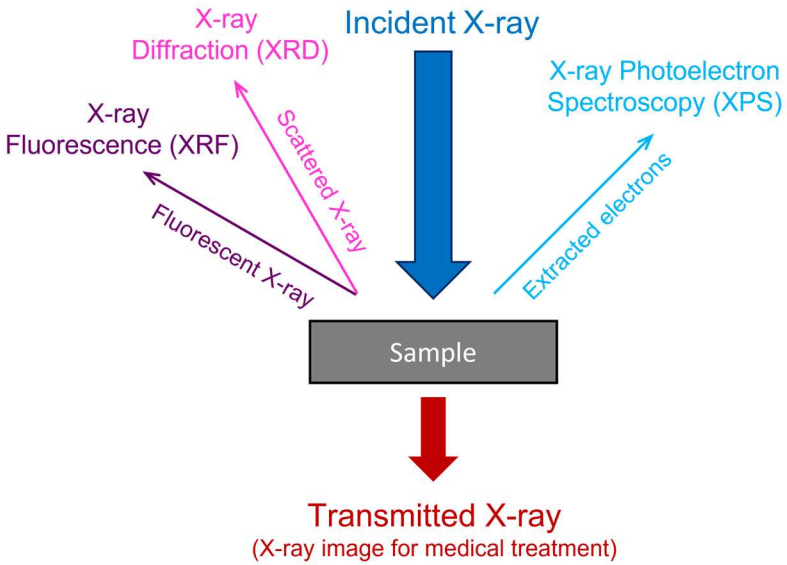

Figure 2.2. Types of X-ray interactions with matter.

While part of the X-ray radiation is transmitted through the material, part is scattered coherently (without energy loss) or incoherently (Compton diffusion), other part is re-irradiated together with electrons and the rest is transformed into heat. From

different type of interactions and by means of its corresponding techniques (see Figure 2.2), information regarding the bulk and surface structure as well as composition of the sample can be obtained.

2.3.3.1. X-Ray Diffraction

In a crystal, atoms are arranged in an ordered and periodic way through space forming crystalline planes. The planes of the same family are separated one each other by a constant distance or spacing (*d*) which is of the same magnitude order as the wavelength of X-rays (0.1-10 Å). Thus, when a crystal is exposed to X-rays, those can be diffracted or scattered mainly though arranged electrons of the crystalline lattice. The scatter can be either incoherent or coherent depending on the X-rays loss energy (higher wavelength than incident beam) or not (same wavelength as incident beam) after being deviated. The direction angle (θ) of coherent scattered radiation is defined by Bragg´s law:

$$n\lambda = 2d \cdot \operatorname{sen}\theta \tag{2.6}$$

Note that according to this law, the beam is diffracted in concrete θ angle, if the difference in path-length of the wave train is an integer multiple (*n*) of the wavelength (constructive interference among rays).

The X-ray diffraction (XRD) technique allows the analysis of crystalline phases both qualitatively and quantitatively [74]. The most widespread method is XRD over powder or polycrystalline samples. The main advantage of this method is that fine powder sample is randomly oriented in all directions, being all crystalline planes exposed to X-rays. In a standard configuration, XRD intensity is recorded as the θ angle of both X-ray source and detector is varied at the same speed so that the angle between them is always 2θ. In that way, a spectrum is obtained formed by several XRD peaks at 2θ positions, which are characteristic of different crystalline phases or planes. Note that the crystalline phase identification is carried out by comparing obtained spectra with the registered in a database called PDF (Powder Diffraction File) established by the ICDD (International Centre for Diffraction Data).

On the other hand, from more intense XRD peak, the size of the crystallite responsible of its appearance can be estimated by Scherrer equation:

$$\tau = \frac{K \cdot \lambda}{\beta \cdot \cos\theta} \tag{2.7}$$

where K a shape factor (0.89 if spherical particles are considered), λ is the wavelength of the incident X-beam (1.5418 Å), θ the position angle (rad) and β is a parameter associated with the wide of the diffraction peak (°). The value of the last parameter is normally corrected considering the extra widening that occurs due to instrumental analysis. Thus, β is defined as:

$$\beta = \beta_{obs} - \beta_{ins} \tag{2.8}$$

where β_{obs} is the observed experimental widening or FWHM (Full Width at Half Maximum) and β_{ins} is the extra widening that depends on the instrument employed for the analysis (0.1° 2θ in this case).

Experimental protocol

Before the analysis, polycrystalline samples were precisely ground to fine powder. Then, a small amount of sample was adhered over a glass holder by few acetone drops, which, once dried, allow powder to be orientated in all positions exposing all crystalline planes.

Crystalline phases of samples were identified by a *PANalytical X'pert PRO* diffractometer with Cu Kα radiation (λ = 1.5418 Å) and Ni filter. The operating conditions were 40 kV and 40 mA and diffractograms were recorded varying incident angle and detector from 5 to 90° 2θ with 0.02° per second sampling interval. For the computer processing and interpretation of diffractograms, *PANalytical X'pert HighScore* specific software was used combined with PDF database provided by ICDD.

On the other hand, the thermo-diffractometric studies were carried out in a *Bruker D8 Advance* diffractometer operating at 30 kV and 20 mA, equipped with a Cu

tube (λ = 1.5418 Å), a *Vantec-1 PSD* detector, and an *Anton Parr HTK2000* high temperature furnace (total time for each temperature was 1 h). The thermo-XRD results were obtained varying sample temperature from 30 to 1010 °C (5 °C min^{-1} heating rate) and recording a pattern every 20 °C. Likewise, each diffractogram was recorded varying 2θ angle from 15 to 70° at 0.0165° s^{-1} rate.

The measurements were carried out in Rocks and Minerals Analysis Unit of the general X-ray service located within Central Analysis Facilities (SGIker) of the University of the Basque Country (UPV/EHU).

2.3.3.2. X-Ray Fluorescence

Sometimes X-ray photon can be energetic enough to enter in the more internal atomic levels of atoms and extract electrons from K, L or M layers. In this case, a phenomenon analogous to that which occurs in anticathode of X-ray source takes place: the irradiated material emits its characteristic X radiation. This phenomenon is consequence of the extraction and later replacement of strongly linked electrons in depth orbitals by others located in upper orbitals. This type of radiation is known as X-ray fluorescence (XRF) and evidently is always accompanied by photoelectron emission [75].

The electron transition from upper to lower orbital releases a photon with an amount of energy equivalent to the energy difference between the initial and final orbital. Then, the wavelength (λ, in m) of fluorescent radiation can be calculated from Planck´s postulate:

$$\lambda = \frac{h \cdot c}{E} \tag{2.9}$$

where h is the Planck´s constant ($4.136 \cdot 10^{-15}$ eV·s), c is the light speed ($299.79 \cdot 10^{6}$ m s^{-1}) and *E* is the energy difference.

The configuration employed in this thesis to analyze the fluorescent radiation consists of separating X-beams by its characteristic wavelength (wavelength-dispersive

analysis) using a monochromator crystal. By means of diffraction, the crystal is able to filter radiation and redirect it to the detector (X-ray counter). The intensity of each characteristic radiation is directly related to the amount of each element in the sample, which allows determine its chemical composition.

Experimental protocol

Prior to the analysis, the sample was mixed with a flux composed by lithium tetraborate (66%) and metaborate (34%) in 20/1 ratio. Then, the solid mixture was melted at around 1200 °C in an induction oven, obtaining a solid pearl with homogenous composition.

The chemical analysis of the pearl was carried out by *AXIOS* spectrometer model of *PANalytical* house with a rhodium tube and three detectors (gas flow, scintillation and Xe sealing). The intensity of the X-ray radiation was converted into chemical composition by calibration curves of well-characterized international rock and mineral patterns.

The measurements were performed in Rocks and Minerals Analysis Unit of the general X-ray service of SGIker.

2.3.3.3. X-ray photoelectron spectroscopy

X-ray Photoelectron Spectroscopy (XPS) is a surface-sensitive analysis method that provides valuable information complementary to that of XRD, such as surface elemental composition and chemical state. This technique is based on photoelectric effect and consists in exciting a surface by X-ray photons so that electrons of the sample to be studied are extracted. For this to happen, the energy of the photon must be higher than the one with which the electron is attached to the atomic orbital, i.e., higher than its binding energy. Then, the kinetic energy (*KE*, in eV) at which the electron is expelled from the atom is equal to the X-ray photon energy ($h\nu$) minus its binding energy (*BE*, in eV) and work a function (Φ) or the minimum thermodynamic work to bring electrons from solid surface to a point in the vacuum space [76]. However, in

practice, a small correction (δ) must be included due to contact potential between instrument and sample and, hence, energy balance is redefined as:

$$KE = \mathrm{h}\nu - BE - \Phi - \delta \tag{2.10}$$

where h is the Planck constant ($4.136 \cdot 10^{-15}$ eV·s) and ν is the photon frequency (s^{-1}).

Note that for photoelectrons to leave the sample into the vacuum, they must travel through the bulk avoiding inelastic collisions, recombination or trapping in other atoms, which reduce their free paths as the depth increases. For that reason, most electrons that reach XPS detector come from the top layers rather than depth ones, providing exclusively surface information (3λ depth). The detector is able to measure the amount of incoming electrons as well as is its kinetic energy, allowing the representation of photoelectronic intensity as function of binding energy. The binding energy value will depend on the nuclear charge (the higher the atomic number (*Z*) of the element, the higher the BE) and the type of the atomic orbital in which the electron is located (s, p, d or f), being *BE* higher as the position is closer to the nucleus. Then, to each element corresponds a set of characteristic XPS peaks at various *BE*, which are registered at different databases. In practice, the position of recorded photoemission peaks can be slightly shifted compared to that of database, due to a different charge state of the element. This 'chemical shift', which is usually discussed in literature, provides information about oxidation state, ligand electronegativity as well as the type and number of atom bindings in a compound.

Experimental protocol

The analysis was conducted on a *SPECS* XPS system equipped with *Phoibos 150 1D-DLD* detector, K_α monochromatic radiation source and "*flood gun*" to compensate the contact potential. The spectrophotometer first accomplishes a fast *BE* survey scan in steps of 40 eV to detect all surface elements and then, it performs high resolution analysis in regions of identified elements (steps of 20 eV) with an electron exit angle of 90°. After that, spectra were analyzed by *CasaXPS* software in order to determine the atomic surface composition of samples. First, the position of XPS peaks was amended

using as pattern the C 1s transition, which appears at 284.6 eV. Then, the deconvolution of the spectra was carried out by using pseudo-Voigth distributions and Shirley-type background subtraction.

The XPS measurements related to alumina supported catalysts were performed in X-ray unit of the Research Technical Services located in University of Alicante. However, the experiments associated with zeolite supported catalysts were carried out in X-ray Photoelectron Spectroscopy unit of the general X-ray service of the University of the Basque Country.

2.3.4. Temperature Programmed methods

Temperature Programmed (TPX) methods are frequently employed in heterogeneous catalysis to perform investigation on reduction/oxidation (RedOx) properties, study reagent adsorption, determine the probe gas-solid activation energy or quantify the number and species of surface-active sites. In all these methods, sample is exposed to programmed temperature changes and reactive probe gas, while its physicochemical changes are monetarized. These little changes are indirectly and precisely recorded by a Thermal Conductivity Detector (TCD), which diagram is depicted in Figure 2.3.

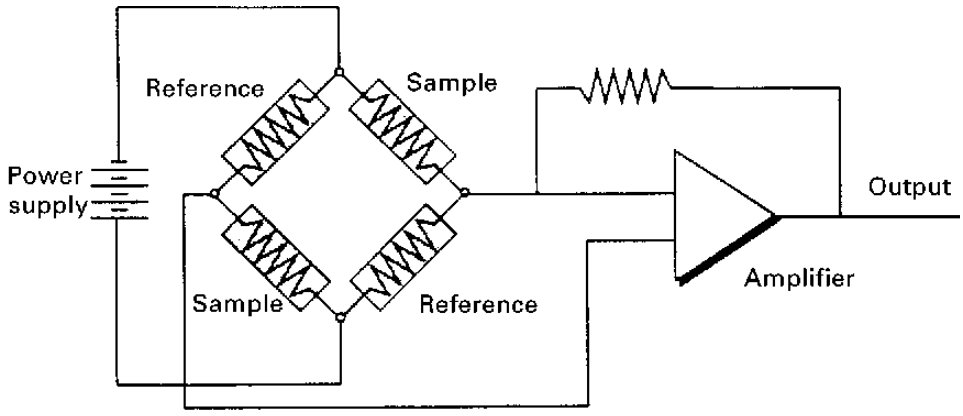

Figure 2.3. Wheatstone bridge diagram.

TCD device compares the thermal conductivity of sample gas (reacted probe gas) with that of reference gas (probe gas), generating a specific voltage difference. The detector is a hot metal piece (katharometer) with two cavities though which gas flows. Inside the cavities there are two pairs of filaments (one pair in each cavity) either composed of platinum, gold, or tungsten at a temperature controlled by heating resistances. The filaments are very sensitive to temperature changes and are connected by an electrical circuit known as Wheatstone bridge.

According to this circuit, when the two pairs of filaments are at the same temperature, the bridge is in equilibrium and no output current is generated. However, when there is a change in outlet gas composition or thermal conductivity, filament temperature varies generating a current. Therefore, a TPX profile is nothing more than a representation of changes in thermal conductivity of outlet gas stream as function of temperature.

2.3.4.1. Temperature Programmed Desorption

Temperature Programmed Desorption (TPD) is another complementary method to volumetric chemisorption analysis. This method also provides valuable information about chemical adsorption of gases on catalysts and consists of three steps: (i) chemisorption of a probe gas up to saturation at starting temperature, (ii) removal of physisorbed volume by inert flushing and (iii) subsequent desorption by linearly increasing temperature [77]. Generally, the employed probe gas depends on the type of molecule to be adsorbed as well as catalytic property to be known. Then, in this thesis, Temperature Programmed Desorption of both CO_2 methanation reagents (CO_2 and H_2) were carried out. CO_2-TPD provides information about the type of basicity of catalyst or basic support, whereas H_2-TPD is used to determine the H_2 adsorption capacity of the metallic surface.

Normally, the chemical nature of all surface active sites over which chemisorption of reagents can take place is not equal, which means that each type of active site interacts with probe gas with different strength and that desorption from them will occur at different temperatures. Therefore, information on the amount and strength

of active sites can be extracted measuring quantitatively the volume of desorbed gas from TPD peaks integration at different temperatures. However, it should be mentioned that this technique present limitations and it is recommended to complement which other techniques such as infrared spectroscopy in order to better define the type of adsorbed species and basic sites.

Experimental protocol

Temperature Programmed Desorption studies of CO_2 and H_2 were conducted on a *Micromeritics AutoChem 2920* instrument coupled to a *MKS Cirrus* mass spectrometer. In CO_2-TPD experiments, first, samples were subjected to different pretreatments depending on their formulation to clean up their surface from impurities, mainly removing adsorbed water and CO_2. Ni/Al_2O_3 and Ru/Al_2O_3 catalysts (in chapter 3) were reduced under 5%H_2/Ar flow for 60 min at 500 °C and 30 min at 300 °C, whereas La_2O_3/Na-BETA samples (in chapter 6) were pre-treated at 500 °C for 60 min under He flow. Then, after cooling down to 50 °C, CO_2 adsorption step was performed by feeding 50 cm^3 STP min^{-1} of 5% CO_2/He flow until saturation. Thereafter, the samples were flushed out with helium for 60 min to remove weakly adsorbed CO_2 from the surface. Finally, desorption was carried out from 50 to 850 °C with a heating rate of 10 °C min^{-1} as the CO_2 desorption was continuously monitored with TCD and mass spectrometer. By these experiments surface basicity and basic sites distribution were analysed.

On the other hand, H_2-TPD experiments were performed following an analogous protocol. First, the metal surface of samples was reduced and cleaned up by 5%H_2/Ar gas stream at 500 °C for 30 min and then cooled down to 50 °C. After that, a 50 mL min^{-1} stream of pure hydrogen was fed long enough for complete adsorption or saturation (around 1 h). Subsequently, catalysts were flushed out with Ar for 30 min in order to remove physisorbed H_2. Finally, the desorption was conducted increasing the temperature up to 850 °C at 10 °C min^{-1} heating rate. These experiments allowed us determining the hydrogen chemisorption capacity as well as chemisorption strength distribution of monometallic and bimetallic catalysts (in chapter 4).

2.3.4.2. Temperature Programmed Reduction with H_2

The Temperature Programmed Reduction (TPR) is a technique widely used in heterogeneous catalysis in particular when the active phase precursors are metal oxides. In a typical TPR run, the sample is exposed to a gaseous reducing agent and temperature is increased at constant rate up to its complete reduction. Throughout this method the reducibility (temperature for complete reduction) or the reduction degree at a given temperature (reduced metal fraction at such temperature) can be determined [78].

Generally, H_2 diluted in inert gas (Ar) is the most used mixture to reduce the sample although other reducing agents, such as CH_4 and CO, are also employed. So, in this thesis, Temperature Programmed Reduction with H_2 (H_2-TPR) were performed to study the reduction events of Ni and Ru supported catalysts. A H_2-TPR profile is usually composed by several H_2 consumption peaks and bands at different temperature, which are characteristic of different reduction events or metal oxides species in the catalyst. From integration and knowing the reduction stoichiometry of the profiles, the reducibility, reduction degree and amount of each species can be estimated. However, note that there are some factors to be considered such as reduction agent flow and concentration, sample mass, particle size and heating, which can affect the integration accuracy.

Experimental protocol

Hydrogen Temperature Programmed Reduction (H_2-TPR) experiments were also carried out on *Micromeritics AutoChem 2920* instrument. As in TPD runs, samples were pre-treated or cleaned at different conditions. Ni-based catalysts were submitted to Ar flow at 350 °C to remove moisture and weakly adsorbed CO_2, whereas La_2O_3 containing samples were oxidized by 5% O_2/He flow at 500 °C to burn strongly adsorbed carbonates. In all cases, the reducing gas flow was 50 mL·min^{-1} of 5% H_2/Ar and the temperature was raised from 50 to 900°C with a heating rate of 10 °C min^{-1}. The water formed during reduction was trapped using a cold trap and the hydrogen consumption

was continuously monitored with the TCD detector. From TPR profiles, the reducibility, reduction degree as well as number of reducible species were estimated.

2.3.5. Electron microscopy

Electron microscopy comprises a set of techniques that provide information regarding textural and structural properties as well as elemental composition of catalyst at nano scale, which makes it a powerful characterization tool. In this thesis, Current and Scanning Transmission Electron Microscopies were employed.

2.3.5.1. Transmission Electron Microscopy

In Transmission Electron Microscopy (TEM) method, is fundamental irradiating the sample with an electron beam to form an image. According to this technique, first, the electrons are emitted by a filament and accelerated by a potential difference. Subsequently, electrons are highly focused though condenser lenses to form a beam perpendicular to the sample so that only the sample area is irradiated. Then, as part of the beam is transmitted though the sample, electrons are dispersed as a consequence of interaction with sample atoms. Finally, the scattered electrons are refocused, magnified and sent to a fluorescence detector, where sample image is imprinted [79].

Unlike light microscope, transmission electron microscope allows to magnify images of very thin samples down to atomic resolution due to smaller de Broglie wavelength of the electron. In heterogeneous catalysis, this enable visualizing morphology and size of metal particles, from which distribution and dispersion can be calculated. Moreover, if resolution is high enough, this technique even allows differentiating lattice fringes of crystals in order to determine their preferential orientation and shape.

Along this thesis, the particle size distribution of monometallic catalysts was determined by measuring the diameter (d, in nm) of at least 200 particles from TEM micrographs. Furthermore, the mean metal dispersion (D_{Me}) was estimated applying the d-FE model [80] as follows:

$$D_{Me}(\%) = \frac{5.01 d_{at} \sum_j n_j \cdot d_j^2 + 2.64 d_{at}^{0.81} \sum_k n_k \cdot d_k^{2.19}}{\sum_i n_i \cdot d_i^2} \times 100 \qquad (2.11)$$

where d_i, d_j and d_k are the diameters of the "i", "j" and "k" particles, n_i is the number of particles with diameter d_i, n_j is the number of particles with diameter d_j ($d_j > 24.0 d_{at}$), n_k is the number of particles with diameter d_k ($d_k \leqslant 24.0\ d_{at}$) and d_{at} is the atomic diameter of Ni (d_{at} = 0.298 nm) or Ru (d_{at} = 0.356 nm).

Experimental protocol

The micrographs of the monometallic catalysts were obtained by a *TECNAI G2 20 TWIN* microscope of *FEI* company, which can operate with a nominal voltage up to 200 kV and is equipped with a thermionic emission electron gun (LaB_6 filament) along with EDAX-EDS microanalysis system. Those devices allow the microscope to obtain TEM micrographs with resolution up to 0.24 nm and performing surface chemical composition analysis.

All powder samples were mixed with ethanol solvent and kept in an ultrasonic bath for 15 min in order to attain a good suspension. After that, a drop of suspension was spread onto a TEM copper grid (300 mesh) covered by a holey carbon film for each sample. Finally, the grids were dried under vacuum to remove the solvent.

The measurement were carried out by the Electronic Microscopy and Material Microanalysis Service of SGIker.

2.3.5.2. Scanning Transmission Electron Microscopy

Normally, TEM microscopes are equipped with extra scanning coils and detectors, allowing them to work in Scanning Transmission electron Microscopy (STEM) configuration. The main difference comparing to TEM configuration is that the electron beam is focused on a specific point of the sample, rather than on the entire surface. Thus, in this case, a scanning of the surface by a raster illumination system allows to visualize here again the magnified image of the sample with higher resolution. STEM

microscopes require exceptionally stable room environments, being the level of vibration, temperature fluctuations, electromagnetic waves and acoustic waves limited in the room housing of the microscope in order to obtain atomic resolution images [81].

Due to their surface scanning capacity, STEM microscopes are usually coupled with High-Angle Annular Dark-Field (HAADF) detector and Energy Dispersive X-ray (EDX) instrument. Unlike the conventional detector, HAADF imaging mode collects incoherently scattered electrons that do not pass through the sample by means of an annulus around the beam, which gives an advantage in terms of signal collection efficiency (it collects more electrons). For that reason, this method is quite more sensitive to variations in the atomic number (*Z*) of atoms in the sample. The high dependence on *Z* makes HAADF a useful imaging mode to identify small areas of an element with a high *Z* (metal particles) on a matrix with a lower *Z* (support). On the other hand, EDX analysis allows determining the elemental composition of the sample from X-ray emitted from the sample, as in the X-ray Fluorescence (XRF) method. Commonly, HAADF imaging is performed in parallel with EDX analysis, so that elemental composition mapping can be depicted over the STEM-HAADF image.

Experimental protocol

STEM micrograps and elemental EDX-maps were obtained by a *Titan Cubed G2 60-300* microscope of *FEI* Company with very high resolution. This instrument is fitted with a high-brightness Field Emission electron Gun (X-FEG), a monochromator, *CEOS GmbH* Cs-corrector for spherical aberration and Super-X EDX system working together with high annular dark field (HAADF) detector for Z contrast imaging and elemental mapping in STEM conditions (camera length of 185 mm). The nominal size of the electron probe used for STEM and EDX maps was 0.5 nm, the probe current was 170pA and the semiconvergence angle was 14 mrad. High-angle annular dark-field (HAADF-STEM) images were collected with an inner detector radius of 63.5 mrad.

The preparation of samples was carried out following the same procedure as for TEM measurements. The measurements, by contrast, were carried out in “Rosalind

Franklin" special module by the Electronic Microscopy and Material Microanalysis Service of SGIker.

2.3.6. Long-wavelength radiation spectroscopy

In addition to short-wavelength X-rays, there are other less energetic electromagnetic radiations from which useful information can be extracted after having interacted with matter. Like X-radiation, they are classified attending their energy or wavelength. In order of decreasing energy, the types of radiation on which the characterization techniques are based are the following: ultraviolet, visible and infrared radiations.

2.3.6.1. Ultraviolet-visible-Near Infrared Diffuse Reflectance Spectroscopy

Ultraviolet-visible-Near Infrared Diffuse Reflectance Spectroscopy (DRS UV-Vis-NIR) is a very useful technique for structural and qualitative characterisation of solid samples. The method is based on the fact that materials are capable of absorbing light rays with certain wavelengths by its valance electrons. As consequence of the absorption, such electrons are excited and transferred from highest occupied (HOMO) to lowest occupied (LUMO) molecular orbitals. In return, the radiation that has not been absorbed is diffusively reflected defining the colour of the material. Therefore, it can be known at what specific wavelengths the material has adsorbed radiation knowing the amount of incident and diffusively reflected light [82].

The UV spectrophotometer is able to measure the intensity of the light diffusively reflected by the sample (I) by a photosensitive cell and compares it to the intensity of light reflected from a reference material (I_0), obtaining a reflectance percentage (%R). After that, from diffuse reflectance experimental values and applying the Schuster-Kubelka-MunK or SKM model the absorption spectrum is obtained. This spectrum provides information related to the type and oxidation state of species in the catalyst, coordination of metal cations, bandgaps and the presence as well as nature of defects.

Experimental protocol

UV-Vis-NIR measurements were carried out in a *Varian Cary 5000* apparatus coupled to a Diffuse Reflectance Internal 2500. The samples were finely grinded and the spectra, which were registered in reflectance mode at RT, were converted into absorbance spectra by SKM function in a range of wavenumber from 200 to 2500 nm.

The analysis was done by the Bizkaia Central Analysis service (SCAB) of SGIker.

2.3.6.2. Fourier transform infrared spectroscopy

The Fourier Transform infrared spectroscopy is one of the basic techniques for characterization of heterogeneous catalysts, since it provides information regarding the type of adsorbed molecules and functional groups. Infrared spectroscopy exploits the fact that molecules absorb IR frequencies that are characteristic of their structure. These absorption and consequent molecule vibration only take place when the frequency of IR radiation matches the vibrational frequency of the molecule, i.e., at resonant frequencies. These frequencies are associated with the strength of the bond and mass of the atoms at its ends. Therefore, depending on its structure, a molecule can vibrate in different ways or modes. Generally, the vibration can generate either a change in the bond length (stretching) or in the bond angle (bending) [83]. Likewise, the bond can stretch in-phase (symmetrical stretching) or out-of-phase (asymmetric stretching) and also it can bend in phase (scissoring and rocking) and out-of-phase (twisting and wagging), as depicted in Figure 2.4.

Normally, FTIR analysis is conducted on cells provided with control of pressure, temperature and composition of the atmosphere. In fact, these devices are able to monitor catalytic reactions *in situ* [84]. On the other hand, the Michelson interferometer is the most important part of modern IR spectrometers, since allows the simultaneous analysis of all wavenumbers avoiding the presence of a monochromator. The interferometer consists of two perpendicular mirrors of which one is mobile and can change the path of the beam. Among them an IR beam splitter is placed, where part of the beam coming from the source is reflected towards first

mirror and the other part is transmitted towards the second mirror. After bouncing, the beams go back to the splitter where interfere and again, one part is transmitted and the other is reflected. However, the interference between the two beams will depend on the path difference between them, being able to draw an interferogram varying the position of the mirror. Finally, the interferogram is converted to IR spectra by Fourier transforms. The FTIR spectra is formed by several peaks and bands at specific frequencies or wavenumbers (the number of waves per cm), which are characteristic of different adsorbed species on catalyst surface.

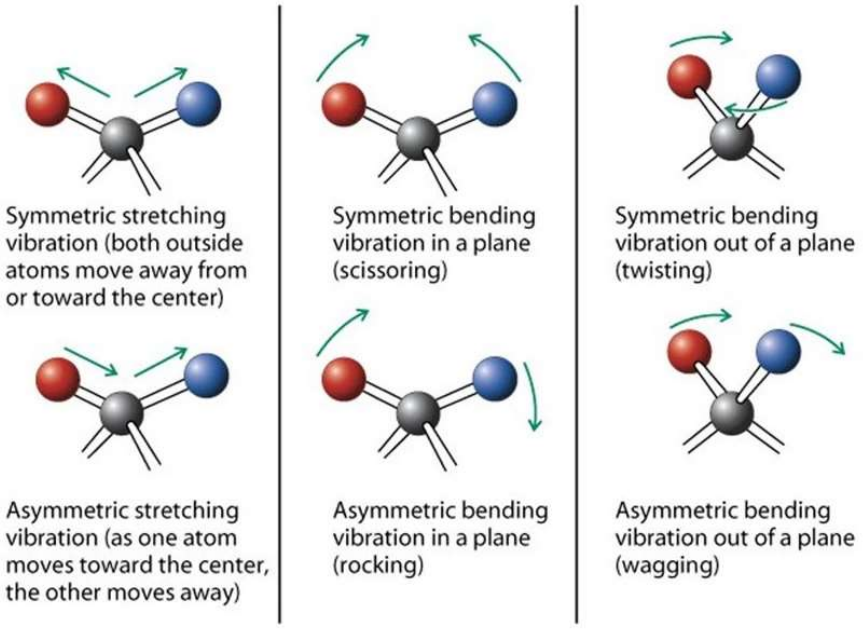

Figure 2.4. Vibration modes leading to IR absorptions.

Experimental protocol

Operando FTIR spectra were collected using an *In-Situ Research Instruments* IR cell, coupled to a *Nicolet 6700* spectrometer equipped with Mercuric Cadmium Telluride (MCT) detector and *Michelson* interferometer. The experimental setup also contains a feed system formed by two lines, two mixers and a set of Mass Flow Controllers (MFC) to introduce different gas mixtures of H_2, CO_2 and Ar. Additionally, a

6-way valve allows quickly switching the gas stream to work in non-stationary conditions (e.g., CO_2 adsorption/reduction experiments).

Powdered samples were pressed at 1.5 tons into 10 mg cm^{-2} wafers which, prior to the experiments, were *in situ* activated/reduced at 500 °C for 1 h under a 5% H_2/Ar flow of 20 mL min^{-1}. After pretreatment, wafers were cooled down under Ar flow to 150 °C, being background spectra collected every 25 °C. After that, *Operando* FTIR experiments were carried out under either CO_2 adsorption or methanation conditions. CO_2 adsorption tests were carried out by exposing samples to a 20 mL min^{-1} stream of 5% CO_2/Ar, whereas in CO_2 methanation experiments a 5% CO_2/ 20% H_2/Ar gas mixture was used. In both cases, experiments were carried out in two steps. Firstly, the used gas mixture was stabilized during 30 min and a series of spectra were collected at 0, 1, 3, 5, 10, 15 and 30 min. Secondly, Temperature Programmed Adsorption (TPA, CO_2/Ar flow) or Temperature Programmed Surface Reaction (TPSR, CO_2/H_2/Ar flow) was run from 150 to 450 °C using a heating rate of 2 °C min^{-1}. Note that the depicted spectra were obtained by subtraction of those recorded under reaction/adsorption conditions every 25 °C and those corresponding to backgrounds. All FTIR spectra were obtained recording 64 scans with a resolution of 4 cm^{-1}.

2.4. REACTION SYSTEM

The reaction system employed to study the catalytic performance of all formulations synthesized in this thesis was a *Microactivity* apparatus of *PID Eng&Tech* company.

2.4.1. Reaction set-up

The experimental equipment is divided into three sections: feed, reaction and analysis sections.

2.4.1.1. Feed section

The feed section consists of 5 pressurized lines (P = 5 bar) by which inert gases as well as reagent and products involved in CO_2 methanation can be fed: H_2, CO_2, CH_4, CO,

He and N_2. The feed is carried out by a set of *Bronkhorst* Mass Flow Controllers (MFC), which precisely regulate the flow rate. Through 1/8-inch pipes, the gases first go to a mixer where the homogeneous reaction stream is formed and then either enter the reactor or bypass it by a 6-way valve. Additionally, water can be fed by means of a *GILSON* 307 pump connected to a 1L deposit. The pump sent water to an evaporator at 150 °C which is located inside the reaction section. Before entering the reactor, water vapor is diluted in the gaseous mixture by a second mixer.

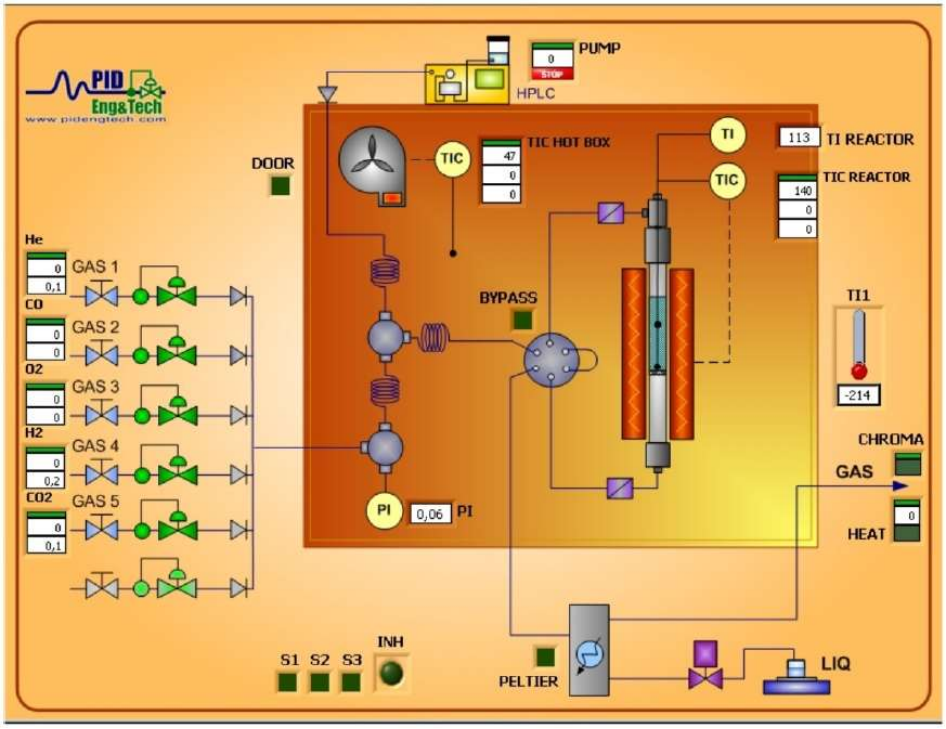

Figure 2.5. Reaction system flow diagram.

2.4.1.2. Reaction section

The reaction section comprises a downflow fixe-bed reactor made of stainless steel (L = 305 mm). Its external (D_{ext}) and internal (D_{int}) diameters (D) measure 143 and 91 mm, respectively (L/D = 3.35). The reactor is centered in a cylindrical and ceramic oven, which contains heating resistances. At a certain height, the reactor has a porous

plate, which allows supporting the catalyst bed and exit of reaction gases. The reaction temperature is measured by a K-type thermocouple in contact with the catalyst bed and is controlled by *TOHO TTM-005* device, which regulates oven resistance power by sending electric signals according to temperature measurements of the thermocouple. Note that the reactor is designed in such a way the catalyst bed is situated in an ideally isothermal zone of 4 cm. Moreover, the reactor and oven are located at a stainless-steel insulating chamber (hot box) at 130 °C, which prevents materials from thermal stress and avoid water condensation within the pipes. Downflow the reactor, there is a Peltier cooling module where the produced water is condensed and retained in a deposit before entering to the analyzer.

2.4.1.3. Analysis section

The outlet gas stream composition was analyzed by Gas Chromatography (GC), which is a physical method through which a gaseous mixture compounds can be separated. In a gas chromatograph, a small volume (0.5 cm^3) of reaction mixture is injected and subsequently dissolved in a fluid (He or Ar) called mobile phase, which carries it through a fixed porous material or stationary phase (column). Due to each component present different interaction (adsorption-desorption cycles) with the stationary phase, their retention time is different, i.e., they travel at different apparent speeds within the mobile phase so that they leave the column at different times. Then, they enter separately into a TCD detector, where they put in contact with a warm filament (250 °C). The different thermal conductivity of each compound causes a change in filament temperature that is converted into an electric signal.

In this thesis, the analysis was conducted on-line in an *Agilent 7890B* gas chromatograph. This equipment includes an oven in which the two separation channels (A and C) are placed and two TCD detectors located at the exit (one for each channel). Channel A uses Ar as carrier gas and contains a molecular sieve column able to separate He, H_2 and N_2. On the contrary, Channel C employs He as carrier fluid and is comprised by two columns in series. The first is of HayeSep type and is used to separate CO_2 from heavier hydrocarbons (C_2^+), whereas the second is a molecular sieve column in which N_2, CH_4 and CO are separated. Besides, this channel disposed of a

needle valve that allows bypassing molecular sieve column avoiding the entry of CO_2. the head pressure of each channel is adjusted by Electronic Pressure Controllers (EPC) and oven temperature by a Temperature Indicator Controller (TIC).

2.4.2. Reaction conditions and activity parameters

CO_2 methanation reaction was performed in a downstream fixed bed reactor (ID = 9 mm). In all cases, except for kinetic experiments, the stainless-steel reactor was loaded with 0.5 g of catalyst particles (d_p = 300-500 µm), which were diluted to 50% (v/v) with quartz particles in order to avoid hot spots. The Ni and Ru catalysts prepared by IWI were firstly reduced at 500 and 400 °C for 1 h with 20% H_2/He, respectively. The samples prepared by GAI were also reduced but at 250 °C in order to remove the passivated nickel layer. After cooling down the samples to 200 °C with He (inert gas), the temperature was raised up to 400 or 500 °C in steps of 25 °C under reactant stream. This gaseous mixture was composed of 16% CO_2 and of either 64% H_2 (H_2/CO_2 = 4) or 80% H_2 (H_2/CO_2 = 5), balanced up to 100% with He (total flow of 250 cm^3 min^{-1}). All reactions, were carried out at atmospheric pressure, WHSV of 30,000 mL h^{-1} g_{cat}^{-1} and GHSV of 10,000 h^{-1} (note that $V_{bed} = V_{cat.} + V_{inert}$).

The catalytic performance was evaluated by CO_2 conversion (X_{CO_2}), CH_4/CO products selectivity (S_{CH_4} or S_{CO}) and yield (Y_{CH_4} and Y_{CO}) which were calculated from reactor inlet and outlet molar flows according to the following equations:

$$X_{CO_2} = \frac{F_{CO_2}^{in} - F_{CO_2}^{out}}{F_{CO_2}^{in}} \times 100 \quad (2.12)$$

$$S_{CH_4} = \frac{F_{CH_4}^{out}}{F_{CO_2}^{in} - F_{CO_2}^{out}} \times 100 \quad (2.13)$$

$$S_{CO} = \frac{F_{CO}^{out}}{F_{CO_2}^{in} - F_{CO_2}^{out}} \times 100 \quad (2.14)$$

$$Y_{CH_4} = X_{CO_2} \times \frac{S_{CH_4}}{100} = \frac{F_{CH_4}^{out}}{F_{CO_2}^{in}} \times 100 \quad (2.15)$$

$$Y_{CO} = X_{CO_2} \times \frac{S_{CO}}{100} = \frac{F_{CO}^{out}}{F_{CO_2}^{in}} \times 100 \quad (2.16)$$

where F_i is the inlet or outlet molar flow of component "*i*" in mol min^{-1}.

Finally, the TurnOver Frequency (*TOF*) numbers, which indicate the number of CO_2 molecules converted per second and per surface metal atoms (active sites), were calculated as follows:

$$TOF_{Me} = \frac{-r_{CO_2}\left(\text{mol } CO_2\ g_{cat.}^{-1}\ s^{-1}\right)}{S_{Me}\left(\text{mol Me}\ g_{cat}^{-1}\right)} = \frac{F_{CO_2}^{in} \times X_{CO_2} \times MW_{Me}}{W \times D_{Me} \times F_{Me}} \quad (2.17)$$

where $-r_{CO_2}$ is the reaction rate in mol g^{-1} s^{-1} calculated under differential reactor conditions (X_{CO_2} < 10%), S_{Me} are the surface metal moles, *MW* is the mass weight of the metal in g mol^{-1}, *W* is the catalyst weight in g, D_{Me} is the metallic dispersion and F_{Me} is the mass fraction of metal in the catalyst.

Chapter 3

ALUMINA-SUPPORTED Ni AND Ru CATALYSTS

ABSTRACT

The present chapter presents a study of the effect of Ni and Ru loadings on the catalytic performance of alumina-supported catalysts for CO_2 methanation reaction. All catalysts have been prepared by Incipient Wetness Impregnation, characterized by several techniques (N_2 physisorption, CO_2-TPD, XRD, H_2-chemisorption, XPS and H_2-TPR) and evaluated for CO_2 methanation in a fixed bed reactor at GHSV = 10,000 h^{-1} and $W / F^0_{CO_2}$ = 4.7 (g cat.) h mol^{-1}. Characterization results show that addition of increasing loadings of Ni and Ru lead to the formation of both CO_2 adsorption and H_2 dissociation active sites, which are necessary to carry out CO_2 hydrogenation into methane. Easily reducible ruthenium is dispersed on γ-Al_2O_3 in form of large agglomerates, whereas Ni presents a higher dispersion and, in return, a great interaction with the support. 12% Ni and 4% Ru result to be the optimal contents providing metal surfaces of 5.1 and 0.6 m^2 g^{-1}, T_{50} values of 340 and 310 °C and activity being quite stable for 24h-on-stream. In terms of turnover frequency (TOF), 4%Ru/Al_2O_3 is quite more efficient than 12%Ni/Al_2O_3 catalyst, probably due to a greater ability of the noble metal to dissociate hydrogen.

3. ALUMINA-SUPPORTED Ni AND Ru CATALYSTS

Commonly, catalysts used in CO_2 methanation consists of group VIII transition metals (active phase) supported over mesoporous solids. The industrially used γ-alumina has proven to be an effective amphoteric support to carry out CO_2 methanation [43, 85]. This support provides medium specific surface area (100-250 m^2 g^{-1}) over which the active site can be well dispersed and contains certain surface basicity (OH^- groups and surface O^{2-} Lewis basic sites) for CO_2 activation. Despite these advantageous catalytic properties, alumina lacks high thermal stability which might lead to sintering of the supported metal [86]. For that reason, before metal incorporation, it is convenient a prior thermal stabilization at the maximum operating temperature, although the specific surface area and pore volume are slightly reduced.

Regarding the active phase, it has already mentioned that Ni and Ru are the most employed metallic elements of group VIII. While Ru is by far more active and selective, its only disadvantage compared to nickel is its exorbitant price ($ 750/ozt according to ref. [87]). In recent literature, there are many works that report separately the catalytic performance of Ni-based and Ru-based formulations at different operating conditions, which makes the comparison between both metals difficult. Previously, Garbarino et al. [85] reported the better catalytic behaviour of commercial 3%Ru/Al_2O_3 compared to 20%Ni/Al_2O_3 catalyst, observing that the former attains equilibrium conversion at a temperature 100 °C lower (300 °C vs. 400 °C).

Note that the activity of the supported catalyst will not only depend on the metal type but also on the metal loading and dispersion. Normally, rising the metal loading or active phase content leads to increased catalytic activity only up to a limited extent, as this in turn also results in a dispersion decrease due to particle sintering at the expense of new active sites formation. Then, the more active, selective and stable catalyst will typically be the one with the best compromise between metal content and particle size [48, 88]. All things considered, we prepared two series of Al_2O_3-supported Ni and Ru catalysts by Incipient Wetness Impregnation (IWI, section 2.2.1) with loadings that assure metal particle size to be effective to dissociate H_2 and activate CO_2

reduction. This chapter aims to compare both formulations at the same reaction conditions and to study the effect of metal loading.

3.1. CHARACTERIZATION

Among others, specific surface area, surface basicity, metal dispersion and reducibility are considered key catalytic parameters to achieve an effective and selective CO_2 hydrogenation into CH_4. A CO_2 methanation catalyst should present high metal and specific surface areas, medium-strength basic sites and high reducibility. Furthermore, the active site must be efficient in H_2 dissociation and the support should be basic to attract and activate CO_2. In that way, the catalyst must be able to effectively adsorb CO_2, then hydrogenate and, finally, desorb CH_4 at low-medium temperature. Thus, the supported catalysts have been characterized by N_2 physisorption, CO_2-TPD, XRD, H_2-chemisorption, H_2-TPR and XPS providing information about surface properties, crystallinity and metal dispersion as well as the nature of Ni and Ru species. In this section, all the characterization results of Ni/Al_2O_3 and Ru/Al_2O_3 catalysts are compared and discussed.

3.1.1. Surface properties

Figure 3.1 shows the N_2 physisorption isotherms as well as the pore size distribution of alumina support used for the prepared catalysts. As it can be noticed, the shape of the isotherms is characteristic of mesoporous solid: a great quantity of N_2 is adsorbed at intermediate relative pressures by multilayer filling with a hysteresis loop at relative pressures higher than 0.65 (type IV isotherm and H2 hysteresis loop according to IUPAC). The values of BET surface area, mesopore volume and average pore size for fresh γ-Al_2O_3 are 214 $m^2\ g^{-1}$, 0.563 $cm^3\ g^{-1}$ and 10.1 nm, respectively (Table 3.1). These values are high enough to perform the impregnation of large metal loadings, allowing the present chapter concerning the effect of active phase content. Textural properties of alumina-supported Ni and Ru catalysts are also summarized in Table 3.1. It can be observed that the raise of Ni content from 4 to 20% leads to a gradual decrease of specific surface area and mesopore volume from 214 $m^2\ g^{-1}$ to 131 $m^2\ g^{-1}$ and from 0.563 $cm^3\ g^{-1}$ to 0.326 $cm^3\ g^{-1}$, respectively.

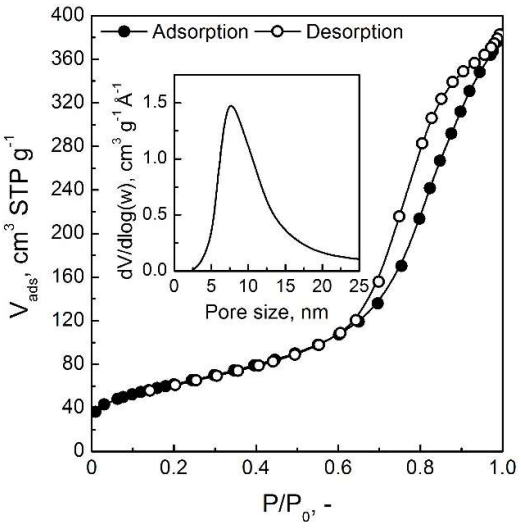

Figure 3.1. N_2 adsorption-desorption isotherms of γ-Al_2O_3.

Table 3.1. Physicochemical properties of alumina-supported Ni and Ru catalysts.

Sample	Ni/Al and Ru/Al[a]	S_{BET}[b] (m^2 g^{-1})	V_{meso}[c] (cm^3 g^{-1})	d_{pore}[d] (nm)	Des. CO_2[e] (μmol g^{-1})	Basicity (μmol CO_2 m^{-2})
Al_2O_3	-	214	0.563	10.1	69	0.32
4%Ni/Al_2O_3	0.038	191	0.435	8.8	80	0.42
8%Ni/Al_2O_3	0.079	175	0.383	8.4	72	0.41
12%Ni/Al_2O_3	0.122	160	0.373	9.0	71	0.44
16%Ni/Al_2O_3	0.175	147	0.369	9.7	68	0.46
20%Ni/Al_2O_3	0.224	131	0.326	9.6	65	0.50
1%Ru/Al_2O_3	0.007	198	0.411	8.0	50	0.25
2%Ru/Al_2O_3	0.015	193	0.429	8.4	51	0.26
3%Ru/Al_2O_3	0.021	185	0.417	8.5	43	0.23
4%Ru/Al_2O_3	0.029	172	0.382	8.5	38	0.22
5%Ru/Al_2O_3	0.032	179	0.425	9.1	48	0.27

[a]Determined by XRF.
[b]Calculated applying BET fit (Equation 2.2).
[c]Estimated from adsorption isotherm ($V_{ads.}$ at P/P_0 = 0.98).
[d]Determined by BJH method (Equation 2.3).
[e]Estimated from CO_2-TPD profiles integration up to 350 °C.

These changes in textural properties are related to partial blockage/filling of alumina mesopores with NiO aggregates and/or to partial collapse of the mesoporous structure [44, 89, 90]. Note that similar trends are observed when varying Ru loading.

Additionally, the effect of Ni and Ru incorporation on the surface basicity was studied by means of CO_2-TPD. Figure 3.2 shows the CO_2-TPD profiles for γ-Al_2O_3 and for the catalysts with the highest contents of Ru and Ni, i.e., 5%Ru/Al_2O_3 and 20%Ni/Al_2O_3.

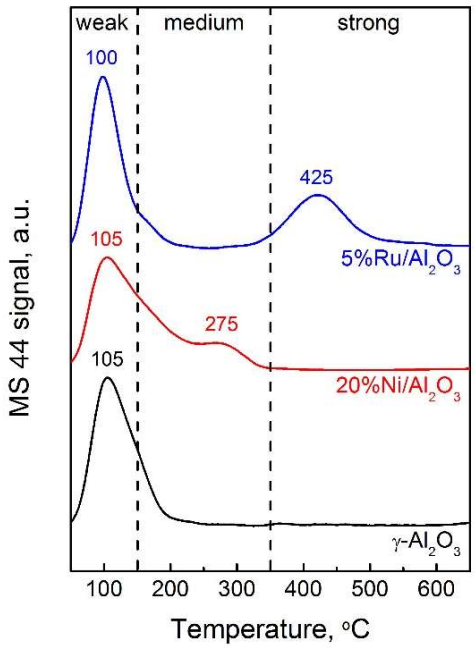

Figure 3.2. CO_2-TPD profiles of γ-Al_2O_3 support, 20%Ni/Al_2O_3 and 5%Ru/Al_2O_3 catalysts.

The prepared samples contain different CO_2 adsorption sites (OH^- groups and surface O^{2-}) with different strength. According to the desorption temperature or chemical bond strength, basic sites can be classified into weak (T < 150 °C), medium (T = 150-350 °C) and strong (T > 350 °C) [44, 91]. It can be observed that bare alumina presents a single desorption peak at 105 °C, assigned to CO_2 desorption from weak Bronsted OH^- groups [92]. Noteworthy, additional CO_2 desorption shoulder and peak are observed around 200 °C and 275 °C by adding 20% Ni, which are associated with

decomposition of both bidentate and monodentate carbonates from medium-strength Lewis basic sites [45]. On the other hand, 5%Ru/Al_2O_3 catalyst shows a new CO_2 desorption peak at 425 °C, which might be attributed to decomposition of quite stable bulk carbonates formed during calcination at 400 °C [93] rather than during the CO_2-TPD test. Unlike Ni/Al_2O_3 samples, Ru/Al_2O_3 catalysts are reduced at a temperature lower than that of calcination, making difficult to remove this type of carbonates. It is expected that this species, which probably is adsorbed on Al_2O_3 surface, does not participate in the reaction.

The CO_2 surface density quantification obtained from integration of MS 44 signal up to 350 °C is also shown in Table 3.1 (last column). Note that the addition of increasing Ni contents to Al_2O_3 rises CO_2 surface density from 0.32 to 0.5 μmol m^{-2}. However, the basicity of Ru/Al_2O_3 at T < 350 °C is lower to that of the support probably due to the replacement of weakly adsorbed CO_2 by stable bulk carbonates during successive calcinations. This increase of surface basicity with addition of Ni could theoretically be explained in terms of electronegativity. The electronegativity values of the elements that participate in CO_2 adsorption are 1.6, 1.9 and 3.5 for Al, Ni and O, respectively. These values indicate that surface O^{2-} and OH^- groups linked to Al must contain higher negative charge density (lower basicity) than those attached to Ni. Then, differences in electronegativity show that Al transfers more negative charge density than Ni to surface O^{2-}. Therefore, considering that CO_2 is an acid gas with a high negative charge density, the sites with the highest CO_2 adsorption capacity (and the lowest negative charge density) correspond to O^{2-} (and OH^- if applicable) linked to Ni.

3.1.2. Crystallinity and metal dispersion

Crystalline phases of reduced catalysts were identified by X-Ray Diffraction. XRD patterns of both calcined and reduced Ni/Al_2O_3 catalysts are shown in Figures 3.3a and b, whereas those of Ru/Al_2O_3 catalysts are displayed in Figures 3.3c and d. In all cases, XRD peaks can be observed at 37.7, 45.8 and 66.8° 2θ, corresponding to gamma-alumina (311), (400) and (440) diffraction planes, respectively (PDF 01-079-1558). These broad peaks together with an elevated XRD signal background point out that this

γ-Al_2O_3 is rather an amorphous than a crystalline solid, which makes the identification of crystalline nano-particles more difficult due to peaks overlapping.

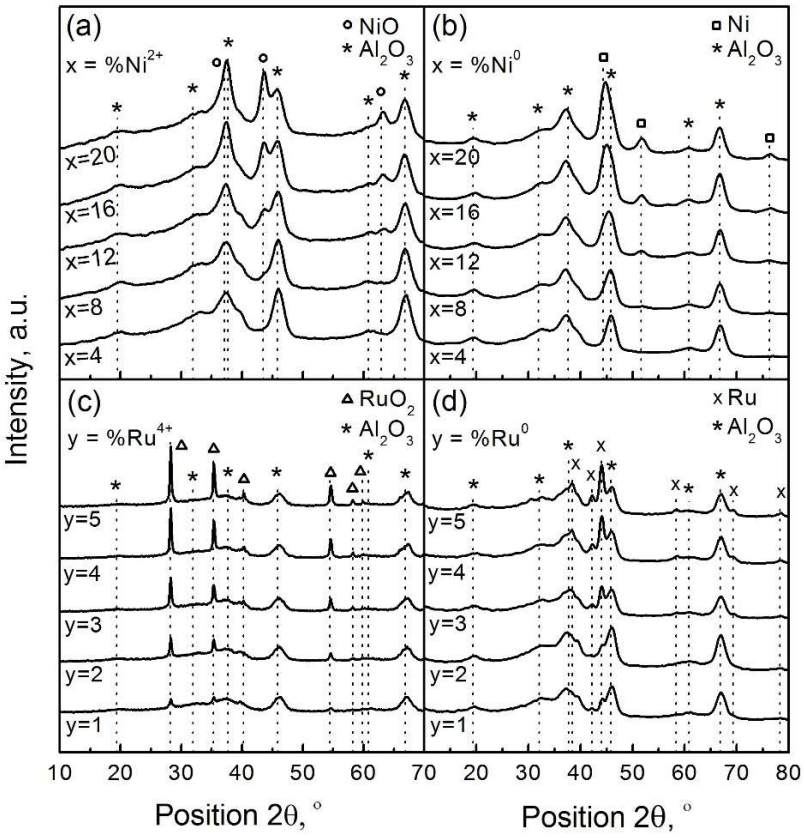

Figure 3.3. XRD patterns of (a, c) calcined and (b, d) reduced gamma-alumina supported catalysts with increasing Ni and Ru contents.

In fact, for Ni/Al_2O_3 catalysts, the presence of crystalline Ni phases was only detected for catalysts with Ni contents higher than 8%. NiO was identified for calcined catalysts [43] (Figure 3.3a) and the appearance of XRD peaks at 44.3, 51.7 and 76.1° 2θ in Figure 3.3b revealed the formation of elemental Ni in reduced catalysts [58]. However, the presence of $NiAl_2O_4$ (peaks located at 37.0, 45.0 and 65.5° 2θ) could not be identified, since it contains the same spatial group with a similar cell parameter of Al_2O_3 (PDF 00-010-0339).

Both crystallite sizes and Ni dispersion are summarized in Table 3.2. The XRD patterns of catalysts with Ni content lower than 12% showed similar diffraction pattern to original Al_2O_3 (not shown), probably due to a high dispersion of Ni species (crystallite sizes lower than 5 nm). Therefore, Ni crystallite sizes could be only estimated by Scherrer formula (Equation 2.7) for 12, 16 and 20% Ni loaded catalysts.

Table 3.2. Crystallite sizes and metal dispersion of the catalysts.

Catalyst	**Crystallite size (nm)[a]**		**Dispersion (D_{Me}, %)[b]**	**Metal surface (S_{Me}, $m^2\ g^{-1}$)[b]**
	NiO or RuO_2	**Ni or Ru**		
4%Ni/Al_2O_3	< 5	< 5	38.3	0.985
8%Ni/Al_2O_3	< 5	< 5	26.1	2.907
12%Ni/Al_2O_3	< 5	4.8	17.9	5.083
16%Ni/Al_2O_3	9	6.1	13.3	6.186
20%Ni/Al_2O_3	8.5	7.3	11.0	7.527
1%Ru/Al_2O_3	29.0	7.4	5.5	0.201
2%Ru/Al_2O_3	34.0	8.1	4.7	0.344
3%Ru/Al_2O_3	37.9	11.0	4.5	0.489
4%Ru/Al_2O_3	41.4	11.3	4.2	0.609
5%Ru/Al_2O_3	43.8	12.1	3.9	0.711

[a]Estimated by Scherrer equation (Equation 2.7).
[b]Calculated by H_2-chemisorption (Equations 2.4 and 2.5, respectively).

In all cases, Ni crystallite sizes lower than the average pore size of Al_2O_3 (10.1 nm, see Table 3.1) were observed, which suggests that Ni could be located inside the pores of the catalytic support. It can be observed that dispersion values obtained by H_2-chemisorption match with the trend observed by XRD: the Ni crystallite size estimated by XRD grows from < 5 to 7.3 nm, whereas D_{Ni} is reduced from 38 to 11% with the increase of Ni loading. As will be seen later, not all nickel can be reduced or is activated after reduction pretreatment for 1 h at 500 °C and therefore, we refer to the dispersion of nickel reducible at those conditions.

In the case of Ru/Al_2O_3 catalysts, diffraction peaks at 28.0, 35.1 and 54.2° 2θ were observed in calcined catalysts, characteristic of tetragonal RuO_2 [56, 94] (Figure 3.3c).

After reduction pretreatment at 300 °C, new XRD peaks were detected at 38.4, 42.2 and 44.0° 2θ confirming the presence of ruthenium in reduced state (PDF 00-006-0663). As it can be clearly observed in Figure 3.3d, the intensity of the peaks grows with the increase of ruthenium content from 1 to 5%. The markedly more intense XRD peaks of hexagonal Ru compared to those of cubic Ni are due to both higher crystallinity and crystallite sizes, which have also been estimated by Scherrer equation and values are also summarized in Table 3.2. Note that Ru crystallite size increases from 7.4 to 12.1 nm, suggesting a small decrease in active phase dispersion. This trend is in line with H_2 chemisorption results: Ru dispersion slightly decreases from 5.5 to 3.9% as metallic content increases from 1 to 5%. Then, the lowest dispersion of 5%Ru/Al_2O_3 catalyst may be associated with the presence of larger Ru particles formed by agglomeration of several Ru nano-crystals.

In order to determine the effect of temperature on the crystallinity of Ni/Al_2O_3 and Ru/Al_2O_3 samples, additionally, thermo-diffractometric studies were carried out. Figure 3.4 shows the XRD spectra waterfall of Ni/Al_2O_3 catalyst precursor from 110 to 1010 °C (steps of 100 °C), including starting reference spectrum at 30°C.

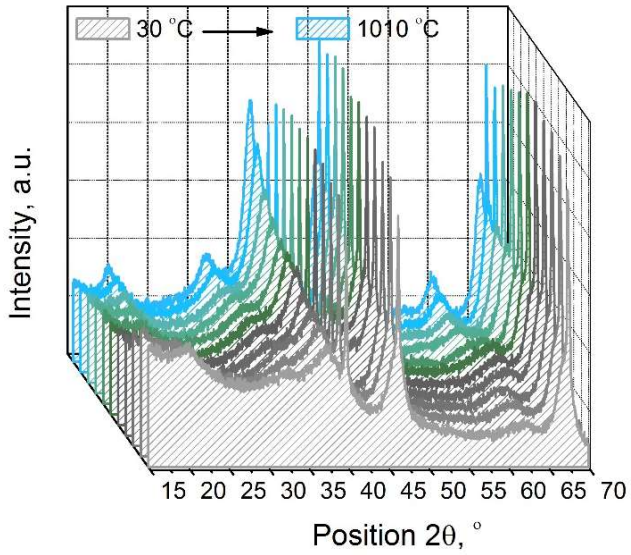

Figure 3.4. Thermo-diffractometric analysis of Ni/Al_2O_3 precursor.

The variations in intensity and position of the diffraction peaks with temperature are related to changes in the sample crystallinity or to the formation/disappearance of crystalline nickel phases. In fact, the unique peaks that remain unchanged in the whole temperature range are those assigned to inevitable diffraction of the platinum sample holder, at 39.7, 46.2 and 67.4° 2θ. Note that the colour of the sample changes with temperature following this sequence: from grey to greenish-grey, from greenish-grey to greenish-blue and from greenish-blue to blue.

In the 30 - 310 °C temperature range, only the characteristic XRD peaks of Al_2O_3 were detected, suggesting that a higher temperature is needed for the formation of Ni crystalline phases. However, from 310 to 610 °C the development of a broad band can be observed at 62.9° 2θ, which is tentatively attributed to highly dispersed greenish-grey NiO. Finally, above 610 °C, the NiO peaks disappearance is followed by the formation of an intense peak at 59.7° 2θ characteristic of blue nickel aluminate spinel ($NiAl_2O_4$) [86, 93]. Additionally, observe that the peak at 37° 2θ gains in intensity above 710 °C, which verify the presence of highly crystalline $NiAl_2O_4$. Therefore, it seems that the formation of spinel phase takes place at temperatures above 600 °C and considering that Ni/Al_2O_3 samples were calcined at 500 °C, the presence of a considerable amount of this compound in the prepared catalysts seems unlikely.

On the other hand, the thermo-XRD patterns waterfall (T = 110 – 1010 °C) of Ru/Al_2O_3 catalyst precursor is shown in Figure 3.5. In this case, the presence of Ru crystalline phase (RuO_2) is detected at temperatures above 210 °C and the XRD intensity at 28, 35 and 54.2° 2θ clearly rises with temperature up to 800 °C, indicating the increasing formation of RuO_2 tetragonal nano-crystals. At temperatures between 810-1010 °C, however, the XRD intensity significantly drops, which is associated with the disappearance of RuO_2 maybe due to the formation of volatile oxides (RuO_X) [49]. Noteworthy, the size of the nano-crystals remains stable (≈ 20 nm) up to 500 °C and afterwards exponentially grows until 60 nm, suggesting a notable decrease of Ru dispersion for temperatures above 500 °C. Therefore, this confirms that the calcination temperature of 400 °C seems to be enough to form crystalline RuO_2 as Ru precursor and avoid an excessive growing of the crystallites.

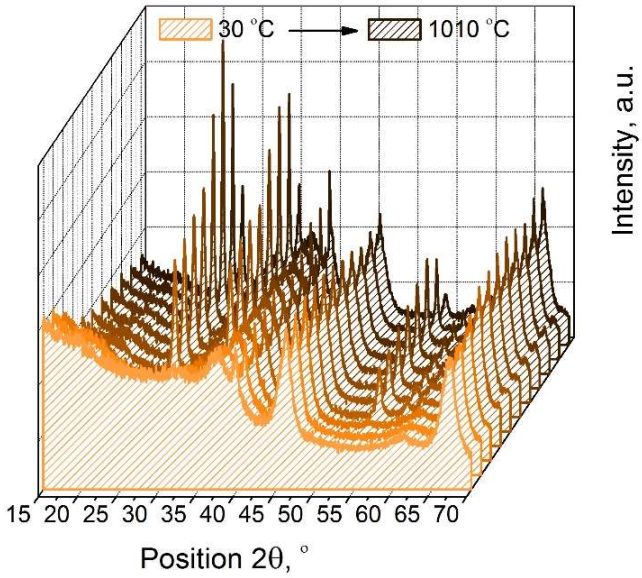

Figure 3.5. Thermo-diffractometric analysis of Ru/Al_2O_3 precursor.

3.1.3. Analysis of Ni and Ru species nature by XPS and H_2-TPR

In order to study the atomic surface composition of prepared catalysts and the nature of surface Ni and Ru species, XPS characterization was carried out. A certain amount of carbon, attributed to atmospheric CO_2 adsorption, was detected by XPS on the surface of all catalysts (between 12 and 15%). Therefore, a direct analysis of the quantitative results of the surface composition is complex and more relevant information is obtained by analyzing the concentration ratios between elements. Figures 3.6a and b show the effect of metal loading on surface Ni/Al and Ru/Al atomic ratios of fresh and used (catalytically tested) samples.

Firstly, note that auxiliary lines in both figures display a proportional evolution of Ni/Al and Ru/Al with metallic contents, i.e., considering that metallic content does not affect the dispersion. That said, it can be observed that in both cases the amount of surface Ni increases with the total amount of Ni in Figure 3.6a. However, the surface Ni/Al ratios are below the auxiliary line, which suggests a certain decrease in Ni dispersion. These results are consistent with XRD results, where an increase of Ni

particle size with the metal loading was observed. Besides, the Ni/Al ratios are lower in the used catalysts compared to the fresh ones, indicating sintering during the catalytic tests.

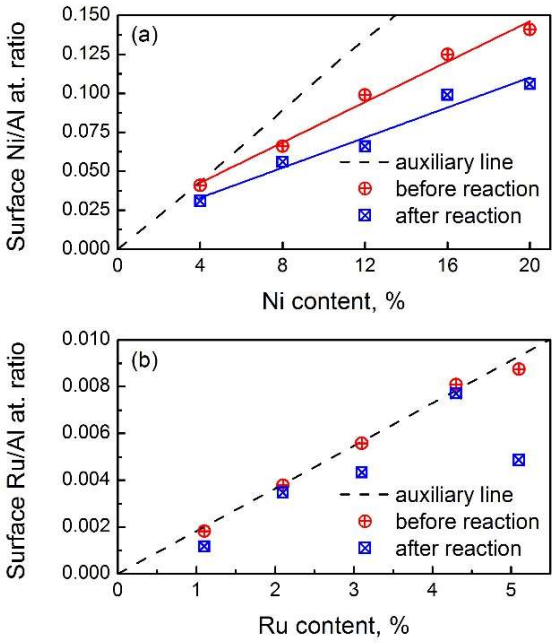

Figure 3.6. Effect of (a) Ni and (b) Ru content on Ru/Al and Ni/Al surface atomic ratios.

The impregnation of different amounts of Ru, however, has a different effect on Ru/Al surface atomic ratio (see Figure 3.6b). In this case, the amount of surface Ru also increases with Ru content; but unlike the Ni/Al ratios, the Ru/Al ratios follow the auxiliary line. This indicates that Ru dispersion does not vary considerably with the increase of metal loading from 1 to 5%. In fact, similar particle sizes of Ru were observed by H_2-chemisorption indicating the same trend. Finally, observe that the Ru/Al ratios are similar in fresh and in used catalysts, i.e., Ru dispersion remains stable during reaction, except for the 5% Ru sample.

Figures 3.7a and b show X-ray photoelectronic spectra corresponding to the nickel $2p_{3/2}$ transition for fresh and used Ni/Al_2O_3 catalysts, respectively. Deconvolutions of

spectra were carried out, since in all cases broad and asymmetric bands were observed, suggesting the presence of different Ni species on the surface. Additionally, dashed black auxiliary lines were included in the graphs, which indicate the energies described in the literature for different nickel species [95, 96].

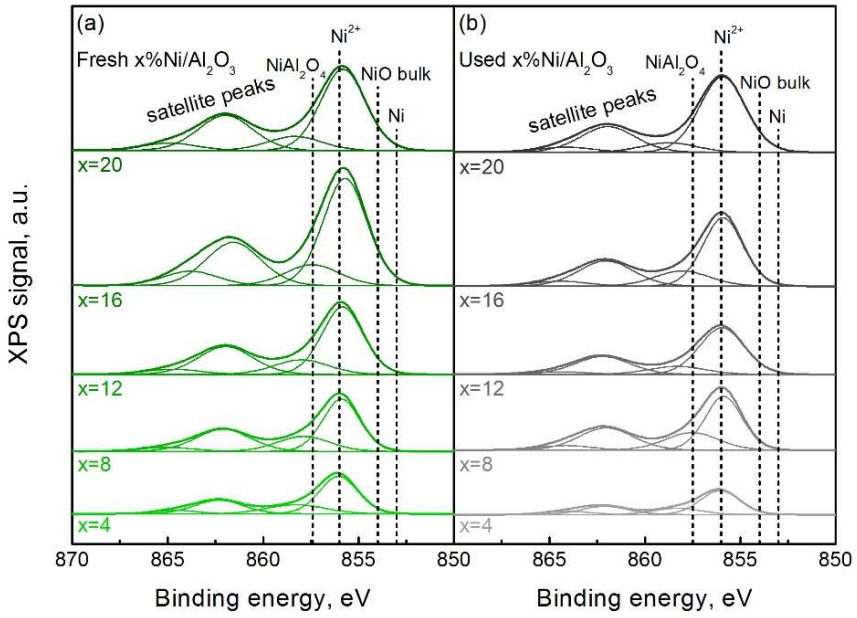

Figure 3.7. Ni $2p_{3/2}$ XPS spectra of (a) fresh and (b) used catalysts.

All these catalysts exhibit peaks close to 856.0 and 858.0 eV with its corresponding shake-up satellites at ~862.0 and~864.5 eV. Note that the first peak is located among 853.9 and 857.0 eV binding energies assigned to bulk NiO and $NiAl_2O_4$, respectively [97]. From this observation, we can discard the presence of great amount of bulk NiO on all catalysts. The main peak at 856 eV corresponds to Ni^{2+} interacting with alumina [98], while the smaller peak at 858 eV is consistent with the formation of nickel spinel $NiAl_2O_4$ [86]. Noteworthy, the slight shift of the main peak towards lower BE with the increase of Ni content could be due to the weakening of metal-support interaction [99]. However, the main peak remains in the same position after reaction, indicating that Ni species are stable during catalytic tests. It should also be mentioned that no Ni^0 specie

was found in used catalysts (Figure 3.7b), since its passivation occurs when the samples are in contact with air.

Ru $3d_{5/2}$ core level XPS spectra of fresh and used Ru/Al_2O_3 catalysts are displayed in Figures 3.8a and b, respectively. As in the case of Ni catalysts, auxiliary dashed black lines indicating reported energies of different Ru species were included in the figures. XPS spectra of fresh catalysts with different content of Ru can be deconvoluted into two contributions assignable to different species of Ru, both cationic, at ~282.3 and ~280.8 eV. These peaks are consistent with the presence of Ru(VI) and Ru(IV) oxides on the catalysts surface [100, 101]. The XPS spectra of used catalysts exhibit the partial reduction of ruthenium oxides during the catalytic tests, showing two peaks at ~281.4 and ~280.0 eV. In this case, these peaks correspond to hydrated RuO_2 and metallic Ru, respectively [102, 103]. Finally, the long tail observed at binding energies higher than 282 eV is due to overlap with C 1s transition.

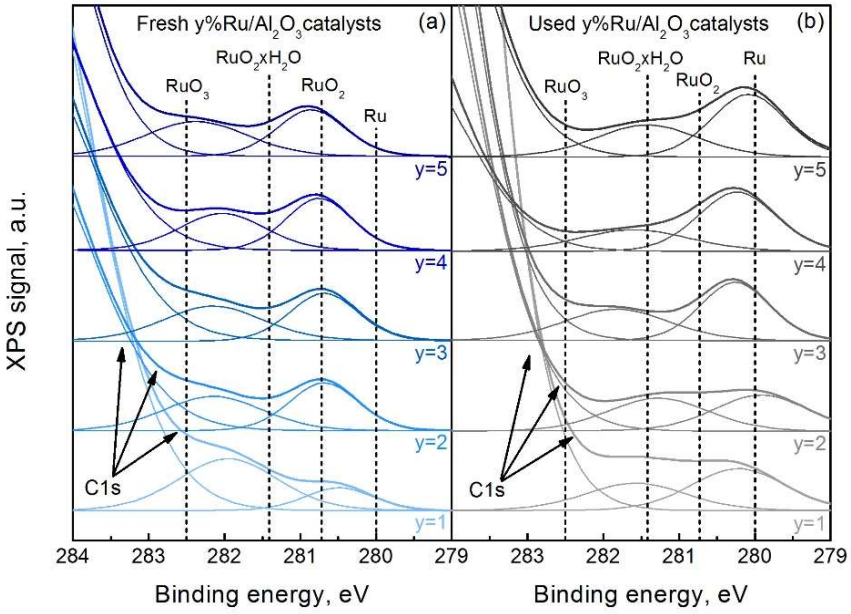

Figure 3.8. Ru $2d_{5/2}$ XPS spectra of (a) fresh and (b) used catalysts.

H_2-TPR experiments were carried out in order to analyze the reduction state of Ni and Ru species dispersed on alumina but also to determine the effect of metal loading over the reducibility of the prepared catalysts. Figures 3.9a and b show H_2-TPR profiles of fresh Ni/Al_2O_3 and Ru/Al_2O_3 catalysts, respectively. First of all, differences in redox properties are evident: the complete reduction of nickel-based catalyst is only achieved by increasing the temperature up to 900 °C, whereas only 250 °C is required for ruthenium loaded catalysts. These distinct redox properties could be translated in different catalytic performances, since it is well known that both active sites (Ni or Ru) must be reduced to carry out the hydrogenation of CO_2 efficiently.

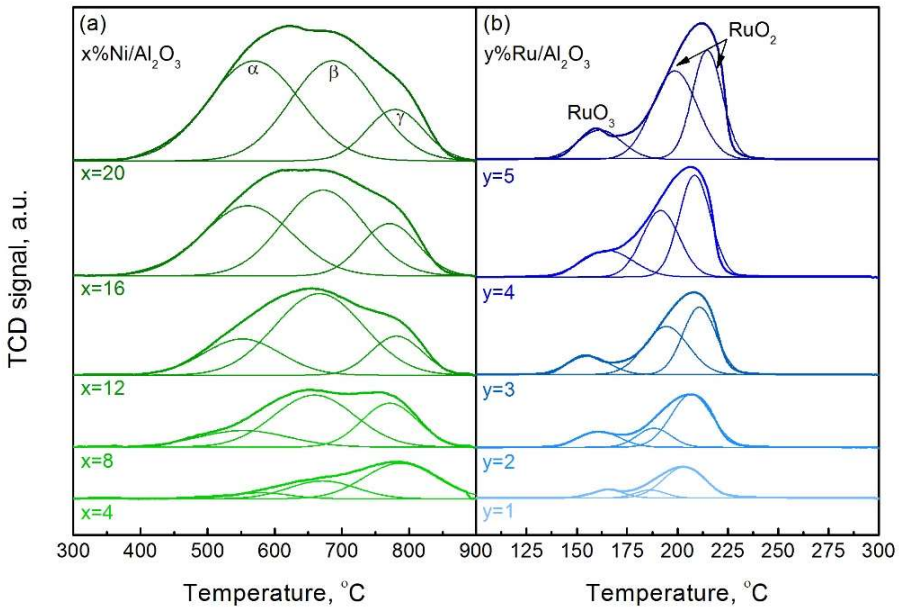

Figure 3.9. H_2-TPR profiles of (a) Ni/Al_2O_3 and (b) Ru/Al_2O_3 catalysts.

With the aim of characterizing the type of nickel and ruthenium species presented in alumina supported catalysts, H_2-TPR profiles were deconvoluted applying Gaussian-type deconvolution. H_2-TPR profiles displayed in Figure 3.9a present 3 deconvoluted H_2 consumption peaks assignable to three different Ni species, named α, β and γ [44, 99, 104]. The peak located at the lowest temperature, close to 550 °C, is attributed to reduction of α-type NiO weakly interacting with alumina. The second peak centered at

670 °C, however, is assigned to reduction of β-type NiO with stronger interaction with the support [86, 105]. Finally, the peak at the highest temperature, with maximum located close to 780 °C, is assigned to reduction of γ-type Ni species forming well dispersed $NiAl_2O_4$ structure, in line with the results observed by thermo-XRD study and XPS. Note that, in accordance with previous XPS results, H_2-TPR profiles shift to lower temperatures with increasing of Ni content, which is related to weakening of metal-support interaction already reported by other authors [90].

Relative amounts of Ni species together with reducibility percentages and H_2/Ni ratios are summarized in Table 3.3. Note that the relative amount of α-type NiO grows progressively with Ni loading, increasing from 8% (4%Ni/Al_2O_3) up to 44% (20%Ni/Al_2O_3), whereas the amount of γ-type NiO decreases from 62 to 14%. Additionally, in order to determine the amount of nickel reducible at 500 °C, additional H_2-TPR tests were run up to 500 °C, for 1 h and under 20% H_2/Ar (not shown).

Table 3.3. Data from H_2-TPR studies of the impregnated Ni and Ru catalysts.

Catalyst	**H_2 uptake (mmol g^{-1})**	**Ni Cont.[a] (wt.%)**	**Species (%)**			**H_2/Ni**	**Reducibility[b] (%)**
			α	**β**	**γ**		
4%Ni/Al_2O_3	0.65	3.8	8	30	62	1.01	10
8%Ni/Al_2O_3	1.26	7.4	18	52	30	0.97	22
12%Ni/Al_2O_3	1.86	10.9	23	60	17	0.97	38
16%Ni/Al_2O_3	2.52	14.8	38	44	18	0.99	47
20%Ni/Al_2O_3	3.16	18.5	45	41	14	1.01	56
Catalyst	**H_2 uptake (mmol g^{-1})**	**Ru Cont. (%)**	**RuO_3/RuO_2 ratio**			**H_2/Ru**	**Reducibility (%)**
1%Ru/Al_2O_3	0.23	1.1	0.17			2.32	100
2%Ru/Al_2O_3	0.45	2.1	0.23			2.27	100
3%Ru/Al_2O_3	0.66	3.1	0.18			2.22	100
4%Ru/Al_2O_3	0.93	4.3	0.24			2.35	100
5%Ru/Al_2O_3	1.08	5.1	0.18			2.18	100

[a]Determined from integration of H_2-TPR profiles.
[b]Reduction conditions: 500 °C for 1h under 20%H_2/Ar. For these calculations Ni(II) has been assumed.

As expected, the percentage of nickel reducible at 500 °C increased from 10 to 56% with Ni loading, confirming the mentioned weakening of metal-support interaction and indicating that in no case will all nickel be reduced during reaction. Finally, note that the H_2/Ni ratio is close to 1 in all cases, which indicates, as previously observed in XPS characterization, that Ni^{2+} is the only specie reducible, according to the following reduction step: $NiO + H_2 \rightarrow Ni + H_2O$.

Figure 3.9b shows deconvoluted H_2-TPR profiles of Ru/Al_2O_3 catalysts. All catalysts exhibit a main H_2 consumption peak with a maximum located at 210 °C, a shoulder at 190 °C and one additional smaller peak, whose reduction starts above 140 °C. The main peak is attributed to reduction of supported RuO_2 into metallic Ru [106-108], whereas the mentioned shoulder at lower temperature is due to reduction of well dispersed RuO_x species [109, 110]. Then, in line with XPS results, the peak at lowest temperature could be related to reduction of RuO_3.

From integration of H_2-TPR signal, total H_2 consumptions, RuO_3/RuO_2 ratios and H_2/Ru ratios were calculated, which are included in Table 3.3. RuO_3/RuO_2 ratios are between 0.17 and 0.24, i.e., all catalysts present similar and considerably higher relative amounts of RuO_2 than of RuO_3. Finally, it should be noted that H_2/Ru molar ratios are between 2.2 and 2.3 (values slightly higher than the required for RuO_2 reduction), which confirms the presence of RuO_2 and trace amounts of RuO_3, according to the following reduction step: $RuO_x + xH_2 \rightarrow Ru + xH_2O$ $(x=2,3)$.

3.2. CATALYTIC PERFORMANCE

According to the Le Chatelier principle, high pressures and low temperatures are beneficial for the equilibrium conversion of CO_2, since CO_2 methanation is an exothermal reaction with decreasing number of moles (5 moles of reagent → 3 moles of product). Not only that, but also H_2/CO_2 ratios higher than the stoichiometric along with a high reactant concentration slow down the equilibrium conversion decrease with temperature (see section 1.4.1). It has been deduced (from thermodynamic calculations) that at atmospheric pressure and temperatures below 400 °C, a CO_2 conversion above 95% can be achieved by feeding a H_2-CO_2 gas mixture in 5:1 ratio.

Hence, in this section, the catalytic performance of the alumina supported Ni and Ru catalysts is measured at atmospheric pressure, using a H_2/CO_2/He feed ratio of 5:1:1.25 and varying the reaction temperature from 200 to 400 °C (the temperature was raised up to 500 °C in the case of Ni/Al_2O_3 catalysts). Moreover, the catalytic properties determined by characterization techniques are related with the activity results and the election of optimal formulations is carried out accordingly. Finally, the best formulations are compared with others reported in literature and their stability is evaluated over 24h-on-stream.

3.2.1. Effect of metal loading

The catalytic performance of the catalysts was evaluated by analyzing CO_2 conversions along with CH_4 yields (Equations 2.12 and 2.15) and in terms of specific activity or *Turn Over Frequency (TOF),* defined as the intrinsic reaction rate per reduced surface metal atoms (Equation 2.17). The CO_2 conversion at different temperatures as a function of the Ni loading is shown in Figure 3.10a. In general, CO_2 conversion exponentially rises with temperature up to 400 °C and then its increase slows down due to the exothermic character of the reaction. The onset temperature for CO_2 methanation is around 250 °C and the highest CO_2 conversions are achieved close to 450 °C for catalysts with Ni contents higher than 8% (X_{CO_2} ≈ 85%). Noteworthy, the Ni loading increase also results in an activity enhancement. In fact, the temperature at which 50% CO_2 conversion is obtained (T_{50} parameter) is reduced by 127 °C when increasing the Ni loading from 4 to 20% (T_{50} = 443 °C and T_{50} = 316 °C, respectively). In this line, catalysts with Ni nominal loadings above 12% provide similar CO_2 conversion values (X_{CO_2} ≈ 80%) when reaction temperature exceeds 400 °C.

Specific activity (*TOF*) values of supported catalysts, which were estimated from CO_2 conversion at differential reactor and chemisorption results (Table 3.2), are shown in Figure 3.10b as a function of metal particle size or metal content (the higher the loading, the higher the particle size). It can be observed that *TOF* increases 50% as Ni particle size grows from around 2.5 (4% Ni) to 6 nm (12% Ni) and then, remains constant at 0.035 s^{-1}. This might suggest that CO_2 methanation on Ni/Al_2O_3 catalysts

with mean Ni particles sizes lower than 6 nm is structure sensitivity, i.e., their specific activity depends on particle size and morphology. However, significant change in *TOF*s are not observed by increasing the metal content from 12 to 20%, indicating that the reaction could be structure insensitive for catalysts with high metal content [111]. In such case, the activity of the catalyst would only depend on the metal surface area (the higher the surface, the higher the CO_2 conversion). Although 20%Ni/Al_2O_3 catalyst presents the highest metal surface (S_{Ni} = 7.5 m^2 g^{-1}), the 12%Ni/Al_2O_3 catalyst contents particles with similar *TOF* value, which provide metal surface high enough (S_{Ni} = 5.1 m^2 g^{-1}) to achieve high CO_2 conversions at intermediate-high temperatures. Therefore, it can be concluded that adding 12% Ni metal loading is sufficient to carry out CO_2 methanation at the reported reaction conditions (W/F_{A0} = 4.7 g h mol^{-1}).

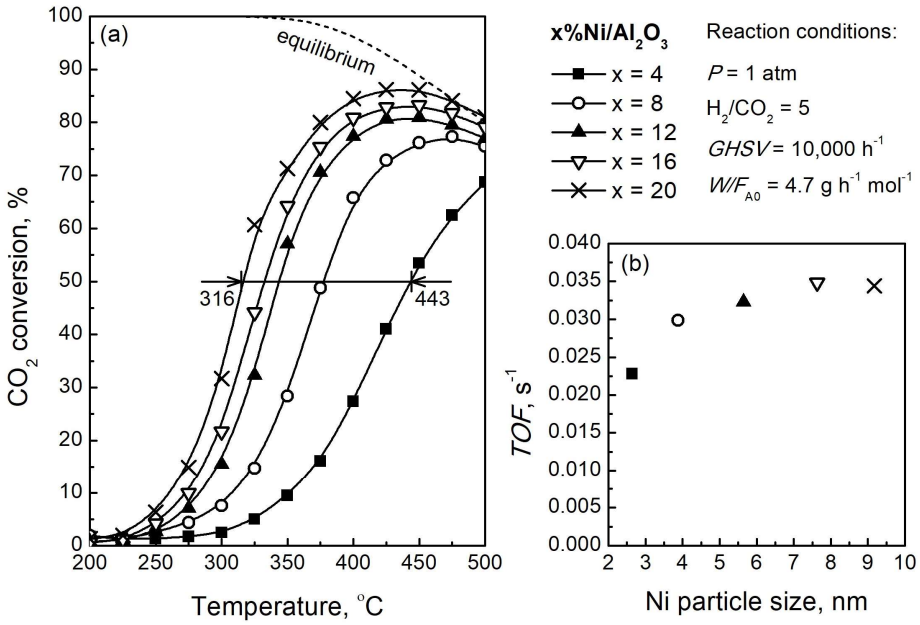

Figure 3.10. (a) Evolution of CO_2 conversion with temperature and (b) Turn Over Frequency (*TOF*) values as a function of particle size at 275 °C for Ni/Al_2O_3 catalysts.

Analogously, Figures 3.11a and b show the influence of temperature and particle size on catalytic performance of Ru/Al_2O_3 catalysts. In this case, higher CO_2 conversions are observed at low temperatures (T < 300 °C) in comparison with Ni based catalysts

(Figure 3.10a). Maximum CO_2 conversion is reached, regardless the Ru content, at 400 °C, being also around 85% for catalysts with high metal content. Taking into account that the variation of Ru loading is much lower, similar T_{50} reduction, as compared to Ni catalysts, is obtained: from 396 °C (1% Ru) to 310 °C (5% Ru). Note that, in line with Ni based catalysts, a higher metal loading provides greater activity and that the same saturation effect is observed, obtaining almost similar CO_2 conversions for catalysts with nominal Ru contents above 3%. Accordingly, 4% of Ru (S_{Ru} = 0.61 m^2 g^{-1}) is the minimum nominal content needed to achieve at least 80% CO_2 conversion above 350 °C and the impregnation of higher Ru loading can be considered unnecessary, since no further enhancement in activity is observed.

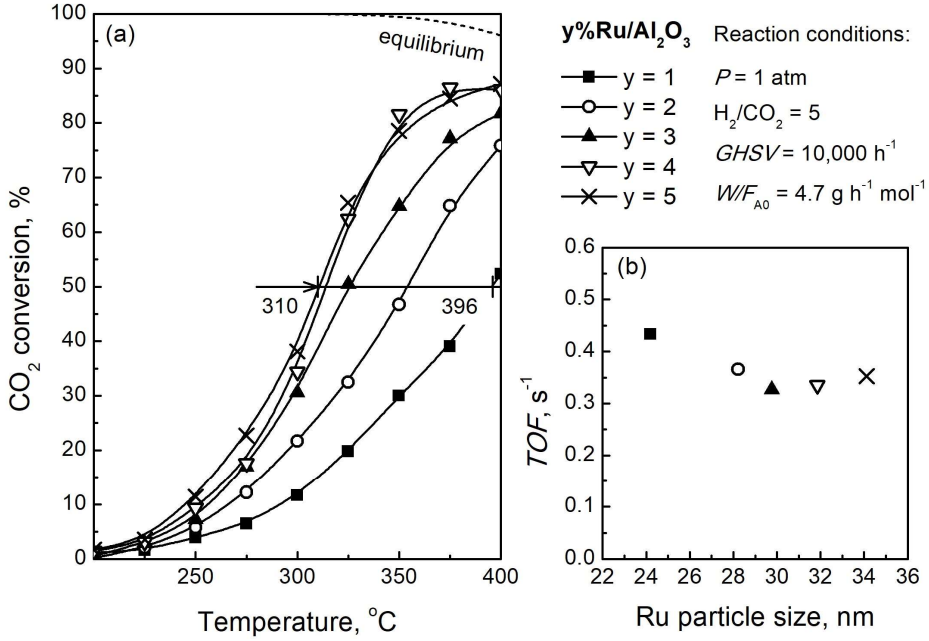

Figure 3.11. (a) Evolution of CO_2 conversion with temperature and (b) Turn Over Frequency (*TOF*) values as a function of particle size (T = 275 °C) for Ru/Al_2O_3 catalysts.

On the other hand, *TOF* values at 275 °C of Ru/Al_2O_3 catalysts were one order of magnitude higher than those of Ni/Al_2O_3 catalysts, confirming that ruthenium is a much more effective metal for CO_2 methanation than nickel. Interestingly, the evolution of specific activity with particle size seems to be the opposite for Ru/Al_2O_3 catalysts: *TOF*

drops from 0.43 to 0.33 s^{-1} by increasing Ru mean particle size from 24 (1% Ru) to 30 nm (3% Ru). Even so, all catalysts present similar specific activity, except for 1%Ru/Al_2O_3 catalyst, which is the one containing slightly smaller particles of 24 nm (D_{Ru} ≈ 5.5%, Table 3.2) with a *TOF* value around 25% superior. Then, everything suggests that increasing dispersion could enhance the specific activity of surface Ru atoms and the use of the noble metal by reducing in turn the cost of the catalyst. Unfortunately, unlike 4%Ru/Al_2O_3, 1%Ru/Al_2O_3 catalysts has not the required loading to achieve equilibrium conversion at medium-high temperature.

3.2.2. Activity and stability of optimal composition Ni and Ru catalysts

In this section the activity of the optimal formulations is further compared and their stability is evaluated over 24h-on-stream. In Figure 3.12, CH_4 yields of 12%Ni/Al_2O_3 and 4%Ru/Al_2O_3 catalysts are evaluated at 300, 350 and 400 °C.

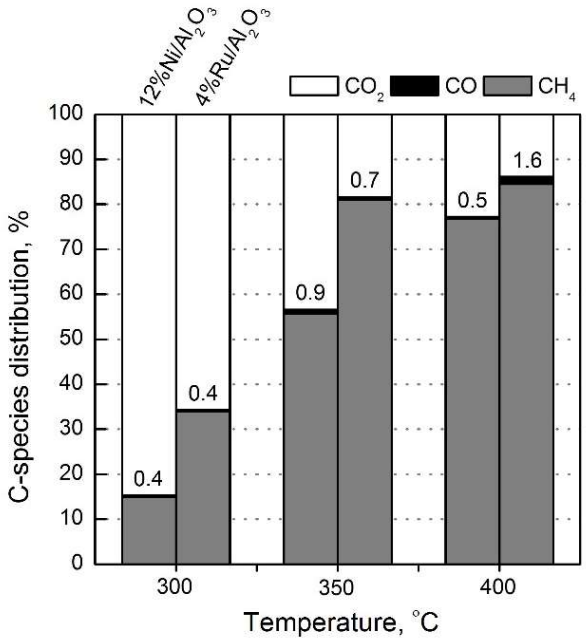

Figure 3.12. Comparison of C-species distribution between 12%Ni/Al_2O_3 and 4%Ru/Al_2O_3 catalysts at 300, 350 and 400 °C.

It can be noticed that increasing temperature leads to higher Y_{CH_4} (highest CH_4 productions are observed at 400 °C) and that 4%Ru/Al_2O_3 is notably more productive than 12%Ni/Al_2O_3 catalyst, in line with the upgrade in CO_2 conversions observed in Figures 3.10 and 3.11. In fact, regardless the studied temperature, Ru containing catalyst produces more methane than Ni based catalyst (35% vs. 15% at 300 °C, 80% vs. 55% at 350 °C and 85% vs. 77% at 400 °C). Noteworthy, CO yields lower than 1% were observed for 12%Ni/Al_2O_3 catalyst and negligible trace amounts of CO were produced by 4%Ru/Al_2O_3 catalyst.

The activity of alumina supported 12% Ni and 4% Ru catalysts was compared with other state-of-art materials recently reported in literature, including commercial samples [56, 57, 85, 90, 112, 113]. Table 3.4 includes the catalysts composition together with the main operational parameters, i.e. H_2/CO_2 molar ratio and W/F_{A0}. As can be observed, the main operational parameters differ from each other, and thus, the comparison is not straightforward.

Table 3.4. Catalytic performance comparison among Ni- and Ru-based catalysts reported in literature.

Composition	**Description**	**H_2/CO_2**	**W/F_{A0} (g h mol^{-1})**	**T_{50} (°C)**	**Reference**
12NiAl	Dry impregnation	5	5	340	This work
25NiO/Ca-Al	Commercial (METH134)	4	6	325	[112]
25Ni-Al	Co-precipitation	3.5	11	300	[90]
17NiO/14La/Al	Dry impregnation	5	8	280	[57]
4RuAl	Dry impregnation	5	5	310	This work
0.5Ru/Al	Commercial	4	25	300	[113]
3Ru/Al	Commercial	5	7	365	[85]
2Ru/30Ce/Al	Wet impregnation	4	11	285	[56]

Although 12NiAl catalyst developed in this work presents a somewhat higher T_{50}, nickel loading is significantly lower with respect to other reported samples. Furthermore, the W/F_{A0} used in this study is the lowest, i.e., a lower amount of catalyst is used to treat the inlet feed stream. On the other hand, the 4RuAl sample developed

in this work presents a similar T_{50} to that reported for other samples. Again, the T_{50} was evaluated in more demanding experimental conditions, with the lowest W/F_{A0}. All considered, it can be concluded that the catalytic performance of Ni and Ru based catalysts prepared in this work is comparable to other state-of-art materials, including commercial samples.

In a final step, the stability of catalysts with the optimum metal contents was studied for 24h-on-stream at 350 °C.

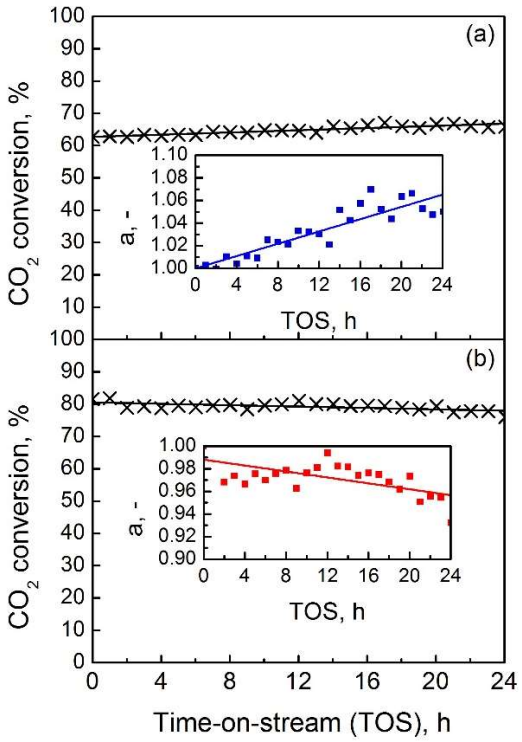

Figure 3.13. Evolution of CO_2 conversion and activity parameter (a) with time-on-stream over 24h for (a) 12%Ni/Al_2O_3 and (b) 4%Ru/Al_2O_3 catalysts.

Interestingly, a slight gain in the CO_2 conversion was observed for 12%Ni/Al_2O_3 catalyst leading to an activity (a) increase of 6% probably due to the activation of new active sites (inset graph, Figure 3.13a). The activity (a) of 4%Ru/Al_2O_3 catalyst, in contrast, decreased around 4% after 24h-on-stream (X_{CO_2} drops from 81.5 to 78.0%),

as shown in Figure 3.13b. This slight decline could be related to both particles sintering or carbon deposition [114].

In order to determine the causes of the slight activation or deactivation, additionally, 12% Ni and 4% Ru aged catalysts were characterized by TG and TEM after 24h-on-stream. Figure 3.14 shows TG and dTG profiles of the aged catalysts recorded from 150 to 850 °C and under 5%O_2/He flow (oxidative atmosphere).

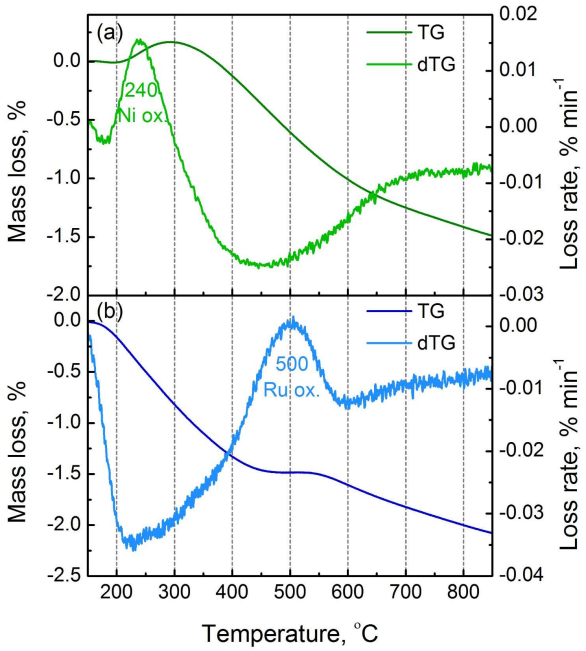

Figure 3.14. TG analysis with 5%O_2/He for aged (a) 12%Ni/Al_2O_3 and (b) 4%Ru/Al_2O_3 catalysts.

Note that, prior to the tests, catalysts were dried at 150 °C for 30 min observing a mass loss of around 1.5% due to water removal in both cases. Overall, no relevant mass losses were observed when increasing the temperature up to 850 °C, which indicates that no carbon deposits were formed during stability tests at 350 °C and under a gas stream with high H_2 concentration. Figure 3.14a displays a mass increase at around 250 °C, which can be attributed to Ni oxidation, and a progressive mass loss up to 850 °C. This loss might be related to structural water removal of alumina. Figure 3.14b,

however, shows the same progressive mass decrease but with a plateau around 500 °C that is related to Ru oxidation or RuO_x species formation. Thus, the formation of coke during stability tests can be discarded in both catalysts.

In a next step, possible metal particles sintering during stability tests was investigated by means of TEM. Spherical Ni particles were observed for reduced 12%Ni/Al_2O_3 catalysts with sizes ranging from 3 to 9 nm, as illustrated by Figure 3.15a.

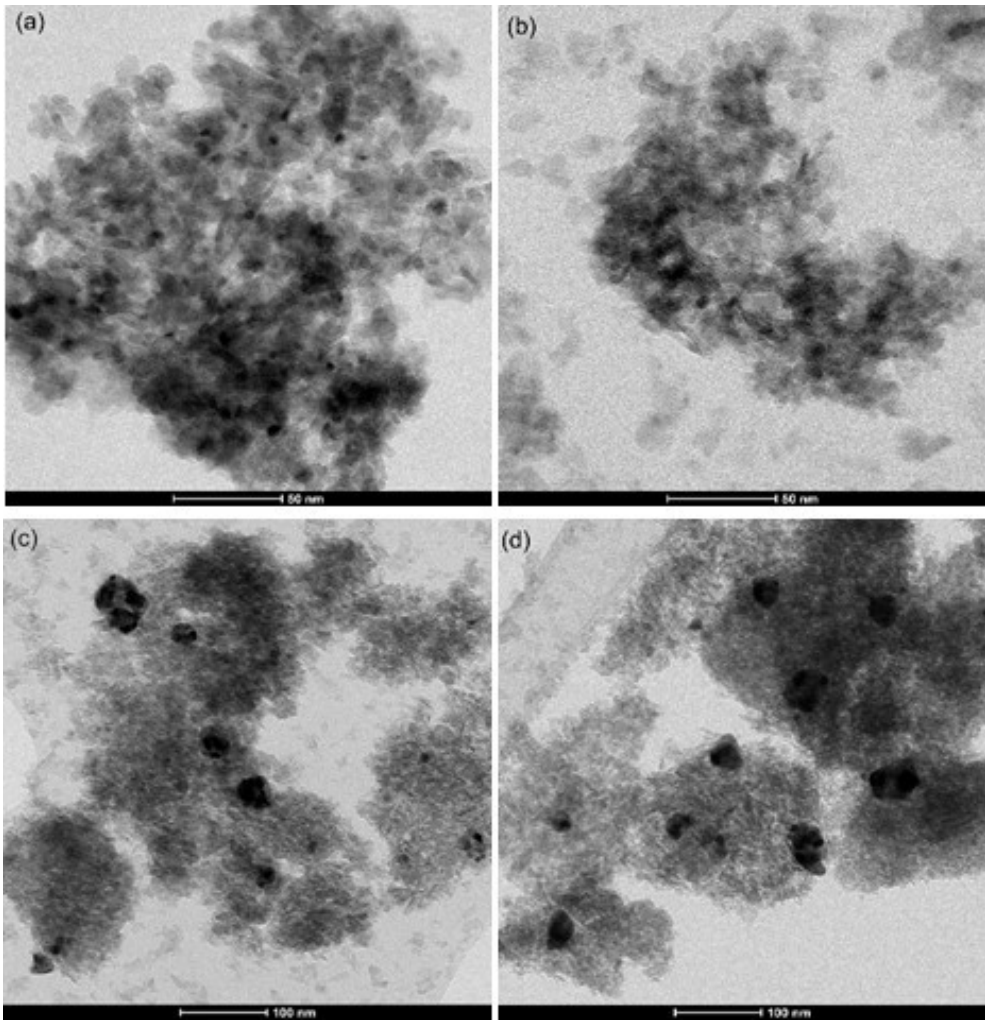

Figure 3.15. TEM micrographs for fresh and aged samples (after 24h-on-stream): (a) fresh and (b) aged 12%Ni/Al_2O_3 catalyst; (c) fresh and (d) aged 4%Ru/Al_2O_3 catalyst.

After stability tests at 350 °C, a particle size distribution somewhat wider (from 3 to 11 nm) and similar morphology of Ni particles was observed (Figure 3.15b). The average particle size, estimated from measuring 50 particles, was 6 nm for reduced and 7 nm for used Ni catalyst, which indicates that no relevant sintering occurred during the stability test. In the case of reduced Ru catalyst, however, a wider particle size distribution was observed. This catalyst presents particles with sizes from 10 to 40 nm, some of them dispersed in form of agglomerates (Figure 3.15c). The smaller particles are oval shaped, whereas the biggest presents hexagonal geometry. After 24h on stream, no relevant changes were observed in particle morphology and in the size distribution (from 11 to 45 nm). The average particle size was 24 nm for reduced and 28 nm for used Ru catalyst, indicating that particles sinter somewhat during the stability test.

According to TGA and TEM results, it can be concluded that activation of additional nickel species as well as slight sintering of Ru particles are the reasons why a slight increase or decrease of CO_2 conversion are observed for Ni/Al_2O_3 and Ru/Al_2O_3 catalysts, respectively. In the case of Ni based catalysts, note that the negative effect of slight particle sintering seems to be hidden by further reduction of nickel oxide with high metal-support interaction during stability test. Finally, it is worth to mention that in both cases the selectivity to methane kept stable, obtaining values higher than 98% (not shown).

3.3. OVERALL VIEW AND CONCLUSIONS

For the research work included in this chapter, a series of alumina-supported Ni and Ru catalysts were prepared by incipient wetness impregnation varying the metal content, characterized by multiple techniques and evaluated for CO_2 methanation. The main conclusions are listed as follows:

- According to basicity results (CO_2-TPD), the impregnation of increasing loadings of Ni results in the formation of new basic sites suggesting that not only Al_2O_3 support but also oxidized Ni species (NiO and $NiAl_2O_4$) are able to

adsorb CO_2 in form of carbonates, which is an essential step in CO_2 methanation mechanism.

- XRD results revealed that alumina-supported Ru crystals tend to grow and agglomerate into large particles with calcination temperature, resulting in low metal dispersion. On the contrary, the increase of temperature does not affect Ni dispersion, but leads to the formation of nickel phases with high interaction with alumina, especially for catalysts with low Ni content.
- According to H_2-chemisorption results, Ni dispersion decreases around 25% by increasing Ni content from 4 to 20% due to the formation of large NiO particles. However, unlike for Ni/Al_2O_3 catalysts, the dispersion of Ru/Al_2O_3 catalysts is not significantly influenced by metal loading.
- The reducibility of the active phase, linked to metal-support interaction, seemed to be a key factor. The reduction of alumina-supported Ru is complete at low temperature (T < 300 °C), while alumina supported Ni is not completely reduced at 500 °C. This indicates that all Ru but not all Ni will be available to dissociate hydrogen during reaction. The reducibility is even lesser for catalysts with low Ni content due to a higher metal-support interaction, in accordance with XPS and H_2-TPR results.
- Considering the saturation effect of CO_2 conversion with metal loading and specific activity, $12\%Ni/Al_2O_3$ (T_{50} = 340 °C) and $4\%Ru/Al_2O_3$ (T_{50} = 310 °C) were the best formulations, providing maximum CO_2 conversions of 80 and 85% around 425 and 375 °C, respectively and being quite stable for 24h-on-stream. The *TOF* values for $4\%Ru/Al_2O_3$ were considerably higher than those observed for $12\%Ni/Al_2O_3$ catalyst at low temperature (T < 300 °C), since ruthenium is more effective in H_2 dissociation/adsorption than nickel, which is another fundamental step of reaction mechanism.

Chapter 4

ENHANCING CO_2 METHANATION ACTIVITY OF Ni/γ-Al_2O_3 CATALYST BY GLYCEROL ASSISTED IMPREGNATION AND Ru PROMOTION

ABSTRACT

Conventional Ni/Al_2O_3 catalyst, currently used for CO_x removal in ammonia production, admits room for improvement as catalysts for application in low temperature CO_2 methanation, which is the aim of this work. The Incipient Wetness Impregnation (IWI) has been replaced by Glycerol Assisted Impregnation (GAI) method and, afterwards, a secondary metal (Ru) has been co-impregnated forming a bimetallic system. The monometallic as well as bimetallic catalysts have been characterized by several techniques (TGA, XRD, N_2-physisorption, TEM, H_2-TPR, H_2-TPD, STEM-EDX and operando FTIR) and tested for CO_2 methanation reaction in a downflow fixed bed reactor (conditions: P = 1 bar, H_2: CO_2 ratio = 4 and WHSV = 30,000 mL h^{-1} g^{-1}). GAI method together with a reducing calcination atmosphere (20%H_2/N_2) results effective to avoid the formation of large metal particles during the synthesis, especially for Ru/Al_2O_3 formulation. In fact, the Ru dispersion of the catalyst prepared by GAI ($RuAl_{GAI}$) is around 5 times higher than that of $RuAl_{IWI}$ catalyst. On the other hand, $NiAl_{GAI}$ presents larger population of reduced particles but bigger in size than $NiAl_{IWI}$ catalyst, which finally provides the former with slightly higher metal surface and superior catalytic performance. By co-impregnating small amounts of Ru (0.5, 1.0 or 1.5 wt%) the Ni surface is considerably increased which, together with Ru synergistic collaboration, results in a methane yield rise from 20 to 44% at 300 °C. The operando FTIR results show no differences in the reaction pathway with GAI preparation method and incorporation of Ru, but different evolution of reaction intermediates concentration with temperature. The bimetallic Ni-RuAl system presents much higher capacity to adsorb CO and hydrogenate the reaction intermediates (adsorbed formates and carbonyls) by dissociated H_2 than its monometallic counterparts.

4. ENHANCING CO_2 METHANATION ACTIVITY OF Ni/γ-Al_2O_3 CATALYST BY GLYCEROL ASSISTED IMPREGNATION AND Ru PROMOTION

Since the early 1960s, Sabatier´s reaction has been industrially applied to remove residual carbon oxides (CO_x) from hydrogen-nitrogen gas mixtures in ammonia production plants [85]. According to this reaction, both CO, which results to be a poison for ammonia synthesis formulations (Fe-based catalysts), and CO_2 are catalytically reduced into inert methane allowing the fine purification of hydrogen-containing gases for NH_3 (Haber & Bosch process). Although more H_2 is consumed, in many cases, CO methanation is preferred rather than its oxidation for simplicity and safety issues (O_2 feed is avoided) [115]. Normally, the exothermic reaction is carried out in an adiabatic fixed bed reactor or methanator, which utilize the high heat release effectively. In fact, the industrial methanator is usually equipped with inter-bed recycling cooling, which allows a proper heat management and avoids the formation of hot spots and damage of the catalytic bed [37]. As an example, the still commercially available Topsoe's Recycle Energy-efficient Methanation Process (TREMP) is illustrated in Figure 4.1.

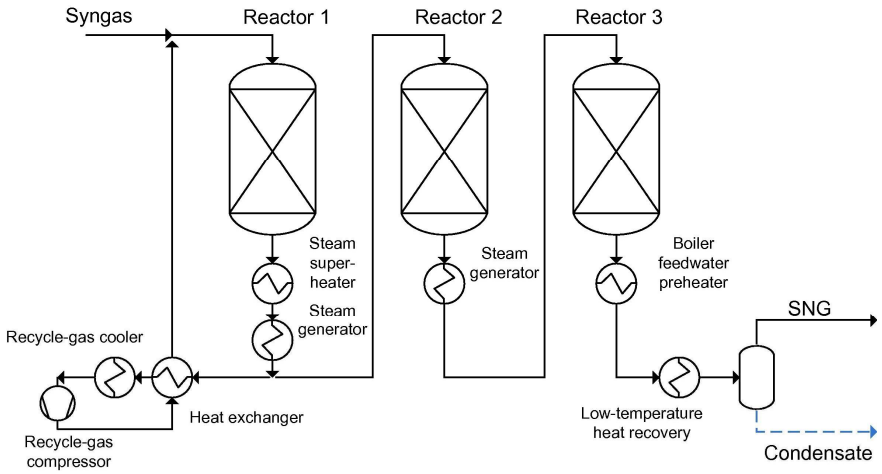

Figure 4.1. TREMP system equipped with 3 fixed-bed methanators, intermediate cooling and gas recycle designed by Haldor Topsoe [37].

The industrial catalysts employed for this application are mostly comprised of Ni supported or dispersed on various metal oxides, among which Al_2O_3, SiO_2, aluminum silicates, Cr_2O_3-Al_2O_3, MgO, CaO and calcium aluminates are the most popular. However, according to Golosman and Efremov [116], the most used and outstanding formulation until now is Ni/Al_2O_3 catalyst prepared by impregnation and co-precipitation. This formulation presents: (i) acceptable resistance to residual poisons, such as carbon monoxide; (ii) high thermal stability without activity loss upon overheating (T > 600 °C); (iii) high mechanical strength so as to avoid dust formation; and (iv) low hydraulic friction under reaction stream. Although the formulation synthesized by co-precipitation is more active than the prepared by impregnation, the preparation procedure of the former is more difficult than that of the latter and, besides, is characterized by large amount of wastewater. Then, impregnation method is more commonly used in industry for large-scale methanation catalyst manufacturing. These catalysts, in counterpart, usually content NiO metal loadings above 20% to reach the same activity level [111, 117].

Nowadays, the catalytic production of Synthetic Natural Gas (SNG) from waste CO_2 and renewable H_2, as a way of storing surplus renewable power (Power-to-Gas process) and reducing CO_2 emission costs, is gaining interest in industry. In fact, various pilot projects have been initiated or are about to be launched around the world, specifically in Europe [118, 119]. Among EU countries, Germany contains the highest installed power share with around 40 MW and a 100 MW power-to-gas pilot plant is being built for industrial use, which will be connected to the grid from 2022 [120]. Accordingly, the main catalyst manufacturers are already developing new catalytic formulations for SNG production. Note that these formulations are not very different from the conventional ones, applied for H_2-rich streams purification, since it has been proven that, generally, catalysts which are effective for CO methanation are so for CO_2 methanation [112, 121]. As an example, the manufacturers Johnson Matthey, Haldor Topsoe and Clariant offer CRG, MCR and METH catalyst ranges, respectively. All these industrial formulations provide good thermal stability and resistance to residual gas poisons to achieve a long life. However, these catalysts are not very active yet at low reaction temperatures and do not tolerate sulfur very well.

Hence, the main objective of this chapter has been to sequentially improve the low temperature activity of the classic Ni/Al_2O_3 formulation, which Ni content was optimized in Chapter 3 (12 wt%), by changing the preparation method and incorporating a secondary metal, such as Ru. Additionally, the present work has aimed to identify which factors are responsible for such improvement. In order to achieve these goals, firstly, the influence of Glycerol Assisted Impregnation (GAI) method on the dispersion and structural characteristics of Al_2O_3-supported Ni and Ru particles was examined. These materials were catalytically compared with equivalent ones prepared by the conventional Incipient Wetness Impregnation (IWI) method in chapter 3. After that, the effect of Ru incorporation on the physicochemical properties and catalytic performance of Ni/Al_2O_3 formulation was studied. Finally, an *operando* FTIR study was carried out. To our knowledge, we pioneer mechanistic analysis of CO_2 methanation reaction on Ni-Ru bimetallic system, identifying the type and evolution of reaction intermediates and determining the roles of both Ni and Ru in the reaction pathway.

4.1. INFLUENCE OF THE PREPARATION METHOD: INCIPIENT WETNESS IMPREGNATION (IWI) VS. GLYCEROL ASSISTED IMPREGNATION (GAI)

It is widely known that the complete hydrogenation of CO_2 into methane is a process with considerable kinetic limitations that can only be achieved by a suitable catalyst. In general, a suitable catalytic formulation consists of a supported catalyst with the active sites (typically Ni or Ru) as dispersed as possible over a basic mesoporous support. Therefore, in recent years, Ni and Ru catalysts with increasingly smaller and, *a priori*, more active metallic particles have been designed mostly thanks to advances in nanomaterials synthesis techniques, which allow increasing the surface/volume ratio and the number of active sites [63, 122]. The reduction of particle size not only leads to higher metallic surface areas but also to changes in particle's morphology, which according to its structure sensitivity could lead to higher, equal or lower Turn Over Frequency (*TOF*) numbers. It has been reported that low coordinated Ni nanoparticles contain more surface defects that act as surface hydrogen traps facilitating its dissociation and improving the specific activity [123]. On the contrary, other authors have reported that, in the case of Ru catalysts, low coordinated or

monolayer sites induce lower CO_2 methanation rates than larger nanoclusters, since they suffer from poisoning by the adsorption of stable carbonyls during reaction [48, 124, 125]. In order to obtain small particles or tuning their structure, several preparation methods have been employed alternative to classical impregnation such as one-pot Evaporation-Induced Self-Assembly (EISA) [126], Microwave-Assisted (MA) [44], Deposition-Precipitation (DP) [111], Co-Precipitation (CP) [104] and polyol method [127] or equivalent Glycerol Assisted Impregnation (GAI) [62].

Usually, the preparation method and calcination procedure have significant influence on the catalytic properties, such as specific surface area and metal dispersion. In this section, the physicochemical properties as well as activity of Ni/Al_2O_3 and Ru/Al_2O_3 catalysts synthesized by novel Glycerol Assisted Impregnation (GAI) are compared with that of their counterparts prepared by conventional Incipient Wetness Impregnation (IWI) method. At first, decomposition of catalyst precursors is studied by TGA; then, catalysts are characterized by N_2 physisorption, XRD and TEM; and finally, the catalytic performance is evaluated.

4.1.1. Determination of calcination temperature by TGA

With the aim of determining how GAI-catalysts precursors are decomposed and the temperature required for their complete calcination, Thermogravimetric Analysis (TGA) was carried out. For comparison purposes, TGA of IWI-catalysts precursors was also conducted (Figures 4.2 and 4.3). Besides, the gaseous products from precursors calcination were monitored by a mass spectrometer connected in series to the thermobalance. Figures 4.2a and c show both TG and dTG profiles of supported Ni catalysts precursors calcined under oxidative (5% O_2/He, IWI catalyst) and reductive (5% H_2/Ar, GAI catalyst) atmospheres, respectively.

In general, the mass loss takes place in different consecutive steps that can be identified by the dTG profiles. In the case of $NiAl_{IWI}$ precursor calcined under O_2/He (Figure 4.2a), the dTG profile presents a main mass loss rate peak at 265 °C and two shoulders at 200 and 350 °C. The first shoulder can be attributed to structural water desorption from Al_2O_3 or water released during dehydration steps of nickel precursor

($Ni(NO_3)_2{\cdot}6H_2O$), whereas the broad peak and the second shoulder are due to nitrate decomposition/oxidation into NO_x (NO and NO_2), as confirmed by MS signals (Figure 4.2b). Mass loss is observed up to 475 °C, confirming that the previously elected calcination temperature (500 °C) is adequate for complete precursor decomposition.

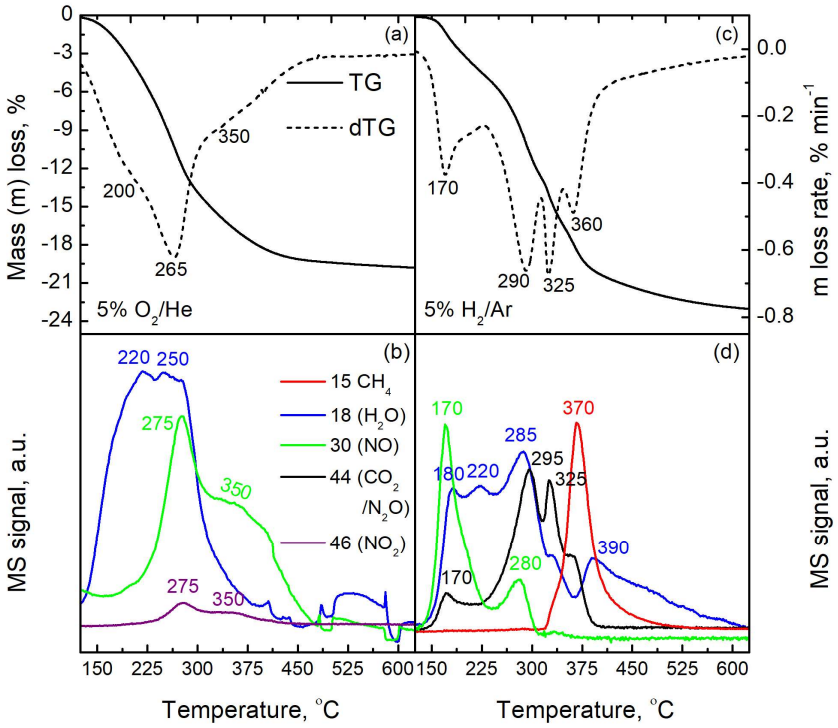

Figure 4.2. TGA (TG and dTG) profiles followed by MS spectra of (a, b) $NiAl_{IWI}$ and (c, d) $NiAl_{GAI}$ catalysts precursors.

The TG profile of the $NiAl_{GAI}$ precursor (Figure 4.2c) is somewhat different due to the presence of an organic compound which, according to literature [62, 63, 122], it could be a metal alkoxide formed from coordination of nickel cations (Ni^{2+}) with glycerol solution. In this case, the dTG profile shows 4 well differentiated negative peaks among 125 and 400 °C. In agreement with MS spectra (Figure 4.2d), the first one at 170 °C could be attributed to NO_3^- reduction into NO and the next two, centered at 290 and 325 °C, to the reduction of the organic template. It can be suggested that the glycerolate is decomposed into smaller molecules (such as ethylene glycol and ethanol)

and surface carbon by hydrogenolysis reactions. In fact, the last mass loss rate peak centered at 360 °C matches with the appearance of methane (*m/z* = 15) in the product stream, suggesting that the remaining surface carbon is being reduced. In this case and according to the TG profile, a calcination temperature of 550 °C is enough for complete $NiAl_{GAl}$ precursor reduction.

Regarding Ru/Al_2O_3 precursors, the TGA profiles of their respective calcinations are shown in Figures 4.3a and c.

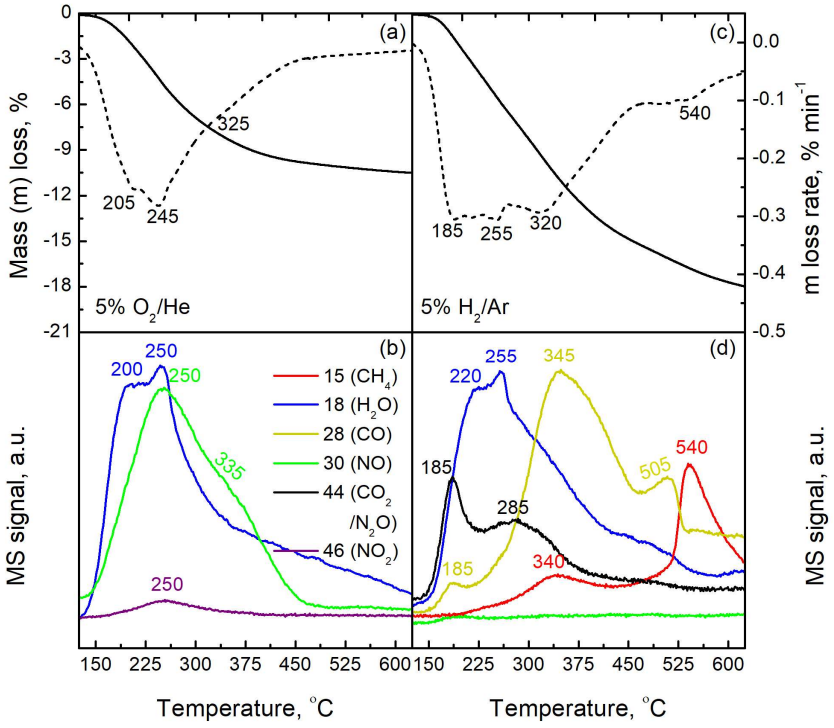

Figure 4.3. TGA (TG and dTG) profiles along with MS spectra of (a, b) $RuAl_{IWI}$ and (c, d) $RuAl_{GAl}$ catalysts precursors.

By comparing those figures with the described above, it can be observed that the mass loss profile of $RuAl_{IWI}$ precursor is similar to that of $NiAl_{IWI}$. In fact, the same calcination steps are identified and confirmed by MS spectra (Figure 4.3b): a first peak at 200 °C due to water release followed by a more intense negative peak together with

a shoulder at 335 °C, which are attributed to nitrate and nitrosyl groups oxidation into NO_x. Although the precursor is completely removed at 450 °C, a calcination temperature somewhat lower (400 °C) was employed in order to avoid an excess growing of RuO_2 crystallites previously observed by Thermo-DRX [128].

Finally, TGA profiles of $RuAl_{GAI}$ precursor calcined under 5%H_2/Ar are shown in Figure 4.3c. Note that the dTG profile presents a broad band which could be divided in 3 negative peaks at 190, 255 and 320 °C, which correspond to several calcination steps. Additionally, a small broad peak can be appreciated at around 540 ˚C. According to MS spectra (see Figure 4.3d), nitrate groups and organic compounds are partially reduced and water is released as product in a first step (negative peak at 190 °C). In a second step (from 250 to 350 ˚C), the organic compound continues being reduced and carbon monoxide (*m/z* = 28) is observed in the products stream. The last peak matches with methane appearance from hydrogenation of remaining surface carbon. In this case, a temperature of 550 ˚C was used for precursor calcination.

It must be highlighted that in all cases the observed total mass loss is similar to that expected for complete calcination of catalyst precursors: 19.9 vs. 17.2% for $NiAl_{IWI}$, 23.5 vs. 27.1% for $NiAl_{GAI}$, 10.9 vs. 9.9% for $RuAl_{IWI}$ and 18.9 vs. 19.6% for $RuAl_{GAI}$.

4.1.2. Physicochemical properties

Once catalysts precursors were calcined according to TGA results, the resulting catalysts were characterized by several techniques. Some physicochemical properties are shown in Table 4.1. It should be noted that the metal content of all catalysts is close to the nominal, indicating that Ni and Ru were successfully incorporated by the two methods (IWI and GAI). In addition, the high specific surface area and pore volume of all catalysts indicate that the textural properties of starting γ-Al_2O_3 (S_{BET} = 214 $m^2\ g^{-1}$ and V_{pore} = 0.563 $cm^3\ g^{-1}$) were not considerably affected by the different impregnation and calcination processes. As expected, supported Ni catalysts presented lower S_{BET} and V_{pore} than RuAl ones, mainly due to their higher metal content. On the other hand, the catalysts prepared by GAI method exhibited slightly lower values of such textural

properties than those prepared by IWI, probably due to the higher calcination temperature.

In regard to XRD analysis of reduced catalysts (not shown), both elemental Ni (XRD peaks at 2θ = 44.5, 51.8 and 76.4 ˚) and Ru (XRD peaks at 2θ = 38.4, 42.2 and 44 ˚) were clearly identified on $NiAl_{GAI}$ and $RuAl_{IWI}$ samples, respectively. However, broad and low-intensity peaks of Ni^0 and no peaks of Ru^0 were detected in $NiAl_{IWI}$ and $RuAl_{GAI}$ XRD patterns, suggesting that the crystalline phases are better dispersed than on $NiAl_{GAI}$ and $RuAl_{IWI}$ catalysts. This fact was confirmed by crystallite size calculation according to Scherrer equation (***τ***, Table 4.1).

Table 4.1. Physicochemical and catalytic properties of monometallic catalysts (*Me* = Ni or Ru).

Catalyst	Me. (%)[a]	S_{BET} ($m^2\ g^{-1}$)[b]	V_{pore} ($cm^3\ g^{-1}$)[c]	τ (nm)[d]	D_{Me} (%)[e]	S_{Me} ($m^2\ g^{-1}$)[e]	*TOF* (s^{-1})[f]	*TOF/l_0* $m^2_{Me}/m_{int.}/s$[f]
$NiAl_{IWI}$	11.2	166	0.373	4.8	19.8	5.62	$1.12\ 10^{-2}$	$3.22\ 10^{-11}$
$NiAl_{GAI}$	10.8	160	0.362	9.7	11.5	8.25	$1.04\ 10^{-2}$	$1.39\ 10^{-11}$
$RuAl_{IWI}$	3.0	202	0.430	11.0	7.2	0.79	$2.03\ 10^{-1}$	$4.84\ 10^{-10}$
$RuAl_{GAI}$	3.1	198	0.412	< 5	34.4	3.90	$7.39\ 10^{-2}$	$6.90\ 10^{-12}$

[a]Determined by ICP.
[b]Calculated by BET method (Equation 2.2).
[c]Estimated from adsorption isotherm ($V_{ads.}$ at P/P_0 = 0.98).
[d]XRD crystallite size estimated by Equation 2.7.
[e]Estimated from TEM micrographs and Equation 2.11.
[f]Calculated by Equations 2.17 and 4.1.

4.1.3. Particle size distribution and metal dispersion

The effect of the preparation method on the morphology as well as on the particle size distribution was determined by TEM. In addition, the mean metal dispersion and metal surface area (Table 4.1) were calculated by d-FE model [80]. The micrographs of Ni catalysts along with their corresponding particle size distribution histograms are displayed in Figure 4.4. In both cases, quasi-spherical supported Ni particles (circled in yellow) were observed. It can be appreciated that the particle size distribution (calculated from measurement of at least 200 particles) is wider in the case of the sample prepared by GAI method. In fact, $NiAl_{IWI}$ catalyst presents Ni particles sizes from

2 to 10 nm, whereas the distribution of $NiAl_{GAI}$ sample ranges from 3 to 19 nm. In this line, the average particle sizes are 5.8 nm (D_{Ni} = 19.8%) and 11.2 nm (D_{Ni} = 11.5%) for $NiAl_{IWI}$ and $NiAl_{GAI}$ catalysts, respectively. Note that these values are in agreement with crystallite sizes estimated by XRD, indicating that the active phase is better dispersed on $NiAl_{IWI}$ catalyst. However, this catalyst presents a reduction degree of 38% at 500 ˚C, i.e., less than the half of total nickel is reduced before the reaction, as determined in the previous chapter [128]. For that reason, the Ni reactive surface area is slightly higher for the catalyst prepared via GAI method (see Table 4.1).

Such differences in dispersion and amount of reducible nickel are related with the calcination step. In the case of $NiAl_{IWI}$ catalyst, the precursor is calcined in air favouring

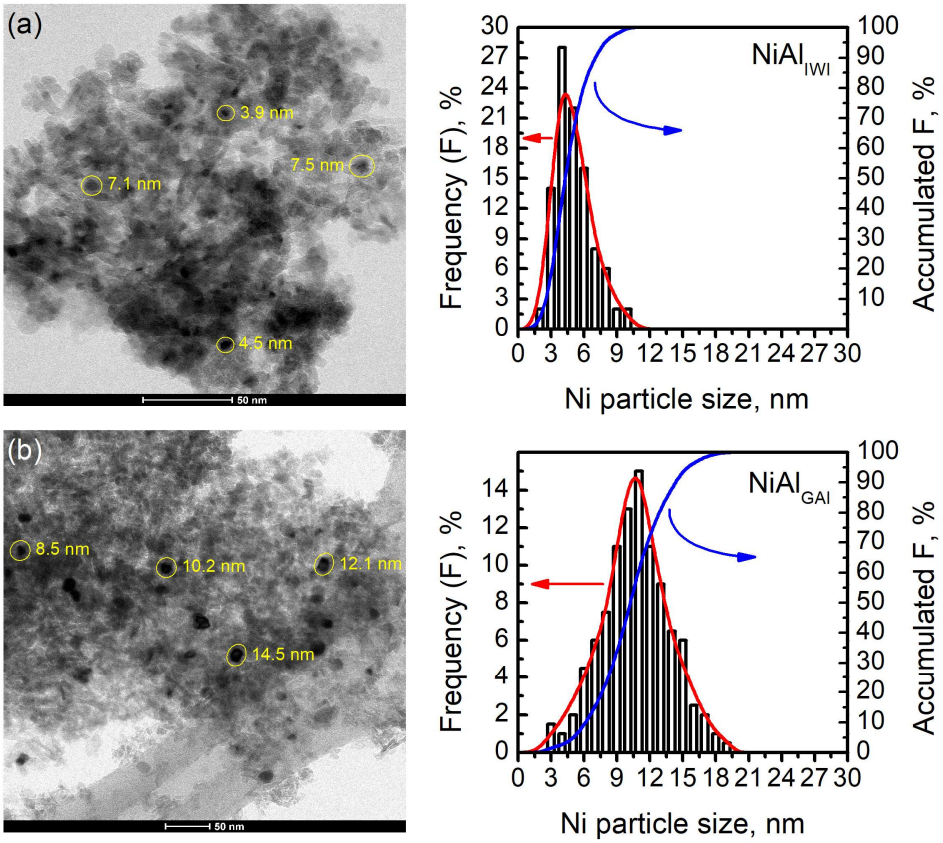

Figure 4.4. TEM micrographs along with particle size distributions of (a) $NiAl_{IWI}$ and (b) $NiAl_{GAI}$ catalytic formulations.

mainly the formation of NiO highly interacting with the support or even $NiAl_2O_4$ inert phase. After reduction treatment at 500 °C, small and well distributed Ni particles are obtained but not all nickel is reduced due to the high metal-support interaction observed by H_2-TPR. This high interaction between NiO and Al_2O_3, which was extensively studied in the literature [99, 104], is also confirmed by examination and comparison of several TEM micrographs: far fewer Ni particles are visualized on $NiAl_{IWI}$ than on $NiAl_{GAI}$ catalyst, indicating a lower Ni reduction extent. On the other hand, the $NiAl_{GAI}$ precursor is calcined under reductive atmosphere (20% H_2/N_2), avoiding the formation of Ni^{2+} species able to react with γ-Al_2O_3 and assuring that all nickel will be reduced after the preparation procedure. Besides, the presence of non-volatile organic compounds apparently prevents Ni crystals from excessive growing. As the temperature increases during the calcination, it seems that incipient nickel nanocrystals are embedded in an organic matrix that acts as a barrier preventing them from sintering [62]. As a result, all Ni is reduced and quite well dispersed in form of 11 nm size particles. Noteworthy, Ding et al. [129] observed a similar Ni particle size distribution for a Ni/SiO_2 prepared by the glycerol assisted impregnation and reported that glycerol resulted to be the best alkanol solvent among those studied.

Analogously, Figure 4.5 shows TEM micrographs together with particle size histograms of monometallic Ru/Al_2O_3 samples. In both catalysts, Ru particles with different morphology were easily visualized (within yellow circles or rectangles). Ruthenium was homogeneously dispersed in form of spherical particles on $RuAl_{GAI}$ while a much more heterogeneous distribution was verified on $RuAl_{IWI}$. The latter presents both oval and hexagonal Ru particles or even aggregates formed by several particles. In this case, the particle size distribution seems to be quite affected by the preparation method. On one side, $RuAl_{IWI}$ catalyst has an unimodal particle size distribution with a long tail ranging from 4 to 32 nm and a corresponding average particle size of 14.8 nm (D_{Ru} = 7.2%). On the contrary, the particle size distribution of $RuAl_{GAI}$ sample, shown in Figure 4.5b, is symmetric and much narrower. It should be noted that this catalyst presents an average particle size of 2.7 nm, which correspond to a dispersion of 34.4%. These results clearly indicate that GAI is a more appropriate synthesis route to disperse Ru over Al_2O_3.

In our former studies based on thermo-XRD results, we reported that RuO_2 crystals tend to grow fast and agglomerate under oxidative calcination conditions due to the formation of volatile RuO_x [128]. That would explain why bigger particles and so long tail are observed in the histogram of the catalyst prepared by IWI method. This fast growth is clearly avoided by GAI method, which includes a non-oxidative calcination.

Furthermore, even more uniform and smaller particles are created due to the organic enclosing effect above explained. Yan et al. [125] obtained similar metallic dispersion (D_{Ru} = 32.2%) in a 3%Ru/Al_2O_3 prepared by incipient wetness impregnation of Ru(III) acetylacetonate precursor and performing the calcination treatment under

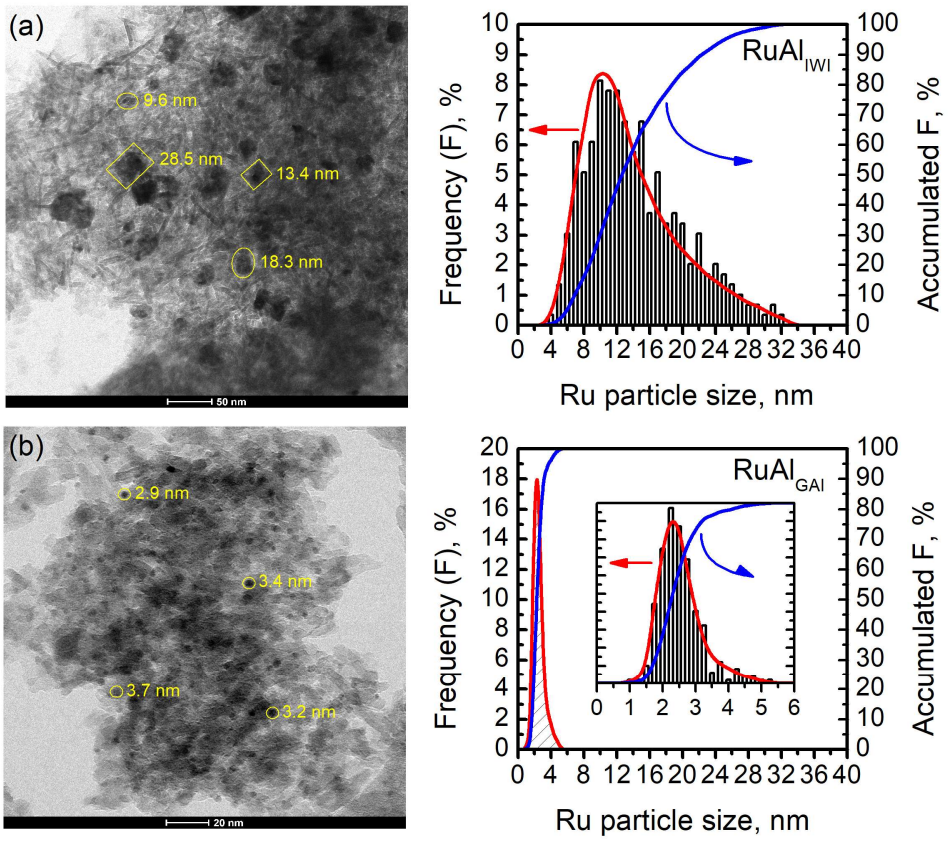

Figure 4.5. TEM micrographs together with particle size distributions of (a) $RuAl_{IWI}$ and (b) $RuAl_{GAI}$ catalysts.

10%H_2/Ar flow. As a result, the $RuAl_{IWI}$ catalyst contains a Ru surface area of 0.79 m^2 g^{-1} while that of $RuAl_{GAI}$ is 3.90 m^2 g^{-1}.

4.1.4. CO_2 hydrogenation into CH_4

In a final step, the catalytic performance of the catalysts was evaluated in order to determine the effect of the preparation method on activity. Figure 4.6 shows the CO_2 conversion (above) along with product selectivity (below) as a function of the reaction temperature for Ni/Al_2O_3 and Ru/Al_2O_3 catalysts, respectively. As previously reported [130], Ru-based catalysts were more active than Ni-based ones due to the higher ability of the former to dissociate hydrogen at lower temperature. Thus, the catalytic activity order is as follows: $RuAl_{GAI}$ > $RuAl_{IWI}$ > $NiAl_{GAI}$ > $NiAl_{IWI}$.

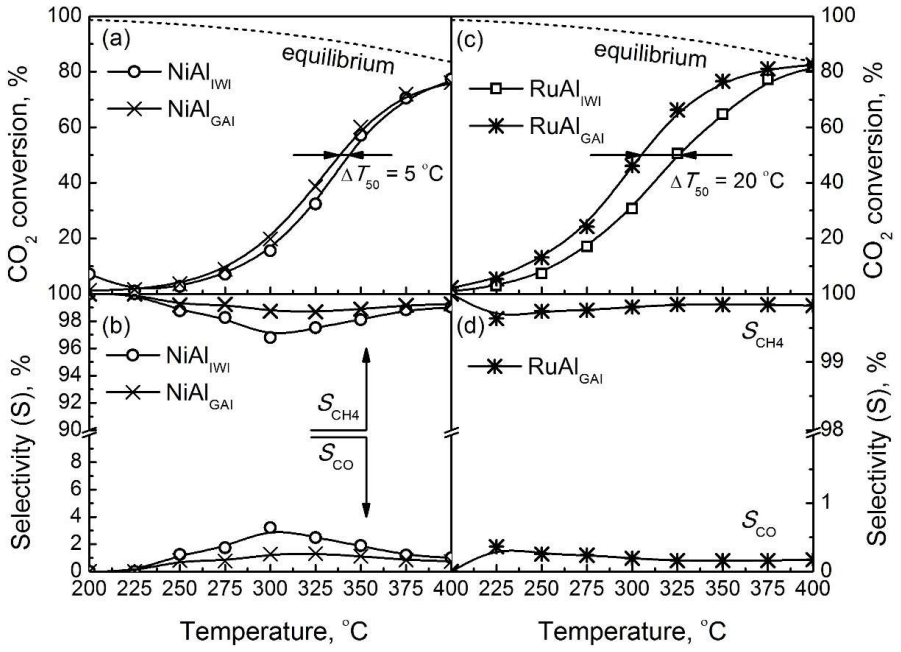

Figure 4.6. Light-off curves with their respective products (CH_4/CO) selectivity profiles of (a, b) monometallic Ni and (c, d) Ru catalysts. Reaction conditions: P = 1 bar, H_2:CO_2 ratio = 4 and WHSV = 30,000 mL h^{-1} g^{-1}.

The activity profiles of Ni/Al_2O_3 samples are not so different, as shown in Figure 4.6a. In both cases, the CO_2 conversion (reaction rate) increases exponentially with

temperature from 225 °C (onset reaction temperature) to 325 °C and then, this increase slows down as the reagents are depleted and equilibrium conversion is approached. It must be noted that the CO_2 conversion is slightly higher for $NiAl_{GAI}$ catalyst in the studied temperature range, resulting in a T_{50} (temperature at which 50% of CO_2 conversion is obtained) only 5 °C lower. However, a more significant difference can be observed in selectivity (Figure 4.6b): $NiAl_{IWI}$ produces more CO than $NiAl_{GAI}$ catalyst at mild temperatures (T ≈ 300 °C), although never more than 3.5% of converted CO_2. In fact, the CO selectivity of $NiAl_{IWI}$ at 300 °C is around 2.5 times higher than that of $NiAl_{GAI}$ catalyst (3.2 vs. 1.3%). The small amount of carbon monoxide is produced either from reverse water gas shift (RWGS) or reforming reactions.

On the other hand, the higher CO_2 conversion and CH_4 selectivity observed for $NiAl_{GAI}$ catalyst are probably related to a higher Ni surface area (8.25 vs. 5.62 $m^2\ g^{-1}$). This hypothesis was supported by calculations of *TOF*s at 250 °C. Note that, by definition, *TOF* assumes that reaction takes place at any point of metal surface. However, under CO_2 methanation conditions, the partial H_2 pressure is at least four times higher than that of CO_2, which disfavors the adsorption of the latter. Consequently, metal particles will be largely covered by H_2. Also, considering that the support (γ-Al_2O_3 in this study) is able to adsorb or active CO_2, it can be assumed that CO_2 methanation takes place at the perimeter of metal-support interface rather than on surface, as reported in a previous work [131]. Therefore, for more realistic comparison, *TOF* was normalized with respect to interfacial length or perimeter (TOF/I_0, Table 4.1). The total metal-support perimeter per metal surface area (I_0) was calculated by Equation 4.1, which was proposed by Kourtelesis et al. [132] and is based on developments reported by Duprez et al. [133].

$$I_0\left(\mathrm{m}_{\mathrm{interface}} / \mathrm{m}^2_{Me}\right) = \frac{S^2_{Me} \times \beta \times \rho_{Me} \times AW_{Me}}{\mathrm{N_A} \times atA_{Me}} \tag{4.1}$$

where S_{Me} is the metallic surface area in $m^2\ g_{Me}^{-1}$, β is a particle shape factor (33.3 for hemispherical particles), ρ_{Me} is the density of the metal in $g\ m^{-3}$, AW_{Me} is the metal atomic weight of the metal in $g\ mol^{-1}$, N_A is the Avogadro number, and atA_{Me} is the area

occupied by a single metal atom ($6.49 \cdot 10^{-20}$ m^2 Ni $atom^{-1}$ and $6.13 \cdot 10^{-20}$ m^2 Ru $atom^{-1}$). It can be observed that TOF/l_0 values (Table 4.1) are of the same order of magnitude, suggesting that the CO_2 methanation rate per metal atom at the interface for supported catalysts with average Ni particle perimeters of 18.2 nm ($NiAl_{IWI}$ catalyst) and 35.2nm ($NiAl_{GAI}$ catalyst) is quite similar.

Recently, the structure sensitivity of CO_2 methanation over supported metals has been studied by various authors. For instance, Vogt at al. [134] clearly reported structure sensitive CO_2 methanation over Ni/SiO_2 catalysts with small particle sizes ranging from 1 to 6 nm, concluding that the more active Ni atoms are those forming clusters of 2-3 nm. The high *TOF* of these clusters was attributed to an intermediate adsorption strength of CO on Ni, which was reported to be a reaction intermediate of CO_2 methanation on Ni/SiO_2 catalyst. However, Beierlein et al. [111] demonstrated that the specific activity does not depend on Ni particle size within a range from 6 to 91 nm, observing a linear correlation between the activity and Ni surface area and concluding that CO_2 methanation on highly loaded Ni/A_2O_3 catalysts is a structure insensitive reaction. Therefore, it seems that structure sensitivity clearly depends on the range of Ni particle size studied as well as the metal-support combination used. In our case, the results agree with the findings of the second authors and structure sensitivity analysis carried out in the previous chapter (see Figure 3.10), since the observed specific activity barely increases when decreasing particle size from 11 to 6 nm.

Analogously, the light-off and selectivity curves of Ru/Al_2O_3 catalysts are displayed in Figures 4.6c and d. In this case, the onset temperature for both samples is 200 °C and the equilibrium CO_2 conversion is reached at the same temperature (X_{CO_2} at 400 °C = 82%). Nevertheless, the increase in CO_2 conversion with temperature for $RuAl_{GAI}$ is faster than for $RuAl_{IWI}$ catalyst, which leads to a notable 20 °C left shift of the light-off curve (i.e., superior activity at low temperature). Regarding the selectivity towards CH_4, it was higher than 99.5% in the range of studied temperatures and only trace amounts of CO in terms of ppm were detected for $RuAl_{GAI}$ catalyst (Figure 4.6d). Considering that metal particles of $RuAl_{GAI}$ are five times smaller than that of $RuAl_{IWI}$ catalyst, one could expect a bigger difference in catalytic performance. This suggests that metal-support

interface of the former is less active, as revealed by TOF/I_0 values also summarized in Table 4.1. Note that TOF/I_0 value is around one order of magnitude lower for $RuAl_{GAI}$ catalyst, suggesting that CO_2 methanation is structure sensitive on RuAl catalysts. Indeed, a lower specific methanation activity on small Ru particles or clusters had already been reported by several authors [48, 124, 125]. According to them, CO formation via RWGS is favoured rather than CO_2 methanation on atomically dispersed or low coordinated small Ru particles. Despite that fact, a considerable T_{50} value gradient of 20 °C is observed, which evidences that a more active catalyst is obtained by GAI method.

4.2. EFFECT OF Ru CO-IMPREGNATION

As mentioned in the previous chapter, the main disadvantage of Ni catalysts with respect to those of Ru is their considerably lower activity at low temperature due to their inferior H_2 dissociation capacity [130]. Instead, the main drawback of Ru catalysts is their exorbitant price. Nevertheless, designing appropriate Ni-Ru bimetallic systems could be a solution to those handicaps. Generally, these bimetallic catalysts are known to exhibit better catalytic properties compared to their monometallic counterparts such as higher conversion, fewer side reactions and increased stability due to a synergistic effect [105, 135, 136]. This synergy only happens as a result of specific electronic interactions and geometric positional relationships between the two metals (combination of “ligand” and “ensemble” effects) [136]. By adding an appropriate secondary metal (Ru) to the catalytic formulation, the electronic properties of the main metal (Ni) are usually altered leading to changes in reagents adsorption and reaction intermediates formation. These changes, in turn, can modify the reaction pathway and the activation energy so that the activity of the catalyst is improved [105]. Recently, Ni-Ru bimetallic systems have proven to be very effective specifically for CO methanation [137-140]. Q. Liu et al. also reported enhanced catalytic activity for CO_2 methanation over 10Ni-1Ru-2CaO/Al_2O_3 formulation due to a significant increase in H_2 and CO_2 chemisorption capacities [141], whereas Wei et al. [142] did not achieve activity improvement by adding Ru to Ni-zeolite (13X and 5A) catalysts. However, the

analysis of Ni-Ru systems in terms of physicochemical and catalytic properties for CO_2 methanation has not been focus of many systematic studies so far.

Once the best preparation method (GAI, according to the results discussed above) had been determined, it was chosen to introduce small amounts of Ru (< 2 wt%) as secondary metal in order to further improve the Ni/Al_2O_3 formulation. So, three bimetallic $Ni\text{-}Ru/Al_2O_3$ formulations with small Ru contents (0.5, 1.0 and 1.5 wt%) were prepared following the same procedure. Hereunder, the characterization as well as activity results of monometallic $NiAl_{GAI}$ and bimetallic catalysts are shown and the effect of Ru co-impregnation on catalytic properties of Ni/Al_2O_3 formulation is discussed.

4.2.1. Metal content and textural properties

The physicochemical properties of $NiAl_{GAI}$ and bimetallic catalysts are shown in Table 4.2. As observed, the metal contents determined by ICP are very close to the nominal values, indicating that no relevant amount of metal was lost during the synthesis. Interestingly, the specific surface area slightly increases with Ru content: 5, 9 and 10%, respectively. This controversial trend can be explained by analysing the pore size distribution of the catalysts, which are displayed in Figure 4.7.

Table 4.2. Physicochemical properties of monometallic and bimetallic catalysts.

Catalyst	Ni (%)[a]	Ru (%)[a]	S_{BET} ($m^2\ g^{-1}$)[b]	H_2 uptake (mmol g^{-1})[c]	Red. ext. (%)[c]	H_2 des. (µmol g^{-1})[d]	D_{Ni} (%)[e]
NiAl	10.8	0	160	2.01	28.4	67.0	11.5
Ni-0.5RuAl	12.6	0.51	168	2.06	57.2	89.3	19.4
Ni-1.0RuAl	11.5	1.12	174	2.17	72.6	125.0	26.3
Ni-1.5RuAl	11.8	1.63	175	2.22	75.2	151.8	31.1

[a]Determined by ICP.
[b]Calculated by BET method (Equation 2.2).
[c]Reduction extent determined from integration of TPR profiles.
[d]Calculated by integration of H_2-TPD profiles at T < 500 °C.
[e]Estimated from STEM micrographs and Equation 2.11.

The monometallic catalysts present a narrow unimodal mesopore size distribution centered at 7.3 nm, whereas bimetallic catalysts exhibit wider and bimodal distributions with maximums between 6 and 10 nm. As already discussed, $NiAl_{GAI}$ catalyst presents similar particles with sizes probably above 7 nm, which partially or completely block the mesopores of the support. However, the bimodal distribution verified for the bimetallic catalysts might be due to the presence of particles with well differentiated size or morphology, which might penetrate into the small pores of γ-Al_2O_3. Ru incorporation widens the distribution but decreases its intensity, which finally results in a slight increase of S_{BET} from 168 to 175 $m^2\ g^{-1}$ and similar pore volume of 0.42 $cm^3\ g^{-1}$. Thus, introduction of Ru makes some improvement in textural properties of Ni/Al_2O_3 catalyst.

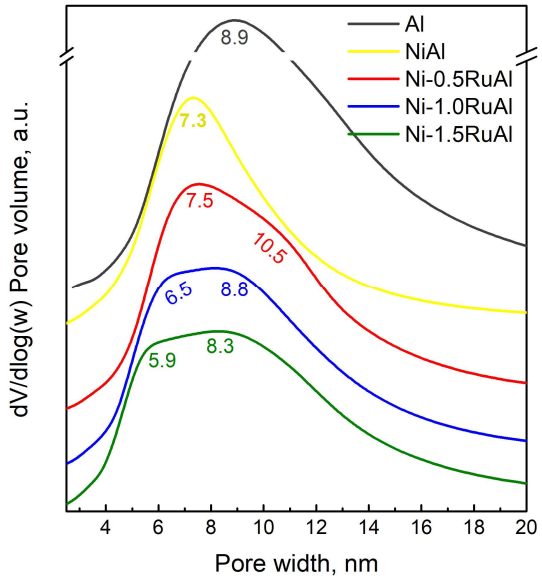

Figure 4.7. Pore size distributions of γ-Al_2O_3, monometallic $NiAl_{GAI}$ as well as bimetallic Ni-Ru catalysts.

XRD analysis was also performed for bimetallic catalysts (not shown). However, no characteristic peaks of both metals were detected (crystallites sizes < 5 nm). This observation is in agreement with N_2 physisorption results and indicates that Ni and Ru are finely dispersed.

4.2.2. Resistance against oxidation and reducibility

With the aim of measuring and comparing the resistance against oxidation of monometallic as well as bimetallic catalysts, $NiAl_{GAl}$ and Ni-1.0RuAl samples were exposed to 3 consecutive RedOx cycles at 325 °C. Each RedOx cycle consisted of feeding 15 oxidative pulses (5 cm^3 of 5%O_2/He) followed by another 15 reductive pulses (5 cm^3 of 5%H_2/Ar). On that way, the effect of O_2, feeded in concentration similar to that of flue gases, on the catalysts was estimated and their reversibility was determined. Note that the resistance to oxidation of $3RuAl_{GAl}$ catalyst was measured at 550 °C in order to ensure that its oxidation was effective. The resistance against oxidation, defined as the percentage of Ni reduced per cycle after sample being exposed to 15 oxidative pulses, was calculated by the following expression:

$$\text{Reversibility of cycle}_i\ (\%) = \frac{n_i(\text{Ni}^0)}{n_i(\text{Ni}^{2+}) + n_{i-1}^{\text{rem.}}(\text{Ni}^{2+})} \times 100 \qquad (4.2)$$

where, $n_i(Ni^{2+})$ are the moles of Ni oxidized in cycle *i*, $n_{i-1}^{\text{rem.}}\left(\text{Ni}^{2+}\right)$ are the moles of Ni that remain oxidized from previous cycles and $n_i(Ni^0)$ are the moles of Ni reduced or recovered in cycle *i*. Note that $n_i(Ni^{2+})$ as well as $n_i(Ni^0)$ were calculated from total O_2 and H_2 uptakes of oxidative and reductive steps, respectively.

The reversibility values of $NiAl_{GAl}$ and Ni-1.0RuAl catalysts are shown in Figure 4.8. It can be clearly observed that the reversibility values of the bimetallic catalyst are superior to those of monometallic one in all cycles, observing the major difference in the third cycle: 60 vs. 42%, respectively. This indicates that incorporation of Ru provides higher resistance to oxidation and/or higher capacity to recover the reductive state than the monometallic $NiAl_{GAl}$. The observed higher reversibility is due to ruthenium role as promotor of nickel reduction in the bimetallic catalyst, i.e., H_2 is firstly dissociated on Ru surface and then can migrate to neighbouring NiO particles facilitating their reduction [138].

Furthermore, it can be noticed that the reversibility of monometallic catalysts decreases from 52% (cycle 1) to 42% (cycle 3), while that of bimetallic catalyst remain

stable around 60%. Although the decrease from second to third cycle is not so pronounced (– 2%), it seems that the reversibility value of $NiAl_{GAl}$ sample could keep decreasing in further consecutive cycles due to a progressive formation of NiO that is no longer able to be reduced by remaining Ni^0.

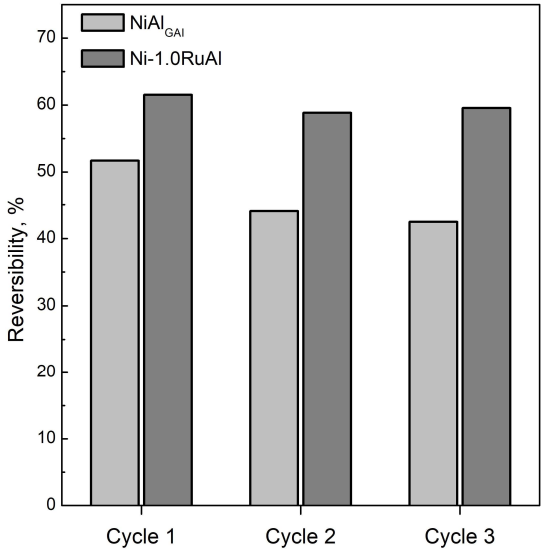

Figure 4.8. Resistance against oxidation, expressed as reversibility, of $NiAl_{GAl}$ and Ni-1.0RuAl catalysts for 3 consecutive RedOx cycles at 325 °C.

The fact that reversibility of bimetallic system is apparently stable, suggests that Ni particles are near to and surrounded by Ru ones, which avoids or at least slows down the formation of non-reversible NiO particles. However, as reported by Rynkowski et al. [135], the presence of Ru does not prevent the formation of spinel type oxides at long term and high temperatures. Finally, it must be highlighted that the H_2 uptake was around 2 times the O_2 uptake at 550 °C for $RuAl_{GAl}$ catalyst, indicating that reversibility is around 100% if RuO_2 formation/reduction stoichiometry is assumed.

Immediately after studying the resistance to oxidation of monometallic NiAl and bimetallic Ni-1.0RuAl catalysts, the reducibility as well as the type of both Ni and Ru species of all samples were studied by H_2-TPR. Previously, catalysts were treated with a 5%O_2/He stream at 500 °C to completely oxidize both metals. Besides, TPR profiles

were deconvoluted into Gaussian peaks to better understand the reduction events. The deconvoluted TPR profiles of bimetallic and monometallic catalysts are shown in Figure 4.9.

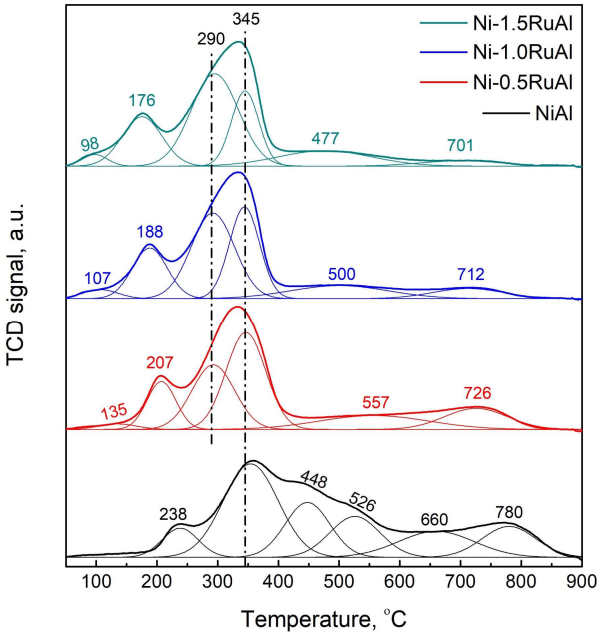

Figure 4.9. H_2-TPR profiles of monometallic $NiAl_{GAI}$ and bimetallic catalysts.

It can be observed that $NiAl_{GAI}$ catalyst uptakes hydrogen in a wide range of temperatures, which indicates the presence of different Ni species (see black profile). Firstly, the peak at 238 °C may be associated with the reduction of external NiO layer, suggesting that a small fraction of nickel particles was not completely oxidized during the pretreatment [143]. On the contrary, the TPR bands appearing between 300 and 600 °C can be attributed to the reduction of α-type NiO particles with different interaction with alumina depending on their location and size (the higher the interaction, the higher the reduction temperature). Likewise, the peak at 660 °C is assigned to the reduction of internally located Ni^{2+} with strong interaction with the support (β-type NiO) [104]. Finally, the small TPR peak at 780 °C suggests the presence of a negligible amount of inert Ni spinel or γ-type NiO [86].

On the other hand, bimetallic catalysts present the same type of Ni species found on the monometallic sample as well as an additional peak around 100 °C whose intensity increases with Ru content (0.5, 1.0 and 1.5%). Based on the literature [52, 135], this little peak is related to RuO_x reduction. Noteworthy, the TPR profiles of bimetallic catalysts are clearly shifted towards lower temperatures. Indeed, the higher the Ru loading, the greater the shift. This behaviour is due to ruthenium role as promotor of nickel reduction, i.e., H_2 is dissociated on pre-reduced Ru and then migrates to neighbour NiO particles facilitating their reduction [138]. Besides, note that ruthenium co-impregnation not only leads to a shift of TPR peak positions but also to a change in the relative amount of Ni species. In fact, a decrease in the relative amount of Ni species reducible above 500 °C is observed by increasing the Ru content. For instance, the relative amount of hardly reducible $NiAl_2O_4$ decreases from 11.5 to 4.1% by adding 1.5% Ru.

The H_2 uptakes as well as the Ni reduction extents below 350 °C (considered an intermediate operation temperature for CO_2 methanation reaction) are summarized in Table 4.2. The H_2 uptake values match with the real contents determined by ICP within ± 5% error, considering that NiO and RuO_2 are the only reducible species. Regarding the reduction extent at 350 °C, it increases with Ru loading from 28.4 to 75.2%, indicating that ruthenium notably enhances the reducibility of nickel at low temperature. This enhancement may result in an increase of catalytic activity at mild temperature, since much more nickel could be reduced in bimetallic catalysts under methanation reaction stream in order to dissociate hydrogen. Moreover, one might think that the presence of Ru also improves nickel resistance against oxidation under such reaction conditions, although it was shown that it does not prevent the formation of spinel type oxides in long term under oxidant streams [135].

4.2.3. H_2 adsorption capacity and Ni dispersion

After analysing the reducibility of the catalysts, the hydrogen adsorption capacity was also determined by TPD. Thus, H_2-TPD profiles of monometallic as well as bimetallic catalysts are depicted in Figure 4.10.

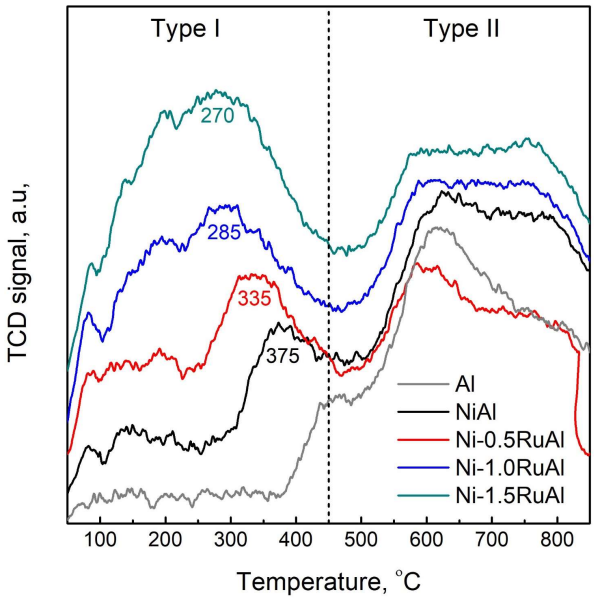

Figure 4.10. H_2-TPD profiles of γ-Al_2O_3 support, monometallic Ni and bimetallic catalysts.

It can be observed that all profiles exhibit two bands, before and after 450 °C. While the band below 450 °C can be generally attributed to H_2 chemisorbed on metal particles (type I), the one at higher temperature is associated with H_2 desorption from the subsurface alumina layers or with the spillover phenomenon (type II) [144]. Indeed, the H_2-TPD profile of bare γ-Al_2O_3 does not show any signal variation below 400 °C but an intense band at higher temperature, which might be related to a dehydroxylation process (Figure 4.10).

Likewise, the band at low temperatures can be divided into several peaks. For instance, the monometallic $NiAl_{GAl}$ catalyst, presents a main peak at 375 °C and additional H_2 desorption below 250 °C. According to Ewald et al. [114], the main peak corresponds to hydrogen chemisorbed on Ni surface while the TCD signal at low temperatures can be ascribed to hydrogen adsorbed on the corners of large Ni particles or on better dispersed particles. Noteworthy, the main peak position shifts towards lower temperatures and its intensity increases with Ru content, suggesting that the

amount of exposed Ni atoms grows accordingly. Such increase in Ni dispersion was also reported by other authors who incorporated Ru [141], Cr [126] or Fe [105].

The amounts of desorbed H_2 calculated from TPD profiles integration are summarized in Table 4.2. Note that this parameter duplicates with co-impregnation of 1.5% Ru on Ni/Al_2O_3 formulation, i.e., the fraction of exposed metal notably rises. Consequently, the ability to supply dissociated hydrogen under methanation reaction conditions remarkably increases with the Ru content. Based on H_2 desorption data, Ni dispersion on the monometallic catalyst was also estimated, resulting a value of 7.9% (11.5% by TEM, Table 4.1). In the case of bimetallic catalysts, dispersion cannot be estimated since exposed atoms of both Ni and Ru, in major and minor extent respectively, contribute in the total H_2 desorption below 450 °C. Anyway, the amount of desorbed H_2 compared to that of $NiAl_{GAl}$ catalyst is more than twice for Ni-1.5RuAl catalyst and hence, this suggests that its metal surface could be around double.

In order to determine the morphology, size and distribution of the supported bimetallic particles, HAADF-STEM analysis was conducted. The high-angle *Z*-contrast annular field imaging together with EDX mapping allowed us differentiating between two or more elements, such as Al ($Z = 13$), Ni ($Z = 28$) and Ru ($Z = 44$). STEM micrographs together with EDX maps of bimetallic catalysts are shown in Figure 4.11.

It can be observed that Ni (red coloured) and Ru (green coloured) are homogenously dispersed as individual spherical particles, which means that no alloy is formed during the calcination at 550 °C [141]. Noteworthy, the Ni-0.5RuAl catalyst presents an average Ni particle size of 7.4 nm (calculated from around 50 particles), 4 nm lower than that obtained for monometallic $NiAl_{GAl}$ catalyst. This parameter is even lower for Ni-1.0RuAl and Ni-1.5RuAl, with values of 6.3 and 5.9 nm, respectively. Therefore, Ni particle size is lowered by increasing the amount of co-impregnated Ru. Regardless the metal loading (0.5, 1.0 or 1.5%), the Ru particle size resulted to be around 4-5 nm for all bimetallic catalysts. Note that some of these particles are located near to Ni ones, especially for catalysts with higher Ru contents (see Figures 4.11e and f).

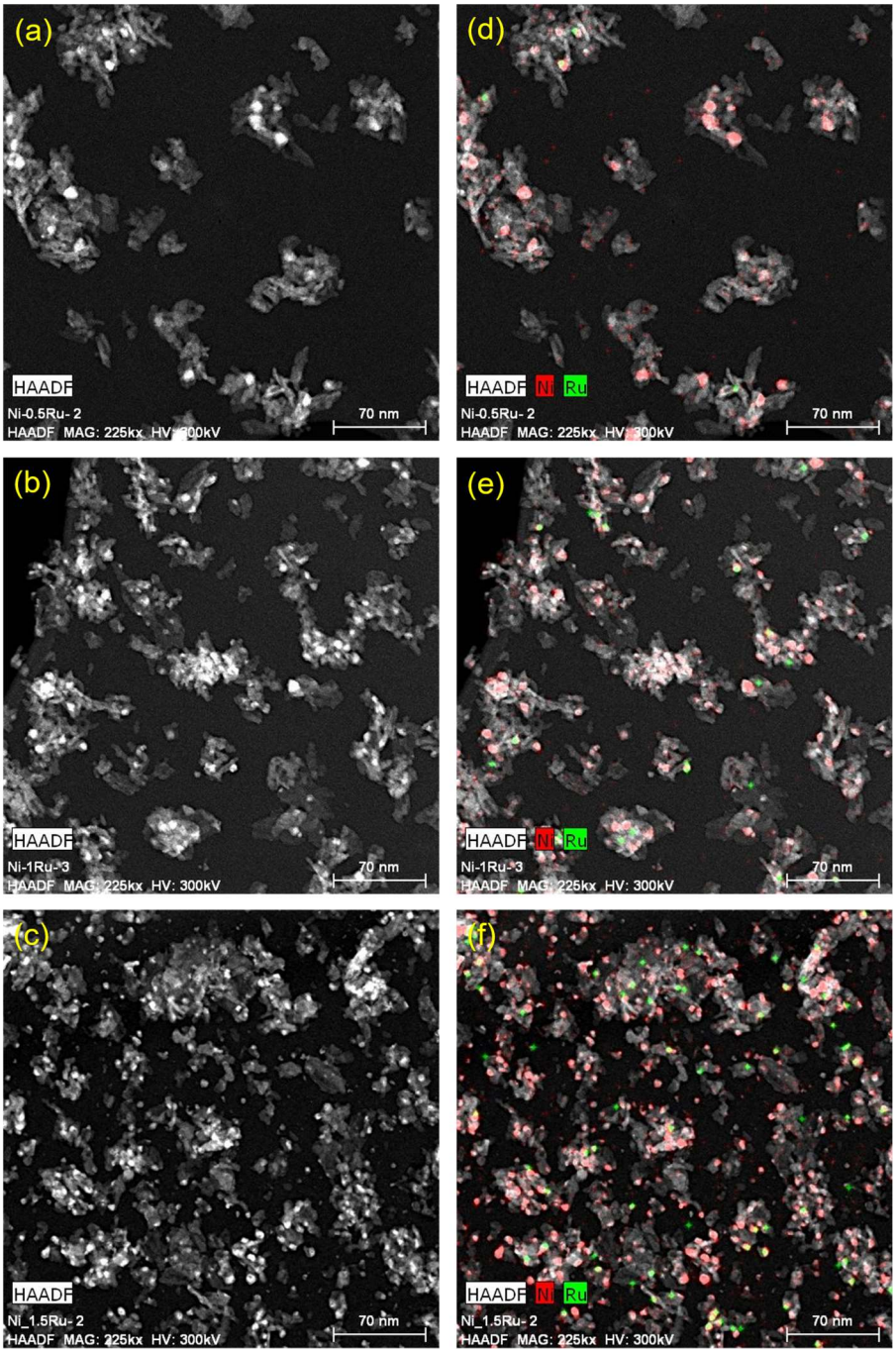

Figure 4.11. STEM micrographs with their respective EDX maps for (a, d) Ni-0.5RuAl, (b, e) Ni-1.0RuAl and (c, f) Ni-1.5RuAl catalysts.

The fact that Ni and Ru particles are next to each other or in intimate contact is in agreement with the enhanced reducibility observed by H_2-TPR: the neighbour Ru particle acts as H supplier via spillover mechanism favouring the reduction of Ni^{2+} [138].

As is in the case of monometallic catalysts, Ni dispersion on bimetallic catalysts was also estimated by d-FE model and the results are summarized in Table 4.2 (page 110). As already observed by H_2-TPD, the Ni dispersion is significantly enhanced with Ru loading. In fact, D_{Ni} rises 9.4, 15.6 and 20.0% by adding 0.5, 1.0 and 1.5% of Ru to Ni/Al_2O_3 formulation, respectively. This behaviour might indicate that both Ru and glycerol solvent act as structural promoters during the calcination process, avoiding the excessive growing or sintering of Ni. Based on the characterization results properly discussed above, it is expected that Ni/Al_2O_3 catalysts performances are improved with the incorporation of small percentage of Ru in the formulation.

4.2.4. Catalytic performance

Thus, once bimetallic catalysts were characterized and the effect of Ru on physicochemical properties of Ni/Al_2O_3 determined, their catalytic performance was studied. The conversion-temperature as well as the selectivity-temperature curves of bimetallic catalysts are shown in Figure 4.12. For comparison purposes, the light-off curves obtained for $NiAl_{GAI}$ and $RuAl_{GAI}$ catalysts are also displayed.

It can be clearly observed that the addition of increasing amounts of co-impregnated Ru leads to a notable increase of the sigmoid curve slope, especially at mild temperatures (from 275 to 325 °C). Accordingly, the T_{50} value is lowered 40 °C by only co-impregnating 1.5%Ru, which indicates that the presence of Ru considerably improves the activity of Ni/Al_2O_3 formulation. Although different trends are observed depending on the temperature, all catalysts exhibit selectivity to CH_4 higher than 98.5% (Figure 4.12b). The slightly lower S_{CH_4} (or higher CO production) observed for bimetallic catalysts at low temperature compared to that of $NiAl_{GAI}$ catalyst may be related to some desorption of CO from low coordinated and inactive Ni and Ru particles. Even so, the methane yield clearly increases with Ru content, being the productivity order at

300 °C as follows: Ni-1.5RuAl (Y_{CH_4} = 51%) > Ni-1.0RuAl (Y_{CH_4} = 44%) > Ni-0.5RuAl (Y_{CH_4} = 32%) > $NiAl_{GAI}$ (Y_{CH_4} = 20%). It should be noted that Ni-1.0RuAl catalyst (T_{50} = 305 °C) shows almost the same activity as $3RuAl_{GAI}$ catalyst, whose noble metal content is three times higher.

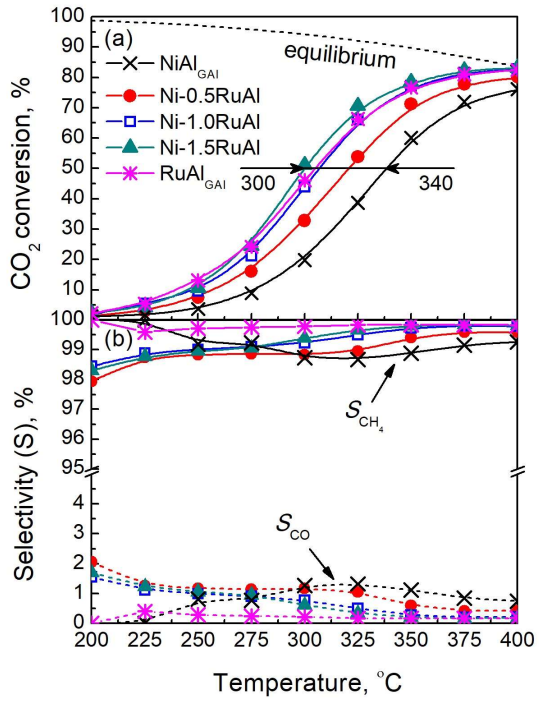

Figure 4.12. Evolution with temperature of (a) CO_2 conversion and (b) product (CH_4/CO) selectivity for $NiAl_{GAI}$ and bimetallic catalysts. Reaction conditions: P = 1 bar, H_2:CO_2 ratio = 4 and WHSV = 30,000 mL h^{-1} g^{-1}.

According to the characterization results, co-impregnation of Ru increases Ni dispersion. Besides, the presence of small Ru particles close to Ni ones considerably improves reducibility and hydrogen chemisorption capacity of nickel. Under reaction conditions, this leads to a greater amount of dissociated H_2, which is an essential reaction intermediate, and hence to a superior activity. Thus, the great enhancement observed in the catalytic performance can be attributed to a synergistic effect between Ni and Ru, as also reported by Liu et al. [141].

The catalytic behaviour of alumina supported Ni and Ru catalysts proved to be quite stable for 24-h-on stream and at stoichiometric feed ratio in the previous chapter [128]. Then, in order to accelerate the aging of the catalyst, the stability of monometallic $NiAl_{GAl}$ and bimetallic Ni-1.0RuAl catalyst was evaluated for 50 h-on-stream under harsher reaction conditions: at 325 °C (far for equilibrium conversion) and under sub-stoichiometric feed ratio (H_2/CO_2 = 3).

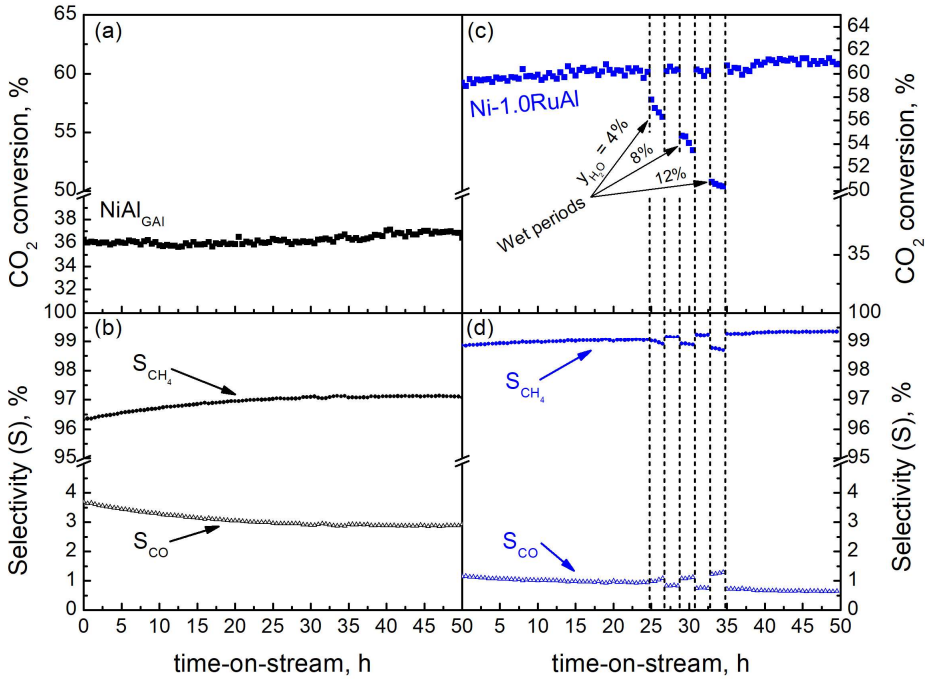

Figure 4.13. Evolution of CO_2 conversion and CH_4/CO selectivity with time-on-stream over 50 h for (a, b) $NiAl_{GAl}$ and (c, d) Ni-1.0RuAl catalysts. Reaction conditions: T = 325 °C, P = 1 bar, H_2/CO_2 ratio = 3 and WHSV = 30,000 mL h^{-1} g_{cat}^{-1}. Stability test of Ni-1.0RuAl catalyst includes 3 wet periods of 2h at y_{H_2O} = 4, 8 and 12%.

Noteworthy, the activity of $NiAl_{GAl}$ catalyst resulted to be stable during the evaluated period, observing CO_2 conversion values within 35 and 37%, as shown in Figure 4.13a. This indicates that the catalyst did not suffer from any type of deactivation such as particle sintering or poisoning [114] even though more CO was

produced (Y_{CO} = 1.33%) as consequence of sub-stoichiometric feed. Besides, the CH_4 selectivity also remained stable, observing values within 96.3 and 97.1% (Figure 4.13b).

In the case of the bimetallic catalyst, the stability test also included three wet periods (t = 2h) in which increasing amounts of water (10, 20 and 30 mL/min) were fed interspersed by dry periods (Figure 4.13c). It can be observed that, before 25 h-on-stream, the catalytic performance remained stable as observed for $NiAl_{GAI}$ catalyst, obtaining CO_2 conversion and CH_4 selectivity average values of 60 and 99%. However, the feed of increasing amounts of water, led to a CO_2 conversion drop of around 3% (y_{H_2O} = 0.04), 6% (y_{H_2O} = 0.08) and 9% (y_{H_2O} = 0.12) without a remarkable CH_4 selectivity decrease (0.1, 0.25 and 0.5%). This behavior indicates that water is strongly adsorbed on part of active sites, temporally rendering them unavailable for the reaction. Nevertheless, the activity was completely recovered when switching to dry conditions, indicating that water adsorption or inhibition effect is reversible at short term. Thus, based on the above activity and stability results, it can be concluded that glycerol assisted impregnation is a viable catalyst preparation method.

However, the individual roles of both Ni and Ru on the CO_2 methanation reaction mechanism are not clear. Such roles, as well as the identification of the reaction intermediates, will be analysed in the following part by *operando* FTIR.

4.3. OPERANDO FTIR MEASUREMENTS

Regarding CO_2 methanation reaction mechanism, several studies have been carried out by means of *operando* FTIR or DRIFTS with the aim of determining the reaction intermediates and elementary reaction steps over supported Ni [134, 136, 145, 146] and Ru [52, 124, 125] catalysts. Although there is still controversy regarding the identification and the role or place of some adsorbed species in the reaction pathway, two widely accepted routes have been proposed: the so-called dissociative and associative mechanisms [147]. The former assumes the dissociative adsorption of CO_2 into adsorbed CO or carbonyl followed by its hydrogenation into CH_4. In the latter, by contrast, CO_2 is molecularly adsorbed in form of carbonates or bicarbonates, which are progressively reduced by H^+ spillover into formate, formyl, methoxy species and,

finally, methane [148]. On the other hand, although it has been shown that bimetallic catalyst have enhanced catalytic properties based on characterization as well as activity results, the individual roles of both Ni and Ru on the CO_2 methanation reaction mechanism are not clear yet. Such roles, as well as the identification of the reaction intermediates, will be analysed in this section by *operando* FTIR study.

4.3.1. CO_2 adsorption

Figure 4.14 shows the evolution of CO_2 adsorption FTIR spectra with temperature for bare γ-Al_2O_3. Immediately after 5% CO_2/Ar exposure at 150 °C (see black spectrum), three clearly distinguishable bands appeared at 1653, 1437 and 1228 cm^{-1}, whose intensity grows with time up to 30 min.

These bands, already identified by many authors in the literature [124, 149-152], correspond to asymmetric as well as symmetric O-C-O stretching ($\nu(OCO)_a$ and $\nu(OCO)_s$) and OH deformation ($\delta_{(OH)}$) vibration modes of bicarbonate species, respectively. Besides, two negative bands can be observed in the hydroxyl region (3800-3600 cm^{-1}) at 3765 and 3665 cm^{-1} together with a narrow positive peak at 3620 cm^{-1}. The negative ones are attributed to the vibration of OH^- groups adsorbed along alumina surface whereas the positive one corresponds to $\nu(OH)$ vibration mode of bicarbonates. The presence of negative bands clearly indicates that bicarbonates are formed from CO_2 chemisorption on OH^- groups of γ-Al_2O_3, which are partially consumed after 30 min CO_2 adsorption [149]. Additionally, other wide and weak bands appear at 1575 and ≈ 1330 cm^{-1}, which might be assigned to $\nu(OCO)_a$ and $\nu(OCO)_s$ vibration modes of (chelating) bidentate carbonates. It is expected that carbonates are formed from CO_2 chemisorption on surface O^{2-} of γ-Al_2O_3 acting as Lewis basic sites [150].

The intensity of bicarbonate bands along with those of bidentate carbonates progressively decreases with temperature until practically disappearing at 400 °C, indicating that these species are not strongly attached to alumina. In fact, the weak-medium bond strength of bicarbonate has already been observed by CO_2-TPD [128, 153]. However, the increase of temperature gives rise to small bands at 1515 and 1457 cm^{-1}, which might be related to formation of more stable organic compounds.

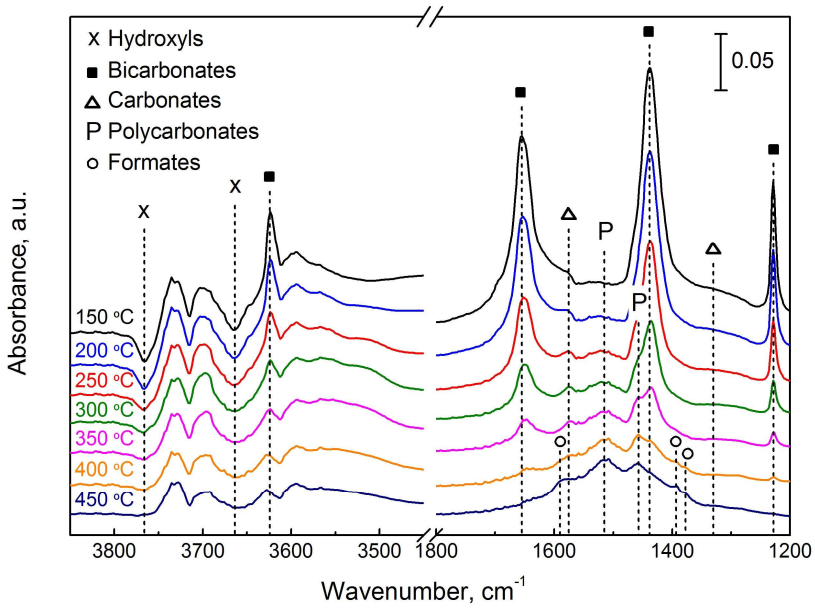

Figure 4.14. FTIR spectra collected during CO_2 adsorption over bare γ-Al_2O_3.

Furthermore, additional discrete bands are observed at 1393 and 1375 cm^{-1}, suggesting the presence of formate species. The formation of formates on alumina have already been reported and we suggest they come from reaction between bicarbonate or carbonate and residual H chemisorbed during the pre-treatment [124].

4.3.2. CO_2 methanation

After studying CO_2 adsorption over the bare support, the CO_2 methanation was analysed by means of *operando* FTIR over monometallic Ni formulations ($NiAl_{IWI}$ and $NiAl_{GAl}$ catalysts). FTIR spectra recorded under reaction conditions from 150 to 450 °C along with their respective C-species evolution for $NiAl_{IWI}$ and $NiAl_{GAl}$ catalysts are shown in Figure 4.15. Starting by the analysis of $NiAl_{IWI}$ catalyst results (Figure 4.15a), note that the black spectrum, which was recorded at 150 °C after 30 min under reaction stream exposure, shows more intense bands in the carbonate region (1800-1200 cm^{-1}) than bare alumina (Figure 4.14). Specifically, the bands assigned to bidentate

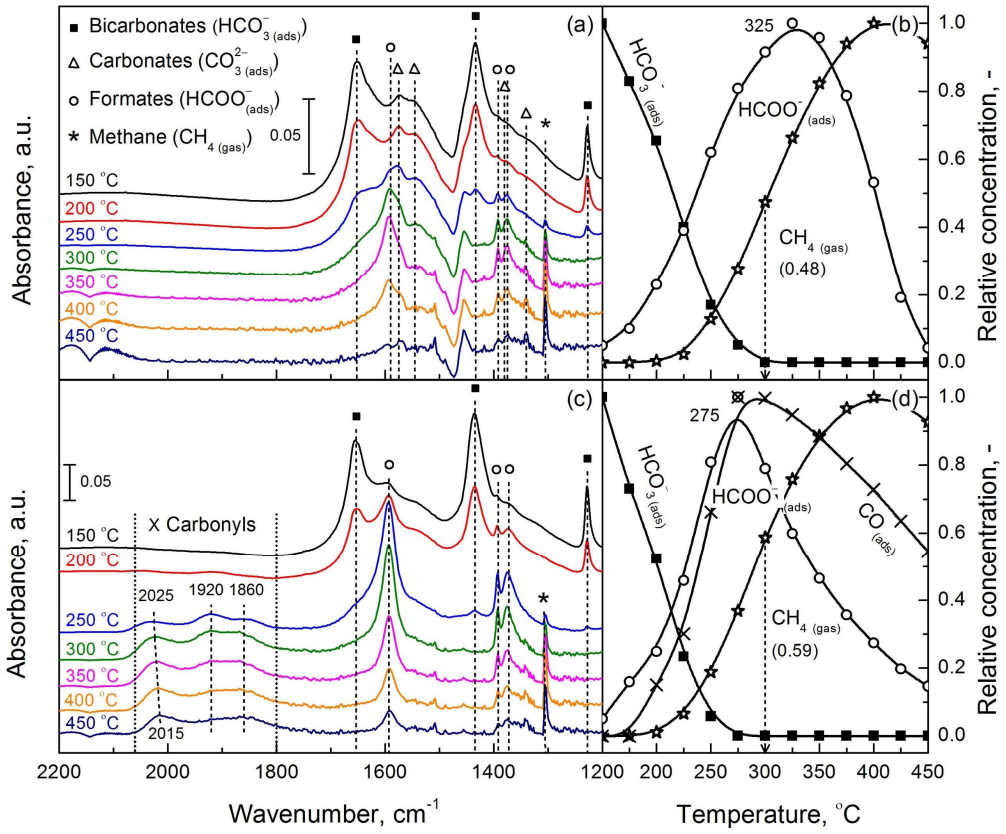

Figure 4.15. FTIR spectra recorded at different temperatures under CO_2 methanation conditions (Feed = 5% CO_2/20% H_2/Ar) along with the corresponding C-species evolution of (a,c) $NiAl_{IWI}$ and (b, d) $NiAl_{GAI}$ catalysts.

carbonates at 1574 and 1330 cm^{-1} overlap with additional new ones at 1545 and 1380 cm^{-1}, which might be assigned to vibration of monodentate carbonates [151, 154].

This greater number of surface carbonates could be associated with the presence of non-reducible $Ni^{2+}O^{2-}$ or even $NiAl_2O_4$ able to adsorb CO_2 [104]. As the temperature increases, these bands disappear giving rise to clear and intense bands at 1595, 1395 and 1375 cm^{-1}, characteristic of 3 vibration modes of formates: asymmetric O-C-O stretching ($\nu(OCO)_a$), CH deformation ($\delta(CH)$) and symmetric OCO stretching ($\nu(OCO)_s$), respectively [52, 124, 153]. Complementary, the band corresponding to CH stretching ($\nu(CH)$) is observed at 2900 cm^{-1} (not shown), confirming the formation of formate

species. After that, new increasing bands appear at 3016 cm^{-1} ($\nu(CH)_a$) and 1305 cm^{-1} ($\delta_{(CH)}$), indicating the formation of methane gas [148]. Note that no bands were verified in the carbonyl region (2100-1800 cm^{-1}) but the characteristic bands of CO gas were observed at 2175 and 2105 cm^{-1}, suggesting that no detectable amount of CO_{ads} could have formed on Ni^0 by CO_2 disproportionation.

Analogously, Figure 4.15b displays FTIR spectra of $NiAl_{GAI}$ catalyst. As expected, the same bands and/or species were identified in the carbonate region but with different concentration. In fact, the bands corresponding to carbonates are less intense at the starting temperature (150 °C) probably due to the absence of NiO or $NiAl_2O_4$ acting as basic sites in the catalyst prepared by GAI method. Notably, unlike $NiAl_{IWI}$, $NiAl_{GAI}$ catalyst presents 3 bands in the carbonyl region (2100-1800 cm^{-1}) located at 2020, 1920 and 1860 cm^{-1}. The first is ascribed to the stretching vibration of terminally or linearly adsorbed CO on top single Ni atoms, whereas the other two can be attributed to weakly and strongly attached bridged carbonyls on neighboring Ni atoms, respectively [134, 136, 155]. Interestingly, the band corresponding to linearly adsorbed CO shifts with temperature, while the others remain at the same frequency. This shift is associated with changes in CO covering on Ni surface and suggests that these CO species participate in the CO_2 methanation mechanism. On the contrary, bridged carbonyls are more stable and may not react with hydrogen [134].

Furthermore, it is wide known that the ν(CO) frequency (in wavenumbers) is associated with the metallic dispersion: the higher the frequency, the higher the dispersion or the lower the Ni particle size. Thus, according to the 3 ν(CO) bands, $NiAl_{GAI}$ catalyst presents particles with different sizes indicative of highly, moderately and poorly dispersed Ni^0 [155]. This observation is consistent with TEM results, according to which a particle size distribution ranging from 3 to 20 nm is observed. Noteworthy, the lack of adsorbed carbonyls on the catalyst prepared by IWI suggests that there are differences in the Ni electronic state when comparing Al_2O_3 supported Ni catalysts. In the case of $NiAl_{IWI}$, it seems that Ni, after reduction pretreatment, is partially oxidized or positively charged ($Ni^{\delta+}$) due to the interaction with remaining non reducible Ni^{2+} species or with Al^{3+} cations exposed on the alumina surface. As the exposed Ni has

electron deficiency, $NiAl_{IWI}$ presents lower affinity to dissociate CO_2 by H-assistance or adsorb CO and, hence, no bands are detectable within 2100-2000 cm^{-1}. Although Ni^{2+} is also able to adsorb CO, no bands were observed among 2300 and 2100 cm^{-1} assignable to CO on Ni^{2+} sites. $NiAl_{GAI}$, by contrast, has much more affinity to CO adsorption since all nickel is in reduced state (Ni^0) after being calcined under reductive atmosphere (GAI synthesis route).

In order to better correlate the evolution of reaction intermediates, the relative concentration of main C-species was calculated at studied temperatures, as shown in the attached figures (Figures 4.15c and d). Note the semi-quantitative profiles were obtained from absorbance measurements and integration of the corresponding FTIR bands according to the presence (or not) of bands overlapping. In all cases, the highest value measured for each species was set arbitrarily to 1 and the rest of values were normalized to the range from 0 to 1 with the aim of obtaining a better comparison among evolutions of each C-species.

It can be observed that, in the case of $NiAl_{IWI}$ catalyst (Figure 4.15c), the relative concentration of bicarbonates decreases as that of formates increases, following a symmetric evolution (T < 250 °C). This suggests that formates mainly arise from bicarbonates although it cannot be excluded that, in minor extent, carbonates are also reduced into formates [153]. After that, from 250 °C to 325 °C, adsorbed bicarbonates disappear and the formation rate of formates slows down up to zero, i.e., its relative concentration reaches a maximum. This slowdown or depletion matches with methane appearance, whose relative concentration increases exponentially in agreement with activity results. Finally, at higher temperatures (T > 350 °C), the relative concentration of formates decreases, while that of methane slowly increases up to 425 °C approaching to the limited thermodynamic equilibrium of an exothermal reaction. Thus, it can be assumed that formates at the metal-support interface could participate in methane formation. However, it cannot be claimed that formates are directly hydrogenated following the associative mechanism, since not bands characteristic of methoxy species (reaction intermediates) or methanol have been detected by FTIR, as reported by Solis-García et al. [145]. Finally, the appearance of CO_{gas} from 300 °C

together with the absence of adsorbed carbonyls indicates that this by-product could be formed from decomposition of formates as follows:

$$HCOO_{(ads)} \rightarrow HCO_{(ads)} + O_{(ads)} \rightarrow CO_{(ads)} + OH_{(ads)} \rightarrow CO_{(gas)} + H_2O_{(gas)} \quad (4.3)$$

On the other hand, the corresponding species evolution of $NiAl_{GAl}$ sample is displayed in Figure 4.15d. Note that, in general, the relative concentration curves for adsorbed species follow the same trend but are clearly shifted towards lower temperatures. In fact, bicarbonates are depleted or transformed into formates faster (at 225 °C) and the maximum of formates concentration curve, which is also volcano-shaped, is clearly shifted 50 °C into the left (275 vs. 325 °C). Carbonyls relative concentration, in turn, increases with temperature up to 300 °C and then starts depleting. We suggest that carbonyls, which appear from 200 °C, might arise from formates decomposition (Equation 4.3) or, less probably, from CO_2 dissociative adsorption. Wang et al. [124] also studied CO_2 methanation by FTIR on a 5%Ru/Al_2O_3 catalyst and concluded that formates are reactive towards the formation of adsorbed CO when it is close to metal particles. From 225 °C, the linearly bonded and, in minor extent, weakly attached bridged carbonyls may be hydrogenated into methane, whereas the strongly attached bridged ones remain stable. From 300 °C, some of the bridged carbonyls could be desorbed as CO_{gas}, as revealed by bands at 2175 and 2105 cm^{-1}. Noteworthy, the general shift of adsorbed species evolution indicate that $NiAl_{GAl}$ catalyst has a greater capacity to dissociate H_2 and provide H, which is essential to carry out the successive steps of reaction mechanism. This leads to a higher activity at mild temperatures, as evidenced by the higher CH_4 relative concentration of $NiAl_{GAl}$ catalyst at 300 °C (0.59 vs. 0.48).

The FTIR spectra as well as evolution with temperature of adsorbed C-species over $RuAl_{GAl}$ and Ni-1.0RuAl catalyst are shown in and Figure 4.16. Note that CO_2 methanation FTIR spectra of $RuAl_{IWI}$ catalyst are not included, since proved to be very similar. Mainly, the same species as in the case of Ni catalysts are observed in carbonate region with similar evolution. However, the position and intensity of bands appearing at carbonyl region are different, i.e., the type and distribution of carbonyl

species are not the same. In fact, FTIR spectra of Ru/Al_2O_3 catalysts show a main band at 2015 cm^{-1} at 150 °C that can be attributed to vibration of linearly adsorbed CO over reduced Ru atoms (Ru-CO) [52, 125, 156]. This band is more intense to that observed for $NiAl_{GAI}$ catalyst, indicating that Ru has a major capacity or more affinity to adsorb CO than Ni. However, unlike $RuAl_{IWI}$ catalyst, $RuAl_{GAI}$ presents a shoulder at 1970 cm^{-1} (Figure 4.16a) related to stretching vibration of terminal CO species located at metal-support interface ((Al_2O_3)Ru-CO) [156].

Note that the main band on both Ru catalysts red shifts with temperature from 2015 to 1990 cm^{-1} due to a decrease in Ru surface coverage by CO, whereas the position of the shoulder observed for $RuAl_{GAI}$ catalyst does not shift and it vanishes

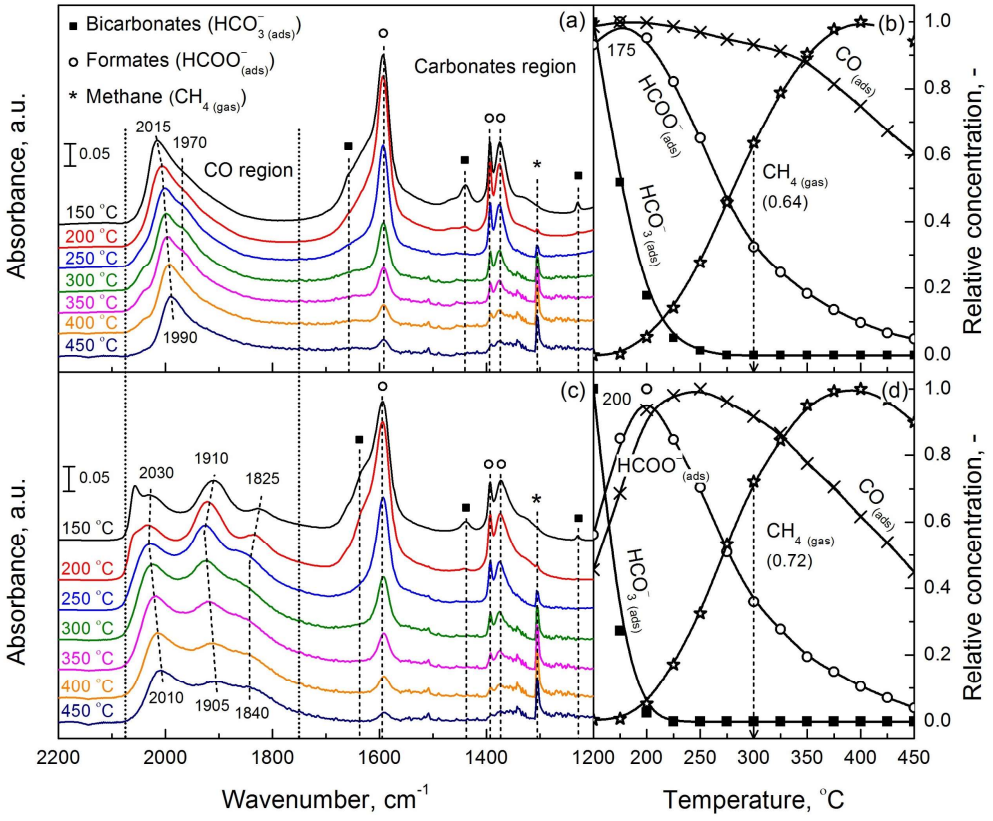

Figure 4.16. FTIR spectra recorded at different temperatures under CO_2 methanation conditions (Feed = 5% CO_2/ 20% H_2/Ar) along with the corresponding C-species evolution of (a,c) $RuAl_{GAI}$ and (b, d) Ni-1.0RuAl catalysts.

above 350 °C along with appearance of CO gas in the cell. Based on these observations, it can be concluded that on-top CO species participates in the reaction but the same cannot be stated for CO species adsorbed at the interface. It seems that this species may not participate in the reaction but eventually desorbed, indicating that $RuAl_{GAl}$ presents a higher fraction of inactive Ru atoms in agreement with the lower TOF/I_0 value obtained.

In the case of the bimetallic catalyst, it should be considered that bands appearing at 2100-1800 cm^{-1} region correspond to carbonyl species adsorbed on both Ni and Ru particles. Thus, what Figure 4.16b shows is a combination of bands previously observed for $NiAl_{GAl}$ and $RuAl_{GAl}$ catalysts, characteristic of above-mentioned CO species. The difference is that a new peak is observed at 2056 cm^{-1} attributed to geminal di-carbonyls on low coordinated Ru [124, 125, 156], which disappear above 250 °C. According to Panagiotopoulou et al. [157], this species disappears with temperature since it is converted into linearly adsorbed CO due to H_2-induced agglomeration of low coordination Ru sites into bigger Ru clusters. Noteworthy, the combination band at 2030 cm^{-1} corresponding to linearly adsorbed carbonyls is significantly more intense than on $NiAl_{GAl}$ catalyst, indicating that CO adsorption is promoted by the co-impregnation of 1% Ru. On the other hand, the band corresponding to weakly attached bridged carbonyls (at 1910 cm^{-1}) is clearly more intense compared to that observed on $NiAl_{GAl}$ catalyst, which confirms that the bimetallic catalyst presents a higher Ni dispersion (26.3 vs. 11.5% according to TEM results). As the temperature increases, bands at 2030 and 1910 cm^{-1} first blue shift up to 250 °C and then red shift to 2010 cm^{-1} and 1905 cm^{-1}, respectively. The red shift matches with the appearance of CH_4 band at 1305 cm^{-1}, suggesting that both species could be reaction intermediates.

Regarding to C-species evolutions of $RuAl_{GAl}$ and Ni-1.0RuAl catalysts (Figures 4.16c and d), it can be seen that they are quite similar (except to that of CO), observing a shift of curves towards lower temperatures with respect to those of monometallic Ni catalysts. The shift is due to an enhanced catalytic activity, as demonstrated by H_2-TPD runs. In fact, the bands corresponding to bicarbonate species vibration at 150 °C are much less intense than those observed for $NiAl_{GAl}$ catalyst in both cases, i.e.,

bicarbonates are more easily hydrogenated into formates. Likewise, formates reach maximum concentration value at lower temperatures: 175 and 200 °C, respectively. After that, formates at the interface are decomposed into carbonyls and, subsequently, part of carbonyls (most probably linear carbonyls) are hydrogenated into CH_4, which relative concentration at 300 °C is 0.64 (for $RuAl_{GAl}$) and 0.72 (for Ni-1.0RuAl).

Finally, it should be highlighted that $RuAl_{GAl}$ presents a considerable higher amount of potentially reactive carbonyls (linearly bonded) but a CH_4 yield similar to that of bimetallic Ni-1.0RuAl catalyst, as can be deduced by comparing its respective spectra and C-species evolution at different temperatures. This suggests that the fraction of carbonyls effectively converted into CH_4 is lower in the monometallic Ru catalyst. In fact, although Ni-1.0RuAl adsorbs less CO, it disposes of an enhanced dissociated hydrogen supply to reduce CO as a result of the Ni-Ru synergetic interaction. Based on these results, it can be concluded that an effective CH_4 formation not only depends on the type and number of adsorbed carbonyls but also on the availability of adjacent H atoms to carry out the C-O bond hydrogenation.

4.3.3. Reaction mechanism

To sum up, Figure 4.17 proposes and depicts the proposed reaction pathways on bimetallic Ni-1.0RuAl catalyst deduced from *operando* FTIR results shown in this section. Firstly, CO_2 is mainly adsorbed on hydroxyl groups (OH^-) of γ-Al_2O_3 to give monodentate bicarbonates (HCO_3^-), whereas H_2 is dissociated and adsorbed on metal surface. After that, dissociated H_2 (H atoms) spillovers and reacts with bicarbonates close to metal particles yielding bidentate formates ($HCOO^-$), which are considered potential reaction intermediates in alumina supported catalysts. Specifically, formates adsorbed at the interface are decomposed into hydroxyls (OH^-) on γ-Al_2O_3 support and carbonyls (CO), which, in the case of monometallic catalysts, are adsorbed either on Ni or Ru surface.

However, in the bimetallic system, CO is expected to preferentially adsorb over Ru nanoparticles due to a higher affinity, whereas H_2 is adsorbed on neighboring Ni particles acting as H atoms reservoir. Then, carbonyls are reduced by adjacent H atoms

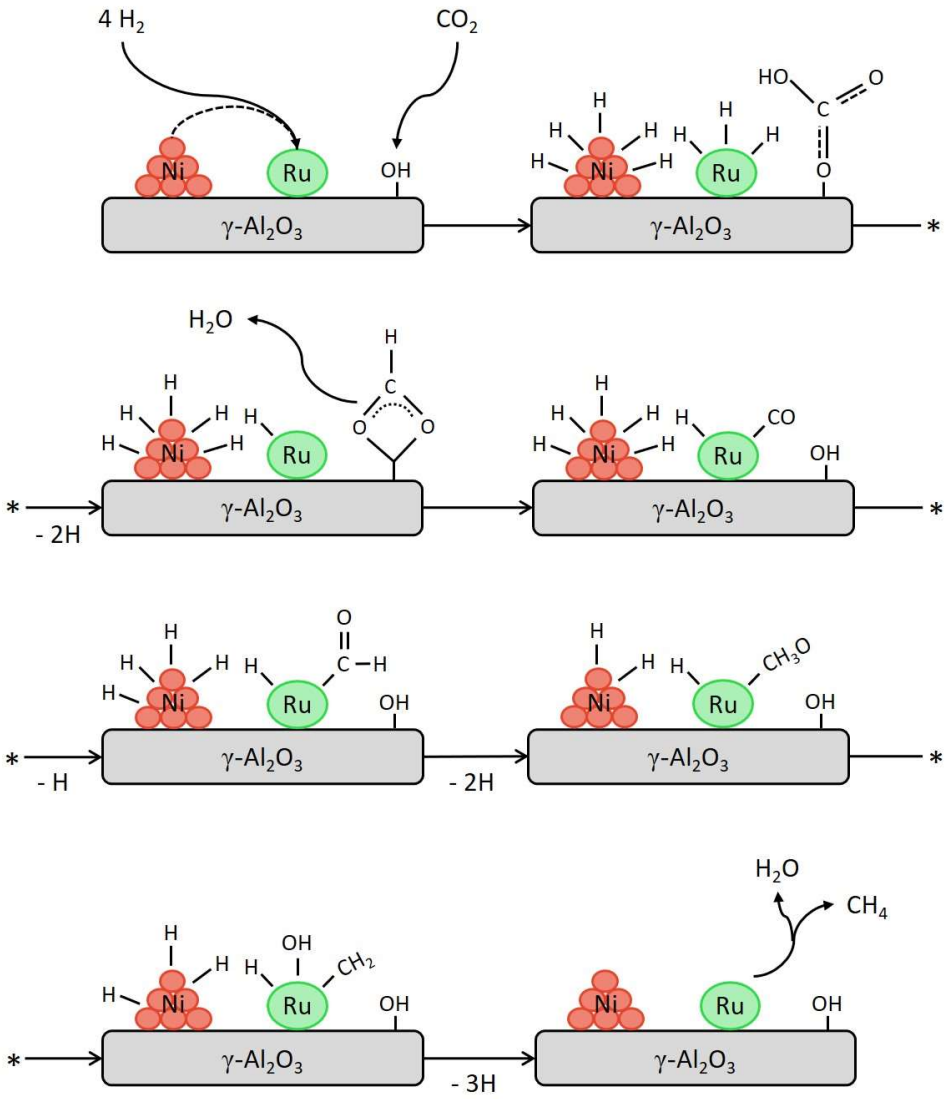

Figure 4.17. CO_2 methanation reaction pathway proposed on Ni-1.0RuAl catalyst.

into formyl (COH, not observed), which are subsequently hydrogenated into CH_XO species (hydroxycarbene (CH_2O) or hydroxymethyl (CH_2OH)). At certain hydrogenation degree (x = 1-3), the CO bond cleavage of CH_xO species occurs (rate determining step), finally releasing CH_4 and H_2 molecules [52, 127, 158].

4.4. OVERALL VIEW AND CONCLUSIONS

In this work, the low temperature activity of Ni/Al_2O_3 formulation is systematically improved through the use of efficient synthesis procedure (GAI vs. IWI) and the addition of Ru. Overall, catalysts prepared by GAI method presented better catalytic performance than those prepared by IWI. In the case of Ni catalysts, the formation of Ni^{2+} strongly interacting with the support was avoided by GAI synthesis route, resulting in a higher Ni surface area available for the reaction. Instead, GAI method led to a notable increase in the metal dispersion on $RuAl_{GAI}$ catalyst due to the glycerol enclosing effect but, in return, the specific activity (TOF/I_0) of Ru nanoparticles resulted to be two order of magnitude lower since reaction is structure sensitive. On the other hand, the activity of Ni/Al_2O_3 was improved even more by co-impregnation of small amounts of Ru as a result of a synergistic combination. In fact, the bimetallic Ni-1.0RuAl catalyst showed remarkably higher Ni dispersion, reducibility, and CO adsorption capacity than $NiAl_{GAI}$ catalyst, observing a methane yield equal to that of $3RuAl_{GAI}$. *Operando* FTIR experiments revealed that CO_2 methanation over alumina-supported Ni and Ru catalysts proceeds via formation of carbonyl species mainly arising from intermediate formates decomposition, followed by its hydrogenation into CH_4. In the bimetallic system, the potentially most reactive species is CO linearly adsorbed over Ru, which is more easily hydrogenated by H atoms supplied from adjacent Ni particles. We conclude that the enhanced CO_2 methanation activity of bimetallic catalyst is not only due to a promoted CO adsorption but also to a higher supply of dissociated H_2.

Chapter 5

KINETICS OF CO_2 METHANATION OVER Ni/Al_2O_3 CATALYST

ABSTRACT

In this chapter, kinetics of CO_2 methanation reaction *on Ni/Al_2O_3 catalyst with low Ni content (10 wt%) is studied. Once the catalyst activity is stabilized, the influence of temperature, total and partial pressure as well as space time are analysed under differential and integral reactor conditions. On the one hand, the data obtained at 325 °C adjust with statistical significance to a power-law model with H_2O inhibition, observing apparent orders and water adsorption constant of 0.24 (CO_2), 0.27 (H_2) and 3.1 atm^{-1}, respectively. On the other hand, the apparent activation energy, calculated by initial reaction rate approach, proved to be 80.1 $kJ \cdot mol^{-1}$. Furthermore, various LHHW-type models are deduced based on mechanistic routes in which CO_2 is dissociatively or molecularly adsorbed (dissociative and H-assisted CO formation mechanisms). Among them, the reaction pathway that considers the formate species decomposition into carbonyls via H-assisted CO formation mechanism and further carbonyls hydrogenation into CHO as rate determining step, presents the best fit of the kinetic data with a mean deviation of 7.0%. This value is significantly lower than that commonly employed to describe the kinetics of Ni-Al formulations with high Ni contents (σ^2 = 20.1%) based on dissociative CO formation. Thus, this works confirms that carbonyls as well as formate species participate in CO_2 methanation mechanism and kinetics on lowly-loaded Ni/Al_2O_3 catalyst.*

5. KINETICS OF CO_2 METHANATION OVER Ni/Al_2O_3 CATALYST

Research works about methanation reaction have been carried out since the beginning of 20th century, after the first publication by Sabatier and Senderens [159]. This reaction awakened great interest in the decades of the 70s and 80s with the problematic oil shortage of that period. As a solution, CO methanation was integrated in coal gasification systems in order to convert 'town gas' or syngas ($CO + H_2$) into natural gas. Accordingly, plenty of studies regarding CO methanation kinetics were published [160-162] and, in turn, the process was settled in industry [163]. However, as CO_2 methanation was not of interest in that period, only few works concerning its intrinsic kinetics were available. Among others, the most outstanding was that presented by Weatherbee and Bartholomew [164] who studied kinetics on $3\%Ni/SiO_2$ catalyst at highly diluted gas streams and reported the first detailed mechanistic model. Nonetheless, CO_2 methanation has been in the spotlight since the beginning of 21st century due to its potential role in mitigating climate change, in storing the renewable surplus power as energy vector and in low-carbon fuel synthesis [163].

Although many formulations have been extensively characterized and catalytically tested, there is still controversy with regard to reaction mechanism and kinetics. On the one hand, remember that two widely accepted mechanisms have been proposed from IR characterization techniques: the so-called dissociative and associative mechanisms [130, 145, 148, 165-167]. The former assumes the dissociative adsorption of CO_2 into carbonyl followed by its hydrogenation into CH_4 [148, 166]. In the latter, by contrast, CO_2 is molecularly adsorbed in form of carbonates, which are progressively reduced into formate, methoxy species and, finally, methane [145, 167]. As discussed in the previous chapter, the CO_2 methanation on alumina supported Ni and Ru catalysts seems to take place via the dissociative rather than by associative mechanism, since carbon monoxide was observed as byproduct instead of methanol in output gas stream (the latter formed from methoxy species). Nevertheless, the formation of considerable amount of formate species along with their evolution with temperature suggested that they could participate in the reaction, specifically in CO formation. Note that these FTIR

results could be of great help when proposing kinetic models that could fit the kinetic data and define the rate determining step (RDS).

On the other hand, it is worth mentioning that only few works in recent literature report on the kinetics of CO_2 methanation on Ni-based [112, 158, 168-173] and Ru-based [113, 124, 174] formulations. Among them, commercial or co-precipitated NiAl type catalyst with only high metal content (> 15% of Ni) has been the most studied since it is the most used in industry for methanation processes [112, 158, 168-170]. However, not only the type of support and the presence of a secondary metal or promoter could alter the kinetics of a catalyst (rate equations) but also the active metal content. Therefore, the main objective of the research work presented in this chapter is to determine a kinetic model able to predict kinetics of CO_2 methanation on a Ni/Al_2O_3 catalyst with low metal content (10 wt% of Ni) under relevant conditions. The secondary objective shall be to establish a connection between the FTIR mechanistic study shown in the previous chapter and reaction kinetics.

In order to achieve these targets, first, the basic physico-chemical properties of the catalyst were determined as well as adsorbed species analyzed by operando FTIR. Then, the activity of the catalyst was evaluated at different temperatures once its activity was stabilized at a temperature far from equilibrium. Finally, kinetic experiments were carried out under differential as well as whole reactor conditions and a discrimination among various power law or LHHW type models based on previous FTIR results was realized.

5.1. CATALYST PREPARATION AND CHARACTERIZATION

A new batch of $10\%Ni/Al_2O_3$ catalyst was prepared by the same way described in chapter 2 (IWI method, section 2.2.1), unlike calcination was performed in air at 600 °C for 6h. As a result, a Ni/Al_2O_3 catalyst with Ni real content of 9.4% was obtained, which was named 10NiAl. Its specific surface area resulted in 172 $m^2\ g^{-1}$, high enough to ensure a proper reagent-active sites contact and, as expected, the reducibility of the sample at 500 °C (determined by H_2-TPR, not shown) proved to be low, since it presents a considerable amount of NiO highly interacting with Al_2O_3 or even $NiAl_2O_4$ formed

during calcination in air. Although this indicates that much of nickel will not be active during reaction (i.e., in the reduced state (Ni^0)), the observed high-metal interaction suggests that its activity should be quite stable during the kinetic experiments. Hence, physico-chemical properties of 10NiAl catalyst were considered adequate to follow with the present kinetic study.

Then, in order to determine the adsorbed species that could participate in reaction and get a first insight on the reaction pathway, CO_2 methanation was studied on 10NiAl catalyst by *operando* FTIR. Spectra recorded under CO_2 methanation conditions at different temperatures are shown in Figure 5.1.

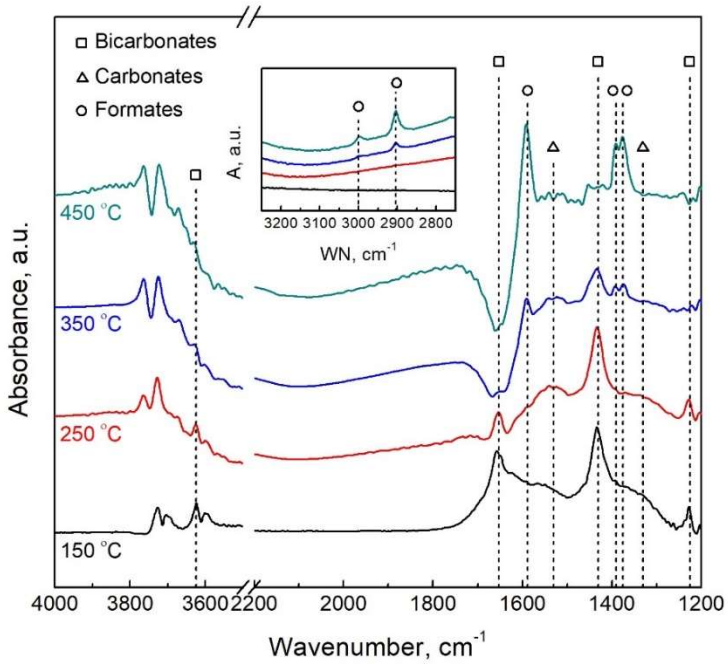

Figure 5.1. *Operando* FTIR spectra recorded under 16% CO_2/ 64% H_2/He reaction stream at 150, 250, 350 and 450 °C for 10NiAl catalyst.

Note that all spectra were recorded after 30 min exposure time (steady state conditions). On the one hand, an intense double band at 2350 cm^{-1} (not shown) together with another two double bands located at 3750-3500 cm^{-1} confirm the

presence of CO_2 gas in the cell. On the other hand, the bands appearing between 1800 and 1200 cm^{-1} indicate the formation of adsorbed C-species on the catalyst surface during reaction, which relative concentration changes with temperature. Three bands are clearly distinguishable at 1652, 1430 and 1225 cm^{-1} at 150 °C, which have been always observed on alumina-supported catalysts throughout this thesis and are attributed to O-C-O stretching (ν(OCO)) and OH deformation (δ_{OH}) of bicarbonate species. Remember that bicarbonates arise from CO_2 adsorption on OH^- groups of γ-Al_2O_3 [124, 145, 167]. Additionally, other weak and broad bands can be observed at 1530 and 1330 cm^{-1}, which might be assigned to ν(OCO) vibration modes of carbonate species in bidentate coordination adsorbed on surface O^{2-} (acting as Lewis basic sites) of both NiO and Al_2O_3 [150, 151].

The increase of temperature leads to the depletion of bicarbonates/carbonates and the appearance of new bands at 1588 (asymmetric O-C-O stretching), 1390 (CH deformation) and 1375 cm^{-1} (symmetric O-C-O stretching) which are characteristics of formate species adsorbed on Al_2O_3 [124]. Besides, the weak bands at around 3000 and 2900 cm^{-1} (ν(CH)) confirm the presence of this species, which could be reaction intermediates [145, 167]. As in the case of $NiAl_{IWI}$ and $NiAl_{GAl}$ catalysts (Chapter 4), the evolution of bands with temperature suggests that formates might come either from nickel-assisted hydrogenation of bicarbonates or carbonates through H spillover mechanism. In fact, the isolated band corresponding to OH stretching vibration mode of bicarbonates (band at 3625 cm^{-1}) clearly decreases as those of ν(CH) of formates increases. Besides, note that the three bands of formates are clearly observed at 450 °C indicating that these species are quite stable with temperature. However, no characteristic bands of methane are observed to verify the participation of formate in the reaction. Likewise, no bands assignable to adsorbed carbonyls are observed in 2200-1800 cm^{-1} region. The absence of such bands indicates: (i) carbonyls are not formed or (ii) their concentration is so low that are not detectable by FTIR.

Thus, the FTIR results show us some surface species on 10NiAl catalyst that will form during reaction, but not clarify which participate in the reaction or what the reaction mechanism is. Anyway, the presence of bicarbonates and then formates

suggests that CH_4 may be formed though similar reaction mechanism deduced in previous chapter.

5.2. CATALYST ACTIVITY AND STABILITY

Prior to the stability test, the activity of $10\%Ni/Al_2O_3$ catalyst was tested varying the temperature from 250 to 500 °C. Figure 5.2a shows the light-off curve, whereas Figure 5.2b depicts selectivity to CH_4 and CO as a function of temperature.

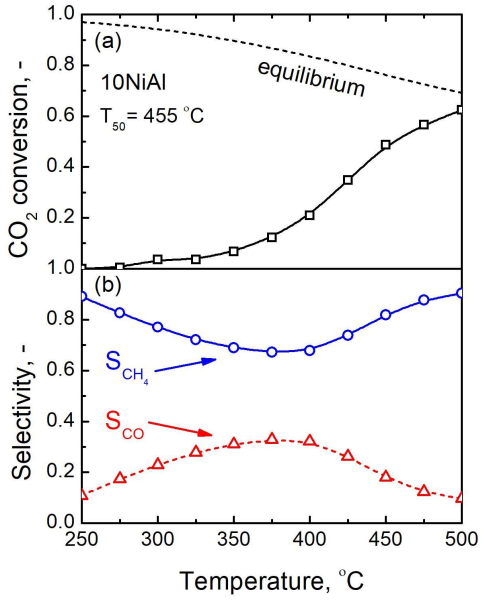

Figure 5.2. (a) Light-off and (b) CH_4/CO selectivity plots of 10NiAl catalyst.

The Ni-based catalyst shows poor activity, being its conversion 0.21 at 400 °C and presenting a T_{50} of 455 °C. Besides, is quite selective into non-desirable CO: S_{CO} is higher than 0.1 in the entire temperature range observing a maximum value of 0.33 at 375 °C. The expected low activity and CH_4 selectivity of this catalyst is related to its high metal-support interaction. As above mentioned, the reducibility of this catalyst at 500 °C (reduction temperature) is around 10% indicating that only a small fraction of Ni has been activated during the one-hour reduction with $20\%H_2/N_2$ and resulting in a low CO_2 hydrogenation activity.

After that, the reaction temperature was kept at 400 °C and the sample exposed to the same feed (250 mL min^{-1} of 16% CO_2/64% H_2/ N_2) for few days in order to stabilize its activity. The evolution of CO_2 conversion and selectivity with time-on-stream (*TOS*) is shown in Figure 5.3. Note that by increasing *TOS* up to 72 h approximately, the CO_2 slowly rises from 0.31 to 0.36, i.e., the catalyst is activated. This trend is similar to that observed on 12%Ni/Al_2O_3 catalyst in Chapter 3 (see Figure 3.13) and is because part of remaining NiO is being reduced leading to a higher active metal surface. Likewise, the selectivity to CH_4 increases from 0.83 to 0.87 since the catalyst has a major capacity to dissociate H_2 and convert CO_2 exclusively into CH_4 (Figure 5.3b).

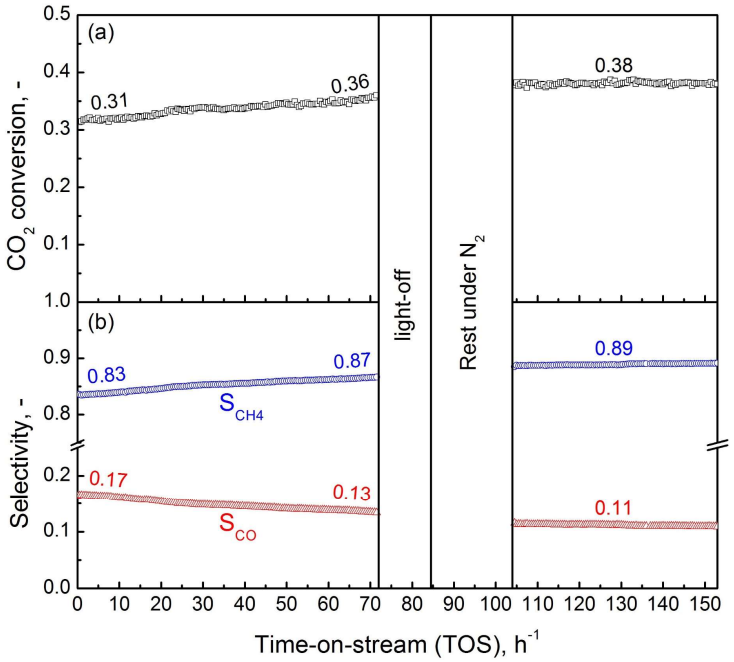

Figure 5.3. Evolution of (a) CO_2 conversion and (b) CH_4/CO selectivity with *TOS* on 10NiAl catalyst at 400 °C and atmospheric pressure.

Immediately after 3 days on stream, the sample was exposed again to temperature changes under reaction mixture (intermediate ligth-off) in order to accelerate activation and further stabilization by reduction of additional NiO sites. Although CO_2 conversion only increased from 0.36 to 0.38, this appeared to be enough

to completely stabilize the activity of the catalyst. In fact, no relevant changes were observed in X_{CO_2} (0.38) and S_{CH_4} (0.89) during last 48h-on-stream, indicating that reduced Ni particles did not suffer from sintering or any other deactivation mechanism.

5.3. DESIGN OF KINETIC EXPERIMENTS

Once activity of 10NiAl catalyst was stabilized (section 4.2), kinetic measurements were carried out over a wide range of operating conditions, i.e., within the following temperature, absolute pressure, total flow rate, H_2/CO_2 feed ratio as well as space-time (W/F_{A0}) ranges: 315 – 430 °C, 2 – 6 bar, 200 – 1100 mL min^{-1}, 2 – 10 and 1.6 – 24.9 g h mol^{-1}. This allowed us to study the effect of temperature, contact time and partial pressure of reagents/products on reaction rate to further estimate kinetic parameters. During parameter variation, the possible activity loss of 10NiAl catalyst was monitored at reference reaction conditions (T = 400 °C and P = 2 atm) before and after series of kinetic measurements recorded at 430 °C. The design of kinetic experiments along with corresponding experimental activity parameters is shown in Table 5.1:

Table 5.1. Design of kinetic experiments and activity parameters.

Exp.[a] #	P (bar)	T (°C)	Q^{in} (mL min^{-1})	W/F_{A0} (g h mol^{-1})	ε_A[b]	$p^{in}_{CO_2}$ (bar)	h[c]	m[d]	v[e]	X_{CO_2} [f]	Y_{CH_4} [g]
1.1	2	325	500	24.89	-0.06	0.06	16	0	0	0.208	0.195
1.2	2	325	500	15.56	-0.10	0.10	10	0	0	0.143	0.133
1.3	2	325	500	12.44	-0.12	0.12	8	0	0	0.123	0.112
1.4	2	325	500	6.22	-0.24	0.24	4	0	0	0.074	0.064
1.5	2	325	500	4.67	-0.32	0.32	3	0	0	0.059	0.050
1.6	2	325	500	3.11	-0.48	0.48	2	0	0	0.044	0.036
2.1	2	325	500	12.44	-0.12	0.12	1	0	0	0.069	0.048
2.2	2	325	500	12.44	-0.12	0.12	2	0	0	0.085	0.067
2.3	2	325	500	12.44	-0.12	0.12	3	0	0	0.094	0.079
2.4	2	325	500	12.44	-0.12	0.12	4	0	0	0.103	0.088
2.5	2	325	500	12.44	-0.12	0.12	5	0	0	0.107	0.094
2.6	2	325	500	12.44	-0.12	0.12	6	0	0	0.110	0.098

Table 5.1. Design of kinetic experiments and activity parameters.

Exp.[a] #	P (bar)	T (°C)	Q^{in} (mL min^{-1})	W/F_{A0} (g h mol^{-1})	ε_A[b]	$p^{in}_{CO_2}$ (bar)	h[c]	m[d]	v[e]	X_{CO_2}[f]	Y_{CH_4}[g]
3.1	2	325	500	9.33	-0.16	0.16	4	0.35	0	0.067	0.056
3.2	2	325	500	9.33	-0.16	0.16	4	0.7	0	0.057	0.046
3.3	2	325	500	9.33	-0.16	0.16	4	1.05	0	0.060	0.049
3.4	2	325	500	9.33	-0.16	0.16	4	1.7	0	0.055	0.043
3.5	2	325	500	9.33	-0.16	0.16	4	2.05	0	0.048	0.036
4.1	2	325	500	9.33	-0.16	0.16	4	0	0.25	0.074	0.063
4.2	2	325	500	9.33	-0.16	0.16	4	0	1.25	0.039	0.030
4.3	2	325	500	9.33	-0.16	0.16	4	0	1.75	0.039	0.030
4.4	2	325	500	9.33	-0.16	0.16	4	0	2.25	0.036	0.027
4.5	2	325	500	9.33	-0.16	0.16	4	0	3.00	0.032	0.024
4.6	2	325	500	9.33	-0.16	0.16	4	0	3.75	0.028	0.021
5.1	2	325	250	9.33	-0.32	0.32	4	0	0	0.101	0.090
5.2	2	325	300	9.33	-0.27	0.27	4	0	0	0.096	0.084
5.3	2	325	400	9.33	-0.20	0.20	4	0	0	0.088	0.076
5.4	2	325	500	9.33	-0.16	0.16	4	0	0	0.083	0.070
5.5	2	325	750	9.33	-0.11	0.11	4	0	0	0.076	0.061
5.6	2	325	1000	9.33	-0.08	0.08	4	0	0	0.079	0.059
6.1	2	315	1100	3.39	-0.20	0.20	4	0	0	0.032	0.026
6.2	2	315	1000	3.73	-0.20	0.20	4	0	0	0.035	0.028
6.3	2	315	800	4.67	-0.20	0.20	4	0	0	0.040	0.033
6.4	2	315	600	6.22	-0.20	0.20	4	0	0	0.048	0.040
6.5	2	315	400	9.33	-0.20	0.20	4	0	0	0.065	0.058
6.6	2	315	200	18.67	-0.20	0.20	4	0	0	0.105	0.097
7.1	2	335	1100	3.39	-0.20	0.20	4	0	0	0.054	0.043
7.2	2	335	1000	3.73	-0.20	0.20	4	0	0	0.058	0.047
7.3	2	335	800	4.67	-0.20	0.20	4	0	0	0.067	0.054
7.4	2	335	600	6.22	-0.20	0.20	4	0	0	0.078	0.066
7.5	2	335	400	9.33	-0.20	0.20	4	0	0	0.105	0.092
7.6	2	335	200	18.67	-0.20	0.20	4	0	0	0.165	0.152

Table 5.1. Design of kinetic experiments and activity parameters.

Exp.[a] #	*P* (bar)	*T* (°C)	Q^{in} (mL min^{-1})	W/F_{A0} (g h mol^{-1})	ε_A[b]	$p^{in}_{CO_2}$ (bar)	h[c]	m[d]	v[e]	X_{CO_2}[f]	Y_{CH_4}[g]
8.1	2	350	1100	3.39	-0.20	0.20	4	0	0	0.078	0.062
8.2	2	350	1000	3.73	-0.20	0.20	4	0	0	0.083	0.067
8.3	2	350	800	4.67	-0.20	0.20	4	0	0	0.095	0.077
8.4	2	350	600	6.22	-0.20	0.20	4	0	0	0.112	0.093
8.5	2	350	400	9.33	-0.20	0.20	4	0	0	0.148	0.130
8.6	2	350	200	18.67	-0.20	0.20	4	0	0	0.228	0.210
9.1	2	355	1100	3.39	-0.20	0.20	4	0	0	0.088	0.070
9.2	2	355	1000	3.73	-0.20	0.20	4	0	0	0.093	0.074
9.3	2	355	800	4.67	-0.20	0.20	4	0	0	0.106	0.085
9.4	2	355	600	6.22	-0.20	0.20	4	0	0	0.126	0.105
9.5	2	355	400	9.33	-0.20	0.20	4	0	0	0.166	0.145
9.6	2	355	200	18.67	-0.20	0.20	4	0	0	0.254	0.234
10.1	2	370	1100	3.39	-0.20	0.20	4	0	0	0.108	0.078
10.2	2	370	1000	3.73	-0.20	0.20	4	0	0	0.114	0.083
10.3	2	370	800	4.67	-0.20	0.20	4	0	0	0.128	0.094
10.4	2	370	600	6.22	-0.20	0.20	4	0	0	0.150	0.116
10.5	2	370	400	9.33	-0.20	0.20	4	0	0	0.192	0.159
10.6	2	370	200	18.67	-0.20	0.20	4	0	0	0.282	0.251
11.1	2	390	1100	3.39	-0.20	0.20	4	0	0	0.160	0.114
11.2	2	390	1000	3.73	-0.20	0.20	4	0	0	0.168	0.121
11.3	2	390	800	4.67	-0.20	0.20	4	0	0	0.186	0.135
11.4	2	390	600	6.22	-0.20	0.20	4	0	0	0.218	0.166
11.5	2	390	400	9.33	-0.20	0.20	4	0	0	0.275	0.225
11.6	2	390	200	18.67	-0.20	0.20	4	0	0	0.381	0.340
12.1	2	410	1100	3.39	-0.20	0.20	4	0	0	0.227	0.159
12.2	2	410	1000	3.73	-0.20	0.20	4	0	0	0.237	0.167
12.3	2	410	800	4.67	-0.20	0.20	4	0	0	0.260	0.186
12.4	2	410	600	6.22	-0.20	0.20	4	0	0	0.298	0.225
12.5	2	410	400	9.33	-0.20	0.20	4	0	0	0.366	0.300

Table 5.1. Design of kinetic experiments and activity parameters.

Exp.[a] #	P (bar)	T (°C)	Q^{in} (mL min^{-1})	W/F_{A0} (g h mol^{-1})	ε_A[b]	$p^{in}_{CO_2}$ (bar)	h[c]	m[d]	v[e]	X_{CO_2}[f]	Y_{CH_4}[g]
12.6	2	410	200	18.67	-0.20	0.20	4	0	0	0.480	0.436
13.1	2	430	1100	3.39	-0.20	0.20	4	0	0	0.306	0.213
13.2	2	430	1000	3.73	-0.20	0.20	4	0	0	0.317	0.222
13.3	2	430	800	4.67	-0.20	0.20	4	0	0	0.347	0.248
13.4	2	430	600	6.22	-0.20	0.20	4	0	0	0.389	0.297
13.5	2	430	400	9.33	-0.20	0.20	4	0	0	0.454	0.381
13.6	2	430	200	18.67	-0.20	0.20	4	0	0	0.556	0.516
14.1	4	430	1000	3.73	-0.20	0.40	4	0	0	0.385	0.327
14.2	4	430	800	4.67	-0.20	0.40	4	0	0	0.430	0.379
14.3	4	430	600	6.22	-0.20	0.40	4	0	0	0.493	0.451
14.4	4	430	400	9.33	-0.20	0.40	4	0	0	0.582	0.553
14.5	4	430	300	12.44	-0.20	0.40	4	0	0	0.638	0.617
14.6	4	430	200	18.67	-0.20	0.40	4	0	0	0.687	0.673
15.1	6	430	1000	3.73	-0.20	0.60	4	0	0	0.414	0.373
15.2	6	430	800	4.67	-0.20	0.60	4	0	0	0.469	0.434
15.3	6	430	600	6.22	-0.20	0.60	4	0	0	0.548	0.520
15.4	6	430	400	9.33	-0.20	0.60	4	0	0	0.643	0.625
15.5	6	430	300	12.44	-0.20	0.60	4	0	0	0.693	0.680
15.6	6	430	200	18.67	-0.20	0.60	4	0	0	0.729	0.720
16.1	2	430	500	24.89	-0.06	0.06	16	0	0	0.914	0.899
16.2	2	430	500	18.67	-0.08	0.08	12	0	0	0.827	0.800
16.3	2	430	500	15.56	-0.10	0.10	10	0	0	0.758	0.722
16.4	2	430	500	12.44	-0.12	0.12	8	0	0	0.678	0.635
16.5	2	430	500	6.22	-0.24	0.24	4	0	0	0.446	0.382
16.6	2	430	500	4.67	-0.32	0.32	3	0	0	0.370	0.300
17.1	2	430	500	12.44	-0.12	0.12	1	0	0	0.201	0.104
17.2	2	430	500	12.44	-0.12	0.12	2	0	0	0.310	0.217
17.3	2	430	500	12.44	-0.12	0.12	3	0	0	0.400	0.315
17.4	2	430	500	12.44	-0.12	0.12	4	0	0	0.475	0.399

Table 5.1. Design of kinetic experiments and activity parameters.

Exp.[a] #	*P* (bar)	*T* (°C)	Q^{in} (mL min^{-1})	W/F_{A0} (g h mol^{-1})	ε_A[b]	$p^{in}_{CO_2}$ (bar)	h[c]	m[d]	v[e]	X_{CO_2}[f]	Y_{CH_4}[g]
17.5	2	430	500	12.44	-0.12	0.12	5	0	0	0.536	0.468
17.6	2	430	500	12.44	-0.12	0.12	6	0	0	0.583	0.523
18.1	2	430	500	9.33	-0.16	0.16	4	0.35	0	0.463	0.394
18.2	2	430	500	9.33	-0.16	0.16	4	0.70	0	0.452	0.380
18.3	2	430	500	9.33	-0.16	0.16	4	1.05	0	0.446	0.373
18.4	2	430	500	9.33	-0.16	0.16	4	1.70	0	0.430	0.353
18.5	2	430	500	9.33	-0.16	0.16	4	2.05	0	0.424	0.347
18.6	2	430	500	9.33	-0.16	0.16	4	0	0.25	0.431	0.363
19.1	2	430	500	9.33	-0.16	0.16	4	0	0.75	0.377	0.312
19.2	2	430	500	9.33	-0.16	0.16	4	0	1.25	0.329	0.269
19.3	2	430	500	9.33	-0.16	0.16	4	0	1.75	0.290	0.234
19.4	2	430	500	9.33	-0.16	0.16	4	0	2.25	0.259	0.206
19.5	2	430	500	9.33	-0.16	0.16	4	0	3.00	0.209	0.162
19.6	2	430	500	9.33	-0.16	0.16	4	0	3.75	0.178	0.135
20.1	2	430	900	7.47	-0.11	0.11	8	0	0	0.548	0.485
20.2	2	430	810	8.30	-0.11	0.11	8	0	0	0.560	0.502
20.3	2	430	720	9.33	-0.11	0.11	8	0	0	0.593	0.537
20.4	2	430	630	10.67	-0.11	0.11	8	0	0	0.629	0.579
20.5	2	430	540	12.44	-0.11	0.11	8	0	0	0.674	0.630
20.6	2	430	450	14.93	-0.11	0.11	8	0	0	0.720	0.685
21.1	4	430	900	7.47	-0.11	0.22	8	0	0	0.625	0.593
21.2	4	430	810	8.30	-0.11	0.22	8	0	0	0.663	0.634
21.3	4	430	720	9.33	-0.11	0.22	8	0	0	0.698	0.672
21.4	4	430	630	10.67	-0.11	0.22	8	0	0	0.742	0.720
21.5	4	430	540	12.44	-0.11	0.22	8	0	0	0.780	0.761
21.6	4	430	450	14.93	-0.11	0.22	8	0	0	0.839	0.826
22.1	6	430	900	7.47	-0.11	0.33	8	0	0	0.686	0.664
22.2	6	430	810	8.30	-0.11	0.33	8	0	0	0.726	0.708
22.3	6	430	720	9.33	-0.11	0.33	8	0	0	0.767	0.751

Table 5.1. Design of kinetic experiments and activity parameters.

Exp.[a] #	P (bar)	T (°C)	Q^{in} (mL min^{-1})	W/F_{A0} (g h mol^{-1})	ε_A[b]	$p^{in}_{CO_2}$ (bar)	h[c]	m[d]	v[e]	X_{CO_2}[f]	Y_{CH_4}[g]
22.4	6	430	630	10.67	-0.11	0.33	8	0	0	0.812	0.799
22.5	6	430	540	12.44	-0.11	0.33	8	0	0	0.857	0.846
22.6	6	430	450	14.93	-0.11	0.33	8	0	0	0.904	0.897
23.1	6	430	500	24.89	-0.06	0.18	16	0	0	0.970	0.969
23.2	6	430	500	18.67	-0.08	0.24	12	0	0	0.923	0.918
23.3	6	430	500	15.56	-0.10	0.29	10	0	0	0.877	0.869
23.4	6	430	500	12.44	-0.12	0.36	8	0	0	0.809	0.798
23.5	6	430	500	6.22	-0.24	0.72	4	0	0	0.544	0.522
23.6	6	430	500	4.67	-0.32	0.96	3	0	0	0.444	0.418
24.1	6	430	500	12.44	-0.12	0.36	1	0	0	0.204	0.167
24.2	6	430	500	12.44	-0.12	0.36	2	0	0	0.362	0.330
24.3	6	430	500	12.44	-0.12	0.36	3	0	0	0.493	0.465
24.4	6	430	500	12.44	-0.12	0.36	4	0	0	0.596	0.571
24.5	6	430	500	12.44	-0.12	0.36	5	0	0	0.676	0.654
24.6	6	430	500	12.44	-0.12	0.36	6	0	0	0.733	0.715
25.1	6	430	500	9.33	-0.16	0.48	4	0	0.25	0.531	0.502
25.2	6	430	500	9.33	-0.16	0.48	4	0	0.75	0.467	0.436
25.3	6	430	500	9.33	-0.16	0.48	4	0	1.25	0.426	0.396
25.4	6	430	500	9.33	-0.16	0.48	4	0	1.75	0.393	0.363
25.5	6	430	500	9.33	-0.16	0.48	4	0	2.25	0.378	0.348
26.1	6	430	500	9.33	-0.16	0.48	4	0.35	0	0.574	0.551
26.2	6	430	500	9.33	-0.16	0.48	4	0.70	0	0.559	0.535
26.3	6	430	500	9.33	-0.16	0.48	4	1.05	0	0.553	0.529
26.4	6	430	500	9.33	-0.16	0.48	4	1.65	0	0.551	0.526
26.5	6	430	500	9.33	-0.16	0.48	4	2.05	0	0.547	0.521

[a]Experiment x.y code (x = dataset number and y = experiment number).

[b]Molar volume change parameter. $\varepsilon_A = -2y^{in}_{CO_2}$.

[c]H_2/CO_2, [d]CH_4/CO_2 and [e]H_2O/CO_2 molar feed ratios.

[f]Calculated by Equation 2.12.

[g]Determined by Equation 2.15.

The partial pressure of reagents (p_{CO_2} and p_{H_2}) and products (p_{CH_4}, p_{H_2O} and p_{CO}) at reactor outlet as a function of parameters defined in Table 5.1 can be calculated from the following expressions:

$$P_{CO_2}^{out} = P_{CO_2}^{in} \frac{1 - Y_{CH_4} - Y_{CO}}{1 + \varepsilon_A Y_{CH_4}} \tag{5.1}$$

$$P_{H_2}^{out} = P_{CO_2}^{in} \frac{h - 4Y_{CH_4} - Y_{CO}}{1 + \varepsilon_A Y_{CH_4}} \tag{5.2}$$

$$P_{CH_4}^{out} = P_{CO_2}^{in} \frac{m + Y_{CH_4}}{1 + \varepsilon_A Y_{CH_4}} \tag{5.3}$$

$$P_{H_2O}^{out} = P_{CO_2}^{in} \frac{v + 2Y_{CH_4} + Y_{CO}}{1 + \varepsilon_A Y_{CH_4}} \tag{5.4}$$

$$P_{CO}^{out} = P_{CO_2}^{in} \frac{Y_{CO}}{1 + \varepsilon_A Y_{CH_4}} \tag{5.5}$$

which are deduced considering that CH_4 (Y_{CH_4}) and CO ($Y_{CO} = X_{CO_2} - Y_{CH_4}$) yields follow the stoichiometry of CO_2 methanation ($CO_2 + 4H_2 \rightarrow CH_4 + 2H_2O$) and reverse water gas shift ($CO_2 + H_2 \rightarrow CO + H_2O$) reactions, respectively.

5.4. KINETIC MODEL AND PARAMETER ESTIMATION

Determining a kinetic model or rate equation consists basically of calculating the kinetic constants and reaction orders. These parameters can be calculated by different computational methods, including linear and non-linear regression. Nevertheless, in order to carry out the data fit is necessary to dispose reaction rate data, which can be determined under differential or integral reactor conditions through differential and integral methods of data analysis. In this section, apparent reaction orders, activation energies, kinetic as well as adsorption constants are estimated from CO_2 conversion

values and CO_2 disappearance rates. Besides, a discrimination among various models is carried out and finally the model that best fits experimental data is validated.

5.4.1. Apparent reaction orders

In order to study the effect of reagents and products partial pressure on the CO_2 hydrogenation rate, experimental datasets obtained at 325 °C were employed. Note that CO_2 conversion is lower than 10% for all those kinetic experiments, indicating that CO_2 methanation takes place under differential reactor conditions. Under such conditions (X < 10%), the reaction rate of CO_2 hydrogenation can be considered the same in all positions of the catalyst bed since the partial pressures of reagents almost no change along the short plug-flow reactor. Then, the design equation of the plug-flow reactor can be expressed as follows:

$$\frac{W}{F_{CO_2}^0} = \frac{X_{CO_2}^{out} - X_{CO_2}^{in}}{-r_{CO_2}} \tag{5.6}$$

from which CO_2 disappearance rate can be defined as:

$$-r_{CO_2} = F_{CO_2}^0 \frac{\left(X_{CO_2}^{out} - X_{CO_2}^{in}\right)}{W} \tag{5.7}$$

where $F_{CO_2}^0$ is the molar CO_2 flow at reactor inlet (mol h^{-1}), X_{CO_2} is the CO_2 conversion and W is the catalyst weight (g). Note that the partial pressures shown in this section refer to the average among the observed at reactor inlet and outlet, since CO_2 methanation rate is also calculated as average value.

Figure 5.4 shows CO_2 disappearance rate as a function of reagent and products concentration at 325 °C. It can clearly be observed that reaction rate increases with CO_2 partial pressure following saturation trend (Figure 5.4a). In fact, by increasing p_{CO_2} from 0.05 to 0.23 bar and then, from 0.23 to 0.47 bar, $-r_{CO_2}$ rises by 42 and 19%, respectively. This trend is in agreement with results reported by Weatherbee et al. in 1982 [164], according to which the CO_2 hydrogenation is quite sensitive to CO_2

concentration at low partial pressures. On the other hand, Figure 5.4b also shows similar positive effect of p_{H_2} on $-r_{CO_2}$, observing an increase of around 59% varying the H_2 partial pressure from 0.11 to 0.70 bar.

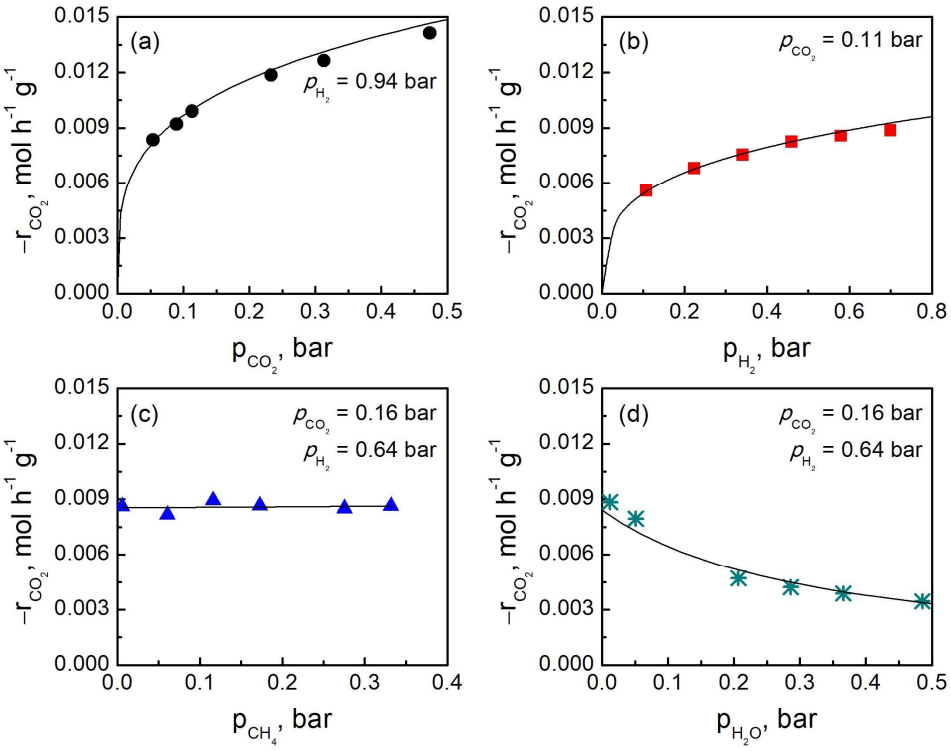

Figure 5.4. Influence of (a) CO_2, (b) H_2, (c) CH_4 and (d) H_2O partial pressures on CO_2 methanation rate at 325 °C, 2 bar (total pressure) and GHSV = 15,000 h^{-1}. Partial pressures are average values among the observed at reactor inlet and outlet.

The influence of reagents was further analyzed fitting the data to a simple power-law expression of the form:

$$-r_{CO_2} = k p_{CO_2}^{\alpha} p_{H_2}^{\beta} \tag{5.8}$$

where k is the kinetic constant at 325 °C; α (CO_2) and β (H_2) are the apparent reaction orders. Through logarithmic linearization and multiple linear regression, the apparent reaction orders of CO_2 and H_2 at 325 °C were estimated, which resulted to be 0.24 and

0.27, respectively. Namely, both reagents have similar influence on reaction rate. Noteworthy, Lefebvre et al. [171] also reported comparable values of CO_2 and H_2 apparent orders at 300 °C (0.3 and 0.42, respectively) for Ni/SiO_2 catalyst.

The influence of CH_4 and H_2O partial pressure is shown in Figures 5.4c and 5.4d, respectively. In both cases, CO_2 and H_2 partial pressures are kept at 0.16 and 0.64. Note that $-r_{CO_2}$ is almost insensitive to methane partial pressure, as reported by many authors [113, 168, 171]. However, varying H_2O partial pressure from 0 to 0.49 bar a considerable decrease in $-r_{CO_2}$ is observed, indicating that water strongly adsorbs on active sites hindering the reagents adsorption and hence, inhibiting the CO_2 hydrogenation rate. Thus, it seems that the kinetic constant also depends on the concentration of adsorbed water or hydroxyls (OH^-). Then, Equation 5.8 could hardly predict the observed water resistance to reaction rate (Figure 5.4d) and it must be modified as follows [169]:

$$-r_{CO_2} = \frac{k p_{CO_2}^{\alpha} p_{H_2}^{\beta}}{1 + K_{H_2O} p_{H_2O}} \tag{5.9}$$

where K_{H_2O} is the water adsorption constant at 325 °C.

Equation 5.9 was linearized representing $1/-r_{CO_2}$ vs. p_{H_2O} and fitted to experimental data in order to estimate the kinetic and water adsorption constants, which were calculated from the intercept and slope of the regression line. *k* and K_{H_2O} parameters proved to be 0.0157 mol h^{-1} g^{-1} $atm^{-0.51}$ and 3.061 atm^{-1}, respectively. Note that these values are reliable since they are positive and of the order of those reported in literature [170].

5.4.2. Apparent activation energy

Once the effect of reactant and products concentration was studied, the apparent activation energy in the absence of catalyst deactivation (after stabilization) was determined in the temperature region from 315 to 430 °C. Figure 5.5 displays CO_2

conversion as a function of temperature and space-time. As shown in the figure (black lines), experimental points were fit to a mathematical expression which considers thermodynamic equilibrium:

$$X_{CO_2} = \frac{\left(W / F^0_{CO_2}\right)^b}{a + \left(W / F^0_{CO_2}\right)^b / X_{eq}} \tag{5.10}$$

where, a and b are the fit coefficients and X_{eq} is the equilibrium conversion depending on temperature.

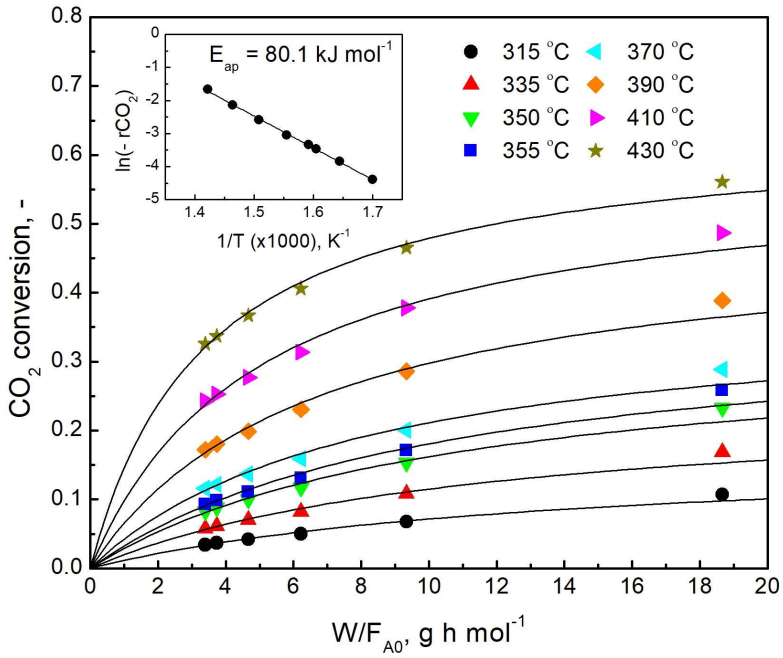

Figure 5.5. Effect of W/F_{A0} on CO_2 conversion at different temperatures together with Arrhenius plot. Symbols refers to experimental data and black lines to the fits.

It can be observed that X_{CO_2} tends towards saturation (at T > 335 °C), as is usual under integral reactor conditions. The initial reaction rates approach was chosen in this case to calculate apparent kinetic constants. This method consists of fitting conversion

vs. space-time curves, which its extrapolation at $W / F^0_{CO_2} = 0$ and corresponding derivatives results in values of initial reaction rates at every temperature,

$$-r^0_{CO_2} = \left(\frac{dX_{CO_2}}{d(W / F^0_{CO_2})} \right)_{W/F^0_{CO_2}=0} = k_{ap}\ f(C^0_{CO_2}, C^0_{H_2}) \tag{5.11}$$

that together with logarithmic Arrhenius expression:

$$\ln(-r^0_{CO_2}) = \ln\left[A_0\ f(C^0_{CO_2}, C^0_{H_2}) \right] - \frac{E_{ap}}{R}\left(\frac{1}{T}\right) \tag{5.12}$$

allows determination of the apparent activation energy from the slope of linear plot of $\ln(-r^0_{CO_2})$ vs. $1/T$, as represented in the inset plot of Figure 5.5.

The apparent activation energy for CO_2 hydrogenation on 10NiAl catalyst, which was calculated by Equation 5.12 and initial reaction rates summarized in Table 5.2, proved to be 80.1 kJ mol^{-1}. The determination of activation energy values has already been conducted by other authors, observing similar values that ranges 70 – 115 kJ mol^{-1} on NiAl type catalysts [112, 168, 169, 171-173].

Table 5.2. Anderson and Mears criteria for assessment of internal and external heat transfer limitations.

***T* (°C)**	$-r^0_{CO_2}$ **mol h^{-1} g^{-1}**	**Anderson (< 0.75)**	**Mears (< 0.15)**
315	1.23 10^{-2}	1.47 10^{-3}	2.93 10^{-3}
335	2.15 10^{-2}	2.40 10^{-3}	4.77 10^{-3}
350	3.15 10^{-2}	3.35 10^{-3}	6.66 10^{-3}
355	3.56 10^{-2}	3.72 10^{-3}	7.41 10^{-3}
370	4.74 10^{-2}	4.73 10^{-3}	9.41 10^{-3}
390	7.51 10^{-2}	7.05 10^{-3}	1.40 10^{-2}
410	1.18 10^{-1}	1.04 10^{-2}	2.07 10^{-2}
430	1.89 10^{-1}	1.58 10^{-2}	3.14 10^{-2}

Finally, the reliability of calculated apparent activation energy was checked by Anderson [175] and Mears [176] criteria (equations in Appendix A1). These criteria allow estimating if internal and external heat transfer limitations can be considered negligible. Despite the high reaction heat of CO_2 methanation ($\Delta H = -165$ kJ mol^{-1}), it should be noted that both criteria were satisfied pointing out that the activation energy was correctly deduced from the Arrhenius expression. As shown in Table 5.2, dimensionless values are far below 0.75 and 0.15, indicating that thermal gradients can be considered apparently negligible both inside the catalyst particle and in the film around the catalyst.

5.4.3. LHHW-type kinetic equations

Power-law equations are usually only applicable in a narrow range of operation conditions due to its simplicity. On the contrary, LHHW-type equations, which are based on reaction mechanism and attempt to predict the rate of the slowest step of the reaction pathway, are applicable in a wider range. These equations, in addition to a kinetic constant as well as an equilibrium gradient, include terms regarding to adsorption of reagent and products (i.e., adsorption constants) and are usually capable to reflect kinetics for the complete range of operational conditions, from differential reactor conditions to thermodynamic equilibrium.

The first step in the deduction of LHHW equation is the proposal of mechanisms. It has already been mentioned that CO_2 methanation can proceed via associative or dissociative type mechanisms, depending if CO_2 molecule is either directly hydrogenated or previously split, respectively. In our case, the kinetic results revealed the appearance of considerable amounts of CO, specially at lowest space times (see Table 5.1), which suggests that adsorbed CO or carbonyls are formed during CO_2 hydrogenation on 10NiAl catalyst according to mechanism with carbonyls as intermediates. Noteworthy, these observations are in agreement with the *operando* FTIR mechanistic study reported in the previous chapter. However, the role of formate species in mechanism is still unclear. It is proposed that adsorbed formates could be either spectator species that do not participate in the reaction or intermediate species playing a role in CO formation. In this line, two reaction pathways are proposed in

Tables 5.3 and 5.4, classified as dissociative or H-assisted mechanism depending on how CO is formed. Note that from each mechanism at least 10 equations can be derived assuming that one of adsorption, reaction or desorption steps is the rate determining step. Models were derived from most probable RDS steps and for simplicity, just two LHHW-type equations with the best fit are shown in this section.

Table 5.3. Elementary steps of proposed dissociative mechanism.

Step	Reaction	Assumption
1	$H_2 + 2^* \rightleftarrows 2H^*$	Quasi equilibrium
2	$CO_2 + 2^* \rightleftarrows CO^* + O^*$	Quasi-equilibrium
3	$CO^* \rightleftarrows CO(g) + ^*$	Quasi-equilibrium
4	$CO^* + H^* \rightleftarrows CHO^* + ^*$	Rate determining step
5	$CHO^* + ^* \rightleftarrows CH^* + O^*$	Low CHO* coverage
6	$CH^* + 3H^* \rightleftarrows CH_4^* + 3^*$	Low CH_x* coverage
7	$CH_4^* \rightleftarrows CH_4(g) + ^*$	Low CH_4* coverage
8	$O^* + H^* \rightleftarrows OH^* + ^*$	Low O^* coverage
9	$OH^* + H^* \rightleftarrows H_2O^* + ^*$	Quasi-equilibrium
10	$H_2O^* \rightleftarrows H_2O(g) + ^*$	Low H_2O^* coverage

The first mechanism follows reaction pathway in Table 5.3. It assumes that H_2 and CO_2 are dissociatively adsorbed forming hydrogen atoms (H) and carbonyls (CO) on Ni^0 surface [166]. Then, carbonyls react with dissociated hydrogen into carbon-hydroxy or adsorbed formyl (CHO, step 4). Subsequently, there is another carbon-oxygen cleavage yielding carbenes (CH_x, step 6), which are further hydrogenated into methane (step 7). At the same time, adsorbed oxygen atoms are sequentially hydrogenated into hydroxyls and water (steps 8 and 9). Note that under certain conditions carbonyls can be desorbed as CO_{gas} instead of being hydrogenated (step 3). As the hydrogenation of carbonyl has been reported to be quite slow [112, 158, 168, 169], step 4 was considered the rate determining step. The previous steps as well as step 9 are assumed to be at quasi-equilibrium, whereas the rest of steps are kinetically irrelevant due to the low coverage of reaction intermediates (extremely fast steps) [113, 158].

Considering those premises, the following rate equation of CO_2 methanation is derived, which deduction is included in Appendix A2:

$$-r_{CO_2} = \frac{k_4 p_{CO_2}^{0.5} p_{H_2}^{0.5} \left(1 - \frac{p_{CH_4} p_{H_2O}^2}{p_{CO_2} p_{H_2}^4 K_{Eq1}} \right)}{\left(1 + \sqrt{K_{H_2} p_{H_2}} + \sqrt{K_{CO_2} p_{CO_2}} + K_{OH} \frac{p_{H_2O}}{p_{H_2}^{0.5}} \right)^2} \tag{5.13}$$

where k_4 is the kinetic constant and K_{H_2}, K_{CO_2}, K_{OH} and K_{CO} are the H_2, CO_2, hydroxyl and CO adsorption constants. Likewise, the kinetic constants as a function of temperature are calculated by Arrhenius law, whereas the adsorption ones by Van't Hoff equation. Both formulas are parameterized to minimize the correlation among pre-exponential factor (A_0) and activation energy (E_A) or adsorption enthalpy (ΔH) resulting in the following expressions derived from Arrhenius law:

$$k = k_0 \exp\left(-\frac{E_A}{R} \left(\frac{1}{T} - \frac{1}{T_{ref}} \right) \right) \tag{5.14}$$

and Van't Hoff equation:

$$K = K_0 \exp\left(-\frac{\Delta H}{R} \left(\frac{1}{T} - \frac{1}{T_{ref}} \right) \right) \tag{5.15}$$

where k and K are kinetic and adsorption constants at different temperatures, whereas k_0 and K_0 are reference constants at T_{ref} (430 °C in this work). Lastly, K_{eq1} is the equilibrium constant of CO_2 methanation that was calculated at every temperature by the following empirical expression:

$$K_{eq1} = 137 \cdot T^{3.998} \exp\left(\frac{158.7}{RT} \right) \tag{5.16}$$

where R or the ideal gas constant is 8.314 J K^{-1} mol^{-1}.

In the second mechanism (Table 5.4), H_2 also dissociates on Ni^0 surface into adsorbed H-atoms, whereas CO_2 is molecularly chemisorbed on surface OH^- groups of Al_2O_3 forming bicarbonates (HCO_3).

Table 5.4. Elementary steps of proposed H-assisted mechanism.

Step	Reaction	Assumption
1	$H_2 + 2^* \rightleftarrows 2H^*$	Quasi equilibrium
2	$CO_2 + OH^* \rightleftarrows HCO_3^*$	Quasi-equilibrium
3	$HCO_3^* + H^* \rightleftarrows HCOO^* + OH^*$	Quasi-equilibrium
4	$HCOO^* + ^* \rightleftarrows CO^* + OH^*$	Rate determining step
5	$CO^* \rightleftarrows CO(g) + ^*$	Quasi-equilibrium
6	$CO^* + H^* \rightleftarrows CHO^* + ^*$	Low CO* coverage
7	$CHO^* + ^* \rightleftarrows CH^* + O^*$	Low CHO* coverage
8	$CH^* + 3H^* \rightleftarrows CH_4^* + 3^*$	Low CH_x* coverage
9	$CH_4^* \rightleftarrows CH_4(g) + ^*$	Low CH_4* coverage
10	$O^* + H^* \rightleftarrows OH^* + ^*$	Low O* coverage
11	$OH^* + H^* \rightleftarrows H_2O^* + ^*$	Quasi-equilibrium
12	$H_2O^* \rightleftarrows H_2O(g) + ^*$	Low H_2O* coverage

After that, bicarbonates close to metal particles react with dissociated H_2 by H spillover mechanism yielding formate species (HCOO) [124], which are decomposed into hydroxyls and carbonyls adsorbed on alumina and Ni surface (step 4). Subsequently, carbonyls are desorbed as carbon monoxide (step 5) and/or sequentially reduced up to CH_4 via CH_xO intermediate species (steps 6-9). As in the first proposed mechanism, surface oxygen atoms as well as hydroxyls are hydrogenated into water (second product) in lumped steps.

In this case, step 4 was also chosen as the rate determining step since FTIR results revealed (Section 5.1.) that formates could be intermediate species of CO_2 methanation. In fact, such species usually appear at high surface concentration in many FTIR or DRIFTS measurements [124, 145, 148, 167] and have been considered in formulating various kinetic models [113, 173]. On the other hand, adsorbed H_2,

formate, hydroxyls and carbonyls are assumed to be in high enough concentration, partially covering the active sites and inhibiting CH_4 formation rate. Thus, the second rate equation, which deduction is included in Appendix A3, is as follows:

$$-r_{CO_2} = \frac{k_4 p_{CO_2} p_{H_2}^{0.5} \left(1 - \frac{p_{CO} p_{H_2O}}{p_{CO_2} p_{H_2} K_{eq2}}\right)}{\left(1 + \sqrt{K_{H_2} p_{H_2}} + K_{CO_2} p_{CO_2} \sqrt{K_{H_2} p_{H_2}} + K_{OH} \frac{p_{H_2O}}{p_{H_2}^{0.5}} + K_{CO} p_{CO}\right)^2} \tag{5.17}$$

where K_{eq2} is the equilibrium constant of reverse water gas shift reaction (K_{RWGS}), which can be deduced at every reaction temperature from WGS equilibrium constant expression [177]:

$$\ln\left(K_{WGS}\right) = -3.732 + \frac{3850}{T} + \left(\frac{470}{T}\right)^2 \tag{5.18}$$

and, then, the reverse-WGS equilibrium constant is:

$$K_{eq2} = K_{RWGS} = \frac{1}{K_{WGS}} \tag{5.19}$$

5.4.4. Model discrimination

Once various kinetic models were proposed, CO_2 hydrogenation rates were calculated at different temperatures and space-times either deriving graphically X vs. W/F_{A0} curves in Figure 5.5 or from analytical derivative of Equation 5.10:

$$-r_{CO_2} = \frac{a \cdot b \cdot \left(W / F_{CO_2}^0\right)^{(b-1)}}{\left(a + \left(W / F_{CO_2}^0\right)^b / X_{eq}\right)^2} \tag{5.20}$$

After that, the fit of the models was carried out by least squares method (nonlinear regression), which consists of finding minimum value of objective function:

$$SSE = \sigma^2 = \sum_i^N \left(y^{\exp} - y^{calc} \right)^2 \quad (5.21)$$

that describes the sum of squared residuals obtained from the difference among experimental and calculated variable *y* (hereunder, reaction rate) for every point, being *N* the total number of kinetic experiments. The fit together with estimation of some kinetic parameters was carried out by *fminsearch* command of MATLAB software (R2014b version), which performs a non-linear multidimensional minimization without restrictions through Nelder-Mead algorithm. The optimization options were: a function tolerance (*TolFun*) of $1 \cdot e^{-10}$, lower bound of step size (*TolX*) of $1 \cdot e^{-3}$ and maximum of 500 interactions (*iter*). Besides, the quality of the fit was estimated to carry out model discrimination by calculating absolute mean deviations as follows:

$$D = \sqrt{\frac{\sigma^2}{N}} \frac{1}{\bar{y}} \times 100 \quad (5.22)$$

where $\bar{y}$ is the mean value of experimental variable (reaction rate in this section).

Figure 5.6 shows the parity plots of power law and LHHW kinetic models. Note that the models are fit to datasets included in the legend (all details in Table 5.1), which are measured at different temperature (*T*), total pressure (*P*) and H_2/CO_2 ratios (*h*). After regression, the power law model with water inhibition (model I) presents a mean absolute residual of 11.5%. Although the fit quality is acceptable, the model underestimates the CO_2 disappearance rate at low temperature ($T < 370$ °C) and does not predict satisfactorily all data at 430 °C (datasets 13-15 and 20 -22), which includes the experiments where CO_2 methanation rate is boosted by increasing H_2/CO_2 ratio into 8 and *P* is varied from 2 to 6 bar (Figure 5.6a). Nevertheless, it must be noted that prediction was considerably improved by adding the water adsorption constant (Equation 5.9). In fact, considering the water inhibition effect, the absolute mean deviation (Equation 5.22) was reduced from 38.6% ($\sigma^2 = 6.10\ 10^{-3}$) to 11.5% ($\sigma^2 = 4.93\ 10^{-4}$). Recently, this model satisfactorily fit kinetic data on a commercial Ni/SiO_2 catalyst [171], but we did not consider suitable to describe some mechanistic aspects.

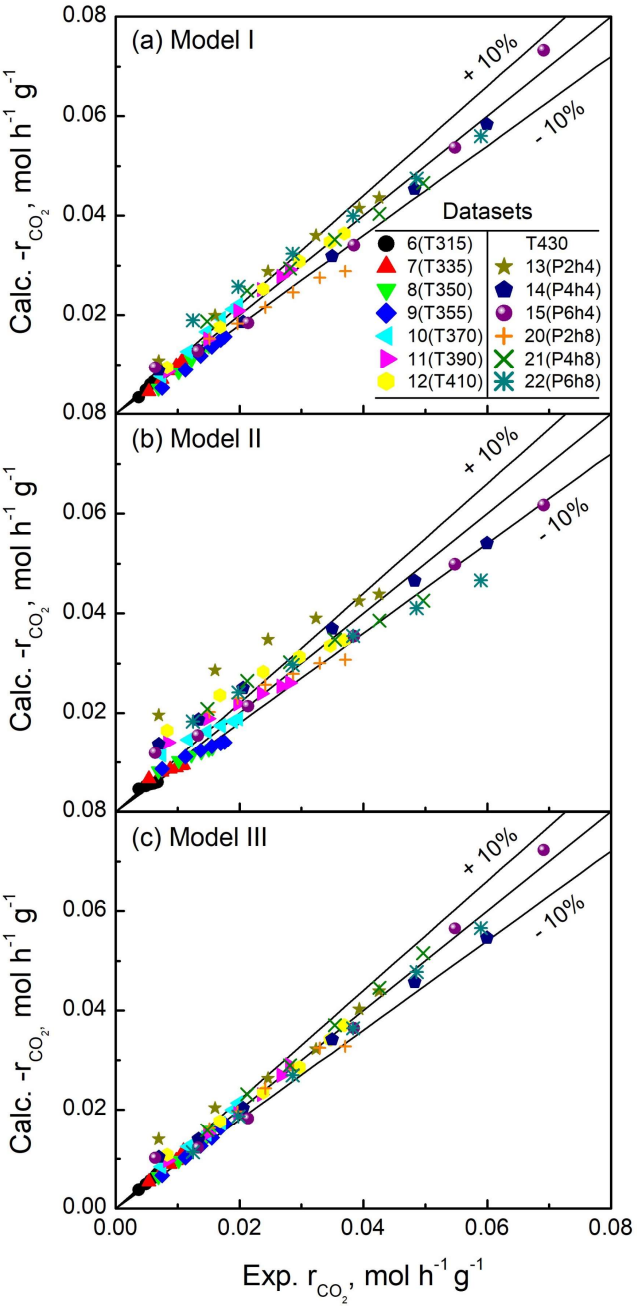

Figure 5.6. Parity plots of (a) Power-law with water inhibition (b) dissociative and (c) H-assisted CO formation models. Datasets 6-15 and 20-22 included in the fit.

The quality fit of the second model (Equation 5.13), which is derived from dissociative CO formation mechanism and assumes the hydrogenation of carbonyl as rate determining step, proved to be less significant than that of model I. In fact, only few points were within ± 10% dispersion region as can be visualized in Figure 5.6b, being its mean absolute residual 20.1% (σ^2 = 1.50 10^{-3}). This LHHW model systematically underestimates $-r_{CO_2}$ under differential reactor conditions (T < 355 °C) and overestimates it with the increase of temperature (at high conversions), observing the highest deviations (even superior to 100%) at 430 °C (dataset 13).

Although this model has currently been validated by many authors who have studied kinetics on Ni/Al_2O_3 and $NiAl(O)_x$ formulations with high Ni content (> 15 wt%) [112, 158, 168, 169], it has lower statistical significance than model I and hence can be discarded. This worse fit could be related to differences in Ni loading, Ni reduced state and Ni particle size, which have been reported to alter the way CO_2 is adsorbed onto the catalyst [155]. Unlike Ni/Al_2O_3 samples with high metal loading, 10NiAl catalyst contains poor reducibility and metal surface area resulting in low affinity to CO adsorption (i.e., low carbonyl concentration), as evidenced by the lack of FTIR carbonyls bands (see Figure 5.1). That may be the reason why the fit quality of this model, whose RDS is the hydrogenation of adsorbed CO, is statistically less significant than other fits reported in literature.

Nevertheless, data are best predicted by model III (Equation 5.17, H-assisted CO formation), observing the lowest variance (σ^2 = 2.40 10^{-4}) and corresponding mean absolute deviation of 8.0% (Figure 5.6c). Noteworthy, most experimental points are within ± 10% dispersion region and not systematic deviation is noticed, i.e., the kinetic equation is able to describe the effect of temperature, pressure as well as H_2/CO_2 ratio over the whole range of conditions employed. The obtained regression results, together with the fact that formates and CO gas are observed by FTIR, clearly suggest that carbonyls arise from formates following the H-assisted mechanism rather than by the CO_2 dissociative adsorption. In fact, this model compared to model II achieves a significant decrease of 12.1% in absolute mean residual.

5.4.5. Extended model validation

In the last step, adsorption constants and enthalpies were estimated by integral method for data analysis together with nonlinear regression. The former requires numerical integration of the plug flow rector design equation:

$$\frac{W}{F_{CO_2}^0} = \int_0^{x_{CO_2}^{out}} \frac{dX_{CO_2}}{-r_{CO_2}} = \int_0^{x_{CO_2}^{out}} \frac{dX_{CO_2}}{f\left(X_{CO_2}\right)} \tag{5.23}$$

where $-r_{CO_2}$ (Equation 5.17) is expressed as a function of conversion (or products yield) defining reagent/product partial pressures as Equations in 5.1-5.5. The numerical integration was accomplished by *ode23* command of MATLAB software, which is able to solve nonstiff differential equation systems by adaptative Runge-Kutta algorithm of 2nd and 3rd order.

It should be noted that the presence of considerable amount of CO at low space-time and high temperature, cannot be neglected when integrating design equation, since partial pressures included in the mechanistic equation are function of both methane (Y_{CH_4}) and CO (Y_{CO}) yields. Therefore, other rate equations must be incorporated to the system to carry out the integration properly, which describe the formation rate of CH_4 and CO. In our case, step 6 of H-assisted CO formation mechanism, the hydrogenation of carbonyl into formyl, is the one that makes most sense to be the rate determining step of CO methanation. From such assumption the following equation is derived (deduction included in Appendix A3):

$$r_{CH_4} = \frac{k_6 p_{CO} p_{H_2}^{0.5} \left(1 - \frac{p_{CH_4} p_{H_2O}}{p_{CO} p_{H_2}^3 K_{eq3}}\right)}{\left(1 + \sqrt{K_{H_2} p_{H_2}} + K_{CO_2} p_{CO_2} \sqrt{K_{H_2} p_{H_2}} + K_{OH} \frac{p_{H_2O}}{p_{H_2}^{0.5}} + K_{CO} p_{CO}\right)^2} \tag{5.24}$$

where K_{eq3} is the equilibrium constant of CO methanation calculated from Gibbs free energy difference among CO_2 methanation and RWGS reactions. Note that the

adsorption constants are the same of that of model III (Equation 5.17), indicating that reaction rate is slowed by the same intermediates (MASI, most abundant surface intermediates). Then, given that the CO_2 conversion is the sum of CH_4 and CO yields, the rate of CO formation is defined as:

$$r_{CO} = \left(-r_{CO_2}\right) - r_{CH_4} \tag{5.25}$$

Figure 5.7 depicts the parity plot of all experimental CO_2 conversion points against the calculated/predicted ones, including additional data (datasets 1-4, 16-19 and 23-26) in which partial pressure effect of CO_2 (blue), H_2 (red), CH_4 (green) and H_2O (blue) was studied.

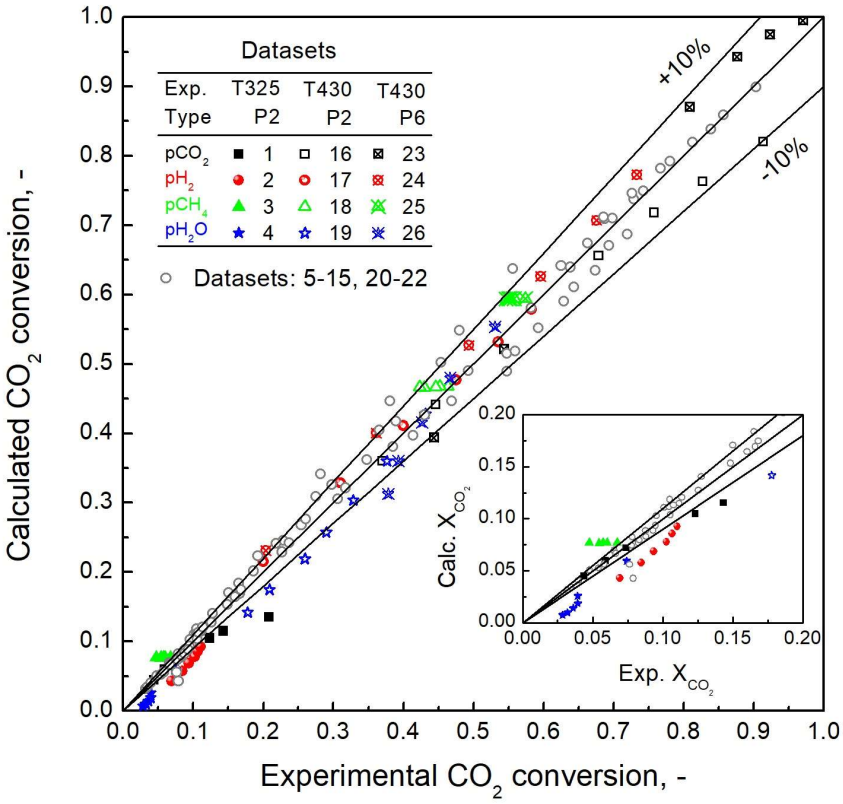

Figure 5.7. Parity plot of model III (153 kinetic measurements).

After incorporation of new points, the prediction accuracy of the model was similar to that above observed, presenting a remarkable low mean deviation (*D*) of 7.0%. Unfortunately, it can be noticed (see inset graph) that the model does not predict satisfactorily the CO_2 conversion in the low activity region (X_{CO_2} < 0.2), observing a general deviation of 30% or even higher when different concentrations of products are fed. In fact, the model poorly predicts the effect of H_2O at 325 °C. However, in the high activity region (X_{CO_2} > 0.2), most experimental points are within the ± 10% region and the model predicts with high statistical significance both the inhibiting effect of water and the insensitivity to p_{CH_4} at 430 °C (*P* = 2 or 6 bar). Therefore, the satisfactory prediction under integral reactor conditions (the region of greatest interest for industrial practice) proves that the model still is adequate.

The regressed constants of the elected mechanistic models are listed in Table 5.2 at different temperatures. Note that the kinetic constants of CO methanation rate (k_6) are one order of magnitude higher than those of reverse water gas shift (k_4), indicating that the former is much faster. Furthermore, the relative high value of adsorption constants verifies that reaction rates are clearly influenced by adsorbed reaction intermediates except for H_2, which adsorption constant value is not significantly different to zero and therefore it can be neglected. Note that the adsorption constant of CO is at least one order of magnitude higher than the rest, suggesting that adsorbed carbonyls have even more inhibiting effect than water or hydroxyls.

On the other hand, the activation energy for CO_2 hydrogenation obtained by regression was similar to the apparent one calculated in section 5.4.2 (91.6 vs. 80.1 kJ mol^{-1}), whereas that of CO methanation proved to be 26.3 kJ mol^{-1}. Regarding the adsorption enthalpies defined in Van't Hoff equation, those were – 7.86, – 26.0 and – 43.2 kJ mol^{-1} for formate (ΔH_{HCOO}), hydroxyls (ΔH_{OH}), and CO (ΔH_{CO}) adsorption, respectively. It must be highlighted that the adsorption constants fulfil the Boudart rules, according to which the entropy change of any adsorption must be negative (ΔS < 0, i.e., more ordered state) and within the range:

$$10 < \Delta S < 12.2 - 0.0014\Delta H \tag{5.26}$$

Table 5.5. Estimated kinetic as well as adsorption constants at different temperatures.

	kinetic constants		adsorption constants		
T **(°C)**	k_4 **(mol h^{-1} g^{-1} atm$^{-1.5}$)**	k_6 **(atm$^{-1.5}$)**	K_{HCOO} **(atm$^{-1.5}$)**	K_{OH} **(atm$^{-0.5}$)**	K_{CO} **(atm^{-1})**
315	0.105	6.66	0.430	5.20	166.0
325	0.143	7.29	0.418	4.76	143.2
335	0.194	7.95	0.407	4.37	124.2
350	0.299	9.01	0.392	3.86	101.1
355	0.345	9.38	0.388	3.71	94.6
370	0.519	10.55	0.374	3.30	78.0
390	0.870	12.23	0.358	2.85	61.1
410	1.415	14.06	0.343	2.49	48.6
430	2.239	16.04	0.330	2.18	39.2
E_A **(kJ mol^{-1})**	91.6	26.3	–	–	–
ΔH_{ads} **(kJ mol^{-1})**	–	–	– 7.86	– 26.0	– 43.2

Thus, Boudart rules verification and entropy change calculation were done applying Van't Hoff equation together with Gibbs function ($\Delta G^\circ = \Delta H^\circ - T\Delta S^\circ$), which derives in the following equation:

$$\ln(\mathrm{K}) = -\frac{\Delta H^\circ}{RT} + \frac{\Delta S^\circ}{R};\ \Delta S^\circ = R \cdot \ln(\mathrm{K}) + \frac{\Delta H^\circ}{RT} \tag{5.27}$$

The calculated entropy values fulfill Boudart rules (Equation 5.19) for formates (ΔS_{HCOO} = – 20.4 J mol^{-1}), hydroxyls (ΔS_{OH} = – 30.4 J mol^{-1}) and CO adsorption (ΔS_{CO} = – 30.9 J mol^{-1}). Noteworthy, formates present the lowest entropy value, which suggests that are the less stable species. Note that both hydroxyls and carbonyls present an entropy value 10 J mol^{-1} higher, confirming that they are the species that mainly inhibit CO_2 methanation rate.

Therefore, since kinetic equations fit experimental data (153 measurements) with high statistical relevance and all kinetic parameters fit physical rules, model III is validated to describe kinetics on 10NiAl catalyst, based on all experimental, mechanistic (FTIR) and kinetic data.

5.5. OVERALL VIEW AND CONLUSIONS

In this chapter, a LHHW mechanistic model is developed through discrimination procedure capable to provide an excellent description of the kinetics over Ni/Al_2O_3 catalyst with low metal content (10 wt%). The elected model, which covers a wide range of operating conditions from differential (X_{CO_2} < 0.1) to equilibrium (X_{CO_2} > 0.8) reactor, can satisfactorily predict the dependence of CO_2 hydrogenation rate with reagents partial pressure (p_{CO_2} and p_{H_2}), the boosting effect of temperature as well as H_2/CO_2 feed ratio in CH_4 formation and the activity inhibitory effect of strongly adsorbed OH^- and CO surface intermediates. The elected rate equations system, which is the one that best fits the kinetic data, assumes formate species decomposition into carbonyls via H-assisted CO formation mechanism (and further carbonyls hydrogenation into CHO) as rate determining step. Noteworthy, its mean absolute deviation (σ^2 = 7%) is significantly lower to that of the model most employed in literature to describe the kinetics of Ni-Al formulation with high Ni contents (σ^2 = 20%), which considers that associative hydrogenation of adsorbed CO formed from direct CO_2 dissociation is the rate determining step. This works confirms that not only carbonyls but also formate species participates in CO_2 methanation mechanism and concludes that it has an important role in kinetics of lowly-loaded Ni/Al_2O_3 catalyst.

Chapter 6

ZEOLITE SUPPORTED CATALYSTS

ABSTRACT

Microporous solids such as zeolites have scarcely been studied yet for CO_2 methanation reaction. Thus, the target of the following study is to evaluate and compare the catalytic performance of easily modulable zeolite (Y and BETA) supported Ni catalysts. The physicochemical properties of the prepared catalysts are characterized with XRD, BET, CO_2-TPD, H_2-TPR and XPS, and CO_2 methanation is carried out in a tubular reactor at conditions of H_2/CO_2 = 4, GHSV = 10,000 h^{-1} and temperatures from 200 to 500 ^oC. Neutralization of both zeolites by Na^+ ion exchange enhance the CO_2 conversion as weak CO_2 adsorption sites and reducibility are promoted. BETA results in a better support than Y zeolite due to the presence of more easily reducible Ni^{2+}, which acts as precursor of active Ni^0 accessible under reaction conditions. Indeed, the surface basicity and Ni dispersion of Ni/BETA catalysts is considerably promoted by impregnation of different loads of La_2O_3, which increase the amount of CO_2 adsorption sites and even active hydrogenation sites (higher Ni dispersion) resulting in a significant increase of activity and selectivity towards CH_4. The optimal Ni-10La_2O_3/Na-BETA formulation presents a T_{50} of 320 ^oC, CO_2 conversion of 65% at 350 °C, with almost total selectivity to CH_4 and maintaining stability for more than 24 h on stream.

6. ZEOLITE SUPPORTED CATALYSTS

As discussed in the previous chapters (Chapters 4-6), gamma-alumina has proven to be a suitable support to carry out CO_2 methanation, since it contains high SSA to disperse the active phase and weak-medium Bronsted basic sites (OH^- groups) over which CO_2 can be adsorbed. In recent years, not only γ-Al_2O_3 but also other mesoporous solids have been investigated as CO_2 methanation supports, such as Al_2O_3 [58], SiO_2 [53], TiO_2 [178], ZrO_2 [179], CeO_2 [180] and Ce-Zr mixed oxides [54]. Among them, CeO_2 or Ce-Zr mixed oxides have resulted in be the best supports due to their well-known ability to vary the oxygen concentration without crystalline phase change, which results in a high and stable oxygen storage capacity [181]. Indeed, Le et al. [182] studied and compared the CO_2 methanation catalytic performance of Ni/CeO_2 with that of Ni catalysts with non-reducible supports (Al_2O_3, SiO_2, TiO_2 and ZrO_2), reporting that the former was the more active. Likewise, Pan et al. [153] attributed a greater CO_2 methanation activity of $Ni/Ce_{0.5}Zr_{0.5}O_2$ catalyst to a greater number of weak and medium basic sites, compared to that of Ni/Al_2O_3 formulation.

On the other hand, microporous solids as catalytic supports for CO_2 methanation have been scarcely studied in the literature for CO_2 methanation. Zeolites are microporous alumino-silicate minerals with ordered crystalline structure, which are built by TO_4 unit blocks (SiO_4^- and AlO_4^-) and are mainly used in refineries to catalyze isomerization, alkilatyon, reforming and cracking reactions [183, 184]. In these industrial fields, zeolites are mostly used as acid catalysts, being its surface protons (H^+) the responsible for hydrocarbon transformation. The amount and bonding strength of these protons is linked to $Al^{\delta-}$ species, which act as Lewis acid sites. Nevertheless, the zeolite also contents basic sites to adsorb CO_2. In fact, the basicity in zeolites is given by the charge and number of surface O^{2-} atoms that act as Lewis basic sites [185]. Note that this property can be modified either by changing Si/Al ratio or/and incorporating compensating metal cations. Furthermore, its high specific surface area makes also possible to modulate the surface basicity by adding great loadings of CO_2 adsorbents such as alkaline earth metals (e.g. Ca^{2+}, Mg^{2+}, Ba^{2+}) [186] and rare earth metals (e.g. La_2O_3, CeO_2, Pr_2O_3) [187].

In this line, recent research has focused on studying zeolite Y supported Ni catalysts for CO_2 methanation. However, as far as we know, BETA type zeolite has not been studied for this application. Therefore, the research work included in this chapter aims to prepare, characterize and compare the catalytic performance of protonic or Na-exchanged Y and BETA zeolite supported Ni catalysts. Additionally, the effect of La_2O_3 as a CO_2 adsorption promoter for the catalytic activity is investigated. The synthesis route followed to prepare new catalyst families is detailed in section 2.2.2. In total, 7 catalysts were synthesized, whose framework type, chemical composition and Si/Al ratios are shown in Table 6.1.

Table 6.1. Nomenclature and chemical composition of the prepared catalysts.

Catalyst	Framework	Si/Al[a]	Na (wt. %)[a]	Ni (wt. %)[a]	La_2O_3 (wt. %)[a]
Ni/H-Y	FAU	2.5	1.4	9.5	-
Ni/Na-Y	FAU	2.6	6.0	9.9	-
Ni/H-BETA	BEA	12.4	0.0	9.2	-
Ni/Na-BETA	BEA	11.9	1.4	9.5	-
Ni-5La_2O_3/Na-BETA	BEA	12.2	1.4	9.6	3.2
Ni-10La_2O_3/Na-BETA	BEA	12.7	1.3	7.8	7.4
Ni-15La_2O_3/Na-BETA	BEA	12.3	1.2	7.3	12.0

[a]Determined by XRF.

6.1. EFFECT OF STRUCTURE AND EXCHANGED Na^+

In terms of catalysis, the zeolites present very interesting properties such as a high degree of crystallinity leading to plenty of framework types, high adsorption capacity of reagents and, specially, shape selectivity of products, which is directly related with the size of cavities and channels. So, in many cases, the transformation of reactants into products depends on how the reagents fit the active site of the zeolite [188]. Normally, only zeolites with pore or channel sizes of at least 8 T atoms (T = Si or Al) are employed as catalytic supports in order to ensure the internal diffusion of any type of reagents. According to their channel or micropore size, the different zeolitic frameworks can be grouped into small (0.4 – 0.45 nm), medium (0.45 – 0.6 nm) and

large (0.6 – 0.8 nm) pore zeolites, being their pores formed by 8, 10 and 12 T atoms, respectively. The zeolites elected for the following research work, commercially known as Y and BETA, present FAU and BEA framework types with 12 atom pore openings. These structures allow CO_2 and H_2 to diffuse easily throughout their pores and the incorporation of certain amount of the active phase (Ni). The structures of the chosen zeolites are depicted in Figure 6.1.

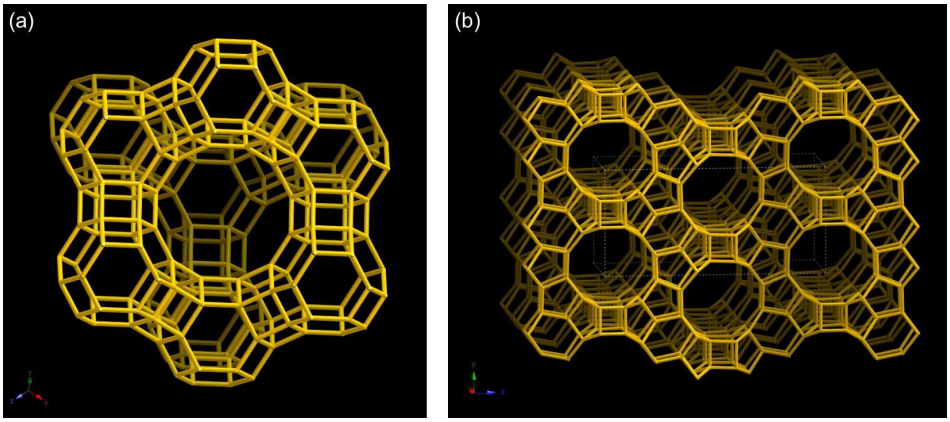

Figure 6.1. Unit cell framework of (a) FAU (Y zeolite) and (b) BEA (BETA zeolite).

As previously mentioned, the basicity of the zeolite can be improved by introducing a compensating cation. In this line, the affinity towards CO_2 of the zeolite will depend on the charge and size of the cation [185]. In the case of incorporating a large compensating cation, the negative charge transfer from neighboring framework oxygen will be low, forming a strong basic site. Otherwise, the charge transfer will be high resulting in a less charged framework oxygen or a weaker basic site. In fact, Vos et al. [189] reported that the basicity increases with the size of the exchangeable cation as follows: $Li^+ < Na^+ < K^+ < Rb^+ < Cs^+$ and $Mg^{2+} < Ca^{2+} < Sr^{2+} < Ba^{2+}$. Note that the basicity not only depends on the cation size but also on its position in the zeolitic framework. Indeed, big cations, such us K^+ and Cs^+, are preferentially exchanged in the supercages of FAU structure (see Figure 6.1), whereas smaller cations (Li^+ and Na^+) are also able to access the sodalite cages, where CO_2 unfortunately could not enter due to its size [190]. Conversely, the polarizing power, e.g., the capacity to physisorb CO_2 of the monovalent

alkaline cations, increases as their radii decreases as follows: $Li^+ > Na^+ > K^+ > Rb^+ > Cs^+$. Although K^+ is a cation with competitive dual adsorption mode (by CO_2 physisorption or carbonate formation on neighbouring framework O), Bacariza et al. [191] carried out an study of the effect of the compensating cation on Ni/USY catalysts, reporting a considerable lower Ni dispersion for K^+-exchanged Ni/USY CO_2 methanation catalyst. Thus, as revealed in the previous part, Na^+ was the chosen alkaline cation in order to increase the CO_2 adsorption capacity of both Ni/Y and Ni/BETA catalysts. Characterization as well as activity results of protonic or Na^+-exchanged zeolite supported catalysts are included in the following two sections.

6.1.1. Zeolite-based catalysts characterization

Figure 6.2 shows XRD patterns of the protonic zeolites (H-Y and H-BETA, Figures 6.2a and b, respectively) as well as of those exchanged with Na^+.

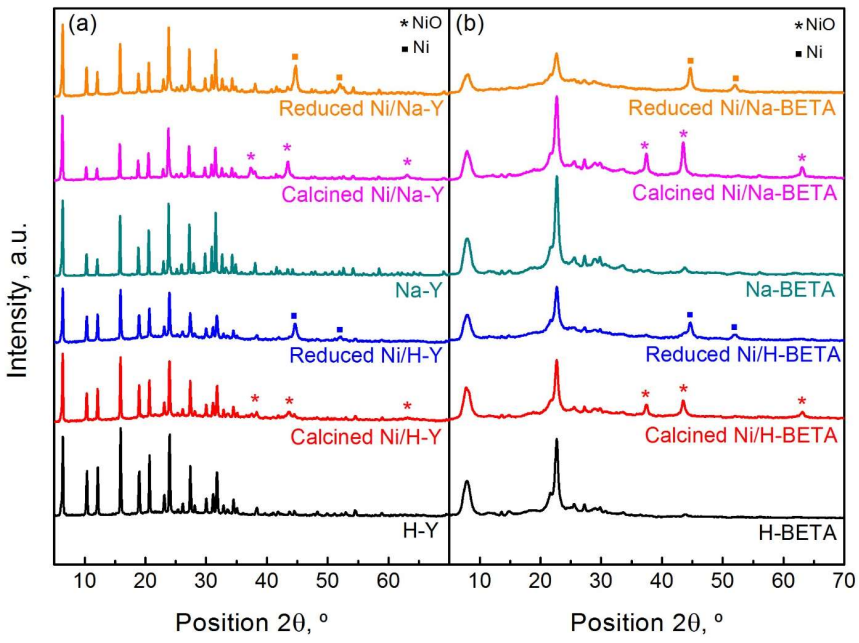

Figure 6.2. XRD patterns of (a) Y-zeolite supported catalysts (calcined and reduced) and (b) BETA-zeolite supported catalysts (calcined and reduced).

It can be observed that the diffractogram of Na-BETA zeolite is almost identical to its counterpart, which means that the crystalline nature of the zeolite was not modified after the incorporation of Na^+. However, minor loss of crystallinity can be detected when Na^+ is incorporated into Y zeolite, as already revealed by other authors [192, 193]. Also, no Na_2O was detected in XRD spectra, assuring a successful exchange of Na^+ in both zeolites. After Ni impregnation, new diffraction peaks at 37.3, 43.3 and 62.9° 2θ revealed the formation of NiO (bunsenite phase) in the impregnated samples [43] which are marked with asterisks. The presence of elemental nickel instead of NiO was detected for the samples reduced at 500 °C for 1h under 20%H_2/He, as revealed by XRD peaks at 44.3 and 51.7 ° 2θ marked with squares [58].

Table 6.2. Physicochemical properties of supports and Ni catalysts.

Sample	τ_{Ni} (nm)[a]	S_{BET} ($m^2 g^{-1}$)[b]	V_{micro} ($cm^3 g^{-1}$)[c]	V_{meso} ($cm^3 g^{-1}$)[c]	Reducible Ni^{2+} at 500 °C (%)[d]
H-Y	-	720.5	0.24	0.07	-
Ni/H-Y	17.0	621.1	0.20	0.10	43
Na-Y	-	832.1	0.29	0.02	-
Ni/Na-Y	19.8	665.9	0.22	0.05	91
H-BETA	-	587.3	0.17	0.60	-
Ni/H-BETA	19.1	485.3	0.12	0.38	95
Na-BETA	-	513.6	0.13	0.38	-
Ni/Na-BETA	20.1	415.7	0.10	0.32	98

[a]Estimated by Scherrer formula (Equation 2.7).
[b]Calculated by complete BET equation.
[c]Determined by application of t-Plot method.
[d]Calculated from H_2-TPR profiles. Red. conditions: 500 °C for 1h (20% H_2/He).

The Ni crystallite sizes, estimated by the Scherrer equation, are displayed in Table 6.2. A smaller crystallite size can be observed for Ni/H-Y catalyst when comparing to Ni/H-BETA catalyst, which is related to differences in zeolitic structure: unlike BEA, FAU structure contains accessible cavities for Ni particles that might result in higher metal dispersion. In the same line, Na^+ incorporation in BETA zeolite produces the formation of bigger Ni crystallites due to the partial pore blockage, which results in less

accessible zeolitic framework [191]. Anyway, no significant differences are observed in the crystallite size, which indicates similar dispersion of the surface Ni for all catalysts.

The N_2 physisorption isotherms of H-Y and H-BETA zeolites are shown in Figure 6.3. In the case of H-Y zeolite the shape of the isotherms is characteristic of a microporous solid: great amount of N_2 is adsorbed at very low pressures by micropore filling and thereafter very little adsorption takes place (isotherm type I according to IUPAC). However, a different isotherm shape is observed for H-BETA zeolite: although a great amount of N_2 is adsorbed at very low relative pressures, more N_2 is also adsorbed at intermediate pressures by multilayer filling (isotherm type IV). The appearance of a hysteresis loop at relative pressures above 0.65 for H-BETA indicates the presence of mesoporous which are suitable for impregnation of high metal loadings.

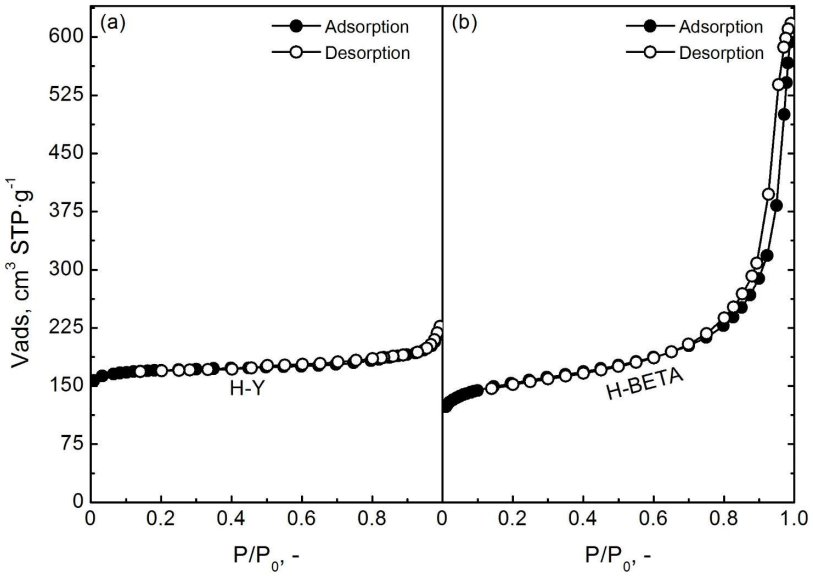

Figure 6.3. N_2 adsorption-desorption isotherms of (a) H-Y and (b) H-BETA zeolites.

Textural properties of the prepared samples are also summarized in Table 6.2. Regardless the presence of Na^+ and after Ni impregnation over H-Y and Na-Y zeolites, a notable decrease of specific surface area (14 and 20%) and micropore volume (17

and 24%) is produced due to the formation of NiO clusters that block the zeolite pores, which reduces the adsorption capacity of the supports [194, 195]. On the other hand, a similar trend can be observed in the textural properties of BETA zeolite after Ni addition, resulting in BET surface reduction of 17 and 19% for H-BETA and Na-BETA, respectively. Additionally, a notorious decrease of both microporous and mesoporous volume is observed. The highest reduction is seen when Ni is impregnated over H-BETA, being microporous and mesoporous volume reduced a 29% and 37%, respectively.

In order to determine the symmetry and the coordination of nickel species dispersed on the zeolites, diffuse reflectance spectroscopy was carried out. Figure 6.4 shows UV-vis-NIR spectra of Y and BETA zeolites after Ni impregnation.

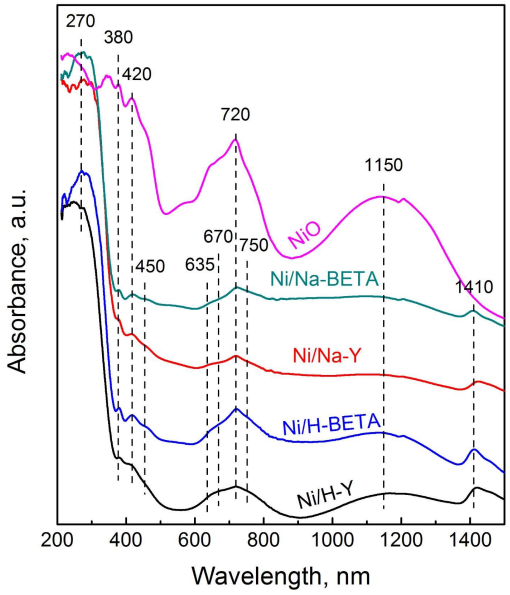

Figure 6.4. UV-vis-NIR spectra of Ni/zeolite catalysts.

In the UV-visible region (from 200 to 800 nm), all catalysts present bands centered at 270, 380, 420 and 720 nm, all of them characteristics of NiO species. The band centered at the lowest wavelength is assigned to $O^{2-} \rightarrow Ni^{2+}$ metal to ligand charge transfer, while the bands at intermediate and high wavelengths are assigned to d-d

electron transitions of Ni^{2+} in octahedral coordination inside NiO [195]. In addition, two bands centered at 450 and 635 nm can be distinguished which correspond to d-d electron transitions of Ni^{2+} exchanged in tetrahedral coordination inside zeolite framework [196-198]. The greenish gray Ni/H-Y catalyst also presents bands at 670 and 750 nm, not so clearly detected in other samples and which are assigned to d-d electron transition of Ni^{2+} ions in octahedral coordination [191, 199, 200]. Furthermore, other two bands can be observed in the NIR domain (from 800 to 2500 nm). The wide band centered at 1150 nm is attributed to the ν_1 ($^3A_{2g} \rightarrow {}^3T_{2g}$) transition of octahedrally coordinated Ni^{2+} and appears in all spectra of prepared samples indicating the presence of NiO. In contrast, the last band centered at 1410 nm is related to vibrations of surface hydroxyl groups of zeolite supports [86] and, as expected, is less intense for Ni/Na-zeolite catalysts than for Ni/H-zeolite catalysts.

The redox properties of the prepared samples were examined by H_2-TPR technique in order to analyze the reducibility of different nickel species dispersed on each zeolite. Figures 6.5a and b show the H_2-TPR runs for Ni/Y and Ni/BETA catalysts, respectively. In line with UV-vis-NIR results, the appearance of several peaks in TPR spectra indicates the presence of various Ni species with different reducibility. On the one hand, four defined H_2 consumption peaks can be observed for Ni/H-Y catalyst (Figure 6.5a). The peak at lowest temperature (450 °C) can be attributed to reduction of surface NiO particles interacting with the zeolitic support, whereas peaks located at 520 and 645 °C are attributed to reduction of tetrahedrally coordinated Ni^{2+} species located on supercages and sodalite cages, respectively [194, 199-202]. The peak at highest temperature, with a maximum at 730 °C, is related to reduction of octahedrally coordinated Ni^{2+} exchanged in hexagonal prisms, as was confirmed by UV-visible. On the other hand, a new peak can be distinguished at 385 °C for Ni/Na-Y catalyst. The position of this reduction peak is similar to the observed in the nickel oxide sample (insight Figure 6.5a), so it is associated with reduction of NiO particles weakly interacting with Na-Y zeolite and located in the external surface. The shift to lower temperature of H_2-TPR profile reveals that Ni/Na-Y is a more easily reducible catalyst than Ni/H-Y catalyst. This fact may be related to a less accessibility of Ni into the zeolite structure and to the donation of electrons from Na^+ to nickel [191].

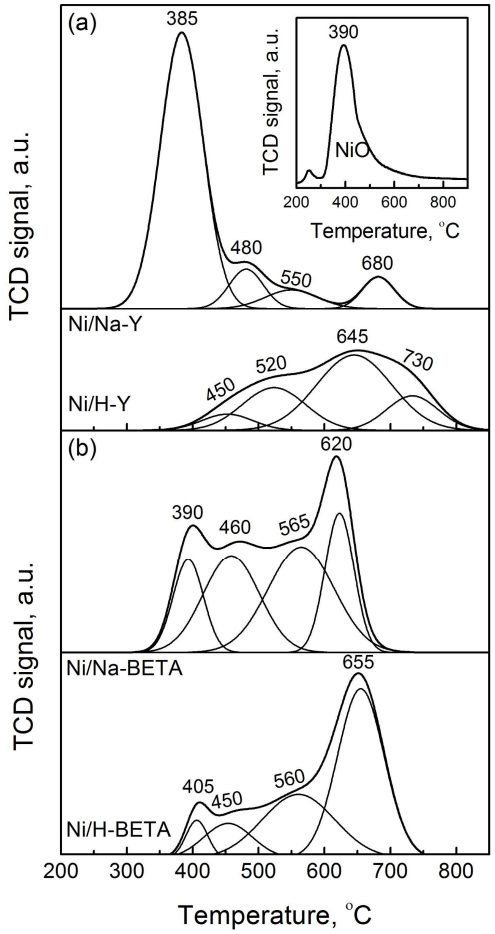

Figure 6.5. TPR profiles of (a) Y-zeolite (protonic and sodium) and (b) BETA-zeolite supported Ni catalysts.

Focusing on BETA supported catalysts (Figure 6.5b), unlike zeolite H-Y, BETA zeolite is not formed by cavities: its structure consists of a three-dimensional system of channels, so nickel location is different to that observed in the zeolite Y. For Ni/BETA catalysts four H_2 reduction peaks are also observed. The peaks at lowest temperatures, with maxima located near 400 and 450 °C, are related to reduction of NiO with different interaction degree with the support. The first peak at the lowest temperature is attributed to reduction of NiO placed on the outer surface while the second peak is assigned to reduction of certain population of NiO clusters with smaller size and higher

interaction with the support [195, 203, 204]. In contrast, peaks at higher temperatures indicate the presence of Ni^{2+} located at different sites: the peak centered around 560 °C is related to reduction of pseudo-tetrahedral Ni^{2+}, whereas the peak located between 620 and 655 °C is related to Ni^{2+} in hexagonal prisms [197, 198, 205-207]. In line with Y zeolite-based catalysts, shift of TPR profile to lower temperatures can be observed in Ni/Na-BETA due to the previously mentioned causes.

With the aim of quantifying the amount of Ni^{2+} reducible at temperatures below 500 °C, additional TPR tests of reduced samples were carried out (not shown). The pre-reduction was done under the same conditions used for the reductions prior to the activity tests: 500 °C for 1h with 20%H_2/He. As expected, TPR profiles of all catalysts exhibited a single H_2 consumption peak between 600 and 700 °C, which is associated with reduction of exchanged nickel. The amount of reduced nickel during pre-reduction process is quantified in the last column of Table 6.2 (page 175). Note that the percentage of reducible Ni^{2+} is above 90% for all catalysts, except for Ni/H-Y (43%), which showed a notable peak at 680 °C. This means that almost all nickel is getting reduced during activity tests for Ni/Na-Y, Ni/H-BETA and Ni/Na-BETA catalysts. Finally, it is worth to mention that calculated H_2/NiO ratios are between 0.9 and 1.1 for all the prepared catalysts, i.e., Ni^{2+} is the only reducible species.

6.1.2. CO_2 methanation activity

The performances of the prepared catalysts were evaluated by analyzing the obtained CO_2 conversions and CH_4 yields. It must be noted that, in all cases, CO was the only secondary product and that the carbon balance closed within $\pm$ 5%. First, Figure 6.6 compares the catalytic activity at increasing temperatures of protonic and sodium zeolites containing Ni. As a general trend, it can clearly be noticed that the presence of exchanged Na^+ in both zeolitic frameworks leads to greater CO_2 conversions in the range of studied temperatures. This effect is more pronounced for Y zeolite supported samples. In fact, the light-off T_{50} curve of Ni/Na-Y catalyst shifts 30 °C to lower temperatures, while light-off curve of Ni/Na-BETA catalyst is only shifted 15 °C. The greater activity of these catalysts, as already explained in H_2-TPR section (Figure 6.5),

is not only in line with the reducibility enhancement but also with the presence of weak CO_2 adsorption sites in Na-based catalysts. According to previous studies, the interaction between CO_2 and the support is improved by the presence of the alkali metal, resulting in a promoted CO_2 activation [191].

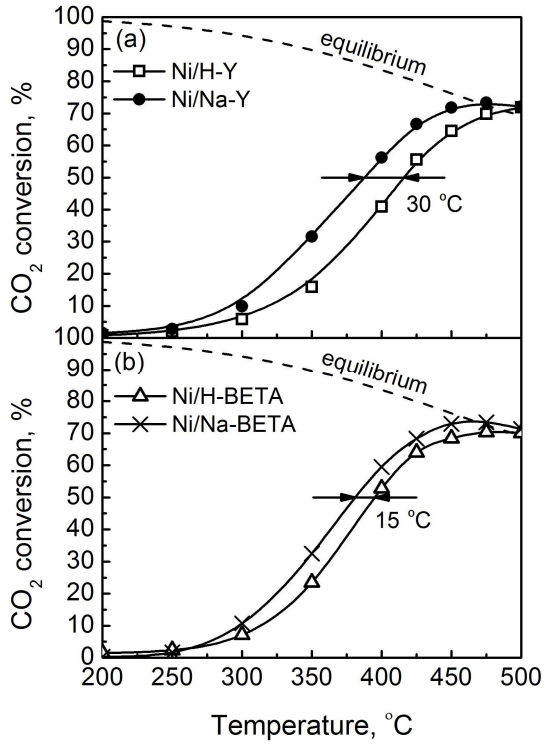

Figure 6.6. Effect of temperature on CO_2 conversion for (a) Y-zeolite (protonic and sodium) and (b) BETA-zeolite supported Ni catalysts.

By comparing CO_2 conversions of Na^+ free catalysts, greater activity is found for the Ni/H-BETA catalyst. On the one hand, Ni/H-Y sample (T_{50} = 415 °C) contains more internally located Ni species providing higher metal dispersion; however, Ni/H-BETA (T_{50} = 393 °C) sample presents a greater amount of reducible Ni species at 500 °C (95% vs. 43%) which are considered the active phase for CO_2 methanation [199, 208]. Therefore, the higher activity of Ni/H-BETA catalysts could be related to a larger available Ni^0 area during methanation reaction, as revealed H_2-TPR results shown in

Figure 6.5. In contrast, when comparing Na-exchanged supported catalysts, similar CO_2 conversions are observed in all range of studied temperatures. In both cases, 50% of CO_2 conversion is reached around 380 °C and the maximum CO_2 conversions are reached at 450 °C (X_{CO_2} = 73%). Although Ni/Na-Y catalyst has greater reducibility, according to the H_2-TPR results, Ni/Na-BETA catalyst contains more Ni^{2+} species inside the framework which could provide higher dispersion. Therefore, the same CO_2 methanation activity shown by both catalysts is explained by the presence of similar available surface of active phase during reaction.

Carbon species distribution at 3 different reaction temperatures for the prepared catalysts is illustrated in Figure 6.7.

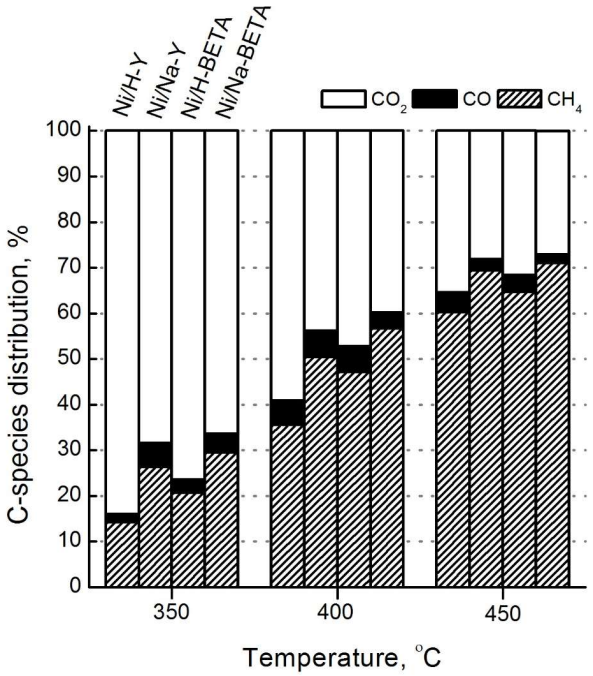

Figure 6.7. CO_2 conversion and C-species distribution at the reactor exit for Ni/zeolite catalysts at 350, 400 and 450 °C.

It can be observed that the highest CH_4 yield is reached at 450 °C, being Na^+ containing catalysts more productive than Ni/H-zeolite catalysts. CO yield, on the

contrary, is somewhat lower for Ni/H-zeolite catalysts at 350 °C and somewhat higher at 400 °C. Regardless the reaction temperature, methane yield of the samples reflects the following order: Ni/Na-BETA > Ni/Na-Y > Ni/H-BETA > Ni/H-Y. Thus, Ni/Na-BETA catalyst results in the most active and productive catalyst, showing maximum CO_2 conversion and CH_4 yield values of 73 and 71%, respectively. Indeed, the best catalytic performance of this catalyst is attributed to the enhanced CO_2 adsorption and to the higher dispersion of reducible Ni species.

6.2. THE INFLUENCE OF BASIC La_2O_3 ADDITION

The rare earth sesquioxides or lanthanide oxides (Ln_2O_3) are well known to be very basic metal oxides. Among them, lanthana (La_2O_3) is the one that exhibit the highest basicity, what makes it an interesting candidate as active phase or support of basic solid catalysts. Nevertheless, one of the main drawbacks of La_2O_3 is its low specific surface area and pore volume, which prevents the proper dispersion of large metal loadings along its surface. Besides, in contact with atmospheric CO_2 and H_2O, lanthana can suffer from strong textural, structural and chemical changes even at low temperature [209]. Accordingly, in order to better benefit from its catalytic properties, it is usually employed as a promoter instead of as a support. In fact, according to recent investigations, this lanthanide oxide acts as an excellent promoter of dry reforming of methane over Ni/Al_2O_3 formulation. Al-Fatesh et al. [210] reported that the addition of La_2O_3 provides strong Lewis basic sites, which leads to an increase of CO_2 chemisorption capacity (formation of $La_2O_2CO_3$) and, consequently, to a decrease of non-desirable carbon deposits formation via reverse Boudouard reaction ($CO_2 + C \rightleftarrows 2CO$). On the other hand, Cui et al. [211] demonstrated that incorporation of La_2O_3 to Ni/γ-Al_2O_3 catalyst enhances the Ni dispersion and slows down the sintering of Ni particles during the reforming reaction. Furthermore, it usually highly interacts with alumina increasing its mechanical strength and its thermal stability, avoiding the phase transition from γ- to α-Al_2O_3 [212, 213]. Thus, it seems that La_2O_3 not only boost the activity but also the stability of dry reforming catalysts.

Noteworthy, this rare earth element has already proven to be an effective promoter of CO_2 methanation. Garbarino et al. [57] reported that lanthanum addition strongly increases the activity and selectivity of Ni/γ-Al_2O_3 catalyst at low temperature (T < 375 °C, kinetic regime), since alumina-lanthana support presents higher basicity than bare alumina, which translates in stronger adsorption of CO_2 in form of carbonates acting as reactant reservoir. Likewise, Wierzbicki et al. [214] showed that incorporation of lanthanum as trivalent cation (La^{3+}) in a hydrotalcite-type catalytic precursor led to an increase of Ni reducibility and dispersion of the resulting catalyst as well as a change of distribution and number of basic sites, which was almost doubled. Considering the background, we decided to take advantage of the high external surface area of Na-BETA to impregnated various increasing loadings of La_2O_3 as structural and basic promoter. In this section, characterization, activity and stability results of Ni-xLa_2O_3/Na-BETA (x = 0, 5, 10, 15wt% of La_2O_3) catalysts are shown and discussed.

6.2.1. Characterization

XRD spectra of calcined and reduced Na-BETA supported Ni catalysts after the impregnation of different amounts of La_2O_3 (5, 10 and 15%) are displayed in Figure 6.8. XRD spectra of calcined catalysts show peaks at 37.3, 43.3 and 62.9° 2θ, whereas spectra of reduced catalysts show peaks at 44.3 and 51.7 ° 2θ. The former correspond to NiO (bunsenite phase), while the latter are characteristic of elemental Ni. However, the absence of La_2O_3 characteristic diffraction peaks at 30.0, 39.5 and 46.1° 2θ corresponding to La_2O_3 suggests the formation of an amorphous phase. In fact, the XRD backgrounds of La containing samples are lifted in 25-35 ° 2θ region with respect to Na-BETA sample, indicating a greater proportion of amorphous material.

Table 6.3 shows Ni crystallite sizes of La-containing catalysts calculated by the Scherrer equation. It can be noticed that Ni dispersion increases with the addition of La_2O_3 loadings; i.e., the higher the content of La_2O_3, the smaller the Ni crystallite size. In fact, the addition of 15% of La_2O_3 to the Ni/Na-BETA catalyst reduces the Ni crystallite size from 20.1 to 7.1 nm, providing higher active phase dispersions, since La_2O_3 acts as a thermal stabilizer of Ni [91, 211, 215].

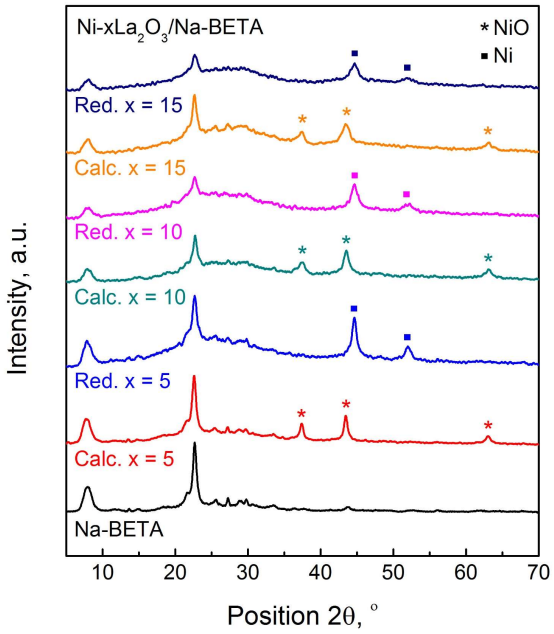

Figure 6.8. XRD patterns of calcined and reduced Ni/Na-BETA catalysts with different content of La_2O_3.

Table 6.3. Physicochemical properties of Ni-La_2O_3/Na-BETA catalysts.

Sample	τ_{Ni} (nm)[a]	S_{EXT} ($m^2\,g^{-1}$)[b]	V_{micro} ($cm^3\,g^{-1}$)[b]
Na-BETA	-	224.9	0.13
Ni/Na-BETA	20.1	191.4	0.1
Ni-5La_2O_3/Na-BETA	12.5	156.8	0.09
Ni-10La_2O_3/Na-BETA	8.7	142.3	0.08
Ni-15La_2O_3/Na-BETA	7.1	132.6	0.07

[a]Estimated by Scherrer equation.
[b]Determined by application of t-Plot method.

N_2 adsorption-desorption isotherms at 77 K of La-containing Ni/Na-BETA catalysts as well as those of Na-BETA support were also measured (not shown). Similar isotherm shapes were observed in all cases (type I and type IV isotherms combination), suggesting that lanthana addition does not modify considerably the textural properties

of Na-BETA zeolite. Note that external surface areas together with pore volumes are summarized in Table 6.3 and evolution of textural properties is depicted in Figure 6.9. It can be seen that impregnation of increasing loadings of La_2O_3 results in a progressive decrease of the external surface area (S_{EXT}), which means that impregnated lanthana is located in the outer surface of the zeolite. In fact, S_{EXT} decreases from 224.9 $m^2 \cdot g^{-1}$ in the Na-BETA catalyst down to 132.6 $m^2 \cdot g^{-1}$ in the 15% lanthana impregnated catalyst. In the same line, specific surface area also decreases with metal content, as shown in Figure 6.9. Regarding the pore volume, a similar trend is observed: the higher the metallic load supported on the zeolite, the lower the pore volume due to partial blockage of pores [194, 195, 216]. It is worth to mention that almost no difference can be observed between 15% and 10% La_2O_3 loaded catalysts.

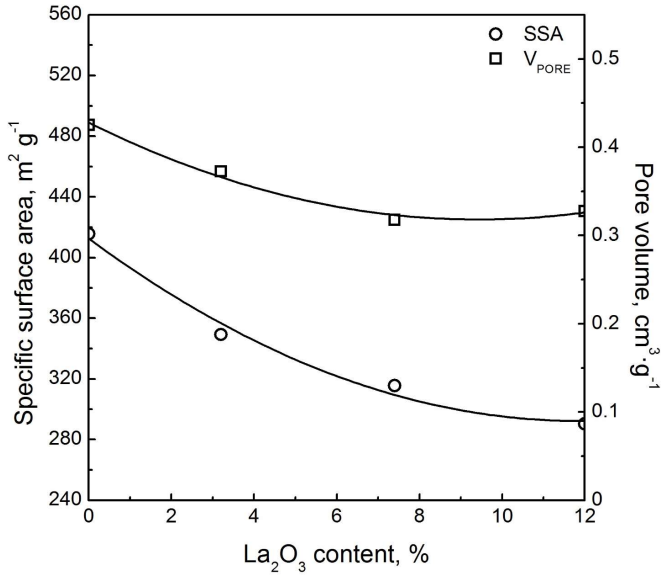

Figure 6.9. Effect of lanthana incorporation onto Na-BETA on the specific surface area and pore volume.

The basicity of different La_2O_3/Na-BETA samples was measured by TPD using CO_2 as probe gas. CO_2-TPD profiles in Figure 6.10 shows that all these samples contain different CO_2 desorption sites. According to desorption temperature, three different basic sites are detected: weak (T < 150 °C), medium (T = 150-550 °C) and strong (T >

550 °C) [91, 153, 209]. For 5%La_2O_3/Na-BETA sample, two peaks centered at 100 and 190 °C are observed, which are attributed to CO_2 desorption from weak (surface OH^-) and medium (acid-base Lewis pairs) basic sites, whereas samples with 10 and 15% of La_2O_3 present one additional peak centered at 640 °C, which is assigned to bulk carbonate decomposition [210]. However, this strongly attached CO_2 may not participate in the CO_2 methanation, since it is desorbed at temperatures above those of reaction. CO_2 desorption quantification obtained from TPD spectra reveal that lanthana impregnation over Na-BETA results in a considerable increase of the surface basicity due to the formation of new basic sites with different strength. Thus, the higher the La_2O_3 content, the higher the number and strength of basic sites.

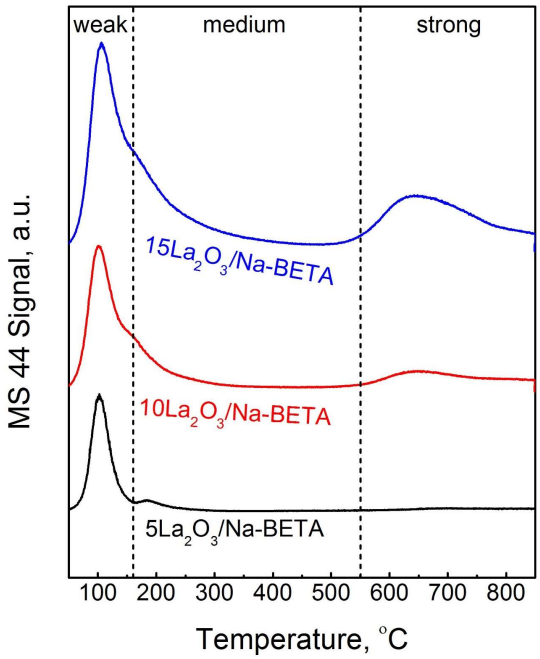

Figure 6.10. CO_2-TPD profiles of Na-BETA promoted with different lanthana loadings.

The effect of La_2O_3 addition on distribution and reducibility of Ni species dispersed on the catalysts was determined by H_2-TPR. Before carrying out these experiments, catalysts were degasified for 30 min with 5%O_2/He at 500 °C in order to remove weakly chemisorbed CO_2. Then, H_2 consumption was followed by a TCD detector and,

additionally, strongly attached CO_2 desorption was followed by mass spectrometry. The H_2-TPR spectra and CO_2 MS profiles of samples with different lanthana content are shown in Figure 6.11. Below 500 °C, a main H_2 consumption peak with a maximum close to 400 °C is observed for all catalysts, which is attributed to reduction of NiO located in the external surface of the zeolite [203, 204]. Above 500 °C, in contrast, the growing mass 44 signal (drawn in dashed line) confirms strongly attached CO_2 desorption and hence, the recorded TCD signal cannot be attributed only to H_2 consumption. Nevertheless, the peak appearing above 600 °C must be related to reduction of Ni^{2+} located inside BEA framework [207].

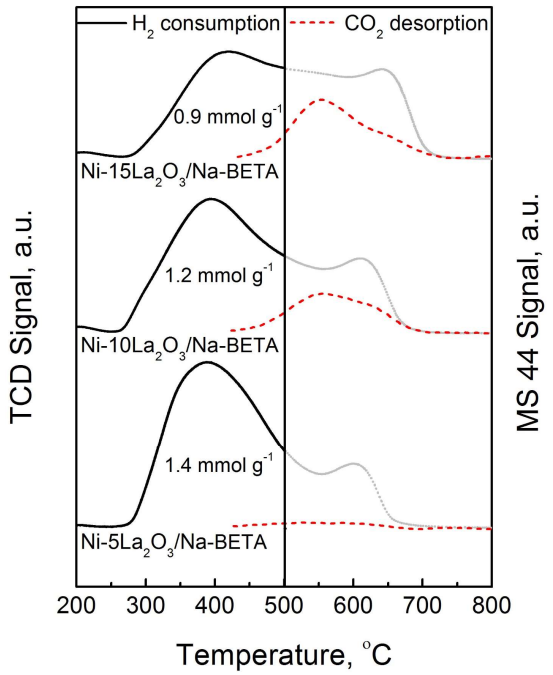

Figure 6.11. Evolution of H_2-TPR and MS 44 signal with temperature for La_2O_3-promoted Ni/Na-BETA catalysts.

When comparing H_2-TPR profiles of the lanthana based catalysts, a shift to higher temperatures with increasing the La_2O_3 loading is observed. This suggests that the presence of La_2O_3 strengthens the interaction between nickel and the support, due to

an increase of the nickel polarization [211, 217]. From integration of TPR profiles up to 500 °C, the reducibility of the samples was estimated and reflects this order: Ni/5La_2O_3/Na-BETA > Ni/10La_2O_3/Na-BETA > Ni/15La_2O_3/Na-BETA. Therefore, the 5% La_2O_3 loaded catalyst presents the highest reducibility. Note that H_2/NiO values are above the stoichiometric ratio, among 1.1 and 1.4, since CO_2 is desorbed during H_2-TPR tests, as demonstrated in Figure 6.11.

In order to analyze the nature and surface distribution of La and Ni species, XPS measurements were carried out. Figures 6.12a and b show XPS spectra corresponding to Ni 2p and La 3d core levels for fresh and used catalysts, respectively.

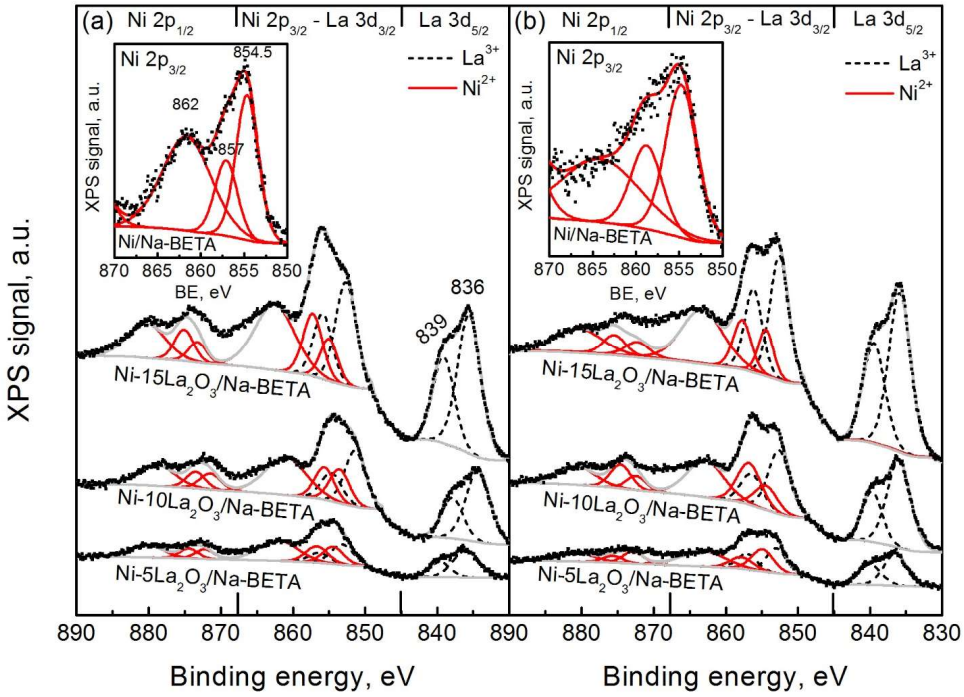

Figure 6.12. XPS spectra for unpromoted and La_2O_3-promoted Ni/Na-BETA catalysts; (a) fresh and (b) after reaction.

First, for fresh Ni/Na-BETA catalyst (insight Figure 6.12a), Ni $2p_{3/2}$ region reveals two peaks at ≈ 854.5 and ≈ 857 eV together with a broad shake-up satellite peak at

around 862 eV. The main peak at lowest binding energies is attributed to NiO weakly interacting with Na-BETA zeolite, whereas the second one corresponds to the Ni^{2+} cation in exchangeable positions [98, 197]. No peak corresponding to reduced nickel (Ni^0) at ≈ 853 eV was detected. On the other hand, La_2O_3 addition to Ni/Na-BETA catalysts reveals a new main peak in the La $3d_{5/2}$ region at ≈ 835.7 and a satellite peak at ≈ 838.9 eV. Note that these peaks, assigned to supported La^{3+} [209], intensify with La_2O_3 content, which indicates a progressive increase of the La on the surface. Additionally, a main peak at ≈ 852.4 eV together with its satellite peak at 856.3 are shown in La $3d_{3/2}$ - Ni $2p_{3/2}$ region, also corresponding to La^{3+}. Regardless the amount of La added in the catalysts, XPS spectra recorded after reaction showed similar binding energies of La^{3+}, i.e., La_2O_3 does not suffer from relevant changes after reaction and no Ni^0 was observed, which indicates that nickel is easily passivated after reaction at ambient temperature [143] (see insight Figure 6.12b).

From integration of XPS spectra, surface carbon content as well as Ni/Si and La/Si atomic ratios of fresh and used Ni-La_2O_3/Na-BETA catalysts were calculated and data is summarized in Table 4. It should be noticed that the content of surface carbon remains similar after reaction in all cases suggesting that no coke was formed during reaction tests. As deduced from Table 4, Ni/Si and La/Si atomic ratios increase with La_2O_3 content, i.e., La_2O_3 addition improves NiO dispersion. This trend is in agreement with XRD results according to which a decrease of NiO crystallite size with La_2O_3 loading was observed. Finally, samples submitted to reaction suffer from a slight decrease of Ni/Si ratio and a small increase of La/Si ratio, probably due to Ni sintering during tests.

Table 6.4. Surface composition of Ni-La_2O_3/Na-BETA catalysts, before and after reaction.

	Before reaction			**After rection**		
Catalyst	**C (at. %)**	**Ni/Si**	**La/Si**	**C (at. %)**	**Ni/Si**	**La/Si**
Ni/Na-BETA	3.0	0.030	-	3.0	0.025	-
Ni-5La_2O_3/Na-BETA	2.9	0.035	0.012	3.9	0.031	0.013
Ni-10La_2O_3/Na-BETA	2.8	0.068	0.032	2.4	0.067	0.037
Ni-15La_2O_3/Na-BETA	3.3	0.110	0.063	2.2	0.086	0.067

The effect of lanthana on nickel dispersion was also analyzed by transmission electron microscopy. Figures 6.13a and d show TEM micrographs of reduced Ni/Na-BETA and Ni-10La_2O_3/Na-BETA catalysts, respectively. Unlike lanthana particles, in those images, Ni particles are clearly observable. Notice that no changes occur in the morphology of nickel particle (spherical) with the impregnation of 10% of La_2O_3. Nevertheless, changes in particle size distribution are observed (visualized and calculated from several TEM images), being the distribution notably narrower for La containing sample. This suggests that lantana, as structural promoter, controls the growth of nickel particle during calcination. In the same line, smaller Ni particles are observed for Ni-10La_2O_3/Na-BETA. It presents an average particle size of 10.1 nm (D_{Ni} = 12%), whereas Ni/Na-BETA catalyst an average of 17.7 nm (D_{Ni} = 7%). Therefore, in agreement with XRD and XPS, La_2O_3 addition enhances nickel dispersion.

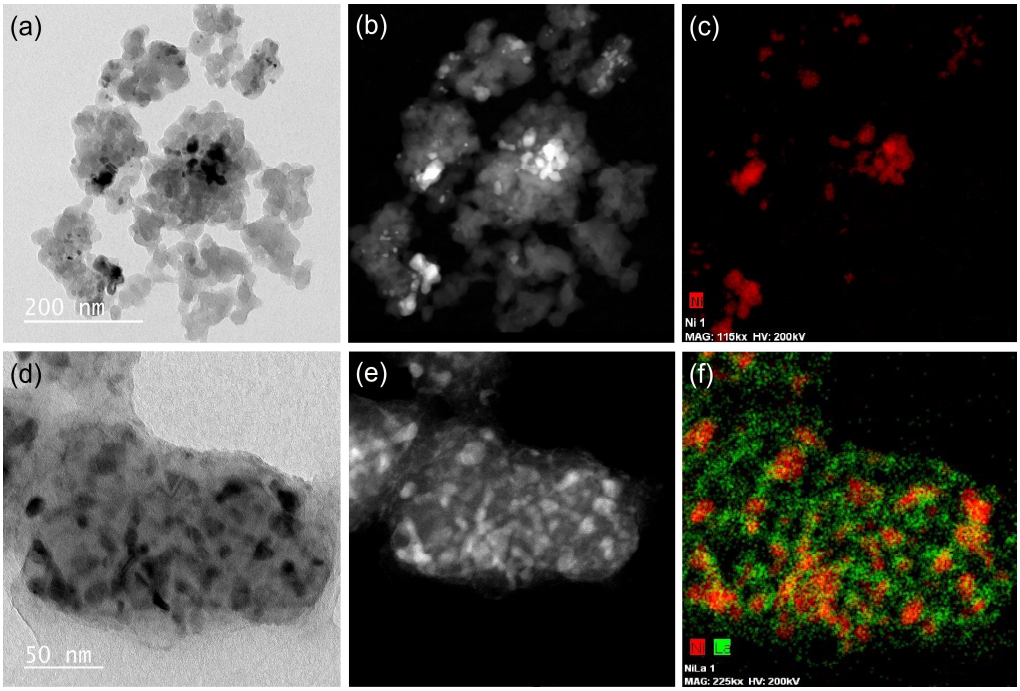

Figure 6.13. TEM micrographs (a and b), STEM images (b and e) and EDX maps (c and f) of Ni/Na-BETA and Ni-10La_2O_3/Na-BETA catalysts.

As the presence of lanthana was not detectable by TEM, additionally, STEM combined with EDX-elemental mapping was performed. This technique is suitable to differentiate between two or more elements, since provides high resolution element mapping. STEM images together with EDX maps of Ni/Na-BETA and Ni-10La_2O_3/Na-BETA catalysts are displayed in Figures 6.13b-c and 6.13e-f, respectively. By comparing STEM image and Ni mapping (red colored) of Ni/Na-BETA sample, it is confirmed that Ni is dispersed as spherical particles. Interestingly, EDX map of Ni-10La_2O_3/Na-BETA catalyst shows that La (green colored) is homogeneously dispersed and partially covering the surface of the zeolite and surrounding nickel. Similar homogeneous dispersion of supported La_2O_3 on Al_2O_3 has already been reported by Boukha et al. [209].

6.2.2. Activity and stability

Figure 6.14 shows the effect of La_2O_3 content on CO_2 conversion and the temperature-dependent equilibrium conversion in a dashed line.

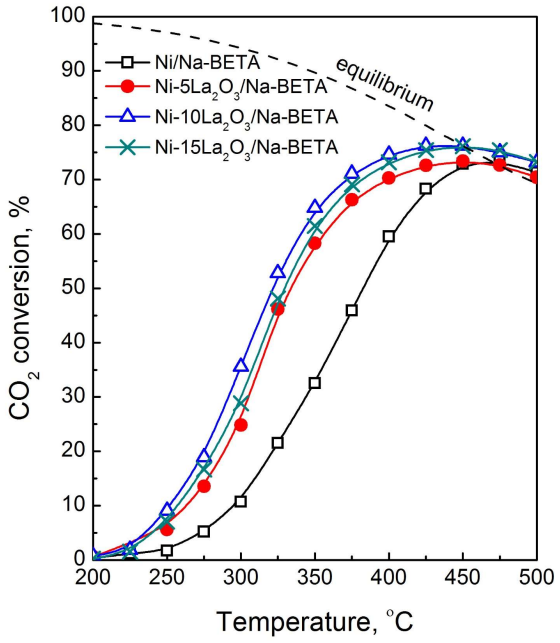

Figure 6.14. Light-off curves of La_2O_3-promoted Ni/Na-BETA catalysts.

The onset temperature for CO_2 methanation is 250 °C and thermodynamic equilibrium is reached for every catalyst. The required temperatures for X_{CO_2} = 50% are 322, 330, 334 and 381°C for Ni-10La_2O_3, Ni-15La_2O_3, Ni-5La_2O_3 and Ni/Na-BETA catalysts, respectively. The increase in La_2O_3 loading from 5 to 10% leads to higher CO_2 conversions at every temperature, which suggests that the related gain in basicity results in the desired promoter effect. However, although the increase in lanthana nominal content (from 5 to 10%) leads to greater activity, impregnation of La_2O_3 loadings above 10% seems not to be necessary since non enhancement in CO_2 methanation is observed.

According to characterization results, the higher CO_2 methanation activity of Ni-10La_2O_3/Na-BETA catalyst in comparison to Ni/Na-BETA catalyst is related to the greater amount of smaller Ni particles (8.7 against 20.1 nm) and to the presence of a considerable higher number of weak and medium basic sites (16 vs. 1 μmol·g^{-1}). Moreover, 10% lanthana loaded catalyst revealed highest reducibility, according to H_2-TPR results. On the other hand, the slight decrease in catalytic activity observed for Ni-15La_2O_3/Na-BETA catalyst is associated with the lower textural properties and reducibility shown in Figures 6.9 and 11. In Figure 6.15, the carbon species distribution at 300, 350 and 400 °C is shown for Ni/Na-BETA and Ni-10La_2O_3/Na-BETA catalysts. As in the case of Ni/zeolite catalysts, CO from RWGS was the only detected by-product being the carbon balance closed between 95 – 105%. It can be observed that CH_4 yield is increased and that CO yield is considerably reduced by addition of 10% of La_2O_3 for all studied temperatures. The greatest difference among product yields occurs at the reaction temperature of 350 °C: CH_4 yield increases from 30 to 65%, whereas CO yield decreases from 4 to 0.4%. In line with characterization results, the better catalytic performance observed in lanthana containing catalyst is related to a higher amount of active sites where CO_2 can be adsorbed and then hydrogenated to methane. According to Wierzbicki et al. [214, 218], lanthanum addition not only provides new medium strength basic sites, but also modifies Ni properties enhancing its CO_2 adsorption capacity. Therefore, it can be concluded that La_2O_3 addition promotes the CO_2 conversion and the CH_4 yield.

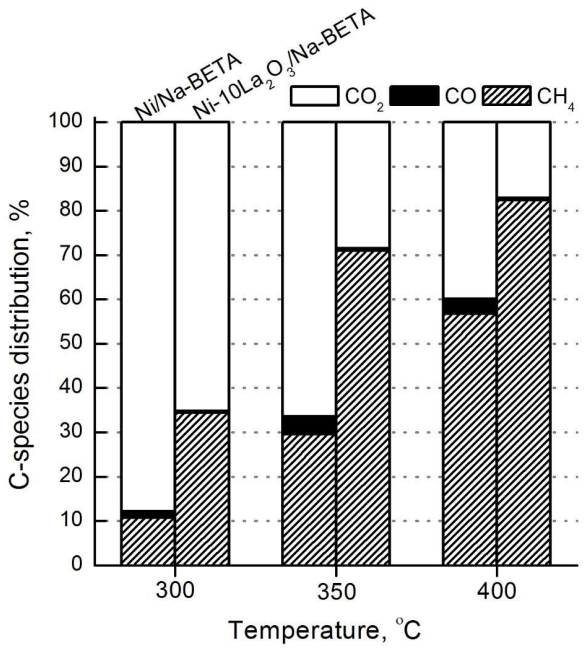

Figure 6.15. CO_2 conversion and C-species distribution of Ni/Na-BETA and Ni-10La_2O_3/Na-BETA catalysts at 300, 350 and 400 °C.

Activity comparison between zeolite-based catalysts prepared in this work with others recently reported in literature is shown in Table 6.5 [53, 58, 91, 199]. Note that the comparison is not straightforward since reaction is performed at different conditions and catalysts do not present the same Ni loading. In general, it can be appreciated that the addition of a promoter enhances notably the catalytic activity for each formulation. For instance, the addition of V_2O_5 to Ni/Al_2O_3 catalyst improves nickel dispersion and prevents coke deposition [58], whereas CeO_2 impregnation on Ni/MCM-41 formulation results in additional CO_2 activation leading to higher conversions [53]. Noteworthy, I. Graça et al. [199] studied the performance of a formulation analogous to ours, using CeO_2 (RedOx promoter) instead of La_2O_3 (structural promoter) and Y instead of BETA zeolite. The activity of the promoted catalysts (14 Ni-7Ce/USY vs. 10Ni-10La_2O_3/Na-BETA) is similar, being slightly lower for 14Ni-7Ce/USY catalyst due to a smaller space time (W/F_{A0}). However, Ni-La-Al hydrotalcite derived catalyst [91] shows the highest catalytic performance: X_{CO_2} and

Table 6.5. Comparison between activity results achieved by the prepared Ni/BETA catalysts and those (unpromoted and promoted) reported in literature.

Catalytic formulation	**Q_{TOTAL} ($cm^3\ min^{-1}$)**	**Feed ratio (H_2/CO_2/He)**	**GHSV (h^{-1})**	**W/F_{A0} ($g\ h\ mol^{-1}$)**	**X_{CO2} at 350 °C (%)**	**S_{CH4} at 350 °C (%)**	**Ref.**
$20NiO/Al_2O_3$	150	12/3/5	NA	1.7	42	97	[1]
$20NiO\text{-}5V_2O_3/Al_2O_3$	150	12/3/5	NA	1.7	76	> 99	[1]
15Ni/MCM-41	250	36/9/10	15000	1.6	50	95	[2]
15Ce-15Ni/MCM-41	250	36/9/10	15000	1.6	60	97	[2]
15Ni-HT	100	12/3/5	12000	NA	74	99	[45]
15Ni2La-HT	100	12/3/5	12000	NA	78	98	[45]
14Ni/USY	250	36/9/10	43000	1.6	42	93	[27]
14Ni-7Ce/USY	250	36/9/10	43000	1.6	57	> 95	[27]
10Ni/Na-BETA	250	16/4/5	10000	4.7	33	88	This work
10Ni-10La/Na-BETA	250	16/4/5	10000	4.7	65	99	This work

S_{CH_4} of 78 and 98% at 350 °C, indicating that zeolite-supported catalysts activity still has room for improvement.

Finally, the stability of the most active catalyst was evaluated after 24h on stream at 350 °C (see Figure 6.16). Note that CO_2 conversion decreases slightly with time. This deactivation could be related to both active site sintering and coke formation. The second hypothesis was dismissed carrying out a thermo-gravimetric test in 5%O_2/He of the aged catalyst according to which no relevant mass loss was observed related to coke oxidation (not shown). After 10h-on-stream, anyway, it seems that catalytic activity remains quite stable since similar CO_2 conversions are observed. In addition, the catalyst is very stable in terms of selectivity: non decrease in CH_4 selectivity is observed after 24 h on stream.

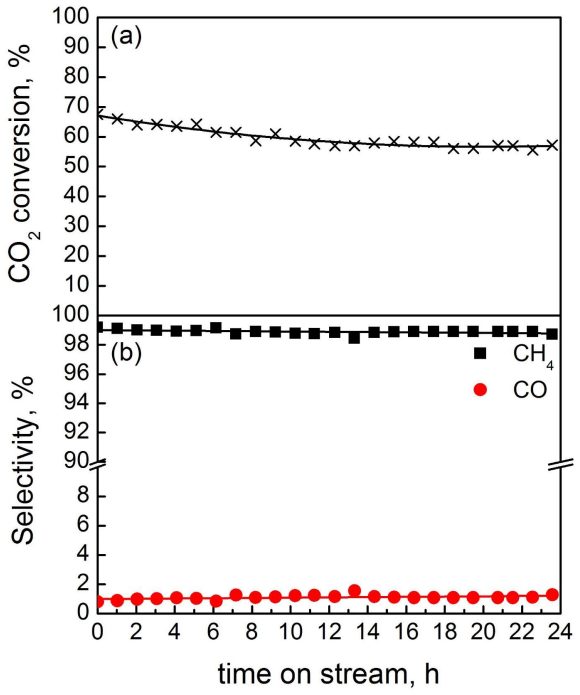

Figure 6.16. Evolution of (a) CO_2 conversion and (b) selectivity to CH_4/CO with time of stream over 24h for Ni-10La_2O_3/Na-BETA catalyst.

6.3. OVERALL VIEW AND CONCLUSIONS

The catalytic performance of Y- and BETA-zeolites supported Ni catalysts for CO_2 methanation was compared and additionally, the effect of La_2O_3 addition as promoter was evaluated.

The reducibility and dispersion of Ni species played an important role in CO_2 methanation: the higher the value of these properties, the better the catalytic performance. Ni is more dispersed in the form of NiO and Ni^{2+} species on H-Y than on H-BETA due to its higher crystallinity and a more accessible framework. However, the reducibility of Ni is higher in the Ni/H-BETA than in the Ni/H-Y catalyst due to a major proportion of NiO species located on the outer surface of the catalyst. After reduction at 500 °C, H-BETA zeolite supported Ni catalysts present a higher surface of reduced nickel (the active phase for CO_2 methanation) and hence, this leads to a superior activity and selectivity. Neutralization of both Y- and BETA-zeolites by addition of exchanged Na^+ improves the catalytic performance (T_{50} decreases in 30 and 15 ^oC, respectively). This enhancement is not only due to a greater reducibility, but also to the generation of some weak basicity that improves CO_2 adsorption over the zeolite. Although not big differences in CO_2 conversions are observed comparing Ni/Na-Y and Ni/Na-BETA catalysts, the latter achieves more selectivity towards CH_4 than Ni/Na-Y. Therefore, it can be concluded that Ni/Na-BETA is the best catalyst among those studied in this chapter to efficiently carry out the hydrogenation of CO_2 into methane.

According to the physicochemical properties of the samples, the addition of increasing loadings of La_2O_3 to Ni-zeolite catalysts promoted dispersion into smaller Ni particles and improved the CO_2 adsorption capacity of the zeolite. These enhancements in the surface basicity and the Ni dispersion provide a greater amount of both basic and active sites, over which CO_2 can be adsorbed and then hydrogenated into CH_4. In fact, double CO_2 conversion with eventually total selectivity towards CH_4 can be achieved especially at low and intermediate temperatures with Ni-10La_2O_3/Na-BETA, which results in the optimal composition. In contrast, higher loading than 10% of La_2O_3 do not achieve additional enhancement of the catalytic performance, since

detrimental of the textural properties exceeds the beneficial effect of CO_2 adsorption and hydrogenation sites. After 24 h on stream, this formulation proved to be quite stable in terms of activity and selectivity.

Chapter 7

MOLECULAR INSIGTHS INTO CO_2 METHANATION MECHANISM ON Ni/BETA CATALYSTS

ABSTRACT

In this chapter, surface CO_2 adsorption and CO_2 methanation reaction are systematically studied by operando FTIR spectroscopy on BETA zeolite supported samples with varying chemical composition (H-BETA, Na-BETA, La_2O_3/Na-BETA, Ni-Na/BETA and Ni-La_2O_3/Na-BETA), which were characterized and evaluated for CO_2 methanation in the previous chapter. This works aims to determine the reaction pathways on Ni/Na-BETA and Ni-10L_2O_3/Na-BETA catalysts, while elucidating the roles of each element in the CO_2 activation and subsequent hydrogenation of adsorbed species. The CO_2 adsorption experiments (5% CO_2/Ar) reveal that the type and concentration of adsorbed species increases by incorporation of exchanged Na^+ and, specially, impregnation of La_2O_3 rare earth oxide. In fact, La_2O_3/Na-BETA sample presents all type of identified C-species: molecular CO_2 physisorbed on Na^+, bidentate carbonates on surface O^{2-} Lewis basic sites, monodentate carbonates on La-sites and bulk lanthanum carbonates. By switching gas stream to reactive 5% CO_2/20% H_2/Ar mixture, adsorbed species except bulk carbonate are hydrogenated into formate, which is considered reaction intermediate for both formulations. However, evolution of surface species absorbance with extension of reaction points out that CO_2 methanation takes place via dissociative mechanism (H-assisted CO formation and further hydrogenation into CH_4) on Ni/Na-BETA catalyst and, on the contrary, through associative mechanism (direct formate hydrogenation into CH_4) on Ni-10La_2O_3/Na-BETA catalyst. The latter results in much more efficient bifunctional catalytic formulation due to synergistic collaboration between Ni^0 (H_2 dissociation) and La_2O_3 (CO_2 adsorption).

7. MOLECULAR INSIGTHS INTO CO_2 METHANATION MECHANISM ON Ni/BETA CATALYSTS

Recent studies, including that of previous chapter, have demonstrated that, in general, the presence of rare earth oxides (e.g., CeO_2, La_2O_3 and Y_2O_3) as promoter [215, 217, 219] or support [220-222] leads to an enhanced catalytic performance of Ni-based catalysts. Among such oxides, CeO_2 has been the most studied due to its well-known capacity to improve Ni dispersion and specially activate CO_2. Indeed, it can alter the reaction pathway partly owing to it provides medium-strength basic centers (surface O^{2-} linked to Ce^{III} or Ce^{IV} and oxygen vacancies) over which CO_2 can be adsorbed facilitating its further hydrogenation into CH_4 [153, 167, 180, 223-225].

The pioneers in studying CO_2 methanation mechanism on Ce-containing Ni catalysts were Aldana et al. [167]. These authors analyzed CO_2 methanation pathway on Ni/SiO_2 and Ni/CeO_2-ZrO_2 catalysts by operando FTIR, concluding that, unlike Ni/SiO_2, Ni/ceria-zirconia formulation does not require the presence of adsorbed CO as reaction intermediate. In fact, they proposed the associative mechanism, which assumes that formate species ($HCOO^-$) is the essential intermediate for methane production. After that, Pan et al. [153, 223] compared the promoting effect of medium strength basic sites over Ni/ceria-zirconia and Ni/Al_2O_3 catalysts. They also found greater CO_2 methanation activity for Ce-containing catalyst, which was attributed to the presence of higher amount of medium strength basic sites. According to them, these sites are responsible of monodentate formate species formation (arising from carbonates (CO_3^{2-})), which seems to be more easily reducible species than those in bidentate coordination observed on Ni/Al_2O_3 catalyst. Finally, Westermann et al. [148, 224] studied CO_2 methanation mechanism over unpromoted [148] and Ce-promoted [224] USY zeolite supported catalysts. According to them, formates coming from physisorbed CO_2 as well as chemisorbed carbonates are almost exclusively dissociated to carbonyls, whereas over Ni-Ce/USY catalyst, which contains enhanced CO_2 adsorption capacity, formates are directly hydrogenated into CH_4.

On the other hand, Wang et al. [180] analyzed CO_2 methanation mechanism on Ru/CeO_2 catalyst by operando DRIFTS. Noteworthy, this catalyst was reported to be more active than Ni/CeO_2 or Ni/Ce-Zr formulations, being able to achieve equilibrium CO_2 conversion at 100 °C lower temperature (250 vs. 350 °C) due to the capacity of Ru to dissociate H_2 (i.e., provide H atoms) at low temperature. They reported that CO_2 hydrogenation into CH_4 takes place via associative mechanism on Ru/CeO_2 sample, according to which formates formed from carboxylates (CO_2^-) are further reduced into methoxy species (CH_xO). Afterwards, methoxy species are released as methanol or further hydrogenated into CH_4. Sharma et al. [225] also observed a mechanism involving methoxy species on Ru-substituted CeO_2 catalyst, but with the difference that such species is formed from adsorbed CO methanation over an oxygen vacancy rather than from direct formate hydrogenation. This change in reaction mechanism compared to that observed on Ru/CeO_2 sample was associated with different structure of Ru-substituted CeO_2 catalyst (supported vs. single phase catalyst).

However, the mechanistic role of La_2O_3 in CO_2 methanation over Ni-based catalysts has scarcely been studied. That motivated the objective of this chapter trying to look for further insights into CO_2 methanation reaction mechanisms at molecular scale over La_2O_3-promoted zeolite Na-BETA supported Ni catalysts evaluated in Chapter 6. In this chapter, CO_2 adsorption as well as CO_2 hydrogenation are systematically studied by FTIR spectroscopy over a series of BETA zeolite supported samples with different and increasing composition (some of them with Na^+, La_2O_3 and/or Ni), in order to identify reaction intermediates and elucidate the role of each component (active metal, promoter and support) on the CO_2 methanation mechanism.

7.1. SURFACE CHARACTERIZATION OF BETA ZEOLITE

The indispensable step before performing any type of IR test is to identify the functional groups of the catalytic support. Thus, first of all, spectra without subtraction of pre-reduced BETA samples were analysed in order to identify the type of adsorbed hydroxyls species on initial supports. Figure 7.1 shows the FTIR spectra of H-BETA and

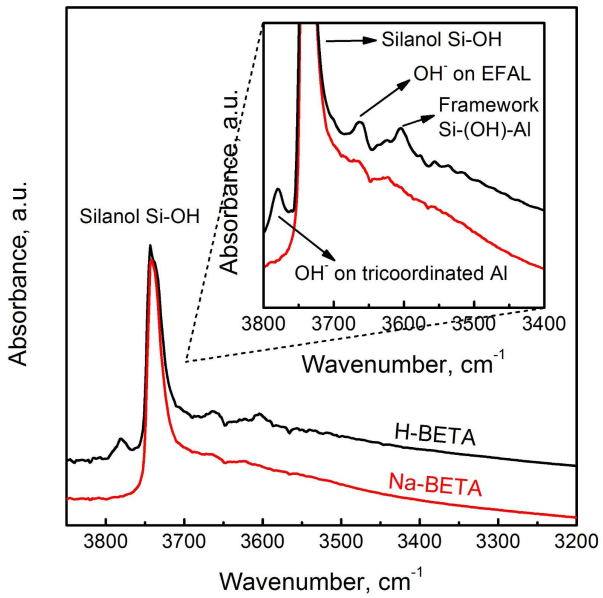

Figure 7.1. FTIR spectra recorded under Ar at 150 °C of H-BETA and Na-BETA supports.

Na-BETA supports in the OH^- region (3850-3450 cm^{-1}) recorded after pretreatment at 500 °C under 5% H_2/Ar flow.

In the case of H-BETA, four bands can be observed, being associated with OH^- groups located in different sites. Indeed, the band at 3605 cm^{-1} could be attributed to bridging hydroxyl groups (Si-(OH)-Al, Brønsted acid sites) in the framework [226]. On the contrary, bands at 3781 and 3663 cm^{-1} correspond to OH^- species on extra framework positions [227], being the first attributed to hydroxyls on tri-coordinated aluminium atoms partly linked to the framework (basic sites), and the latter to OH^- groups on extra framework aluminium aggregates. Finally, the intense peak at around 3740 cm^{-1} is due to silanol groups (Si-OH) vibration [226]. It can be observed that the spectrum of Na-BETA sample does not present hydroxyl bands at some frequencies, which indicates that Na^+ was successfully incorporated in framework Brønsted sites by replacing protons (H^+) and maybe also in extra-framework positions.

7.2. CO_2 ACTIVATION

The IR spectra of CO_2 adsorbed on metal oxides usually show bands that can be assigned to chemisorbed as well as physically adsorbed molecules. The identification of such species is essential to understand the mechanism of heterogeneously catalysed CO_2 methanation reaction. As mentioned elsewhere, the first elemental step in CO_2 hydrogenation mechanism is CO_2 adsorption or activation. Thus, in this section, the interaction of CO_2 with the surface of BETA zeolite supported samples and catalysts with different and increasing composition is studied. First, evolution of CO_2 adsorption FTIR spectra is followed with exposure time (t = 0-30 min) and then, the effect of temperature (T = 150-400 °C) on chemisorbed species concentration is analysed in Temperature Programmed Adsorption (TPA) experiments.

The spectra recorded at 150 °C during CO_2 adsorption on H-BETA and Na-BETA are shown in Figure 7.2. As seen, after flowing 20 mL min^{-1} 5% CO_2/Ar though the sample, several bands are differentiated, whose absorbance is increased with exposure time. According to Busca and Lorenzelli [228], the coordination of adsorbed carbonate species can be identified on the basis of the ν_3 splitting vibration ($\Delta\nu_3$). These authors suggested that the frequency separation among ν_3 asymmetric O-C-O stretching bands follows the order: monodentate carbonates ($\Delta\nu_3 \approx 100$ cm^{-1}) < bidentate carbonates ($\Delta\nu_3 \approx 300$ cm^{-1}) < bridged carbonates ($\Delta\nu_3 > 300$ cm^{-1}). In this work, the assignation has been done under this criterion.

In the case of H-BETA sample (Figure 7.2a), 6 bands are observed in the carbonate appearing region (1800-1200 cm^{-1}). The one at 1674 cm^{-1} could correspond to a type of adsorbed bidentate carbonate, whereas those at 1520 and 1430 cm^{-1} to the vibration of trace amounts of monodentate carbonates. Instead, the weak band at 1577 together with the broad band at 1355 cm^{-1} might be assigned to the presence of formate species. On the contrary, the remaining band at 1633 cm^{-1} is attributed to a bending vibration mode of adsorbed water. In the hydroxyl region (3850-3450 cm^{-1}), other 5 bands appear. It has been reported that CO_2 adsorption generates some perturbation in OH^- region, that may explain the appearance of bands at 3727, 3702,

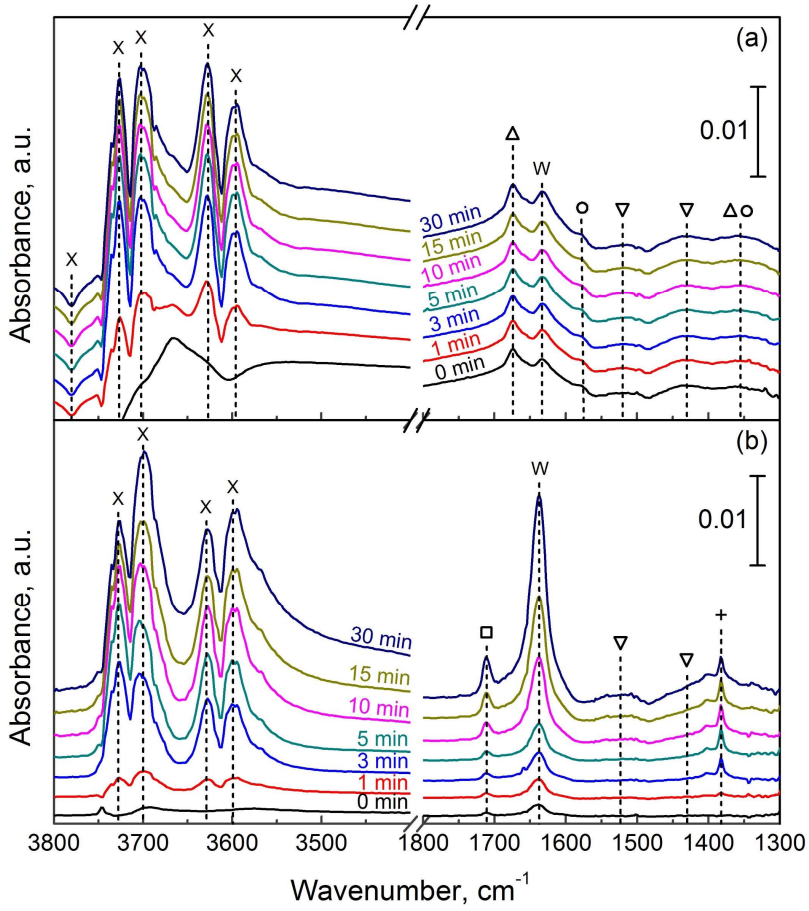

Figure 7.2. FTIR spectra recorded during CO_2 adsorption at 150 °C and different exposure times of (a) H-BETA and (b) Na-BETA samples. Adsorbed species: hydroxyls (X), water (W), bridged bidentate carbonates (□), chelating bidentate carbonates (△), monodentate carbonates (▽) and formates (○).

3627 and 3596 cm^{-1} [229]. The negative band around 3780 cm^{-1}, previously assigned to OH^- groups on EFAL (tri-coordinated Al species), suggests that some hydroxyl groups are taking part in the formation of adsorbed CO_2 species.

On the other hand, Na-BETA spectra (Figure 7.2b) present more intense bands in the carbonate region that are associated with the presence of a higher amount of chemisorbed CO_2 species on the surface of this sample. The band along with the

shoulder at around 1523 and 1430 cm^{-1}, also observed on H-BETA, could be assigned to monodentate carbonates ($\Delta\nu_3$ = 93 cm^{-1}), whereas the new band at 1711 cm^{-1} might correspond to asymmetric O-C-O stretching vibration ($\nu_3(OCO)_a$) of bridging bidentate carbonates whose corresponding symmetric vibration ($\nu_3(OCO)_s$) band cannot be identified since it is located after the cut-off limit of zeolite (at frequency < 1300 cm^{-1}) [230, 231]. However, the sharp and narrow peak at 1382 cm^{-1} is attributed to the symmetric stretching vibration mode of physisorbed CO_2 (ν_1), which becomes IR active as a result of interaction with the compensating cation (Na^+) [148, 224, 229, 231, 232]. This band matches with another increasing band at 2055 cm^{-1} (not shown), which is assigned to the asymmetric vibration of carbon dioxide. Besides, note that some authors have associated the presence of combination bands ($\nu_3 + \nu_1$ and $\nu_3 + 2\nu_2$) at 3714 and 3598 cm^{-1} with the presence of physisorbed CO_2 [232, 233].

By comparing the spectrum of both H-BETA and Na-BETA samples after 30 min 5% CO_2/Ar exposure, it can be appreciated that bands at around 3700 and 3600 cm^{-1} are more intense on Na-BETA than H-BETA, suggesting some contribution of the above-mentioned combination bands and confirming the presence of a greater amount of physisorbed CO_2 on the former support. Besides, the band around 1635 cm^{-1}, which is assigned to adsorbed water (with some contribution of bidentate carbonates), is also more intense on Na^+-exchanged zeolite. In this line, some authors have found the formation of water as part of the carbonate chemisorption mechanism on zeolite [230, 233] or Al_2O_3 [151], which would explain why more adsorbed water is observed on Na-BETA. These IR observations are in agreement with activity results reported in the previous chapter (section 6.1.2), confirming that Na^+ addition increases catalytic activity due to an enhanced CO_2 adsorption. Finally, it should be highlighted that no bands corresponding to bicarbonates are observed on zeolites, which confirms that, unlike γ-Al_2O_3 support (Chapter 4), BETA zeolite does not present OH^- groups with basic character able to activate CO_2 [222].

After that, the effect of La_2O_3 addition on Na-BETA was also investigated by FTIR spectroscopy. Spectra collected during CO_2 adsorption at 150 °C are displayed in Figure 7.3 as well as a comparative spectrum of Na-BETA sample in black dashed lines

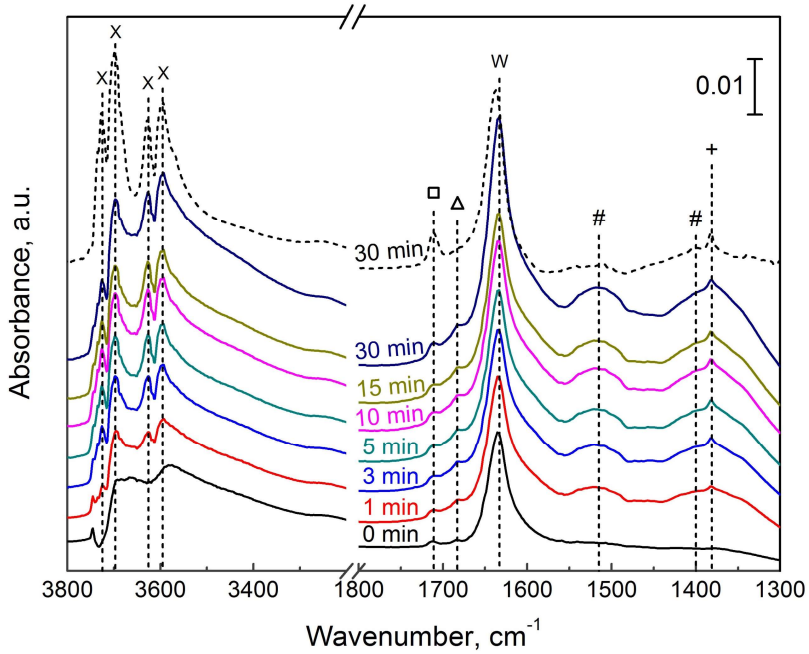

Figure 7.3. FTIR spectra recorded during CO_2 adsorption on La_2O_3/Na-BETA sample at 150 °C. Na-BETA spectrum after 30 min of CO_2/Ar exposure is presented with dashed lines. Adsorbed species: hydroxyls (X), water (W), bridged bidentate carbonates (□), chelating bidentate carbonates (△), monodentate carbonates or bulk lanthanum carbonates (#) and physisorbed CO_2 (+).

after 30 min exposure. Note that CO_2 exposure immediately gives rise to new broad bands centred at around 1515 and 1390 cm^{-1}. This doublet, whose intensity increases up to 15 min of exposure time, was first observed by Rosynek and Magnuson [234] and could be related to the presence of both monodentate carbonates adsorbed on La_2O_3 and bulk lanthanum carbonates. Verykios and co-workers [235, 236] also observed similar bands on Ni/La_2O_3 catalyst and associated them with formation of lanthanum oxycarbonate ($(LaO)_2CO_3$) resulting from reaction between La_2O_3 and CO_2 at high temperature (T = 700 °C). However, in our case, this phase may be formed from interaction of CO_2 with $La(OH)_3$ formed during catalyst reduction:

$$La(OH)_3 + CO_2 \rightarrow (LaOH)CO_3 + H_2O \qquad (7.1)$$

and further thermal decomposition (T = 150 – 200 °C) of lanthanum hydroxycarbonate compound [234, 237]:

$$2(LaOH)CO_3 \rightarrow (LaO)_2CO_3 + CO_2 + H_2O \quad (7.2)$$

Unfortunately, we were unable to identify neither La_2O_3 or $(LaO)_2CO_3$ phases by XRD in the previous chapter (section 6.2.1) due to its high dispersion and hence, we cannot determine what is the contribution of each phase.

Additionally, small bands at 1711 and 1680 cm^{-1} are observed again, which are attributed to bidentate carbonates on zeolite, together with a sharper band at 1381 cm^{-1} indicating the presence of physisorbed CO_2. As expected, the absorbance of these bands is lower on La_2O_3/Na-BETA sample since the external surface of the zeolite is partially covered by the lanthanide after impregnation. This suggests that less CO_2 is physisorbed due to less available Na^+ sites. However, it must be taken into account that the relative concentration of chemisorbed species is much higher on La_2O_3/Na-BETA than on Na-BETA after 30 min exposure (see spectrum with dashed lines), which clearly indicates that La_2O_3 improves the CO_2 chemisorption capacity of the support in line with CO_2-TPD results shown in the previous chapter. Note that the characteristic band of adsorbed water (at 1634 cm^1) is also seen on the impregnated sample, which could be related to the formation of carbonates. In fact, as above mentioned, interaction of $La(OH)_3$ with CO_2 causes proton displacement from and simultaneous condensation of surface OH^- ions yielding water (Equation 7.1).

In a final step, the influence of Ni impregnation and temperature on FTIR CO_2 adsorption was examined. Figure 7.4 shows the CO_2 adsorption spectra of Ni/Na-BETA and Ni-10La_2O_3/Na-BETA catalysts in a temperature range from 150 to 400 °C. Before TPA experiments, the CO_2 adsorption at 150 °C on both catalysts was also studied varying the exposure time (till 30 min) and as comparison, the spectra after 30 min adsorption of Na-BETA and La_2O_3/Na-BETA samples are included in black dashed lines. Generally, the bands in carbonyl region (2200-1800 cm^{-1}) are almost not appreciable, indicating that supported Ni^0 particles are hardly capable to dissociate CO_2 in absence of H_2 [124, 156]. Besides, by comparing spectra of catalysts with those of their

corresponding supports, no FTIR bands potentially assignable to new species are detected. Nevertheless, the higher absorbance of bidentate carbonate species observed in catalysts spectra suggests that the presence of Ni^{2+} in exchangeable positions and NiO non-reducible at 450 °C during FTIR pretreatment (determined by UV-Vis and H_2-TPR in the previous chapter) could contribute to the formation of a greater number of those species.

In the case of Ni/Na-BETA catalyst, increasing of temperature generally led to the disappearance of some FTIR bands but also to the formation of new ones. It can be observed that the band assigned to bridged bidentate carbonates (at 1711 cm^{-1}) increases with temperature up to 300 °C and then decreases vanishing at 400 °C. However, the band attributed to carbonates in chelating coordination (at 1678 cm^{-1}) reach maximum absorbance at 350 °C and does not completely disappear above 400 °C. This band follows the same trend with temperature than the smaller one located around 300 cm^{-1} lower frequency (band at 1375 cm^{-1}) and hence, according to criterion of Busca et al. [228], those can be assigned to $\nu_3(OCO)_a$ and $\nu_3(OCO)_s$ vibrations of chelating bidentate carbonates. Noteworthy, the evolution of temperature of bands at 1711 and 1678 cm^{-1} suggests that bridged bidentate carbonates might be transformed into chelating ones, whose concentration increases though heating and as water (band at 1635 cm^{-1}) is removed in line with the adsorption mechanism proposed by Steven at al. [230].

On the other hand, band at 1587 cm^{-1}, which is revealed by increasing of temperature and then remain stable, seems to be coupled with other at 1420 cm^{-1}, According to their positions, these stable bands might be related with the presence of carboxylate species [238]. Furthermore, new small band can be observed at around 1610 cm^{-1}, which could correspond to formate species, as we will see in detail later. In our case, these small amounts of formates could arise from a combination of carbonates with remaining surface dissociated hydrogen formed during the pretreatment (reduction with 5%H_2/Ar at 500 °C), as already reported in literature by Westermann et al. [148].

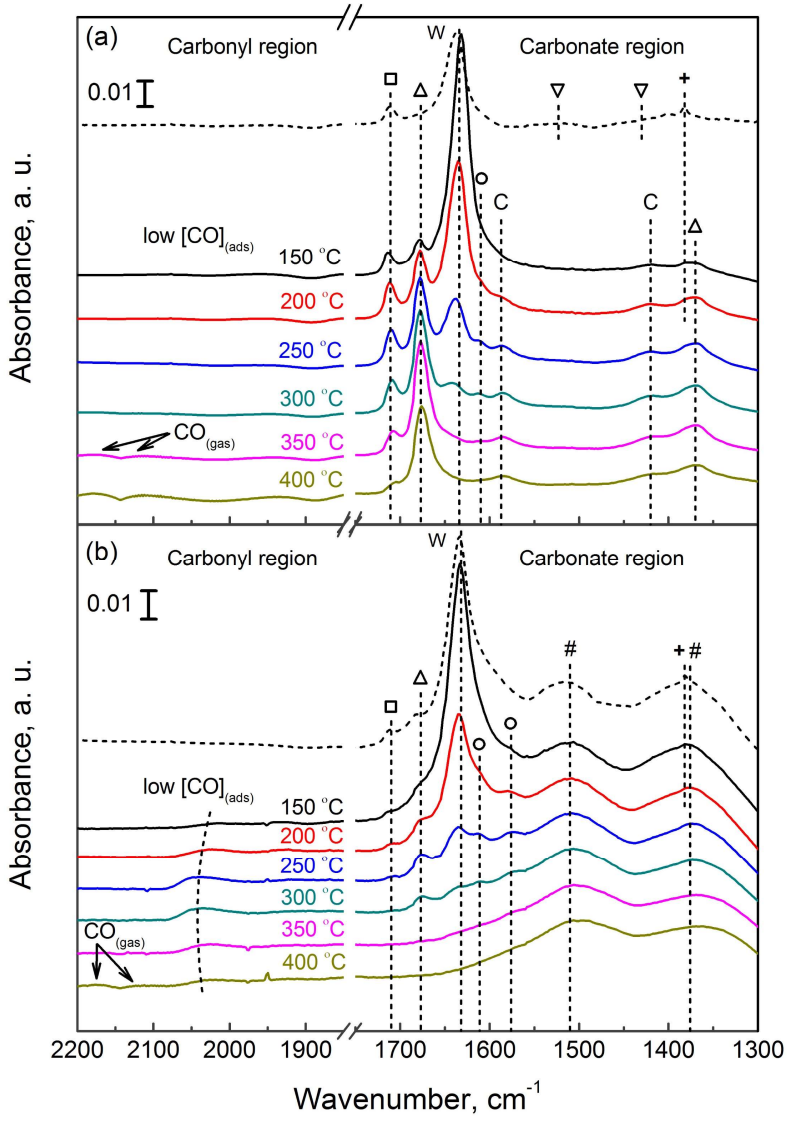

Figure 7.4. FTIR spectra of adsorbed CO_2 at different temperatures on (a) Ni/Na-BETA and (b) Ni-10La_2O_3/Na-BETA catalysts. Species: hydroxyls (X), water (W), bridged bidentate carbonates (□), chelating bidentate carbonates (△), monodentate carbonates (▽), monodentate carbonates or bulk lanthanum carbonates (#), physisorbed CO_2 (+), formates (○) and carboxylates (C).

On Ni-10La_2O_3/Na-BETA sample, more intense bands can be observed in the carbonate region from 1600 to 1200 cm^{-1},whose intensity decreases with temperature. The bands assigned to bidentate carbonates on Na-BETA and Ni/Na-BETA are also seen and, as mentioned before, are less intense due to a lower relative concentration of these species on La_2O_3 containing catalysts. Note that the absorbance of bands at 1510 and 1410 cm^{-1}, which are related to monodentate carbonates on La-sites and probably to vibration of bulk lanthanum carbonates ($(LaO)_2CO_3$ phase), first increase and then remain stable with temperature. This suggests that carbonates on lanthanum oxide are thermally more stable than bidentates adsorbed on Na-BETA zeolite and proves that the rare earth metal is able to adsorb/activate CO_2 in all range of studied temperatures. This finding agree with CO_2-TPD results shown in the previous chapter (section 6.2.1) and with previously reported by Jing et al. [239], according to which the CO_2 desorption peak above 550 °C was assigned to bulk carbonate decomposition. In this line, Garbarino et al. [57, 240] observed by IR the formation of stable carbonate species over Ni-4La_2O_3/Al_2O_3 and Ni-4La_2O_3/SiO_2-Al_2O_3 catalysts, concluding that lanthanum acts as reactant reservoir during CO_2 methanation. As already mentioned, the shoulder at around 1577 cm^{-1} is characteristic of adsorbed formate species formed from trace amounts of adsorbed H atoms. Finally, note that on both catalysts the intensities of bands in the OH^- region together with the band at 1633 cm^{-1} decrease with temperature due to both water and CO_2 desorption.

Thus, it can be confirmed that both catalysts are able to adsorb CO_2, observing similar species (physisorbed CO_2 and chemisorbed carbonates in mono- and bidentate coordinations). However, the number of chemisorbed carbonates is much higher on Ni-10La_2O_3/Na-BETA catalyst, which evidences that the presence of the rare earth metal boosts CO_2 activation.

7.3. HYDROGENATION OF ADSORBED SPECIES

Once different type as well as evolution with temperature of adsorbed CO_2 species were studied, CO_2 hydrogenation reaction was monitored by *operando* FTIR spectroscopy. Temperature Programmed Surface Reactions (TPSR) were carried out

under meaningful CO_2 methanation conditions (Q = 20 mL min^{-1} and feed = 5%CO_2/20%H_2/Ar) on Ni/Na-BETA and Ni-10La_2O_3/Na-BETA catalysts in order to determine which species are hydrogenated (reaction intermediates) and which not (spectator species). Note that the chosen gas volume was as small as possible to increase the time resolution of online analysis and remove contribution of the gas phase to the spectra [226].

The spectra of pre-reduced catalysts recorded at different temperatures and under TPSR methanation conditions are shown in Figure 7.5. A main band at 1633 cm^{-1} together with other 4 bands and some elevation of the background in the OH^- region can be appreciated in Ni/Na-BETA FTIR spectrum at 150 °C (Figure 7.5a). As reported before, this suggests that the zeolite is first hydrated due to carbonate formation and then with the extension of the reaction. As in CO_2 adsorption experiments (Figure 7.4a), the more intense bands corresponding to different types of bidentate carbonates are also observed at 1710 and 1675 cm^{-1}, but their intensity fastly decrease with temperature rather than increase. The vanishing of these bands at T < 200 °C matches with the appearance of an overlapped band at 1610 cm^{-1} coupled with another two weak bands at 1381 and 1347 cm^{-1}, which can be assigned to asymmetric O-C-O stretching, C-H bending and symmetric O-C-O stretching of formate species probably adsorbed on Ni [148, 153, 224, 241-243]. Also, the band attributed to C-H stretching vibration ν(CH) appears at around 2855 cm^{-1}, which confirms the presence of formate species. Therefore, the observed trends point out that bidentate carbonates might be hydrogenated into formates.

Some authors have reported that the coordination of formates can be identified by the frequency difference between O-C.O stretching vibrations [153, 241, 242]. According to that criterion, a frequency separation among $\nu(OCO)_a$ and $\nu(OCO)_s$ higher than 250 cm^{-1} would correspond to monodentate formate, whereas a frequency separation similar or lower than 250 cm^{-1} to bridged or bidentate formates. In our case, the separation is around 265 cm^{-1} and, hence, we could consider that monodentate formates are formed [243, 244]. Moreover, note that three weak bands appear in 2200-1800 cm^{-1} region, which were not identified during CO_2 adsorption. These bands

were also observed over $NiAl_{GAI}$ catalyst (Chapter 4) and are associated with vibration of carbonyls on Ni^0 surface. Similarly, the band at 2060 cm^{-1} is attributed to stretching vibration of linearly adsorbed carbonyls (Ni-CO), while the other bands at 1930 and 1845 cm^{-1} could be ascribed to ν(CO) of weakly and strongly attached bridged carbonyls (Ni_2-CO) [245, 246]. Nonetheless, the absorbance of carbonyl bands is poorer than that observed in $NiAl_{GAI}$ catalyst spectra (Figure 4.12), since Ni dispersion of Ni/Na-BETA catalyst is lower according to TEM results (D_{Ni} = 7 vs. 12%).

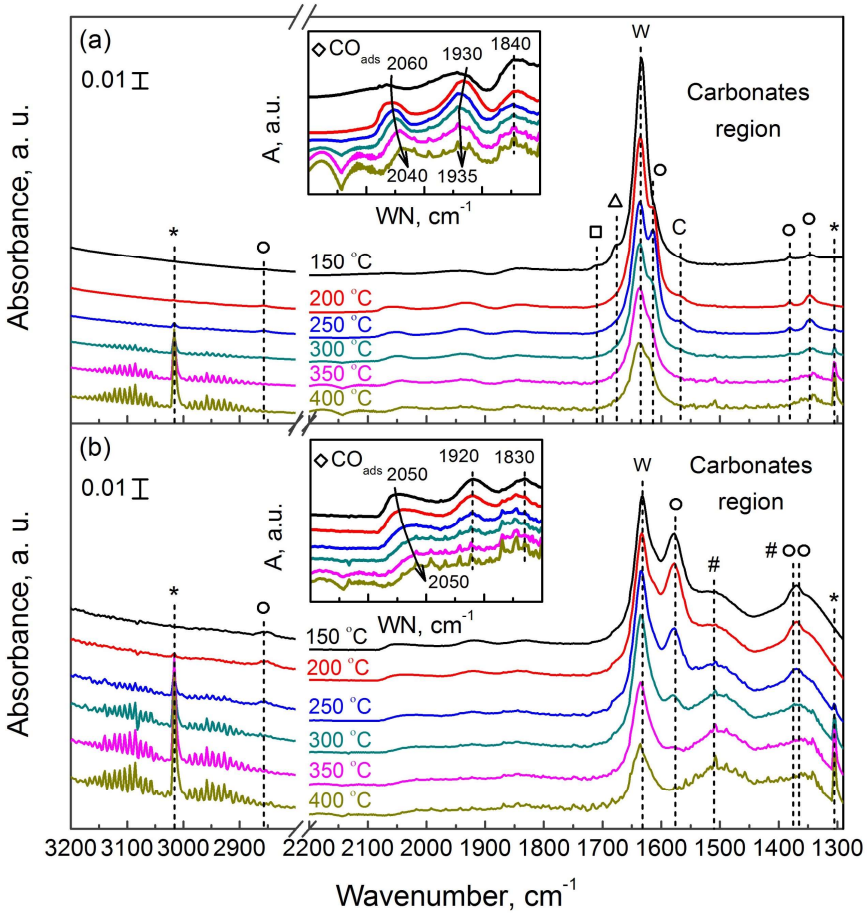

Figure 7.5. CO_2 methanation FTIR spectra recorded at different temperatures on (a) Ni/Na-BETA and (b) Ni-10La_2O_3/Na-BETA catalysts. Species: water (W), bridged bidentate carbonates (□), chelating bidentate carbonates (△), carboxylates (C), monodentate carbonates or bulk lanthanum carbonates (#), formates (○), methane gas (*) and carbonyls (◊).

Noteworthy, the presence of carbonyl species under CO_2/H_2 mixtures indicates that it is mainly formed by a H-assisted pathway [148, 224]. Thus, as in the case of alumina supported catalysts (Chapter 4), it seems that carbonyls may come from the decomposition of formates rather than by direct CO_2 dissociation [247]. The bands corresponding to linearly adsorbed CO and weakly attached bridged carbonyls first shift to the left (increase in Ni^0 surface coverage) and then to the right (decrease in Ni^0 surface coverage) with temperature, suggesting that both species participate in the reaction. The shift to the right (red shift) is more pronounced for the linear carbonyls indicating that is the most reactive species, as observed for Ni/Al_2O_3 catalysts. On the contrary, the band at 1840 cm^{-1} does not shift, i.e., strongly attached bridged CO might be a spectator species. Finally, the bands at 3016 and 1305 cm^{-1} correspond to C-H asymmetric stretching and deformation vibrations of methane, whereas the bands at 2175 and 2115 cm^{-1} are assigned to carbon monoxide in gas phase. Those bands, which appear from 250 °C, confirm that CO_2 hydrogenation is taking place on Ni/Na-BETA in line with activity results.

Analogously, Figure 7.5b shows spectra recorded during CO_2 methanation at 150 °C for Ni-10La_2O_3/Na-BETA catalyst. As in CO_2 adsorption experiments, more bands are observed on La_2O_3 containing catalyst due to the presence of a higher number of chemisorbed species. The broad bands corresponding to vibration of adsorbed monodentate carbonates or bulk lanthanum carbonates (1510/1400 cm^{-1}) are clearly identified, but only the one previously attributed to chelating bidentate carbonates at 1675 cm^{-1}. As in the case of Ni/Na-BETA catalyst, the latter rapidly disappear with temperature indicating that bidentate carbonates could be further hydrogenated. However, the broad bands remain more or less stable with temperature, which may suggest that (i) the rate of carbonate formation is higher than the rate of its hydrogenation or (ii) lanthanum carbonate is a spectator species.

Notably, the bands assignable to formate species are much more intense over this catalyst. These bands appear at 2855, 1578, 1380 and 1370 cm^{-1} and, in this case, are assigned to ν(C-H), $\nu(OCO)_{as}$, δ(C-H) and $\nu(OCO)_{sy}$ vibration modes of bidentate formates on La_2O_3 surface, since the ν(OCO) frequency separation among is lower than

250 cm^{-1} ($\Delta\nu$ = 208 cm^{-1}) [153, 241, 242]. However, it should be mentioned that other authors attributed these bands to formates in monodentate coordination [167, 223]. Regardless the coordination, this species is expected to form from reaction among dissociated hydrogen and surface carbonates adsorbed on La-sites. Although the concentration of formates is clearly higher on Ni-10La_2O_3/Na-BETA catalyst, the intensity of carbonyls bands is even lower to that observed for less active un-promoted catalyst. This fact points out that most of formates are not being decomposed into carbonyls and that CO_2 methanation over the promoted catalyst may occur via different mechanism. Finally, the bands corresponding to gas CH_4 are clearly observable from low temperature (T = 200 °C), whereas the bands corresponding to gas CO were barely perceptible only at high temperature (T > 400 °C).

In addition, with the aim of realizing a semi-quantitative analysis, the absorbance of main adsorbed C-species at different temperatures of Ni/Na-BETA and Ni-10La_2O_3/Na-BETA catalysts is summarized in Tables 7.1 and 7.2. Note that absorbance of each species refers to the height value or is calculated from integration of the corresponding IR band in Figure 7.5, depending on the presence (or not) of band overlapping. Because of absorbance of CO_2 and CH_4 in gas phase present a linear relation, we were able to quantify the extension of reaction by parameter ξ

$$\xi = 1 - \frac{A_{CO_2}}{A^0_{CO_2}} \tag{7.3}$$

where $A^0_{CO_2}$ refers to absorbance of CO_2 at initial temperature (T = 150 °C), where CH_4 in gas phase is hardly noticeable. The reader must note that this parameter is qualitatively similar to CO_2 conversion but not quantitatively, since the reaction is carried out under quite different conditions.

In the case of Ni/Na-BETA catalyst (Table 7.1), the rise of temperature results in a rapid disappearance of chelating bidentate carbonates a T > 200 °C (not shown in Table 7.1) and a progressive drop in absorbance of water ($H_2O_{(ads)}$). However, surface formates ($HCOO^-_{(ads)}$) absorbance increases up to 225 °C and then decreases, almost

vanishing above 350 °C. Likewise, the amount of IR radiation absorbed by carbonyls ($CO_{(ads)}$) reaches the maximum value at similar temperature but, afterwards, the drop is not so marked in part due to the presence of carbonyl species in stable bridged configuration (band at 1840 cm^{-1}). The slight depletion of carbonyls matches with the increase in the absorbance of CH_4, which confirms that this species is a reaction intermediate.

Table 7.1. Absorbance values of main C-species observed for Ni/Na-BETA catalysts at different temperatures.

T (°C)	Absorbance (a.u.)						Reaction extension (ξ)[c]
	$H_2O_{(ads)}$[a]	$HCOO^-_{(ads)}$[b]	$CO_{(ads)}$[b]	$CO_{2\,(gas)}$[b]	$CH_{4\,(gas)}$[b]	$CO_{(gas)}$[b]	
150	0.310	0.052	0.355	44.2	0	0	0.00
175	0.299	0.198	0.572	43.6	0	0	0.02
200	0.217	0.242	0.762	42.3	0.003	0	0.04
225	0.184	0.316	0.729	41.2	0.011	0	0.07
250	0.167	0.275	0.733	39.9	0.034	0.011	0.10
275	0.157	0.209	0.689	38.6	0.078	0.021	0.13
300	0.144	0.155	0.699	36.9	0.156	0.050	0.17
325	0.132	0.130	0.709	35.0	0.277	0.085	0.21
350	0.119	0	0.673	32.5	0.438	0.117	0.27
375	0.101	0	0.630	30.3	0.617	0.140	0.31
400	0.083	0	0.562	28.8	0.739	0.154	0.35

[a]Refers to height value of characteristic FTIR band.
[b]Determined from integration of characteristic band.
[c]Calculated by Equation 7.3.

However, the fact that absorbances of CH_4 and CO above 300 °C are of the same order of magnitude points out that the catalyst is quite selective towards CO at the given reaction conditions, i.e., only part of adsorbed CO formed from formates decomposition is hydrogenated into methane ($CH_{4\,(gas)}$) while the rest is desorbed as carbon monoxide ($CO_{(gas)}$). Regarding extension of reaction, it follows the same growth with temperature as an exothermal reaction, observing the highest value at 400 °C

(ξ = 0.35). Therefore, it can be deduced that CH_4 is produced on Ni/Na-BETA following this sequence: physisorbed CO_2 → carbonates → formates → carbonyls → $CH_{4\,(gas)}$.

Table 7.2 also summarizes main C-species absorbance at different temperatures on Ni-10La_2O_3/Na-BETA catalyst. As in the case of the unpromoted catalyst, a progressive depletion of water is observed with the extension of reaction (specifically at *T* > 300 °C) in line with the water adsorption constant decrease observed by the kinetic study on 10NiAl catalyst in Chapter 5. The absorbance of lanthanum carbonates, on the contrary, first slightly increases up to 300 °C and then decreases, suggesting that at least part of them participate in the reaction. Although we cannot definitively conclude, it makes more sense that more accessible surface carbonate is the species that reduce into formates rather than thermally stable bulk carbonate ($(LaO)_2CO_3$), which could be considered as spectator species [57, 234, 240]. Regarding the formate species, their absorbance increases up to 200 °C and then progressively decreases until

Table 7.2. Absorbance values of main C-species observed for Ni-10La_2O_3/Na-BETA catalyst at different temperatures.

T (°C)	Absorbance (a.u.)						Reaction extension (ξ)[c]
	$H_2O_{(ads)}$[a]	$CO_3^{2-}{}_{(ads)}$[a]	$HCOO^-{}_{(ads)}$[a]	$CO_{2\,(gas)}$[b]	$CH_{4\,(gas)}$[b]	$CO_{(gas)}$[b]	
150	0.200	0.070	0.143	46.2	0.002	0	0.00
175	0.209	0.071	0.154	43.8	0.003	0	0.05
200	0.193	0.072	0.160	41.8	0.038	0	0.10
225	0.192	0.073	0.147	39.9	0.094	0	0.14
250	0.191	0.075	0.119	37.6	0.269	0	0.19
275	0.189	0.077	0.090	35.0	0.456	0	0.24
300	0.177	0.081	0.056	31.5	0.708	0.020	0.32
325	0.157	0.077	0.045	28.5	0.893	0.023	0.38
350	0.127	0.071	0.036	25.9	1.104	0.031	0.44
375	0.105	0.065	0.029	24.0	1.219	0.047	0.48
400	0.077	0.058	0.020	22.1	1.368	0.071	0.52

[a]Refers to height value of characteristic FTIR band.
[b]Determined from integration of characteristic band.
[c]Calculated by Equation 7.3.

almost disappearing at 400 °C. The negative linear relation between $HCOO^-_{(ads)}$ and $CH_{4\,(gas)}$, which can be deduced from Table 7.2, and the fact that bands of carbonyls ($CO_{(ads)}$) as well as $CO_{(gas)}$ are barely appreciable (see Figure 7.5b) suggest that formates are directly hydrogenated into methane instead of being decomposed into CO, according to the associative mechanism or formate route [167].

Noteworthy, the energetic viability of this mechanism has already been studied by DFT calculations and compared to that of dissociative mechanism (carbonyl route) on a similar Ni-La_2O_3/SBA-15 formulation with excellent Ni-La_2O_3 contact [248]. According to that study, the steps involving the formate route present lower energy barriers than those of carbonyl route, indicating that associative mechanism is more favourable thermodynamically on Ni-La_2O_3 surface model in agreement with our FTIR results. Besides, the hydrogenation of formates seems to be the step with the higher energy barrier (1.02 eV) or the rate determining step, which supports the fact that a higher concentration of formates is observed by FTIR on Ni-10La_2O_3/Na-BETA catalyst. After that, in an intermediate step towards methane formation, formates are expected to be converted into methoxy species [145, 242]. Unfortunately, we were unable to identify characteristic bands of such species (bands around 1170 and 1090 cm^{-1}) because of signal cut-off at wavenumbers lower than 1300 cm^{-1}. All observation considered, it can be deduced that CH_4 is produced on Ni-La_2O_3/Na-BETA mainly following this sequence: physisorbed CO_2 → carbonates → formates → CH_4.

Finally, it can be seen that, in general, CH_4 absorbance of La-containing catalyst is notably higher than that of unpromoted catalyst in all range of reaction temperatures. In fact, the CH_4 absorbance at 300 °C is more than four times higher for Ni-10La_2O_3/Na-BETA catalyst (0.71 vs. 0.16), which confirms that CO_2 methanation is much more effective on the La-promoted catalyst. However, reaction extension is only around 2 times higher (ξ = 0.32 vs. 0.17), pointing out that Ni/Na-BETA is much more selective towards CO. In line with CO_2-TPD, STEM, and activity results reported in the previous chapter, this significantly greater activity of Ni-10La_2O_3/Na-BETA catalyst is not only due to higher Ni surface over which H_2 is dissociated but also to the presence of neighbouring La_2O_3 that deals to adsorb CO_2. In Ni/Na-BETA formulation, instead, Ni

has to deal with two functionalities (adsorb CO_2 and dissociate H_2) resulting in much less effective CO_2 hydrogenation into methane.

7.4. PROPOSAL OF REACTION MECHANISMS

To sum up, the type and evolution (with time and temperature) of adsorbed species and reaction intermediates, which were analysed in CO_2 activation and adsorbed species hydrogenation sections, allowed us to propose two reaction pathways. The CO_2 methanation mechanisms proposed over Ni/Na-BETA and Ni-10La_2O_3/Na-BETA catalysts are summarized and depicted in Figures 7.6a and b, respectively. Note that some species included in the proposal were not observed by FTIR but deduced from other mechanistic studies.

The reaction mechanism over Ni/Na-BETA catalyst proposed in Figure 7.6a is dissociative type, i.e., follows the CO route. CO_2 is first physisorbed (via Van der Waals forces) on Na^+ sites and then chemisorbed on BETA Lewis basic sites (surface O^{2-}) complexed to Na^+ mainly in form of (chelating or bridged) bidentate carbonates, whereas H_2 is dissociatively adsorbed on Ni^0 surface (steps 1-2). Afterwards, adsorbed CO_2 reacts with dissociated hydrogen to yield monodentate formates adsorbed onto Ni^0 surface (step 3), which are later decomposed into carbonyls and hydroxyls (step 4). Specifically, linearly adsorbed carbonyls are expected to sequentially be hydrogenated into CH_XO species (formyl (-CHO), hydroxycarbene (-CH_2O) or hydroxymethyl (-CH_2OH)) until the second CO bond cleavage occurs, which finally leads to release of CH_4 and H_2O molecules. It should be highlighted that this mechanism is quite similar to that observed over alumina supported Ni and Ru catalysts in Chapter 4 (section 4.3), which was later validated by CO_2 methanation kinetic study on 10NiAl catalyst included in Chapter 5. However, in this case, the rate determining step of CO_2 methanation seems to be adsorbed CO hydrogenation rather than formates decomposition, since carbonyl is the main reaction intermediate within the range of studied temperatures.

On the contrary, the reaction pathway on Ni-10La_2O_3/Na-BETA catalysts is associative type (Figure 7.6b). In this case, H_2 is also adsorbed on Ni^0 particles but CO_2 is mainly chemisorbed on La_2O_3 as monodentate carbonates and/or forming $(LaO)_2CO_3$

phase (step 1-2). Subsequently, H atoms migrate by spillover mechanism and react with carbonates close to Ni particles, yielding bidentate formates on La-sites and releasing a water molecule (step 3). Finally, formates are further hydrogenated into -

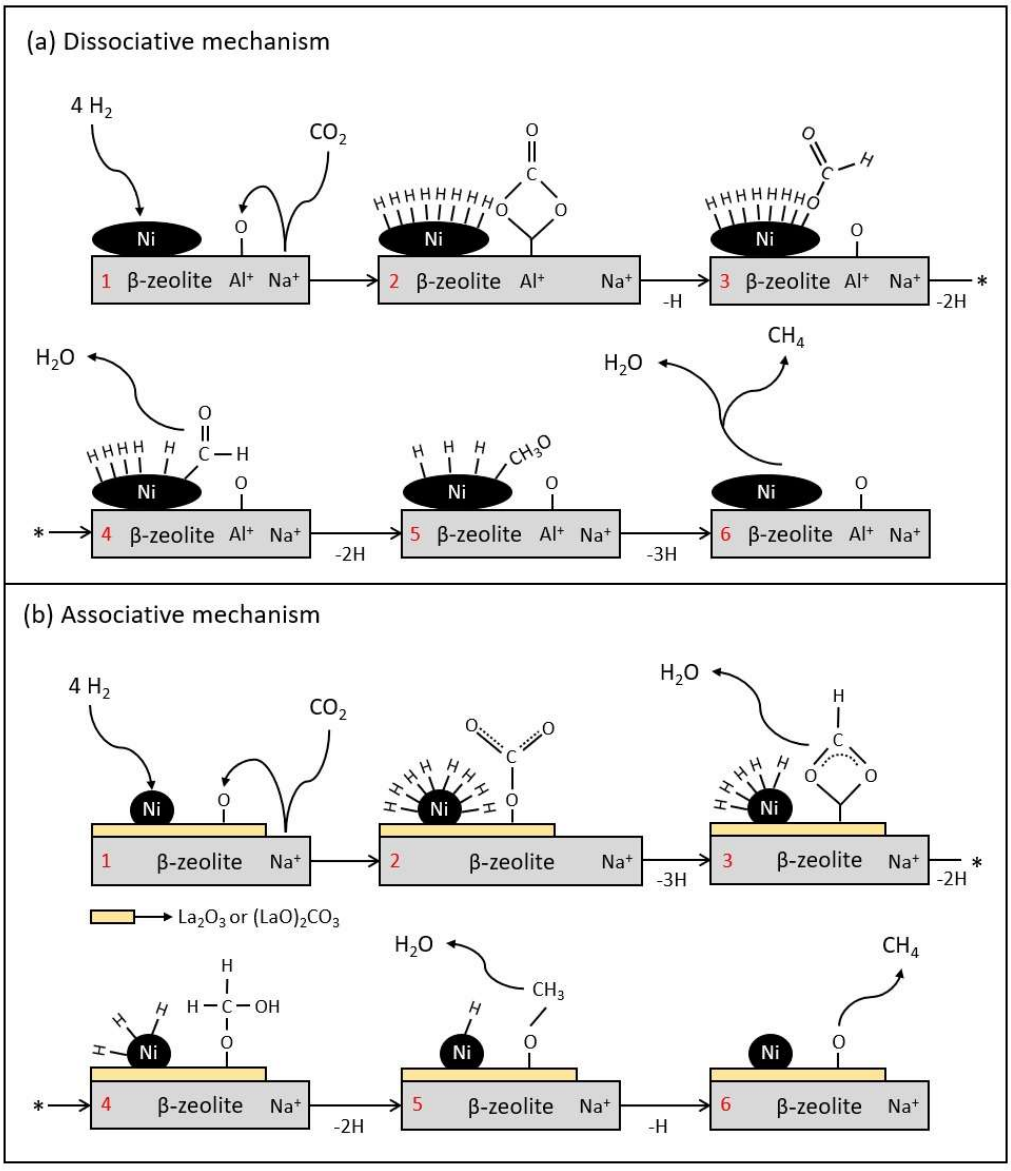

Figure 7.6. CO_2 methanation reaction mechanisms proposed on (a) Ni/Na-BETA and (b) Ni-10%La_2O_3/Na-BETA catalysts.

OCH_2OH species (not observed), then methoxy groups ($-OCH_x$, not observed) and finally methane, releasing the second water molecule along the way (step 4-6). Although the mechanism is different to that deduced by operando FTIR and kinetic study in previous chapters, Ni-10La_2O_3/Na-BETA formulation shows similar catalytic activity than optimal Ni-1RuAl catalyst (Chapter 4). In fact, these catalysts, which are very selective to CH_4 (S_{CH_4} > 98%), achieve 50% CO_2 conversion at 320 and 305 °C, respectively. In the case of Ni-1.0RuAl catalysts, the noble metal acts as electronic modifier promoting intermediate CO formation and enhancing the H_2 dissociation capacity of nickel. On the contrary, addition of La_2O_3 basic promoter to Ni/Na-BETA formulation improves considerably CO_2 adsorption/activation capacity. Regardless the reaction pathway, both optimal formulation developed throughout this doctoral thesis are able to achieve equilibrium CO_2 conversion under conditions relevant to industry.

7.5. OVERALL VIEW AND CONCLUSION

This chapter includes operando FTIR measurements under CO_2 adsorption and CO_2 methanation conditions over zeolite BETA supported formulations, through which the mechanistic roles of different elements (BETA, Na^+, La_2O_3 and Ni) that make up optimized Ni-10La_2O_3/Na-BETA catalyst are defined.

CO_2 adsorption FTIR experiments confirmed that the incorporation of alkaline Na^+ by IE to BETA zeolite enhances its CO_2 adsorption capacity. Due to the polarizing power of Na^+ (Z^+/r^2i_{onic} = 0.74), a much greater amount of CO_2 is physisorbed along Na-BETA 3D channels than along those of H-BETA, facilitating its subsequent chemisorption over the external surface oxygen of BETA zeolite in form of potentially reactive chelating and bridging bidentate carbonates. Nevertheless, the surface basicity of Na-BETA support is clearly increased after 10% La_2O_3 impregnation. The partial coverage of the external surface of the zeolite by the rare earth metal results in the presence of remarkably higher concentration of chemisorbed carbonates, among which only those close to Ni particles participate in the reaction.

Under 5%CO_2/20%H_2/Ar gas mixture, some of adsorbed species are hydrogenated into reaction intermediates on Ni/Na-BETA and Ni-10La_2O_3/Na-BETA catalysts. It

appears that formates, which arise from both carbonates and physisorbed CO_2 hydrogenation, are reaction intermediates on both formulations but follow different hydrogenation pathways. In the case of Ni/Na-BETA catalyst, this species is adsorbed on Ni^0 surface and seems to be decomposed with temperature into carbonyls, which are sequentially hydrogenated into CH_4 passing by CH_XO species formation (dissociative mechanism). This mechanism is the same observed over alumina supported Ni and Ru catalysts. However, over Ni-10La_2O_3/Na-BETA catalyst, this species seems to be adsorbed on neighbouring La_2O_3/$(LaO)_2CO_3$ surface instead of on Ni^0 (bands appearing at shifted positions). In a next step, formates further react with dissociated H_2 to form unstable methoxy species, which lead finally to methane gas according to associative mechanism. Unlike Ni/Na-BETA, Ni-10La_2O_3/Na-BETA sample is a bifunctional catalytic formulation, in which La_2O_3 handles CO_2 adsorption in form of carbonates and neighbouring nickel provides spillovered H atoms to hydrogenate carbonates into methane. This synergistic collaboration between Ni and La_2O_3 leads to a more effective CO_2 methanation comparable to that of Ni-1.0RuAl catalyst.

Chapter 8

SUMMARY AND CONCLUSIONS

8. SUMMARY AND CONCLUSIONS

8.1. SUMMARY

Since the beginning of industrial revolution in 18th century, human activity and related anthropogenic CO_2 emissions have exponentially increased so as global population. The human impact on the earth has growth to such an extent that, nowadays, elevated GHG concentration in atmosphere combined with destruction and degradation of countless ecosystems have caused notorious global warming of around 1.5 °C since pre-industrial period, leading to climate change already evident in any corner of the Earth. Accordingly, the scientific community together with politicians are developing a strategic plan including a series of actions to progressively decarbonize the energetic system, which would contribute to significantly reduce the global carbon footprint and face the climate crisis. In this context, the Carbon Capture and Utilisation (CCS) technologies are considered to have an important role in stabilizing atmospheric CO_2 concentration at medium term. Among them, Power-to-Gas (Gas = CH_4) technology is gaining interest since not only promotes the installation of useful and necessary renewable energies and hydrogen electrolysers but also contributes to reduce CO_2 emissions while generating Synthetic Natural Gas (SNG) in cyclic CCS processes. This technology requires an active, selective and stable catalyst to carry out Sabatier reaction or CO_2 methanation using renewable H_2 at mild industrial conditions.

In this thesis, two blocks or families of catalytic formulations have been developed to efficiently catalyse CO_2 methanation: alumina and zeolite supported catalysts. Each formulation has systematically been optimized by both improving the synthesis route and adding an electron-modifier or basic promoter. The CO_2 hydrogenation reaction pathways has been examined at molecular scale over mono- and bimetallic formulations of both blocks, elucidating two reaction mechanisms. This thesis also includes a CO_2 methanation kinetic study on Ni/Al_2O_3 catalyst with low Ni content (10 wt%), from which a kinetic model with high statistical significance is deduced.

As starting point, Ni/Al_2O_3 and Ru/Al_2O_3 catalysts with different metal contents have been prepared by conventional Incipient Wetness Impregnation (IWI). These

formulations have been widely characterized to determine the effect of metal loading on specific physicochemical properties required to carry out CO_2 methanation efficiently: good metal dispersion, high reducibility, weak-medium basicity and elevated H_2 adsorption capacity. The catalytic performance of all catalysts has been evaluated in a fixed-bed reactor at atmospheric pressure, H_2/CO_2 = 5 and GHSV of 10,000 h^{-1} (W/F_{A0} = 4.7 g h^{-1} mol^{-1}), trying to relate the activity results with physicochemical properties. The activity results, together with a structure-sensitive analysis, has allowed us to determine which Ni and Ru metal loading is optimal and perform direct comparison of catalytic properties of both metals.

Hereunder, new catalysts have been prepared by Glycerol Assisted Impregnation (GAI) combined with reducing calcination environment, with the idea of improving reducibility and metal dispersion of Ni/Al_2O_3 and Ru/Al_2O_3 catalysts, respectively. The physicochemical properties of GAI-catalysts are compared with those of IWI-catalysts, determining the role of glycerol and reducing atmosphere during synthesis. Besides, the effect of incorporating small amounts of Ru to Ni/Al_2O_3 is analysed, defining the optimal Ru content in bimetallic formulation. On the other hand, *operando* FTIR experiments conducted in a reaction FTIR cell under CO_2 methanation conditions have allowed us to elucidate the reaction mechanism over alumina-supported Ni and Ru catalysts, observing differences in the surface species evolution with temperature over mono- and bimetallic catalysts.

Reaction kinetics on Ni/Al_2O_3 catalyst with low Ni content (10 wt%) has been studied at varying temperature (T = 315 – 430 °C), total pressure (P = 2 – 6 bar), space-time (W/F_{A0} = 1.6 – 24.9 g h mol^{-1}) and feed ratio (H_2/CO_2 = 2 – 16), allowing to obtain kinetic data from differential (X < 0.1) to equilibrium reactor conditions. The influence of mentioned parameters on reaction rate is examined and various LHHW-type models are deduced from two proposed reaction pathways: dissociative and H-assisted CO formation mechanisms. A model discrimination is conducted by analysis data differential method together with least squares regression in terms of quality fit (σ^2, mean deviation). The model with highest statistical significance has been validated by data analysis integral method combined with least squares regression, estimating all

kinetic and adsorption constants in the reaction rate equation. In a pioneering way, the role of formates in kinetics is considered.

The second block of catalysts consists of commercial Y and BETA zeolite supported Ni catalysts alternative to Ni/γ-Al_2O_3 formulation. First, the effect of zeolitic structure (BEA and FAU) and replacement of exchangeable H^+ by Na^+ on Ni dispersion, speciation, and reducibility has been examined, leading to choose Na-BETA as more suitable CO_2 methanation support. After that, increasing loadings of La_2O_3 (5, 10 and 15 wt%) have been incorporated to Na-BETA to determine the effect of further increasing surface basicity. Besides, the particle size, morphology and relative location of Ni^0 and La_2O_3 sites have been determined and compared to those of Ni/Na-BETA. Finally, the promoting effect of La_2O_3 (three contents) has been checked in catalytic tests (P = 1 atm, H_2/CO_2 = 4 and W/F_{A0} = 4.7 g h^{-1} mol^{-1}) determining the optimal La_2O_3 loading.

A substantial progress has been made on the insight into reaction mechanism on Ni/Na-BETA and Ni-La_2O_3/Na-BETA catalysts. CO_2 adsorption experiments have been carried out over samples with increasing composition to identify the type of adsorbed species on different surface sites. Subsequently, the hydrogenation of those species at different temperatures is followed by *operando* FTIR to identify potential reaction intermediates and to analyse the evolution of their concentration with the extension of reaction. These FTIR observations have allowed us to propose a different reaction pathway on Ni-La_2O_3/Na-BETA catalyst (associative mechanism), in which formates species seems to play a major role.

8.2. MAIN CONCLUSIONS

The analysis of results shown throughout this doctoral thesis and, in turn, relation with other works reported in recent literature allowed to draw specific conclusions, reported at the end of each chapter in the thesis. To recap, the most relevant main conclusions are summarized in the following.

1. ***On the alumina supported Ni and Ru catalysts prepared by Incipient Wetness Impregnation (IWI).***
   a) Alumina supported Ni and Ru IWI-catalysts with metal loadings ranging from 4 to 20 wt.% and from 1 to 5 wt.% are suitable to carry out CO_2 methanation. NiO and RuO_2 are the main crystalline phases presented in each formulation before the reduction which is mandatory to obtain active sites (Ni^0 and Ru^0). Complete reduction of NiO/Al_2O_3 precursor requires rising the temperature up to 900 °C due to a high metal-support interaction, whereas RuO_2/Al_2O_3 sample is completely reduced at temperature below 300 °C.
   b) Both formulations present weak-medium strength basicity provided by Al_2O_3 but also by NiO in the case of Ni/Al_2O_3 catalyst, resulting in a more basic formulation. Increasing the Ni loading leads to higher reducibility (or amount of reduced Ni at 500 °C) but in return to lower dispersion due to the formation of bigger particles (from 3 to 7 nm). However, increasing Ru content does not cause any significant change in either reduction or dispersion.
   c) The CO_2 methanation is structure sensitive over Ni particles ranging from 2 to 10 nm, but practically insensitive over Ru/Al_2O_3 catalysts with poor dispersion (D_{Ru} = 4 – 5 %). Considering the saturation effect and structure sensitivity analysis, 12%Ni/Al_2O_3 (T_{50} = 340 °C) and 4%Ru/Al_2O_3 (T_{50} = 310 °C) catalysts are the optimal formulations. Regardless the size, the specific activity of Ru particles is higher than of Ni ones due to the higher capacity of noble metal to dissociate H_2 at low temperature.

2. ***On the alumina supported Ni and Ru catalysts prepared by Glycerol Assisted Impregnation (GAI).***

   The GAI impregnation method along with reductive calcination resulted in an effective synthesis route to avoid detrimental excessive NiO-Al_2O_3 interaction and to remarkably improve Ru dispersion of $NiAl_{IWI}$ and $RuAl_{IWI}$ catalysts, respectively. Therefore, the activity of both monometallic catalysts prepared by GAI was higher to that of IWI-catalysts at expense of lesser Ni dispersion of $NiAl_{GAI}$ catalyst (T_{50} = 335 °C) and lower Ru specific activity (TOF/l_0) of $RuAl_{GAI}$ catalyst (T_{50} = 305 °C). The synergistic collaboration between Ni and Ru within Ni-1.0RuAl catalytic system translated into improvement of Ni resistance against oxidation, smaller Ni particle size, related higher H_2 adsorption capacity and hence, to superior catalytic activity compared to that of monometallic Ni catalyst. Noteworthy, in the range of studied temperatures, the CH_4 yield of Ni-1.0RuAl catalyst (T_{50} = 305 °C) was very similar to that of $RuAl_{GAI}$ with a Ru content three times higher. In Ni-Ru/Al_2O_3 system, Ru promotes CO formation and enhances capacity of nickel to dissociate H_2.

3. ***On the kinetics of CO_2 methanation on 10NiAl catalyst.***

   The CO_2 methanation kinetics on 10NiAl catalyst is favoured at increasing temperature, low space times, feed ratios higher than stoichiometric ($H_2/CO_2 > 4$) and rising partial pressures of CO_2 and H_2 up to a certain limit, in agreement with thermodynamics of an exothermal reaction with negative molar volume change. In fact, the highest CO_2 conversion (X_{CO_2} = 0.97) is observed at T = 430 °C, W/F_{A0} =25 g h mol^{-1}, H_2/CO_2 = 16 and P = 6 atm. The CO_2 disappearance rate is insensitive to CH_4 concentration but is clearly affected by H_2O and CO partial pressures, whose strong adsorption inhibits active sites. The LHHW-type model that best fits kinetic results (σ^2 = 7%) is in line with mechanism proposed over alumina-supported catalysts and assumes the decomposition of formates as the rate determining step (RDS). The model that considers the hydrogenation of carbonyls as RDS, which is the most used to describe kinetics on NiAl formulations with high metal content (Ni > 15 wt.%), shows lower statistical significance or higher mean deviation (σ^2 = 20%). This revealed that RDS of CO_2 methanation kinetics on Ni-based catalysts is affected

by the metal loading.

4. On the CO_2 methanation over zeolite-based catalysts

Ni-zeolite catalysts containing Na^+ in exchangeable positions (Ni/Na-Y and Ni/Na-BETA) showed higher activity than protonic zeolite supported ones, not only due to the presence of weak basic sites on the former but also to an enhancement of reducibility. The catalytic performance of Ni/Na-BETA was higher than that of Ni/Na-Y, since unlike Y sample, BETA zeolite contains mesoporosity (high externa surface area) allowing a better dispersion of 10% Ni in form of particles within mesopores. Taking advance of that great S_{ext}, the CH_4 yield is boosted by incorporating increasing loads of La_2O_3 into Ni/Na-BETA, 10% of La_2O_3 being the optimal. Addition of the rare earth oxide translated into an increase of medium-strong surface basicity and double Ni dispersion. Thus Ni-La_2O_3/Na-BETA (T_{50} = 320 °C) achieved 50% CO_2 conversion with 99% CH_4 selectivity at remarkable 60 °C lower temperature than Ni/Na-BETA catalyst.

5. On the reaction mechanism over zeolite-based catalysts

Systematic *operando* FTIR experiments under CO_2 methanation conditions allowed identifying the role that plays each component of Ni-10La_2O_3/Na-BETA catalyst in reaction mechanism. In such catalytic system, exchanged Na^+ is responsible for CO_2 physisorption facilitating the posterior formation of carbonates, specially on lanthanum surface but also on zeolite surface and NiO sites. As in the case of alumina supported catalysts, formates adsorbed on Ni-La_2O_3 interface seems to be reaction intermediates, produced from hydrogenation of carbonates. However, this species is further hydrogenated into CH_4 via methoxy species formation rather than being decomposed into carbonyls, i.e., CO_2 methanation over La_2O_3-promoted catalysts occurs via a different mechanism. The Ni-La_2O_3/Na-BETA catalyst is a more efficient bifunctional catalyst than Ni/Na-BETA, in which the lanthanide promotes CO_2 activation and Ni exclusively dissociates H_2 to later reduce the adsorbed CO_2 species.

Chapter 9

NOMENCLATURE

9. NOMENCLATURE

Abbreviations and acronyms

BET	Brunauer, Emmet and Teller
BJH	Barret, Joyner and Halenda
EDX	Energy Dispersed X-Ray Spectroscopy
EPS	Electronic Pressure Controller
ETF	Enhanced Transparency Framework
FTIR	Fourier Transform Infrared Spectroscopy
FWHM	Full Width at Half Maximum
GAI	Glycerol Assisted Impregnation
GHG	Greenhouse Gases
GHSV	Gas Hour Space Velocity
GMST	Global Mean Surface Temperature
HAADF	High-Angle Annular Dark Field
ICDD	International Centre for Diffraction Data
IEA	International Energy Agency
IUPAC	International Union of Pure and Applied Chemistry
IPCC	Intergovernmental Panel on Climate Change
IWI	Incipient Wetness Impregnation
MFC	Mass Flow Controller
MS	Mass Spectroscopy
NDCs	Nationally Determined Contributions
PDF	Powder Diffraction File
PtG	Power to Gas
RDS	Rate Determining Step
RWGS	Reverse Water Gas Shift

SAT	Surface Air Temperature
SNG	Synthetic Natural Gas
SST	Sea Surface Temperature
STEM	Scanning Transmission Electron Microscopy
TCD	Thermal Conductivity Detector
TD	Thermal Decomposition
TEM	Transmission Electron Microscopy
TGA	Thermogravimetric Analysis
TIC	Temperature Indicator Controller
TPA	Temperature Programmed Adsorption
TPD	Temperature Programmed Desorption
TPO	Temperature Programmed Oxidation
TPR	Temperature Programmed Reduction
TPSR	Temperature Programmed Surface Reaction
UNFCCC	United Nations Framework Convention on Climate Change
UV-vis-NIR	Ultraviolet-visible-Near Infrared
WHSV	Weight Hour Space Velocity
XPS	X-Ray Photoelectron Spectroscopy
XRD	X-ray Diffraction
XRF	X-ray Fluorescence

Variables and physical constants

A_m	Cross-sectional area of a gas molecule, nm^2
atA_{Me}	Effective atomic metal area, $m^2\ atom^{-1}$
BE	Binding energy of the electron, eV
C	BET constant
c	Light speed, $299.79\ 10^6\ m\ s^{-1}$

D	Absolute mean deviation, %
$D_{ext.}$	Reactor external diameter, mm
D_{int}	Reactor internal diameter, mm
D_{Me}	Metal dispersion, %
d_{pore}	Pore size or diameter, nm
d	Metal particle diameter, nm
d_p	Diameter of catalyst particle, µm
E_{ap}	Apparent activation energy, kJ mol^{-1}
F_{Me}	Metal fraction in the catalyst, g_{Me} g^{-1}
F_i^{in}	Molar flow of species i at reactor inlet, mol min^{-1}
F_i^{out}	Molar flow of species i at reactor outlet, mol min^{-1}
h	Planck constant, 4.136 10^{-15} eV s
I_0	Metal-support perimeter per metal surface area, m^{-1}
k	kinetic constant
K	Adsorption constant
KE	Kinetic energy of the electron, eV
m	mass, g
Me	Metal type (Me = Ni or Ru)
MW	Molecular weight, g mol^{-1}
N_A	Avogadro constant, 6.023 10^{23} atom mol^{-1}
N_S	Metal surface atoms per catalyst gram
N_T	Total number of metal atoms per catalyst gram
P	Total pressure, bar
P_0	Saturation pressure, Pa
p_i	Partial pressure of species i, bar
Q	Volumetric feed flow, mL min^{-1}

R	Ideal gas constant, 8.314 J mol^{-1} g^{-1}
r_{CH_4}	Methane formation rate, mol h^{-1} g^{-1}
r_{CO}	CO formation rate, mol h^{-1} g^{-1}
$-r_{CO_2}$	CO_2 disappearance rate, mol h^{-1} g^{-1}
$-r_{CO_2}^0$	Initial reaction rate, mol h^{-1} g^{-1}
r_{pore}	Pore radius, Å
S_{BET}	BET surface area, m^2 g^{-1}
S_{EXT}	External surface area, m^2 g^{-1}
S_{CH_4}	Selectivity to CH_4, %
S_{CO}	Selectivity to CO, %
S_{Me}	Metal surface area, m^2 g^{-1}
T	Temperature, °C
T_{50}	Temperature to achieve 50% CO_2 conversion
TOF	Turn Over Frequency, h^{-1}
V_{des}	Desorbed volume per catalyst gram, cm^3 g^{-1}
V_m	Gas volume required to form a monolayer, cm^3 g^{-1}
V_{meso}	Mesopore volume, cm^3 g^{-1}
V_{micro}	Micropore volume, cm^3 g^{-1}
V_{mol}	Molar gas volume, cm^3 mol^{-1}
V_{pore}	Pore volume, cm^3 g^{-1}
W	Catalyst weight, g
W/F_{A0}	Space-time, g h mol^{-1}
X_{CO_2}	CO_2 conversion, %
Y_{CH_4}	CH_4 yield, %
Y_{CO}	CO yield, %

Greek letters

α	Apparent reaction order of CO_2
β	Apparent reaction order of H_2
β_{obs}	Experimental XRD peak width, °
β_{ins}	Instrumental contribution to peak width, °
δ	Deformation vibration frequency, cm^{-1}
ε_A	Molar volume change parameter
θ	Diffraction angle of coherent scattered radiation, °
λ	Wavelength, Å
ν	Stretching vibration frequency, cm^{-1}
ξ	Extension of reaction
υ	Contact angle
σ^2	Sum of squared residuals
τ	XRD crystallite size for Ni and Ru, nm
Φ	Work Function,
ψ	Surface tension of adsorbate, N m^{-1}

Chapter 10

REFERENCES

10. REFERENCES

[1] Core Writing Team, R.K. Pachauri and L.A. Meyer, “Climate Change 2014: Synthesis Report”, Intergovernmental Panel on Climate Change (IPCC) (2014) 151.

[2] G. Centi and S. Perathoner, "CO_2-based energy vectors for the storage of solar energy", Greenhouse Gas. Sci. Technol. 1 (2011) 21-35.

[3] K. Hashimoto, M. Yamasaki, K. Fujimura, T. Matsui, K. Izumiya, M. Komori, A.A. El-Moneim, E. Akiyama, H. Habazaki, N. Kumagai, A. Kawashima and K. Asami, "Global CO_2 recycling—novel materials and prospect for prevention of global warming and abundant energy supply", Mater. Sci. Eng. A 267 (1999) 200-206.

[4] J.P. Crank and L.S. Jacoby, "2 - What Is Global Warming?", in: "Crime, Violence, and Global Warming", J.P. Crank and L.S. Jacoby (Eds.), Anderson Publishing, Ltd., 2015, pp. 23-50.

[5] G.A. Florides and P. Christodoulides, "Global warming and carbon dioxide through sciences", Environ. Int. 35 (2009) 390-401.

[6] H. Jian-Bin, W. Shao-Wu, L. Yong, Z. Zong-Ci and W. Xin-Yu, "The Science of Global Warming", Adv. Clim. Chang. Res. 3 (2012) 174-178.

[7] J. Atkinson, "What is Earth’s Energy Budget? Five Questions with a Guy Who Knows". http://www.nasa.gov/feature/langley/what-is-earth-s-energy-budget-five-questions-with-a-guy-who-knows, 2017 (last accessed: May 2021).

[8] Nasa Earth Observatory, "Climate Forcings and Global Warming". https://earthobservatory.nasa.gov/features/EnergyBalance/page7.php, 2009 (last accessed: May 2021).

[9] M.R. Allen, O.P. Dube, W. Solecki, F. Aragón-Durand, W. Cramer, S. Humphreys, M. Kainuma, J. Kala, N. Mahowald, Y. Mulugetta, R. Perez, M. Wairiu and K. Zickfeld, "Framing and Context", in: "Global Warming of 1.5 °C", V. Masson-Delmotte, P. Zhai, H.-O. Pörtner, D. Roberts, J. Skea, P.R. Shukla, A. Pirani, W. Moufouma-Okia, C. Péan, R. Pidcock, S. Connors, J.B.R. Matthews, Y. Chen, X. Zhou, M.I. Gomis, E. Lonnoy, T. Maycock, M. Tignor and T. Waterfield (Eds.), Intergovernmental Panel on Climate Change (IPCC), 2018, pp. 49-91.

[10] R. Jackson, "The Effects of Climate Change". https://climate.nasa.gov/effects, (last accessed: May 2021).

[11] US Department of Commerce, NOAA, "Global Monitoring Laboratory - Carbon Cycle Greenhouse Gases". https://www.esrl.noaa.gov/gmd/ccgg/trends/mlo.html, (last accessed: May 2021).

[12] International Energy Agency, "Global Energy Review 2020, IEA, Paris". https://www.iea.org/reports/global-energy-review-2020, 2020 (last accessed: May 2021).

[13] International Energy Agency, "World Energy Outlook 2018, IEA, Paris". https://www.iea.org/reports/world-energy-outlook-2018, 2018 (last accessed: May 2021).

[14] UNFCCC, "What is the United Nations Framework Convention on Climate Change?". https://unfccc.int/process-and-meetings/the-convention/what-is-the-united-nations-framework-convention-on-climate-change, 2021 (last accessed: May 2021).

[15] L.C. Lau, K.T. Lee and A.R. Mohamed, "Global warming mitigation and renewable energy policy development from the Kyoto Protocol to the Copenhagen Accord—A comment", Renew. Sustain. Energy Rev. 16 (2012) 5280-5284.

[16] United Nations Framework Convention on Climate Change, "The Paris Agreement". https://unfccc.int/process-and-meetings/the-paris-agreement/the-paris-agreement, 2021 (last accessed: May 2021).

[17] M. Planelles, "Las medidas más importantes de la nueva ley de cambio climático". https://elpais.com/clima-y-medio-ambiente/2021-04-08/las-medidas-mas-importantes-de-la-nueva-ley-de-cambio-climatico.html, 2021 (last accessed: May 2021).

[18] International Energy Agency, "Sustainable Recovery, IEA, Paris". https://www.iea.org/reports/sustainable-recovery, 2020 (last accessed: May 2021).

[19] T. Abbasi and S.A. Abbasi, "Decarbonization of fossil fuels as a strategy to control global warming", Renew. Sustain. Energy Rev. 15 (2011) 1828-1834.

[20] International Energy Agency, "CCUS in Clean Energy Transitions, IEA, Paris". https://www.iea.org/reports/ccus-in-clean-energy-transitions, 2020 (last accessed: May 2021).

[21] M. Aresta, A. Dibenedetto and E. Quaranta, "State of the art and perspectives in catalytic processes for CO_2 conversion into chemicals and fuels: The distinctive contribution of chemical catalysis and biotechnology", J. Catal. 343 (2016) 2-45.

[22] International Energy Agency, "About CCUS, IEA, Paris". https://www.iea.org/reports/about-ccus, 2021 (last accessed: May 2021).

[23] C. Song, "Global challenges and strategies for control, conversion and utilization of CO_2 for sustainable development involving energy, catalysis, adsorption and chemical processing", Catal. Today 115 (2006) 2-32.

[24] International Energy Agency, "Hydrogen, IEA, Paris". https://www.iea.org/reports/hydrogen, 2020 (last accessed: May 2021).

[25] International Energy Agency, "The Future of Hydrogen, IEA, Paris". https://www.iea.org/reports/the-future-of-hydrogen, 2019 (last accessed: May 2021).

[26] A.V. da Rosa and J.C. Ordóñez, "Chapter 11 - Hydrogen Storage", in: "Fundamentals of Renewable Energy Processes", 4th edition, A.V. da Rosa and J.C. Ordóñez (Eds.), Academic Press, Oxford, 2022, pp. 471-516.

[27] G. Centi and S. Perathoner, "Opportunities and prospects in the chemical recycling of carbon dioxide to fuels", Catal. Today 148 (2009) 191-205.

[28] C. Chen, W. Cheng and S. Lin, "Study of iron-promoted Cu/SiO_2 catalyst on high temperature reverse water gas shift reaction", Appl. Catal. A: Gen. 257 (2004) 97-106.

[29] D. Scott L. Swartz, M. M. Seabaugh, C. T. Holt and W. J. Dawson, "Fuel processing catalysts based on nanoscale ceria", Fuel Cells Bulletin 4 (2001) 7-10.

[30] L. WANG, S. ZHANG and Y. LIU, "Reverse water gas shift reaction over Co-precipitated Ni-CeO_2 catalysts", J. Rare Earths 26 (2008) 66-70.

[31] X. Su, J. Xu, B. Liang, H. Duan, B. Hou and Y. Huang, "Catalytic carbon dioxide hydrogenation to methane: A review of recent studies", J. Energy Chem. 25 (2016) 553-565.

[32] A.A. Olajire, "Valorization of greenhouse carbon dioxide emissions into value-added products by catalytic processes", J. CO_2 Util. 3-4 (2013) 74-92.

[33] B.J. Liaw and Y.Z. Chen, "Liquid-phase synthesis of methanol from CO_2/H_2 over ultrafine CuB catalysts", Appl. Catal. A: Gen. 206 (2001) 245-256.

[34] F. Arena, K. Barbera, G. Italiano, G. Bonura, L. Spadaro and F. Frusteri, "Synthesis, characterization and activity pattern of Cu–ZnO/ZrO_2 catalysts in the hydrogenation of carbon dioxide to methanol", J. Catal. 249 (2007) 185-194.

[35] A.T. Aguayo, J. Ereña, I. Sierra, M. Olazar and J. Bilbao, "Deactivation and regeneration of hybrid catalysts in the single-step synthesis of dimethyl ether from syngas and CO_2", Catal. Today 106 (2005) 265-270.

[36] T. Riedel, M. Claeys, H. Schulz, G. Schaub, S. Nam, K. Jun, M. Choi, G. Kishan and K. Lee, "Comparative study of Fischer–Tropsch synthesis with H_2/CO and H_2/CO_2 syngas using Fe- and Co-based catalysts", Appl. Catal. A: Gen. 186 (1999) 201-213.

[37] S. Rönsch, J. Schneider, S. Matthischke, M. Schlüter, M. Götz, J. Lefebvre, P. Prabhakaran and S. Bajohr, "Review on methanation – From fundamentals to current projects", Fuel 166 (2016) 276-296.

[38] M. Götz, J. Lefebvre, F. Mörs, A. McDaniel Koch, F. Graf, S. Bajohr, R. Reimert and T. Kolb, "Renewable Power-to-Gas: A technological and economic review", Renew. Energy 85 (2016) 1371-1390.

[39] J. Gao, Y. Wang, Y. Ping, D. Hu, G. Xu, F. Gu and F. Su, "A thermodynamic analysis of methanation reactions of carbon oxides for the production of synthetic natural gas", RSC Adv. 2 (2012) 2358-2368.

[40] C. Jia, J. Gao, Y. Dai, J. Zhang and Y. Yang, "The thermodynamics analysis and experimental validation for complicated systems in CO_2 hydrogenation process", J. Energy Chem. 25 (2016) 1027-1037.

[41] K. Stangeland, D. Kalai, H. Li and Z. Yu, "CO_2 Methanation: The Effect of Catalysts and Reaction Conditions", Energy Procedia 105 (2017) 2022-2027.

[42] I. Hussain, A.A. Jalil, S.M. Izan, M.S. Azami, K. Kidam, N. Ainirazali and A. Ripin, "Thermodynamic and experimental explorations of CO_2 methanation over highly active metal-free fibrous silica-beta zeolite (FS@SiO_2-BEA) of innovative morphology", Chem. Eng. Sci. 229 (2021) 116015.

[43] S. Abate, C. Mebrahtu, E. Giglio, F. Deorsola, S. Bensaid, S. Perathoner, R. Pirone and G. Centi, "Catalytic Performance of γ-Al_2O_3–ZrO_2–TiO_2–CeO_2 Composite Oxide Supported Ni-Based Catalysts for CO_2 Methanation", Ind. Eng. Chem. Res. 55 (2016) 4451-4460.

[44] F. Song, Q. Zhong, Y. Yu, M. Shi, Y. Wu, J. Hu and Y. Song, "Obtaining well-dispersed Ni/Al_2O_3 catalyst for CO_2 methanation with a microwave-assisted method", Int. J. Hydrogen Energy 42 (2017) 4174-4183.

[45] D. Wierzbicki, R. Baran, R. Dębek, M. Motak, T. Grzybek, M.E. Gálvez and P. Da Costa, "The influence of nickel content on the performance of hydrotalcite-derived catalysts in CO_2 methanation reaction", Int. J. Hydrogen Energy 42 (2017) 23548-23555.

[46] M. Yamasaki, H. Habazaki, T. Yoshida, E. Akiyama, A. Kawashima, K. Asami, K. Hashimoto, M. Komori and K. Shimamura, "Compositional dependence of the CO_2 methanation activity of Ni/ZrO_2 catalysts prepared from amorphous NiZr alloy precursors", Appl. Catal. A: Gen. 163 (1997) 187-197.

[47] M. Li, H. Amari and A.C. van Veen, "Metal-oxide interaction enhanced CO_2 activation in methanation over ceria supported nickel nanocrystallites", Appl. Catal. B: Environ. 239 (2018) 27-35.

[48] J.H. Kwak, L. Kovarik and J. Szanyi, "CO_2 Reduction on Supported Ru/Al_2O_3 Catalysts: Cluster Size Dependence of Product Selectivity", ACS Catal. 3 (2013) 2449-2455.

[49] C. Janke, M.S. Duyar, M. Hoskins and R. Farrauto, "Catalytic and adsorption studies for the hydrogenation of CO_2 to methane", Appl. Catal. B: Environ. 152-153 (2014) 184-191.

[50] T. Abe, M. Tanizawa, K. Watanabe and A. Taguchi, "CO_2 methanation property of Ru nanoparticle-loaded TiO_2 prepared by a polygonal barrel-sputtering method", Energy Environ. Sci. 2 (2009) 315-321.

[51] D.C. Upham, A.R. Derk, S. Sharma, H. Metiu and E.W. McFarland, "CO_2 methanation by Ru-doped ceria: the role of the oxidation state of the surface", Catal. Sci. Technol. 5 (2015) 1783-1791.

[52] J.A.H. Dreyer, P. Li, L. Zhang, G.K. Beh, R. Zhang, P.H.-. Sit and W.Y. Teoh, "Influence of the oxide support reducibility on the CO_2 methanation over Ru-based catalysts", Appl. Catal. B: Environ. 219 (2017) 715-726.

[53] M.C. Bacariza, I. Graça, S.S. Bebiano, J.M. Lopes and C. Henriques, "Micro- and mesoporous supports for CO_2 methanation catalysts: A comparison between SBA-15, MCM-41 and USY zeolite", Chem. Eng. Sci. 175 (2018) 72-83.

[54] F. Ocampo, B. Louis, L. Kiwi-Minsker and A. Roger, "Effect of Ce/Zr composition and noble metal promotion on nickel based $Ce_xZr_{1-x}O_2$ catalysts for carbon dioxide methanation", Appl. Catal. A: Gen. 392 (2011) 36-44.

[55] D. Pandey and G. Deo, "Effect of support on the catalytic activity of supported Ni–Fe catalysts for the CO_2 methanation reaction", J. Ind. Eng. Chem. 33 (2016) 99-107.

[56] S. Tada, O.J. Ochieng, R. Kikuchi, T. Haneda and H. Kameyama, "Promotion of CO2 methanation activity and CH4 selectivity at low temperatures over Ru/CeO2/Al2O3 catalysts", Int. J. Hydrogen Energy 39 (2014) 10090-10100.

[57] G. Garbarino, C. Wang, T. Cavattoni, E. Finocchio, P. Riani, M. Flytzani-Stephanopoulos and G. Busca, "A study of Ni/La-Al_2O_3 catalysts: A competitive system for CO_2 methanation", Appl. Catal. B: Environ. 248 (2019) 286-297.

[58] Q. Liu, F. Gu, X. Lu, Y. Liu, H. Li, Z. Zhong, G. Xu and F. Su, "Enhanced catalytic performances of Ni/Al_2O_3 catalyst via addition of V_2O_3 for CO methanation", Appl. Catal. A: Gen. 488 (2014) 37-47.

[59] Iglesias, A. Quindimil, F. Mariño, U. De-La-Torre and J.R. González-Velasco, "Zr promotion effect in CO_2 methanation over ceria supported nickel catalysts", Int. J. Hydrogen Energy 44 (2019) 1710-1719.

[60] C. Perego and P. Villa, "Catalyst preparation methods", Catal. Today 34 (1997) 281-305.

[61] D.C. de Carvalho, J.M. Filho, O.P. Ferreira, A.C. Oliveira, E.M. Assaf and Y. Villasana, "Synthesis of Novel Catalytic Materials: Titania Nanotubes and Transition Metal Carbides, Nitrides, and Sulfides", in: "Advanced Catalytic Materials: Current Status and Future Progress", J.M. Domínguez-Esquivel and M.A. Ramos-Murillo (Eds.), Springer International Publishing, 2019, pp. 13-40.

[62] S. Gudyka, G. Grzybek, J. Gryboś, P. Indyka, B. Leszczyński, A. Kotarba and Z. Sojka, "Enhancing the deN_2O activity of the supported $Co_3O_4|\alpha$-Al_2O_3 catalyst by glycerol-assisted shape engineering of the active phase at the nanoscale", Appl. Catal. B: Environ. 201 (2017) 339-347.

[63] J. Zhao, Y. Liu, M. Fan, L. Yuan and X. Zou, "From solid-state metal alkoxides to nanostructured oxides: A precursor-directed synthetic route to functional inorganic nanomaterials", Inorg. Chem. Front. 2 (2015) 198-212.

[64] F. Pinna, "Supported metal catalysts preparation", Catal. Today 41 (1998) 129-137.

[65] A. Baiker, "Experimental methods for the characterization of catalysts. I. Gas adsorption methods, pycnometry and porosimetry", Int. Chem. Eng. 25:1 (1985).

[66] K. Oura, M. Katayama, A.V. Zotov, V.G. Lifshits and A.A. Saranin, "Atomic Structure of Surfaces with Adsorbates", in: "Surface Science: An Introduction", K. Oura, M. Katayama, A.V. Zotov, V.G. Lifshits and A.A. Saranin (Eds.), Springer, Berlin-Heidelberg, 2003, pp. 195-227.

[67] S.J. Gregg and J. Jacobs, "An examination of the adsorption theory of Brunauer, Emmett, and Teller, and Brunauer, Deming, Deming and Teller", Trans. Faraday Soc. 44 (1948) 574-588.

[68] S. Brunauer, P.H. Emmett and E. Teller, "Adsorption of Gases in Multimolecular Layers", J. Am. Chem. Soc. 60 (1938) 309-319.

[69] S.K.S. W, "Empirical method for analysis of adsorption isotherms.", Chem. Ind. (Chichester) (1968) 1520-1521.

[70] K. Kaneko, "Determination of pore size and pore size distribution: 1. Adsorbents and catalysts", J. Membr. Sci. 96 (1994) 59-89.

[71] P. Schneider, "Adsorption isotherms of microporous-mesoporous solids revisited", Appl. Catal. A: Gen. 129 (1995) 157-165.

[72] R. Geyer, J. Hunold, M. Keck, P. Kraak, A. Pachulski and R. Schödel, "Methods for Determining the Metal Crystallite Size of Ni Supported Catalysts", Chem. Ing. Tech. 84 (2012) 160-164.

[73] J. Okal, M. Zawadzki, L. Kępiński, L. Krajczyk and W. Tylus, "The use of hydrogen chemisorption for the determination of Ru dispersion in Ru/γ-alumina catalysts", Appl. Catal. A: Gen. 319 (2007) 202-209.

[74] H.P. Klug and L.E. Alexander, X-Ray Diffraction Procedures: For Polycrystalline and Amorphous Materials, 2nd Edition, Wiley, New York, 1974.

[75] B. Beckhoff, B. Kanngießer, N. Langhoff, R. Wedell and H. Wolff, Handbook of Practical X-Ray Fluorescence Analysis, Springer-Verlag, Berlin Heidelberg, 2006.

[76] J.M. Campos-Martín, "Espectroscopia fotoelectrónica de Rayos X (XPS)", in: "Técnicas de Análisis y Caracterización de Materiales", M. Faraldos and C. Goberna (Eds.), CSIC, Madrid, 2003, pp. 425-463.

[77] R.J. Gorte, "Temperature-programmed desorption for the characterization of oxide catalysts", Catal. Today 28 (1996) 405-414.

[78] S. Bhatia, J. Beltramini and D.D. Do, "Temperature programmed analysis and its applications in catalytic systems", Catal. Today 7 (1990) 309-438.

[79] J.M. Thomas and C. Ducati, "Transmission Electron Microscopy", in: "Characterization of Solid Materials and Heterogeneous Catalysts - From Structure to Surface Reactivity", M. Che and C. Védrine (Eds.), Wiley-VCH, Weinheim, 2012, pp. 655-701.

[80] Borodziński and M. Bonarowska, "Relation between Crystallite Size and Dispersion on Supported Metal Catalysts", Langmuir 13 (1997) 5613-5620.

[81] A. Muller and J. Grazul, "Optimizing the environment for sub-0.2 nm scanning transmission electron microscopy", J. Electron Microsc. 50 (2001) 219-226.

[82] D.A. Skoog, D.M. West, F.J. Holler and S.R. Crouch, Analytical Chemistry: An Introduction, 7th ed., Sounders College Pub., 2000.

[83] Schrader, Infrared and Raman Spectroscopy - Methods and Applications, VCH, Weinheim, 1995.

[84] B.M. Weckhuysen, In-situ spectroscopy of catalysts, American Scientific Publishers, Stevenson Ranch, Calif., 2004.

[85] G. Garbarino, D. Bellotti, P. Riani, L. Magistri and G. Busca, "Methanation of carbon dioxide on Ru/Al_2O_3 and Ni/Al_2O_3 catalysts at atmospheric pressure: Catalysts activation, behaviour and stability", Int. J. Hydrogen Energy 40 (2015) 9171-9182.

[86] Z. Boukha, C. Jiménez-González, B. de Rivas, J.R. González-Velasco, J.I. Gutiérrez-Ortiz and R. López-Fonseca, "Synthesis, characterisation and performance evaluation of spinel-derived Ni/Al_2O_3 catalysts for various methane reforming reactions", Appl. Catal. B: Environ. 158-159 (2014) 190-201.

[87] Mining.com, "Metal market". https://www.mining.com/markets/, (last accessed: June 2021).

[88] H.C. Wu, Y.C. Chang, J.H. Wu, J.H. Lin, I.K. Lin and C.S. Chen, "Methanation of CO_2 and reverse water gas shift reactions on Ni/SiO_2 catalysts: the influence of particle size on selectivity and reaction pathway", Catal. Sci. Technol. 5 (2015) 4154-4163.

[89] S. Rahmani, M. Rezaei and F. Meshkani, "Preparation of promoted nickel catalysts supported on mesoporous nanocrystalline gamma alumina for carbon dioxide methanation reaction", J. Ind. Eng. Chem. 20 (2014) 4176-4182.

[90] R. Daroughegi, F. Meshkani and M. Rezaei, "Enhanced activity of CO_2 methanation over mesoporous nanocrystalline Ni–Al_2O_3 catalysts prepared by ultrasound-assisted co-precipitation method", Int. J. Hydrogen Energy 42 (2017) 15115-15125.

[91] Wierzbicki, R. Debek, M. Motak, T. Grzybek, M.E. Gálvez and P. Da Costa, "Novel Ni-La-hydrotalcite derived catalysts for CO_2 methanation", Catal. Commun. 83 (2016) 5-8.

[92] R. Dębek, M. Radlik, M. Motak, M.E. Galvez, W. Turek, P. Da Costa and T. Grzybek, "Ni-containing Ce-promoted hydrotalcite derived materials as catalysts for methane reforming with carbon dioxide at low temperature – On the effect of basicity", Catal. Today 257 (2015) 59-65.

[93] Z. Boukha, C. Jiménez-González, M. Gil-Calvo, B. de Rivas, J.R. González-Velasco, J.I. Gutiérrez-Ortiz and R. López-Fonseca, "MgO/$NiAl_2O_4$ as a new formulation of reforming catalysts: Tuning the surface properties for the enhanced partial oxidation of methane", Appl. Catal. B: Environ. 199 (2016) 372-383.

[94] S. Toemen, Abu Bakar, Wan Azelee Wan and R. Ali, "Effect of ceria and strontia over Ru/Mn/Al_2O_3 catalyst: Catalytic methanation, physicochemical and mechanistic studies", J. CO_2 Util. 13 (2016) 38-49.

[95] E. Heracleous, A.F. Lee, K. Wilson and A.A. Lemonidou, "Investigation of Ni-based alumina-supported catalysts for the oxidative dehydrogenation of ethane to ethylene: structural characterization and reactivity studies", J. Catal. 231 (2005) 159-171.

[96] H. Li, H. Li, W. Dai, W. Wang, Z. Fang and J. Deng, "XPS studies on surface electronic characteristics of Ni–B and Ni–P amorphous alloy and its correlation to their catalytic properties", Appl. Surf. Sci. 152 (1999) 25-34.

[97] C. Heine, B.A.J. Lechner, H. Bluhm and M. Salmeron, "Recycling of CO_2: Probing the Chemical State of the Ni(111) Surface during the Methanation Reaction with Ambient-Pressure X-Ray Photoelectron Spectroscopy", J. Am. Chem. Soc. 138 (2016) 13246-13252.

[98] H. Kim, K. Kang, H. Kwak and J.H. Kim, "Preparation of supported Ni catalysts on various metal oxides with core/shell structures and their tests for the steam reforming of methane", Chem. Eng. J. 168 (2011) 775-783.

[99] C. Jiménez-González, Z. Boukha, B. de Rivas, J.J. Delgado, M.Á Cauqui, J.R. González-Velasco, J.I. Gutiérrez-Ortiz and R. López-Fonseca, "Structural characterisation of Ni/alumina reforming catalysts activated at high temperatures", Appl. Catal. A: Gen. 466 (2013) 9-20.

[100] K.S. Kim and N. Winograd, "X-Ray photoelectron spectroscopic studies of ruthenium-oxygen surfaces", J. Catal. 35 (1974) 66-72.

[101] S. Kawi, S.Y. Liu and S.-. Shen, "Catalytic decomposition and reduction of N_2O on Ru/MCM-41 catalyst", Catal. Today 68 (2001) 237-244.

[102] K. Qadir, S.H. Joo, B.S. Mun, D.R. Butcher, J.R. Renzas, F. Aksoy, Z. Liu, G.A. Somorjai and J.Y. Park, "Intrinsic Relation between Catalytic Activity of CO Oxidation on Ru Nanoparticles and Ru Oxides Uncovered with Ambient Pressure XPS", Nano Lett. 12 (2012) 5761-5768.

[103] S. Carenco, C. Sassoye, M. Faustini, P. Eloy, D.P. Debecker, H. Bluhm and M. Salmeron, "The Active State of Supported Ruthenium Oxide Nanoparticles during Carbon Dioxide Methanation", J. Phys. Chem. C 120 (2016) 15354-15361.

[104] A. Morales-Marín, J.L. Ayastuy, U. Iriarte-Velasco and M.A. Gutiérrez-Ortiz, "Nickel aluminate spinel-derived catalysts for the aqueous phase reforming of glycerol: Effect of reduction temperature", Appl. Catal. B: Environ. 244 (2019) 931-945.

[105] K. Ray and G. Deo, "A potential descriptor for the CO_2 hydrogenation to CH_4 over Al_2O_3 supported Ni and Ni-based alloy catalysts", Appl. Catal. B: Environ. 218 (2017) 525-537.

[106] P. Betancourt, A. Rives, R. Hubaut, C.E. Scott and J. Goldwasser, "A study of the ruthenium–alumina system", Appl. Catal. A: Gen. 170 (1998) 307-314.

[107] V. Mazzieri, F. Coloma-Pascual, A. Arcoya, P.C. L'Argentière and N.S. Fígoli, "XPS, FTIR and TPR characterization of Ru/Al_2O_3 catalysts", Appl. Surf. Sci. 210 (2003) 222-230.

[108] T. Mitsui, K. Tsutsui, T. Matsui, R. Kikuchi and K. Eguchi, "Support effect on complete oxidation of volatile organic compounds over Ru catalysts", Appl. Catal. B: Environ. 81 (2008) 56-63.

[109] R. Lanza, S.G. Järås and P. Canu, "Partial oxidation of methane over supported ruthenium catalysts", Appl. Catal. A: Gen. 325 (2007) 57-67.

[110] K. Kousi, D.I. Kondarides, X.E. Verykios and C. Papadopoulou, "Glycerol steam reforming over modified Ru/Al_2O_3 catalysts", Appl. Catal. A: Gen. 542 (2017) 201-211.

[111] D. Beierlein, D. Häussermann, M. Pfeifer, T. Schwarz, K. Stöwe, Y. Traa and E. Klemm, "Is the CO_2 methanation on highly loaded $Ni-Al_2O_3$ catalysts really structure-sensitive?", Appl. Catal. B: Environ. 247 (2019) 200-219.

[112] C.V. Miguel, A. Mendes and L.M. Madeira, "Intrinsic kinetics of CO_2 methanation over an industrial nickel-based catalyst", J. CO_2 Util. 25 (2018) 128-136.

[113] L. Falbo, M. Martinelli, C.G. Visconti, L. Lietti, C. Bassano and P. Deiana, "Kinetics of CO_2 methanation on a Ru-based catalyst at process conditions relevant for Power-to-Gas applications", Appl. Catal. B: Environ. 225 (2018) 354-363.

[114] S. Ewald, M. Kolbeck, T. Kratky, M. Wolf and O. Hinrichsen, "On the deactivation of Ni-Al catalysts in CO_2 methanation", Appl. Catal. A: Gen. 570 (2019) 376-386.

[115] A. Muñoz-Murillo, L.M. Martínez T., M.I. Domínguez, J.A. Odriozola and M.A. Centeno, "Selective CO methanation with structured RuO_2/Al_2O_3 catalysts", Appl. Catal. B: Environ. 236 (2018) 420-427.

[116] E.Z. Golosman and V.N. Efremov, "Industrial catalysts for the carbon oxides hydrogenation", Catal. Ind. (2012) 36-55.

[117] M.A. Ermakova and D.Y. Ermakov, "High-loaded nickel–silica catalysts for hydrogenation, prepared by sol–gel: Route: structure and catalytic behavior", Appl. Catal. A: Gen. 245 (2003) 277-288.

[118] G. Gahleitner, "Hydrogen from renewable electricity: An international review of power-to-gas pilot plants for stationary applications", Int. J. Hydrogen Energy 38 (2013) 2039-2061.

[119] I.A. Gondal, "Hydrogen integration in power-to-gas networks", Int. J. Hydrogen Energy 44 (2019) 1803-1815.

[120] M. Yue, H. Lambert, E. Pahon, R. Roche, S. Jemei and D. Hissel, "Hydrogen energy systems: A critical review of technologies, applications, trends and challenges", Renew. Sustain. Energy Rev.146 (2021) 111180.

[121] G. Garbarino, D. Bellotti, E. Finocchio, L. Magistri and G. Busca, "Methanation of carbon dioxide on Ru/Al_2O3: Catalytic activity and infrared study", Catal. Today 277 (2016) 21-28.

[122] B. Favier, D. Pla and M. Gómez, "Metal-based nanoparticles dispersed in glycerol: An efficient approach for catalysis", Catal. Today 310 (2018) 98-106.

[123] J. Liu, C. Li, F. Wang, S. He, H. Chen, Y. Zhao, M. Wei, D.G. Evans and X. Duan, "Enhanced low-temperature activity of CO_2 methanation over highly-dispersed Ni/TiO_2 catalyst", Catal. Sci. and Technol. 3 (2013) 2627-2633.

[124] X. Wang, Y. Hong, H. Shi and J. Szanyi, "Kinetic modeling and transient DRIFTS–MS studies of CO_2 methanation over Ru/Al_2O_3 catalysts", J. Catal. 343 (2016) 185-195.

[125] Y. Yan, Q. Wang, C. Jiang, Y. Yao, D. Lu, J. Zheng, Y. Dai, H. Wang and Y. Yang, "Ru/Al_2O_3 catalyzed CO_2 hydrogenation: Oxygen-exchange on metal-support interfaces", J. Catal. 367 (2018) 194-205.

[126] Q. Liu, Z. Zhong, F. Gu, X. Wang, X. Lu, H. Li, G. Xu and F. Su, "CO methanation on ordered mesoporous Ni–Cr–Al catalysts: Effects of the catalyst structure and Cr promoter on the catalytic properties", J. Catal. 337 (2016) 221-232.

[127] S. Navarro-Jaén, J.C. Navarro, L.F. Bobadilla, M.A. Centeno, O.H. Laguna and J.A. Odriozola, "Size-tailored Ru nanoparticles deposited over γ-Al_2O_3 for the CO_2 methanation reaction", Appl. Surf. Sci. 483 (2019) 750-761.

[128] A. Quindimil, U. De-La-Torre, B. Pereda-Ayo, A. Davó-Quiñonero, E. Bailón-García, D. Lozano-Castelló, J.A. González-Marcos, A. Bueno-López and J.R. González-Velasco, "Effect of metal loading on the CO_2 methanation: A comparison between alumina supported Ni and Ru catalysts", Catal. Today 356 (2020) 419-432.

[129] C. Ding, J. Wang, G. Ai, S. Liu, P. Liu, K. Zhang, Y. Han and X. Ma, "Partial oxidation of methane over silica supported Ni nanoparticles with size control by alkanol solvent", Fuel 175 (2016) 1-12.

[130] W. Wang, S. Wang, X. Ma and J. Gong, "Recent advances in catalytic hydrogenation of carbon dioxide", Chem. Soc. Rev. 40 (2011) 3703-3727.

[131] A. Cárdenas-Arenas, A. Quindimil, A. Davó-Quiñonero, E. Bailón-García, D. Lozano-Castelló, U. De-La-Torre, B. Pereda-Ayo, J.A. González-Marcos, J.R. González-Velasco and A. Bueno-López, "Design of active sites in Ni/CeO_2 catalysts for the methanation of CO_2: tailoring the Ni-CeO_2 contact", Appl. Mater. Today 19 (2020) 100591.

[132] M. Kourtelesis, P. Panagiotopoulou and X.E. Verykios, "Influence of structural parameters on the reaction of low temperature ethanol steam reforming over Pt/Al_2O_3 catalysts", Catal. Today 258 (2015) 247-255.

[133] D. Duprez, P. Pereira, A. Miloudi and R. Maurel, "Steam dealkylation of aromatic hydrocarbons: II. Role of the support and kinetic pathway of oxygenated species in toluene steam dealkylation over group VIII metal catalysts", J. Catal. 75 (1982) 151-163.

[134] C. Vogt, E. Groeneveld, G. Kamsma, M. Nachtegaal, L. Lu, C.J. Kiely, P.H. Berben, F. Meirer and B.M. Weckhuysen, "Unravelling structure sensitivity in CO_2 hydrogenation over nickel", Nat. Catal. 1 (2018) 127-134.

[135] J.M. Rynkowski, T. Paryjczak and M. Lenik, "Characterization of alumina supported nickel-ruthenium systems", Appl. Catal. A: Gen. 126 (1995) 257-271.

[136] S. Kikkawa, K. Teramura, H. Asakura, S. Hosokawa and T. Tanaka, "Isolated Platinum Atoms in Ni/γ-Al_2O_3 for Selective Hydrogenation of CO_2 toward CH_4", J. Phys. Chem. C 123 (2019) 23446-23454.

[137] S. Tada, D. Minori, F. Otsuka, R. Kikuchi, K. Osada, K. Akiyama and S. Satokawa, "Effect of Ru and Ni ratio on selective CO methanation over Ru–Ni/TiO_2", Fuel 129 (2014) 219-224.

[138] C. Yuan, N. Yao, X. Wang, J. Wang, D. Lv and X. Li, "The SiO_2 supported bimetallic Ni–Ru particles: A good sulfur-tolerant catalyst for methanation reaction", Chem. Eng. J. 260 (2015) 1-10.

[139] K.K. Mohaideen, W. Kim, K.Y. Koo and W.L. Yoon, "Highly dispersed Ni particles on Ru/NiAl catalyst derived from layered double hydroxide for selective CO methanation", Catal. Commun. 60 (2015) 8-13.

[140] S. Li, D. Gong, H. Tang, Z. Ma, Z. Liu and Y. Liu, "Preparation of bimetallic Ni@Ru nanoparticles supported on SiO_2 and their catalytic performance for CO methanation", Chem. Eng. J. 334 (2018) 2167-2178.

[141] Q. Liu, S. Wang, G. Zhao, H. Yang, M. Yuan, X. An, H. Zhou, Y. Qiao and Y. Tian, "CO_2 methanation over ordered mesoporous NiRu-doped CaO-Al_2O_3 nanocomposites with enhanced catalytic performance", Int. J. Hydrogen Energy 43 (2018) 239-250.

[142] L. Wei, N. Kumar, W. Haije, J. Peltonen, M. Peurla, H. Grénman and W. de Jong, "Can bi-functional nickel modified 13X and 5A zeolite catalysts for CO_2 methanation be improved by introducing ruthenium?", Mol. Catal. 494 (2020) 111115.

[143] M.I. Alymov, N.M. Rubtsov, B.S. Seplyarskii, R.A. Kochetkov, V.A. Zelensky and A.B. Ankudinov, "Combustion and passivation of nickel nanoparticles", Mendeleev Commun. 27 (2017) 631-633.

[144] S. Velu and S.K. Gangwal, "Synthesis of alumina supported nickel nanoparticle catalysts and evaluation of nickel metal dispersions by temperature programmed desorption", Solid State Ion. 177 (2006) 803-811.

[145] A. Solis-Garcia, J.F. Louvier-Hernandez, A. Almendarez-Camarillo and J.C. Fierro-Gonzalez, "Participation of surface bicarbonate, formate and methoxy species in the carbon dioxide methanation catalyzed by ZrO_2-supported Ni", Appl. Catal. B: Environ. 218 (2017) 611-620.

[146] C. Liang, L. Zhang, Y. Zheng, S. Zhang, Q. Liu, G. Gao, D. Dong, Y. Wang, L. Xu and X. Hu, "Methanation of CO_2 over nickel catalysts: Impacts of acidic/basic sites on formation of the reaction intermediates", Fuel 262 (2020) 116521.

[147] A. Cárdenas-Arenas, A. Quindimil, A. Davó-Quiñonero, E. Bailón-García, D. Lozano-Castelló, U. De-La-Torre, B. Pereda-Ayo, J.A. González-Marcos, J.R. González-Velasco and A. Bueno-López, "Isotopic and in situ DRIFTS study of the CO_2 methanation mechanism using Ni/CeO_2 and Ni/Al_2O_3 catalysts", Appl. Catal. B: Environ. 265 (2020) 118538.

[148] Westermann, B. Azambre, M.C. Bacariza, I. Graça, M.F. Ribeiro, J.M. Lopes and C. Henriques, "Insight into CO_2 methanation mechanism over NiUSY zeolites: An operando IR study", Appl. Catal. B: Environ. 174-175 (2015) 120-125.

[149] Morterra, A. Zecchina, S. Coluccia and A. Chiorino, "I.r. spectroscopic study of CO2 adsorption onto η-Al_2O_3", J. Chem. Soc., Faraday Trans. 73 (1977) 1544-1560.

[150] J.I. Di Cosimo, V.K. Díez, M. Xu, E. Iglesia and C.R. Apesteguía, "Structure and Surface and Catalytic Properties of Mg-Al Basic Oxides", J. Catal. 178 (1998) 499-510.

[151] K. Föttinger, R. Schlögl and G. Rupprechter, "The mechanism of carbonate formation on Pd-Al_2O_3 catalysts", Chem. Commun. (2008) 320-322.

[152] M.B. Jensen, S. Morandi, F. Prinetto, A.O. Sjåstad, U. Olsbye and G. Ghiotti, "FT-IR characterization of supported Ni-catalysts: Influence of different supports on the metal phase properties", Catal. Today 197 (2012) 38-49.

[153] Q. Pan, J. Peng, T. Sun, S. Wang and S. Wang, "Insight into the reaction route of CO_2 methanation: Promotion effect of medium basic sites", Catal. Commun. 45 (2014) 74-78.

[154] T. Burger, F. Koschany, O. Thomys, K. Köhler and O. Hinrichsen, "CO_2 methanation over Fe- and Mn-promoted co-precipitated Ni-Al catalysts: Synthesis, characterization and catalysis study", Appl. Catal. A: Gen. 558 (2018) 44-54.

[155] G. Poncelet, M.A. Centeno and R. Molina, "Characterization of reduced α-alumina-supported nickel catalysts by spectroscopic and chemisorption measurements", Appl. Catal. A: Gen. 288 (2005) 232-242.

[156] P. Panagiotopoulou, "Hydrogenation of CO_2 over supported noble metal catalysts", Appl. Catal. A: Gen. 542 (2017) 63-70.

[157] P. Panagiotopoulou, D.I. Kondarides and X.E. Verykios, "Mechanistic Study of the Selective Methanation of CO over Ru/TiO_2 Catalyst: Identification of Active Surface Species and Reaction Pathways", J. Phys. Chem. C 115 (2011) 1220-1230.

[158] T. Burger, P. Donaubauer and O. Hinrichsen, "On the kinetics of the co-methanation of CO and CO_2 on a co-precipitated Ni-Al catalyst", Appl. Catal. B: Environ. 282 (2021) 119408.

[159] P. Sabatier and J.-B. Senderens, Comptes Rendus Des Séances De L'Académie Des Sciences, Section VI–Chimie, Imprimerie Gauthier-Villars, Paris (1902).

[160] G.A. Mills and F.W. Steffgen, "Catalytic methanation", Catal. Rev. Sci. Eng. 8 (1974) 159-210.

[161] M.A. Vannice, "The catalytic synthesis of hydrocarbons from carbon monoxide and hydrogen", Catal. Rev. Sci. and Eng. 14 (1976) 153-191.

[162] I. Alstrup, "On the Kinetics of CO Methanation on Nickel Surfaces", J. Catal. 151 (1995) 216-225.

[163] S. Roensch, J. Koechermann, J. Schneider and S. Matthischke, "Global Reaction Kinetics of CO and CO_2 Methanation for Dynamic Process Modeling", Chem. Eng. Technol 39 (2016) 208-218.

[164] G.D. Weatherbee and C.H. Bartholomew, "Hydrogenation of CO_2 on group VIII metals. Kinetics and mechanism of CO_2 hydrogenation on Nickel", J. Catal. 77 (1982) 460-472.

[165] K. Jalama, "Carbon dioxide hydrogenation over nickel-, ruthenium-, and copper-based catalysts: Review of kinetics and mechanism", Catal. Rev.-Sci. and Eng. 59 (2017) 95-164.

[166] J.L. Falconer and A.E. Zağli, "Adsorption and methanation of carbon dioxide on a nickel/silica catalyst", J. Catal. 62 (1980) 280-285.

[167] P.A.U. Aldana, F. Ocampo, K. Kobl, B. Louis, F. Thibault-Starzyk, M. Daturi, P. Bazin, S. Thomas and A.C. Roger, "Catalytic CO_2 valorization into CH_4 on Ni-based ceria-zirconia. Reaction mechanism by operando IR spectroscopy", Catal. Today 215 (2013) 201-207.

[168] F. Koschany, D. Schlereth and O. Hinrichsen, "On the kinetics of the methanation of carbon dioxide on coprecipitated $NiAl(O)_x$", Appl. Catal. B: Environ. 181 (2016) 504-516.

[169] P. Marocco, E.A. Morosanu, E. Giglio, D. Ferrero, C. Mebrahtu, A. Lanzini, S. Abate, S. Bensaid, S. Perathoner, M. Santarelli, R. Pirone and G. Centi, "CO_2 methanation over Ni/Al hydrotalcite-derived catalyst: Experimental characterization and kinetic study", Fuel 225 (2018) 230-242.

[170] I. Champon, A. Bengaouer, A. Chaise, S. Thomas and A. Roger, "Carbon dioxide methanation kinetic model on a commercial Ni/Al_2O_3 catalyst", J. CO_2 Util. 34 (2019) 256-265.

[171] J. Lefebvre, S. Bajohr and T. Kolb, "A comparison of two-phase and three-phase CO_2 methanation reaction kinetics", Fuel 239 (2019) 896-904.

[172] A. Loder, M. Siebenhofer and S. Lux, "The reaction kinetics of CO_2 methanation on a bifunctional Ni/MgO catalyst", J. Ind. Eng. Chem. 85 (2020) 196-207.

[173] Z. Bian, Y.M. Chan, Y. Yu and S. Kawi, "Morphology dependence of catalytic properties of Ni/CeO_2 for CO_2 methanation: A kinetic and mechanism study", Catal. Today 347 (2020) 31-38.

[174] M.S. Duyar, A. Ramachandran, C. Wang and R.J. Farrauto, "Kinetics of CO_2 methanation over $Ru/\gamma\text{-}Al_2O_3$ and implications for renewable energy storage applications", J. CO_2 Util. 12 (2015) 27-33.

[175] J.B. Anderson, "A criterion for isothermal behaviour of a catalyst pellet", Chem. Eng. Sci. 18 (1963) 147-148.

[176] D.E. Mears, "Tests for Transport Limitations in Experimental Catalytic Reactors", Ind. Eng. Chem. Process Des. and Dev. 10 (1971) 541-547.

[177] D. Förtsch, "On the basic effects on the gas composition governed by the water-gas shift equilibrium", Energy 205 (2020) 117883.

[178] J. Xu, X. Su, H. Duan, B. Hou, Q. Lin, X. Liu, X. Pan, G. Pei, H. Geng, Y. Huang and T. Zhang, "Influence of pretreatment temperature on catalytic performance of rutile TiO_2-supported ruthenium catalyst in CO_2 methanation", J. Catal. 333 (2016) 227-237.

[179] H. Takano, Y. Kirihata, K. Izumiya, N. Kumagai, H. Habazaki and K. Hashimoto, "Highly active Ni/Y-doped ZrO_2 catalysts for CO_2 methanation", Appl. Surf. Sci. 388 (2016) 653-663.

[180] F. Wang, S. He, H. Chen, B. Wang, L. Zheng, M. Wei, D.G. Evans and X. Duan, "Active Site Dependent Reaction Mechanism over Ru/CeO_2 Catalyst toward CO_2 Methanation", J. Am. Chem. Soc. 138 (2016) 6298-6305.

[181] T. Sakpal and L. Lefferts, "Structure-dependent activity of CeO_2 supported Ru catalysts for CO_2 methanation", J. Catal. 367 (2018) 171-180.

[182] T.A. Le, M.S. Kim, S.H. Lee, T.W. Kim and E.D. Park, "CO and CO_2 methanation over supported Ni catalysts", Catal. Today 293-294 (2017) 89-96.

[183] T.F. Degnan, "Applications of zeolites in petroleum refining", Top. Catal. 13 (2000) 349-356.

[184] A. Primo and H. Garcia, "Zeolites as catalysts in oil refining", Chem. Soc. Rev. 43 (2014) 7548-7561.

[185] D. Barthomeuf, "Acidity and Basicity in Zeolites", Stud. Surf. Sci. Catal. 65 (1991) 157-169.

[186] A. Bermejo-López, B. Pereda-Ayo, J.A. González-Marcos and J.R. González-Velasco, "Ni loading effects on dual function materials for capture and in-situ conversion of CO_2 to CH_4 using CaO or Na_2CO_3", J. CO_2 Util. 34 (2019) 576-587.

[187] M.C. Bacariza, M. Biset-Peiro, I. Graca, J. Guilera, J. Morante, J.M. Lopes, T. Andreu and C. Henriques, "DBD plasma-assisted CO_2 methanation using zeolite-based catalysts: Structure composition-reactivity approach and effect of Ce as promoter", J. CO_2 Util. 26 (2018) 202-211.

[188] B. Smit and T.L.M. Maesen, "Towards a molecular understanding of shape selectivity", Nature 451 (2008) 671-678.

[189] A.M. Vos, P. Mignon, P. Geerlings, F. Thibault-Starzyk and R.A. Schoonheydt, "Probing the basicity of zeolite frameworks with N_2O_4: A DFT approach", Micropor. Mesopor. Mat. 90 (2006) 370-376.

[190] G.D. Pirngruber, P. Raybaud, Y. Belmabkhout, J. Cejka and A. Zukal, "The role of the extra-framework cations in the adsorption of CO_2 on faujasite Y", Phys. Chem. Chem. Phys. 12 (2010) 13534-13546.

[191] M.C. Bacariza, R. Bértolo, I. Graça, J.M. Lopes and C. Henriques, "The effect of the compensating cation on the catalytic performances of Ni/USY zeolites towards CO_2 methanation", J. CO_2 Util. 21 (2017) 280-291.

[192] S. Yang, J. Kim and W. Ahn, "CO_2 adsorption over ion-exchanged zeolite beta with alkali and alkaline earth metal ions", Micropor. Mesopor. Mat. 135 (2010) 90-94.

[193] P. Concepción-Heydorn, C. Jia, D. Herein, N. Pfänder, H.G. Karge and F.C. Jentoft, "Structural and catalytic properties of sodium and cesium exchanged X and Y zeolites, and germanium-substituted X zeolite", J. Mol. Catal. A Chem. 162 (2000) 227-246.

[194] A.N. Pinheiro, A. Valentini, J.M. Sasaki and A.C. Oliveira, "Highly stable dealuminated zeolite support for the production of hydrogen by dry reforming of methane", Appl. Catal. A: Gen. 355 (2009) 156-168.

[195] G. Naresh, V. Vijay Kumar, C. Anjaneyulu, J. Tardio, S.K. Bhargava, J. Patel and A. Venugopal, "Nano size Hβ zeolite as an effective support for Ni and NiCu for CO_x free hydrogen production by catalytic decomposition of methane", Int. J. Hydrogen Energy 41 (2016) 19855-19862.

[196] J. Dědeček, L. Čapek, D. Kaucký, Z. Sobalík and B. Wichterlová, "Siting and Distribution of the Co Ions in Beta Zeolite: A UV–Vis–NIR and FTIR Study", J. Catal. 211 (2002) 198-207.

[197] A. Śrębowata, R. Baran, D. Łomot, D. Lisovytskiy, T. Onfroy and S. Dzwigaj, "Remarkable effect of postsynthesis preparation procedures on catalytic properties of Ni-loaded BEA zeolites in hydrodechlorination of 1,2-dichloroethane", Appl. Catal. B: Environ. 147 (2014) 208-220.

[198] A. Śrębowata, I. Zielińska, R. Baran, G. Słowik and S. Dzwigaj, "Ag–Ni bimetallic SiBEA zeolite as an efficient catalyst of hydrodechlorination of 1,2-dichloroethane towards ethylene", Catal. Commun. 69 (2015) 154-160.

[199] I. Graça, L.V. González, M.C. Bacariza, A. Fernandes, C. Henriques, J.M. Lopes and M.F. Ribeiro, "CO_2 hydrogenation into CH_4 on NiHNaUSY zeolites", Appl. Catal. B: Environ. 147 (2014) 101-110.

[200] M.C. Bacariza, I. Graça, A. Westermann, M.F. Ribeiro, J.M. Lopes and C. Henriques, "CO_2 Hydrogenation Over Ni-Based Zeolites: Effect of Catalysts Preparation and Pre-reduction Conditions on Methanation Performance", Top. Catal. 59 (2016) 314-325.

[201] M. Suzuki, K. Tsutsumi, H. Takahashi and Y. Saito, "T.p.r. study on reducibility of nickel ions in zeolite Y", Zeolites 9 (1989) 98-103.

[202] A. Luengnaruemitchai and A. Kaengsilalai, "Activity of different zeolite-supported Ni catalysts for methane reforming with carbon dioxide", Chem. Eng. J. 144 (2008) 96-102.

[203] J. Aguado, D.P. Serrano, J.M. Escola and L. Briones, "Deactivation and regeneration of a Ni supported hierarchical Beta zeolite catalyst used in the hydroreforming of the oil produced by LDPE thermal cracking", Fuel 109 (2013) 679-686.

[204] D.P. Serrano, J.M. Escola, L. Briones, S. Medina and A. Martínez, "Hydroreforming of the oils from LDPE thermal cracking over Ni–Ru and Ru supported over hierarchical Beta zeolite", Fuel 144 (2015) 287-294.

[205] P.M. Lima, T. Garetto, C.L. Cavalcante and D. Cardoso, "Isomerization of n-hexane on Pt–Ni catalysts supported on nanocrystalline H-BEA zeolite", Catal. Today 172 (2011) 195-202.

[206] T. Lehmann, T. Wolff, C. Hamel, P. Veit, B. Garke and A. Seidel-Morgenstern, "Physico-chemical characterization of Ni/MCM-41 synthesized by a template ion exchange approach", Micropor. Mesopor. Mat. 151 (2012) 113-125.

[207] Z. Zheng, C. Sun, R. Dai, S. Wang, X. Wu, X. An, Z. Wu and X. Xie, "Ethanol Steam Reforming on Ni-Based Catalysts: Effect of Cu and Fe Addition on the Catalytic Activity and Resistance to Deactivation", Energy Fuels 31 (2017) 3091-3100.

[208] J. Ren, H. Guo, J. Yang, Z. Qin, J. Lin and Z. Li, "Insights into the mechanisms of CO_2 methanation on Ni(111) surfaces by density functional theory", Appl. Surf. Sci. 351 (2015) 504-516.

[209] Z. Boukha, L. Fitian, M. López-Haro, M. Mora, J.R. Ruiz, C. Jiménez-Sanchidrián, G. Blanco, J.J. Calvino, G.A. Cifredo, S. Trasobares and S. Bernal, "Influence of the calcination temperature on the nano-structural properties, surface basicity, and catalytic behavior of alumina-supported lanthana samples", J. Catal. 272 (2010) 121-130.

[210] A.S. Al-Fatesh, M.A. Naeem, A.H. Fakeeha and A.E. Abasaeed, "Role of La_2O_3 as Promoter and Support in Ni/γ-Al_2O_3 Catalysts for Dry Reforming of Methane", Chin. J. Chem. Eng. 22 (2014) 28-37.

[211] Y. Cui, H. Zhang, H. Xu and W. Li, "The CO_2 reforming of CH_4 over Ni/La_2O_3/α-Al_2O_3 catalysts: The effect of La_2O_3 contents on the kinetic performance", Appl. Catal. A: Gen. 331 (2007) 60-69.

[212] S. Kang, D. Lee and S. Kwon, "Lanthanum doping for longevity of alumina catalyst bed in hydrogen peroxide thruster", Aerosp. Sci. Technol. 46 (2015) 197-203.

[213] P. Alphonse and B. Faure, "Thermal stabilization of alumina modified by lanthanum", Micropor. Mesopor. Mat. 196 (2014) 191-198.

[214] D. Wierzbicki, R. Baran, R. Dębek, M. Motak, M.E. Gálvez, T. Grzybek, P. Da Costa and P. Glatzel, "Examination of the influence of La promotion on Ni state in hydrotalcite-derived catalysts under CO_2 methanation reaction conditions: Operando X-ray absorption and emission spectroscopy investigation", Appl. Catal. B: Environ. 232 (2018) 409-419.

[215] W. Ahmad, M.N. Younis, R. Shawabkeh and S. Ahmed, "Synthesis of lanthanide series (La, Ce, Pr, Eu & Gd) promoted Ni/γ-Al_2O_3 catalysts for methanation of CO_2 at low temperature under atmospheric pressure", Catal. Commun. 100 (2017) 121-126.

[216] B. Pawelec, R. Mariscal, R.M. Navarro, J.M. Campos-Martin and J.L.G. Fierro, "Simultaneous 1-pentene hydroisomerisation and thiophene hydrodesulphurisation over sulphided Ni/FAU and Ni/ZSM-5 catalysts", Appl. Catal. A: Gen. 262 (2004) 155-166.

[217] R. Yang, C. Xing, C. Lv, L. Shi and N. Tsubaki, "Promotional effect of La_2O_3 and CeO_2 on Ni/γ-Al_2O_3 catalysts for CO_2 reforming of CH_4", Appl. Catal. A: Gen. 385 (2010) 92-100.

[218] D. Wierzbicki, M. Motak, T. Grzybek, M.E. Gálvez and P. Da Costa, "The influence of lanthanum incorporation method on the performance of nickel-containing hydrotalcite-derived catalysts in CO_2 methanation reaction", Catal. Today 307 (2018) 205-211.

[219] A. Quindimil, U. De-La-Torre, B. Pereda-Ayo, J.A. González-Marcos and J.R. González-Velasco, "Ni catalysts with La as promoter supported over Y- and BETA- zeolites for CO_2 methanation", Appl. Catal. B: Environ. 238 (2018) 393-403.

[220] S. Sato, R. Takahashi, M. Kobune and H. Gotoh, "Basic properties of rare earth oxides", Appl. Catal. A: Gen. 356 (2009) 57-63.

[221] V. Alcalde-Santiago, A. Davó-Quiñonero, D. Lozano-Castelló, A. Quindimil, U. De-La-Torre, B. Pereda-Ayo, J.A. González-Marcos, J.R. González-Velasco and A. Bueno-López, "Ni/LnOx Catalysts (Ln=La, Ce or Pr) for CO_2 Methanation", ChemCatChem 11 (2019) 810-819.

[222] E. Köck, M. Kogler, T. Bielz, B. Klötzer and S. Penner, "In Situ FT-IR Spectroscopic Study of CO_2 and CO Adsorption on Y_2O_3, ZrO_2, and Yttria-Stabilized ZrO_2", J. Phys. Chem. C 117 (2013) 17666-17673.

[223] Q. Pan, J. Peng, S. Wang and S. Wang, "In situ FTIR spectroscopic study of the CO_2 methanation mechanism on Ni/$Ce_{0.5}Zr_{0.5}O_2$", Catal. Sci. Technol. 4 (2014) 502-509.

[224] A. Westermann, B. Azambre, M.C. Bacariza, I. Graça, M.F. Ribeiro, J.M. Lopes and C. Henriques, "The promoting effect of Ce in the CO_2 methanation performances on NiUSY zeolite: A FTIR In Situ/Operando study", Catal. Today 283 (2017) 74-81.

[225] S. Sharma, K.B. Sravan Kumar, Y.M. Chandnani, V.S. Phani Kumar, B.P. Gangwar, A. Singhal and P.A. Deshpande, "Mechanistic Insights into CO_2 Methanation over Ru-Substituted CeO_2", J. Phys. Chem. C 120 (2016) 14101-14112.

[226] F. Thibault-Starzyk and F. Maugé, "Infrared Spectroscopy", in: "Characterization of Solid Materials and Heterogeneous Catalysts: From Structure to Surface Reactivity", M. Che and J.C. Védrine (Eds.), Wiley-VCH Verlag GmbH & Co. KGaA., 2012, pp. 3-48.

[227] J.P. Marques, I. Gener, P. Ayrault, J.C. Bordado, J.M. Lopes, F. Ramôa Ribeiro and M. Guisnet, "Infrared spectroscopic study of the acid properties of dealuminated BEA zeolites", Micropor. Mesopor. Mat. 60 (2003) 251-262.

[228] G. Busca and V. Lorenzelli, "Infrared spectroscopic identification of species arising from reactive adsorption of carbon oxides on metal oxide surfaces", Mater. Chem. 7 (1982) 89-126.

[229] S.E. Siporin, B.C. McClaine and R.J. Davis, "Adsorption of N_2 and CO_2 on Zeolite X Exchanged with Potassium, Barium, or Lanthanum", Langmuir 19 (2003) 4707-4713.

[230] R.W. Stevens Jr., R.V. Siriwardane and J. Logan, "In situ Fourier transform infrared (FTIR) investigation of CO_2 adsorption onto zeolite materials", Energy Fuels 22 (2008) 3070-3079.

[231] A. Villarreal, P. Castillo-Villalón and J. Ramírez, "Analysis of the interaction of CO_2 with Na, K, and Ca-exchanged Mordenite. An infrared spectroscopic study", J. Mex. Chem. Soc. 61 (2017) 102-108.

[232] Q. Liu, A. Mace, Z. Bacsik, J. Sun, A. Laaksonen and N. Hedin, "NaKA sorbents with high CO_2-over-N_2 selectivity and high capacity to adsorb CO_2", Chem. Commun. 46 (2010) 4502-4504.

[233] P. Galhotra, J.G. Navea, S.C. Larsen and V.H. Grassian, "Carbon dioxide ($C^{16}O_2$ and $C^{18}O_2$) adsorption in zeolite Y materials: effect of cation, adsorbed water and particle size", Energy Environ. Sci. 2 (2009) 401-409.

[234] M.P. Rosynek and D.T. Magnuson, "Infrared study of carbon dioxide adsorption on lanthanum sesquioxide and trihydroxide", J. Catal. 48 (1977) 417-421.

[235] Z. Zhang, X.E. Verykios, S.M. MacDonald and S. Affrossman, "Comparative Study of Carbon Dioxide Reforming of Methane to Synthesis Gas over Ni/La_2O_3 and Conventional Nickel-Based Catalysts", J. Phys. Chem. 100 (1996) 744-754.

[236] A. Slagtern, Y. Schuurman, C. Leclercq, X. Verykios and C. Mirodatos, "Specific Features Concerning the Mechanism of Methane Reforming by Carbon Dioxide over Ni/La_2O_3 Catalyst", J. Catal. 172 (1997) 118-126.

[237] V.A. Tsipouriari, Z. Zhang and X.E. Verykios, "Catalytic Partial Oxidation of Methane to Synthesis Gas over Ni-Based Catalysts: I. Catalyst Performance Characteristics", J. Catal. 179 (1998) 283-291.

[238] G.B. Deacon and R.J. Phillips, "Relationships between the carbon-oxygen stretching frequencies of carboxylato complexes and the type of carboxylate coordination", Coord. Chem. Rev. 33 (1980) 227-250.

[239] J. Gao, L. Jia, W. Fang, Q. Li and H. Song, "Methanation of carbon dioxide over the $LaNiO_3$ perovskite catalysts activated under the reactant stream", J. Fuel Chem. Technol. 37 (2009) 573-577.

[240] P. Riani, I. Valsamakis, T. Cavattoni, V. Sanchez Escribano, G. Busca and G. Garbarino, "Ni/SiO_2-Al_2O_3 catalysts for CO_2 methanation: Effect of La_2O_3 addition", Appl. Catal. B: Environ. 284 (2021) 119697.

[241] P.G. Gopal, R.L. Schneider and K.L. Watters, "Evidence for production of surface formate upon direct reaction of CO with alumina and magnesia", J. Catal. 105 (1987) 366-372.

[242] C. Li, K. Domen, K. Maruya and T. Onishi, "Spectroscopic identification of adsorbed species derived from adsorption and decomposition of formic acid, methanol, and formaldehyde on cerium oxide", J. Catal. 125 (1990) 445-455.

[243] P. Hongmanorom, J. Ashok, G. Zhang, Z. Bian, M.H. Wai, Y. Zeng, S. Xi, A. Borgna and S. Kawi, "Enhanced performance and selectivity of CO_2 methanation over phyllosilicate structure derived Ni-Mg/SBA-15 catalysts", Appl. Catal. B: Environ. 282 (2021) 119564.

[244] X. Jia, X. Zhang, N. Rui, X. Hu and C. Liu, "Structural effect of Ni/ZrO_2 catalyst on CO_2 methanation with enhanced activity", Appl. Catal. B: Environ. 244 (2019) 159-169.

[245] M. Agnelli, H.M. Swaan, C. Marquez-Alvarez, G.A. Martin and C. Mirodatos, "CO Hydrogenation on a Nickel Catalyst: II. A Mechanistic Study by Transient Kinetics and Infrared Spectroscopy", J. Catal. 175 (1998) 117-128.

[246] M. Marwood, R. Doepper and A. Renken, "In-situ surface and gas phase analysis for kinetic studies under transient conditions: The catalytic hydrogenation of CO_2", Appl. Catal. A: Gen. 151 (1997) 223-246.

[247] A. Quindimil, M.C. Bacariza, J.A. González-Marcos, C. Henriques and J.R. González-Velasco, "Enhancing the CO_2 methanation activity of γ-Al_2O_3 supported mono- and bi-metallic catalysts prepared by glycerol assisted impregnation", Appl. Catal. B: Environ. 296 (2021) 120322.

[248] X. Wang, L. Zhu, Y. Zhuo, Y. Zhu and S. Wang, "Enhancement of CO_2 Methanation over La-Modified Ni/SBA-15 Catalysts Prepared by Different Doping Methods", ACS Sustain. Chem. Eng. 7 (2019) 14647-14660.

APPENDIX A

MATHEMATICAL EXPRESSIONS

APPENDIX A. MATHEMATICAL EXPRESSIONS

A1. ASSESSMENT OF HEAT TRANSFER LIMITATIONS

In order to assess heat transfer limitation Anderson's and Mear´s criteria are employed. For both criteria, initial reaction rates ($-r^0_{CO_2}$) in Table 5.2 are inserted as observed reaction rates r_A^{obs} in mol kg^{-1} s^{-1} and the activation energy (E_A) is considered similar to the apparent one (E_{ap}) expressed in kJ mol^{-1}.

Intraparticle heat transport can be ignored if the Anderson´s criterion is fulfilled:

$$\frac{\left(-r_A^{obs}\right)\cdot\left|\Delta H_{Rx}\right|\cdot\rho_{cat.}\cdot r_{cat.}^2}{\lambda\cdot T} < \frac{0.75\cdot R\cdot T}{E_A} \qquad \text{(A1.1)}$$

where ΔH_{RX} is the reaction heat (kJ mol^{-1}), $\rho_{cat.}$ is the solid density of catalyst pellet (kg m^{-3}), $r_{cat.}$ is the radius of catalyst pellet (m), λ is the thermal conductivity of the gas phase approximated by the rule of Wassiljeva (kW m^{-1} K^{-1}) and R is the ideal gas constant (8.31 10^{-3} kJ mol^{-1} K^{-1}).

External heat transfer limitation can be neglected if the Mears' criterion is satisfied:

$$\frac{\left(-r_A^{obs}\right)\cdot\rho_b\cdot r_{cat.}\cdot E_{ap}\cdot\left|\Delta H_{Rx}\right|}{h\cdot T^2\cdot R} < 0.15 \qquad \text{(A1.2)}$$

where ρ_b is the bulk density of the catalyst bed (kg m^{-3}) and h is the heat transfer coefficient between gas and pellet (kW m^{-2} s^{-1}) calculated assuming that Nusselt number is 2, since the Reynolds number for this system is much smaller than 1.

A2. DERIVATION OF LHHW KINETIC RATE EQUATION FROM DISSOCIATIVE CO FORMATION MECHANISM

The kinetic rate equation is derived analogously to the methodology of reference [168] and from mechanism proposed in Table 5.3. The CO_2 disappearance rate is equal to the

rate of elementary step 4 (formation of formyl species), which is considered as rate determining step:

$$-r_{CO_2} = r_4 = k_4 \Theta_{CO} \Theta_H \tag{A2.1}$$

where Θ_{CO} and Θ_H are the coverages of hydrogen and carbonyl and k_4 is the forward kinetic constant of elementary step 4.

The coverage of hydrogen is easily derived by assuming dissociative Langmuir adsorption in quasi-equilibrium:

$$k_1 p_{H_2} \Theta_*^2 = k_{-1} \Theta_H \tag{A2.2}$$

$$\Theta_H = \sqrt{\frac{k_1}{k_{-1}} p_{H_2} \Theta_*^2} = \sqrt{K_1 p_{H_2}} \Theta_* \tag{A2.3}$$

where K_1 is the equilibrium constant of step 1 and Θ_* is the fraction of free active sites. On the other hand, carbonyls arise from dissociative adsorption of CO_2, which is also assumed as Langmuir adsorption in quasi-equilibrium.

$$k_2 p_{CO_2} \Theta_*^2 = k_{-2} \Theta_{CO} \Theta_O \tag{A2.4}$$

$$\Theta_{CO} = \frac{k_2}{k_{-2}} \frac{p_{CO_2} \Theta_*^2}{\Theta_O} = K_2 \frac{p_{CO_2} \Theta_*^2}{\Theta_O} \tag{A2.5}$$

At steady state, the oxygen hydrogenation rate (step 8) is two times the rate of carbonyls hydrogenation (RDS). Then,

$$r_8 = k_8 \Theta_O \Theta_H = 2\left(-r_{CO_2}\right) = 2k_3 \Theta_O \Theta_H \tag{A2.6}$$

and the oxygen coverage can be expressed as function of carbonyls coverage:

$$\Theta_O = \frac{2k_3 \Theta_{CO}}{k_6} \tag{A2.7}$$

Inserting equation A2.7 in Equation A2.5, CO coverage finally results in:

$$\Theta_{CO} = K_2 \frac{p_{CO_2}\Theta_*^2}{2k_4\Theta_{CO}/k_8} \rightarrow \Theta_{CO}^2 = K_2 \frac{p_{CO_2}\Theta_*^2 k_8}{2k_4} \rightarrow \Theta_{CO} = \sqrt{\frac{K_2 k_8}{2k_4} p_{CO_2}}\,\Theta_* \qquad \text{(A2.8)}$$

Thus, the reaction rate can be expressed as:

$$-r_{CO_2} = k_4\Theta_{CO}\Theta_H = k_4\sqrt{\frac{K_2 k_8}{2k_4} p_{CO_2}}\,\Theta_*\sqrt{K_1 p_{H_2}}\,\Theta_* = k_4\sqrt{\frac{K_2 k_8 K_1}{2k_4} p_{CO_2} p_{H_2}}\,\Theta_*^2 \qquad \text{(A2.9)}$$

Assuming that dissociated hydrogen atoms, carbonyls and hydroxyls are the most abundant surface intermediates (MASI) the balance of active sites can be formulated as follows:

$$1 = \Theta_* + \Theta_H + \Theta_{CO} + \Theta_{OH} \qquad \text{(A2.10)}$$

$$\Theta_{CO}^2 = K_2 \frac{p_{CO_2}\Theta_*^2 k_8}{2k_4} \rightarrow \Theta_{CO} = \sqrt{\frac{K_2 k_8}{2k_4} p_{CO_2}}\,\Theta_* \qquad \text{(A2.11)}$$

Considering that steps 9 and 10 are in equilibrium the hydroxyl coverage can be expressed as:

$$k_9\Theta_{OH}\Theta_H = k_{-9}\Theta_{H_2O}\Theta_* \;\rightarrow\; \Theta_{OH} = \frac{k_{-9}}{k_9}\frac{\Theta_{H_2O}\Theta_*}{\Theta_H} = \frac{\Theta_{H_2O}}{K_9\sqrt{K_1 p_{H_2}}} \qquad \text{(A2.12)}$$

where the water coverage can be expressed as function of water partial pressure:

$$k_{10}\Theta_{H_2O} = k_{-10}p_{H_2O} \;\rightarrow\; \Theta_{H_2O} = \frac{k_{-10}}{k_{10}} p_{H_2O}\Theta_* = \frac{p_{H_2O}}{K_{10}}\Theta_* \qquad \text{(A2.13)}$$

Then, the hydroxyl coverage is defined as:

$$\Theta_{OH} = \frac{p_{H_2O}\Theta_*}{K_9 K_{10}\sqrt{K_1 p_{H_2}}} \qquad \text{(A2.14)}$$

Introducing equation A2.3, A2.8 and A2.15 in equation A2.11, the fraction of free active sites can be formulated as function of known variables:

$$1 = \Theta_* + \sqrt{K_1 p_{H_2}}\,\Theta_* + \sqrt{\frac{K_2 k_8}{2k_4} p_{CO_2}}\,\Theta_* + \frac{p_{H_2O}\Theta_*}{K_9 K_{10}\sqrt{K_1 p_{H_2}}} \tag{A2.15}$$

$$\Theta_* = \frac{1}{1 + \sqrt{K_1 p_{H_2}} + \sqrt{\frac{K_2 k_8}{2k_4} p_{CO_2}} + \frac{p_{H_2O}}{K_{10} K_9 \sqrt{K_1 p_{H_2}}}} \tag{A2.16}$$

Finally, considering the thermodynamic equilibrium, the reaction rate results in:

$$-r_{CO_2} = \frac{k_4 \sqrt{\frac{K_2 k_8 K_1}{2k_4} p_{CO_2} p_{H_2}}}{\left(1 + \sqrt{K_1 p_{H_2}} + \sqrt{\frac{K_2 k_8}{2k_4} p_{CO_2}} + \frac{p_{H_2O}}{K_{10} K_9 \sqrt{K_1 p_{H_2}}}\right)^2} \tag{A2.17}$$

Grouping constants in convenience, the reaction rate is expressed as:

$$-r_{CO_2} = \frac{k_4 p_{CO_2}^{0.5} p_{H_2}^{0.5} \left(1 - \frac{p_{CH_4} p_{H_2O}^2}{p_{CO_2} p_{H_2}^4 K_{Eq1}}\right)}{\left(1 + \sqrt{K_{H_2} p_{H_2}} + \sqrt{K_{CO_2} p_{CO_2}} + K_{OH} \frac{p_{H_2O}}{p_{H_2}^{0.5}}\right)^2} \tag{A2.18}$$

A3. DERIVATION OF LHHW KINETIC RATE EQUATIONS FROM H-ASSISTED CO FORMATION MECHANISM

The CO_2 disappearance rate equation as well as CH_4 and CO formation rates equations are deduced from H-assisted CO formation mechanism proposed in Table 5.4. The CO_2 disappearance rate is equal to the rate of elementary step 4 (decomposition of formates into CO).

$$-r_{CO_2} = r_4 = k_4 \Theta_{HCOO} \Theta_* \tag{A3.1}$$

Considering that Langmuir H_2 adsorption (step 1) is in quasi-equilibrium, the H_2 coverage can be expressed as:

$$k_1 p_{H_2} \Theta_*^2 = k_{-1} \Theta_H \rightarrow \Theta_H = \sqrt{\frac{k_1}{k_{-1}} p_{H_2} \Theta_*^2} = \sqrt{K_1 p_{H_2}} \Theta_* \tag{A3.2}$$

According to this mechanism, CO_2 is molecularly adsorbed on OH^- groups of Al_2O_3 in form of bicarbonates (step 2), which are further hydrogenated into formates (step 3). Assuming that step 2 and 3 are also in quasi-equilibrium, the bicarbonates coverage is easily accessible:

$$k_2 p_{CO_2} \Theta_{OH} = k_{-2} \Theta_{HCO_3} \rightarrow \Theta_{HCO_3} = \frac{k_2}{k_{-2}} p_{CO_2} \Theta_{OH} = K_2 p_{CO_2} \Theta_{OH} \tag{A3.3}$$

and the formates coverage:

$$k_3 \Theta_{HCO_3} \Theta_H = k_{-3} \Theta_{HCOO} \Theta_{OH} \rightarrow \Theta_{HCOO} = \frac{k_3}{k_{-3}} \frac{\Theta_{HCO_3} \Theta_H}{\Theta_{OH}} = K_3 \frac{\Theta_{HCO_3} \Theta_H}{\Theta_{OH}} \tag{A3.4}$$

which after inserting the coverage of hydrogen (Equation A3.2) and bicarbonates (Equation A3.4) results in:

$$\Theta_{HCOO} = \frac{K_2 K_3 p_{CO_2} \Theta_{OH} \sqrt{K_1 p_{H_2}} \Theta_*}{\Theta_{OH}} = K_2 K_3 p_{CO_2} \sqrt{K_1 p_{H_2}} \Theta_* \tag{A3.5}$$

Then, replacing formates coverage in Equation A3.1 the rate equation can be formulated as:

$$-r_{CO_2} = k_4 K_2 K_3 \sqrt{K_1} p_{CO_2} \sqrt{p_{H_2}} \Theta_*^2 \tag{A3.6}$$

Assuming that hydrogen dissociated atoms, formates, carbonyls and hydroxyls occupy most of the active sites, the active sites balance is expressed as:

$$1 = \Theta_* + \Theta_H + \Theta_{HCOO} + \Theta_{CO} + \Theta_{OH} \tag{A3.7}$$

The carbonyls coverage is derived from step 5 in quasi-equilibrium:

$$k_5\Theta_{CO} = k_{-5}p_{CO}\Theta_* \rightarrow \Theta_{CO} = \frac{k_{-5}}{k_5}p_{CO}\Theta_* = \frac{p_{CO}}{K_5}\Theta_* \tag{A3.8}$$

whereas the coverage of hydroxyls is derived assuming step 11 in quasi-equilibrium and low H_2O coverage in step 12.

$$k_{11}\Theta_{OH}\Theta_H = k_{-11}\Theta_{H_2O}\Theta_* \rightarrow \Theta_{OH} = \frac{k_{-11}}{k_{11}}\frac{\Theta_{H_2O}\Theta_*}{\Theta_H} = \frac{\Theta_{H_2O}}{K_{11}\sqrt{K_1 p_{H_2}}} \tag{A3.9}$$

where the water coverage can be expressed as function of water partial pressure:

$$k_{12}\Theta_{H_2O} = k_{-12}p_{H_2O} \rightarrow \Theta_{H_2O} = \frac{k_{-12}}{k_{12}}p_{H_2O}\Theta_* = \frac{p_{H_2O}}{K_{12}}\Theta_* \tag{A3.10}$$

Then, the hydroxyl coverage is defined as:

$$\Theta_{OH} = \frac{p_{H_2O}\Theta_*}{K_{11}K_{12}\sqrt{K_1 p_{H_2}}} \tag{A3.11}$$

Introducing Equations A3.2, A3.7, A3.9 and A3.12 in equation A3.8, the fraction of free active sites can be formulated as function of known variables:

$$1 = \Theta_* + \sqrt{K_1 p_{H_2}}\Theta_* + K_2K_3p_{CO_2}\sqrt{K_1 p_{H_2}}\Theta_* + \frac{p_{CO}}{K_5}\Theta_* + \frac{p_{H_2O}\Theta_*}{K_{11}K_{12}\sqrt{K_1 p_{H_2}}} \tag{A3.12}$$

$$\Theta_* = \frac{1}{1 + \sqrt{K_1 p_{H_2}} + K_2K_3p_{CO_2}\sqrt{K_1 p_{H_2}} + \frac{p_{CO}}{K_5} + \frac{p_{H_2O}}{K_{11}K_{12}\sqrt{K_1 p_{H_2}}}} \tag{A3.13}$$

Considering the thermodynamic equilibrium of RWGS the reaction rate is written as:

$$-r_{CO_2} = \frac{k_4 K_2 K_3 \sqrt{K_1} p_{CO_2} \sqrt{p_{H_2}} \left(1 - \frac{p_{CO} p_{H_2O}}{p_{CO_2} p_{H_2} K_{eq2}}\right)}{\left(1 + \sqrt{K_1 p_{H_2}} + K_2 K_3 p_{CO_2} \sqrt{K_1 p_{H_2}} + \frac{p_{CO}}{K_5} + \frac{p_{H_2O}}{K_{11} K_{12} \sqrt{K_1 p_{H_2}}}\right)^2} \quad \text{(A3.14)}$$

which, after grouping adsorption constants for convenience results in:

$$-r_{CO_2} = \frac{k_4 p_{CO_2} p_{H_2}^{0.5} \left(1 - \frac{p_{CO} p_{H_2O}}{p_{CO_2} p_{H_2} K_{eq2}}\right)}{\left(1 + \sqrt{K_{H_2} p_{H_2}} + K_{CO_2} p_{CO_2} \sqrt{K_{H_2} p_{H_2}} + K_{OH} \frac{p_{H_2O}}{p_{H_2}^{0.5}} + K_{CO} p_{CO}\right)^2} \quad \text{(A3.15)}$$

On the other hand, the rate of CH_4 formation is considered the same as that of step 6 (formation of formyl species):

$$r_{CH_4} = r_6 = k_6 \Theta_{CO} \Theta_H \quad \text{(A3.16)}$$

Inserting the coverages of carbonyl (Equation A3.9) and hydrogen (Equation A3.2) defined above, the CH_4 formation rate is expressed as:

$$r_{CH_4} = k_6 \frac{p_{CO}}{K_5} \Theta_* \sqrt{K_1 p_{H_2}} \Theta_* \rightarrow r_{CH_4} = k_6 \frac{\sqrt{K_1}}{K_5} p_{CO} p_{H_2}^{0.5} \Theta_*^2 \quad \text{(A3.17)}$$

As the active site over which CH_4 is formed is assumed to be the same as that for formates decomposition (Ni-Al_2O_3 interface), the fraction of free active sites can be considered equal. Then,

$$r_{CH_4} = \frac{k_6 \frac{\sqrt{K_1}}{K_5} p_{CO} p_{H_2}^{0.5}}{\left(1 + \sqrt{K_1 p_{H_2}} + K_2 K_3 p_{CO_2} \sqrt{K_1 p_{H_2}} + \frac{p_{CO}}{K_5} + \frac{p_{H_2O}}{K_{11} K_{12} \sqrt{K_1 p_{H_2}}}\right)^2} \quad \text{(A3.18)}$$

Grouping constants similarly and considering equilibrium of CO methanation, the CH_4 formation rate results in:

$$r_{CH_4} = \frac{k_6 p_{CO} p_{H_2}^{0.5} \left(1 - \frac{p_{CH_4} p_{H_2O}}{p_{CO} p_{H_2}^3 K_{eq3}} \right)}{\left(1 + \sqrt{K_{H_2} p_{H_2}} + K_{CO_2} p_{CO_2} \sqrt{K_{H_2} p_{H_2}} + K_{OH} \frac{p_{H_2O}}{p_{H_2}^{0.5}} + K_{CO} p_{CO} \right)^2} \qquad \text{(A3.19)}$$

Finally, being CO the only by-product, its formation rate is deduced by difference:

$$r_{CO} = \left(-r_{CO_2} \right) - r_{CH_4} \qquad \text{(A3.20)}$$

APPENDIX B

LIST OF DERIVED CONTRIBUTIONS

APPENDIX B. LIST OF DERIVED CONTRIBUTIONS

B1. SCIENTIFIC PUBLICATIONS

Authors: A. Quindimil, U. De-La-Torre, B. Pereda-Ayo, J.A. González-Marcos, J.R. González-Velasco.

Title: Ni catalysts with La as promoter supported over Y- and BETA- zeolites for CO_2 methanation.

Source: Appl. Catal. B: Environ. 238 (2018) 393-403.

Impact factor (2018): 14.229.

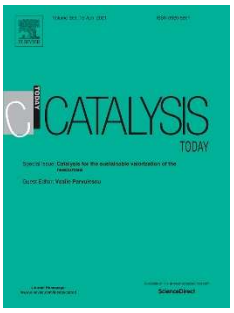

Authors: A. Quindimil, U. De-La-Torre, B. Pereda-Ayo, A. Davó-Quiñonero, E. Bailón-Garcia, D. Lozano-Castelló, J.A. González-Marcos, A. Bueno-López, J.R. González-Velasco.

Title: Effect of metal loading on the CO_2 methanation: A comparison between alumina supported Ni and Ru catalysts.

Source: Catal. Today 356 (2020) 419-432.

Impact factor (2020): 5.825.

Authors: A. Quindimil, M.C. Bacariza, J.A. González-Marcos, C. Henriques, J.R. González-Velasco.

Title: Enhancing the CO_2 methanation activity of γ-Al_2O_3 supported mono- and bi-metallic catalysts prepared by glycerol assisted impregnation.

Source: Appl. Catal B: Environ. 296 (2021) 120322.

Impact factor (2021): n.a.

B2. CONGRESS CONTRIBUTIONS

II Encuentro de Jóvenes Investigadores de la Sociedad Española de Catálisis (JJII 2016), Ciudad Real (Spain), 27-29 June 2016.

Contribution type: Flash Oral.

Title: Catalizadores Ni/zeolita para metanación de CO_2.

Authors: A. Quindimil, B. Pereda-Ayo, U. De-La-Torre, J.A. González-Marcos, J.R. González-Velasco.

Reunión de la Sociedad Española de Catálisis (SECAT'17), Oviedo (Spain), 26-28 June 2017.

Contribution type: Oral.

Title: Catalizadores Ru/Al_2O_3 para la conversión de CO_2 en gas natural sintético (GNS).

Authors: A. Quindimil, B. Pereda-Ayo, J.A. González-Marcos, J.R. González-Velasco.

13th European Congress on Catalysis (EUROPACAT 2017), Florence (Italy), 27-31 August 2017.

Contribution type: Poster.

Title: Alumina supported Ni and Ru catalysts for CO2 Hydrogenation to methane.

Authors: A. Quindimil, B. Pereda-Ayo, J.A. González-Marcos, J.R. González-Velasco.

10th World Congress of Chemical Engineering (WCCE10), Barcelona (Spain), 1-5 October 2017.

Contribution type: Oral.

Title: Ca- and La-promoted Ni/BETA catalysts for CO_2 methanation.

Authors: A. Quindimil, B. Pereda-Ayo, José A. González-Marcos, J.R. González-Velasco.

III Encuentro de Jóvenes Investigadores de la Sociedad Española de Catálisis (JJII 2018), Valencia (Spain), 25-27 June 2018.

Contribution type: Poster.

Title: Catalizadores bimetálicos Ni-Ru/Al_2O_3 para la producción de gas natural sintético.

Authors: A. Quindimil, A. Bermejo, U. De-La-Torre, B. Pereda-Ayo, J.A. González-Marcos, J.R. González- Velasco.

Reunión Bienal de la Sociedad Española de Catálisis (SECAT'19), Córdoba (Spain), 24-26 June 2019.

Contribution type: Poster.

Title: Aspectos cinéticos comparativos de Ni/Al_2O_3 y Ru/Al_2O_3 en la metanación de CO_2.

Authors: A. Quindimil, U. De-La-Torre, A. Davó-Quiñonero, E Bailón-García, D. Lozano-Castelló, J.A. González-Marcos, A. Bueno-López, J.R. González-Velasco.

14th European Congress on Catalysis (EUROPACAT 2019), Florence (Italy), 18-23 August 2019.

Contribution type: Poster.

Title: Bimetallic catalysts for CO_2 hydrogenation: Effect of Ru addition on alumina supported Ni dispersion.

Authors: A. Quindimil, A. Bermejo-López, U. De-La-Torre, B. Pereda-Ayo, J.A. González-Marcos, J.R. González-Velasco.

IV Encuentro de Jóvenes Investigadores de la Sociedad Española de Catálisis (JJII 2020), Bilbao (Spain), 21-23 September 2020.

Contribution type: Oral.

Title: Metanación de CO_2 sobre catalizadores de Ni/Al_2O_3 optimizados.

Authors: A. Quindimil, M.C. Bacariza, J.M. Lopes, J.A. González-Marcos, C. Henriques, J.R. González-Velasco.